New numerical solutions for the description of volcanic particle dispersal

Tsunematsu, Kae

How to cite

TSUNEMATSU, Kae. New numerical solutions for the description of volcanic particle dispersal. 2012. doi: 10.13097/archive-ouverte/unige:26675

This publication URL: https://archive-ouverte.unige.ch//unige:26675
Publication DOI: 10.13097/archive-ouverte/unige:26675

UNIVERSITÉ DE GENÈVE
Section de Science de la Terre
Département de Minéralogie

FACULTÉ DES SCIENCES
Professeur Costanza Bonadonna
Professeur Bastien Chopard

NEW NUMERICAL SOLUTIONS FOR THE DESCRIPTION OF VOLCANIC PARTICLE DISPERSAL

THÈSE

présentée à la Faculté des sciences de l'Université de Genève
pour obteinr le grade de Docteur en sciences, mention Sciences de la Terre

par

Kae TSUNEMATSU
de
Yokohama (Japon)

Thèse N° 4521

GENÈVE
2012

UNIVERSITÉ
DE GENÈVE

FACULTÉ DES SCIENCES

Doctorat ès sciences
Mention sciences de la Terre

Thèse de *Madame Kae TSUNEMATSU*

intitulée :

"New Numerical Solutions for the Description of Volcanic Particle Dispersal"

La Faculté des sciences, sur le préavis de Madame C. BONADONNA, professeure associée et directrice de thèse (Département de minéralogie), de Monsieur B. CHOPARD, professeur ordinaire et codirecteur de thèse (Département d'informatique), J.-L. FALCONE, docteur (Département d'informatique), A. COSTA, docteur (Istituto Nazionale di Geofisica e Vulcanologia, Sezione di Napoli, Italia) et Ch. HUBER, professeur (School of Earth and Atmospheric Sciences, Georgia Institute of Technology, Atlanta, United States of America), autorise l'impression de la présente thèse, sans exprimer d'opinion sur les propositions qui y sont énoncées.

Genève, le 17 janvier 2013

Thèse - 4521 -

Le Doyen, Jean-Marc TRISCONE

N.B. - La thèse doit porter la déclaration précédente et remplir les conditions énumérées dans les "Informations relatives aux thèses de doctorat à l'Université de Genève".

Acknowledgement

At first, I would like to thank my supervisors Prof. Costanza Bonadonna and Prof. Bastien Chopard. They not only gave me an opportunity to come back to research field but also supported me for whole five years academically and privately. I would like to also thank Dr. Jean-Luc Falcone who is a great teacher of programming and one of my best friends.

I am very grateful to Prof. Jeremy Phillips at University of Bristol for the advice of plume dynamics, and Prof. Roland Bouffanais at Singapore University of Technology and Design for his lecture and advice of turbulent theory.

I thank all my collegues of our volcanology group, Licia, Sebastian, Celine, Wim, Fabiricio, Laura, Irene, Mohsen, Linda, Helen, Riccardo, Federico and also Coline. I was very lucky to have another office in Battelle and I would like to thank my colleagues there: Andrea, Christoph, Daniel (Lagrava),Bernd, Ranaivo, Orestis, Jonas, Yann, Mohamed, Xavier. I would like to appreciate technical and admistrative support of Nicolas, Daniel (Agulleiro) and Germaine.

I am so grateful to all professors and my friends from Section of Earth Sciences, especially Lina and Christina helped me from the beginning of my project.

My abstract in French is translated by Prof. Marie Augendre at University Lumiere Lyon2. I would like to express my appreciation to her as she cheered me when I was writing my thesis privately as well.

My friends in Geneva and Japan helped me too. I am grateful for them. I would like to Special Thanks to Marie-Franoise and Family Rivest for their heartwarming hospitality. They treated me as a member of the family and I could not finish my thesis if they were not there.

At last but not least, I would like to thank my parents and my sister to support anytime, anywhere even I was not in good condition. They never leave me alone. It is my great honor to be a daughter of Kuniko and Tomofumi Tsunematsu and to be a sister of Eiko Tsunematsu Asano.

Contents

Résumé

Lorsque les volcans entrent en éruption de manière explosive, ils rejettent de grandes quantités de particules de toutes tailles (du micron au mètre) qui se dispersent dans l'atmosphère avant de se déposer au sol sous forme de tephra. Les modèles numériques de transport et de dispersion de ces particules sont importants à la fois pour l'évaluation des aléa associés et pour la compréhension des dynamiques éruptives. Les particules les plus grosses (blocs et bombes) sont généralement rapidement découplées de la phase gazeuse et suivent des trajectoires paraboliques indépendantes. Lapilli et cendres ($< 64\ mm$) sont d'ordinaire transportés à l'intérieur d'un panache vertical qui s'étend finalement horizontalement [*umbrella cloud*], lorsque un équilibre de densité est atteint. Les lapilli et cendres les plus grossiers reviennent au sol en quelques heures, tandis que les cendres les plus fines peuvent rester en suspension dans l'atmosphère durant des jours voire des semaines.

Les études de la distribution granulométrique totale donnent des indications sur les dynamiques éruptives et les mécanismes de fragmentation. Elles sont nécessaires aux simulations numériques du transport et de la dispersion des particules. Néanmoins, cette distribution est difficile à mesurer précisement, principalement en raison de la piètre conservation des dépôts de tephra. A partir d'une comparaison quantitative de données de terrain et de simulations numériques, nous montrons comment les dépôts de tephra des grandes éruptions explosives doivent être échantillonnés au moins jusqu'à 100-300 km du cratère afin d'en dériver la distribution granulométrique complète, cendres fines incluses.

Plusieurs modèles de dispersion des tephra existent déjà dans la littérature, mais des aspects importants du transport et de la sédimentation des particules requièrent toujours de meilleurs paramétrages. Les modéles d'automates cellulaires et la méthode de Boltzmann sur reséau fournissent des solutions numériques simples pour des systèmes physiques très compliqués ; ils peuvent être aisément améliorés en ajoutant de nouveaux processus physiques. Il a notamment été démontré que les automates cellulaires (CA) sont, sur le plan computationnel, plus efficace que la méthode de Boltzmann sur reséau (LB) pour décrire le transport et la dispersion des particules.

Nous avons tout d'abord développé un modèle CA à deux dimensions (2D), avec une libération des particules depuis le point d'inflexion d'un panache vertical [*plume corner*], qui montre une bonne correspondance avec

les observations de terrain pour les grandes éruptions explosives. Par contre, la description de la dispersion à partir de panaches inclinés [*bent-over plumes*] et de la sédimentation par agrégation a besoin d'un meilleur paramétrage. Le modèle CA en 2D a donc été étendu à la troisième dimension (3D).

Dans notre modèle CA en 3D, les particules sont libérées depuis le cratère, transportes à l'intérieur du panache puis dispersées dans l'atmosphère. La diffusion des particules est décrite à partir d'une vitesse aléatoire, qui correspond aux variations de vitesse de la turbulence. La prise en compte de la dynamique du panache améliore significativement la description des particules dans la région proximale du cratère ($< 50km$). Les stratégies des CA combinent les avantages des méthodes lagrangiennes et eulériennes : elles permettent, comme les premières, de suivre la trajectoire des particules, et sont, comme les secondes, faciles à paralléliser.

Les trajectoires balistiques sont modélisées en 3D à partir d'une méthode de simulation à évènements discrets (DES). Les simulations multi particules mises en oeuvre incluent des collisions particule à particule. Nous montrons comment ces collisions peuvent soit augmenter soit diminuer la distance de déposition. Les projectiles représentent un aléa volcanique significatif en raison de la grande vitesse et de leur température, qui peut endommager végétation et infrastructures. Notre modèle DES est utilisé pour évaluer le aléa balistique à Vulcano (Italie), à partir de cartes de probabilités et de distribution d'énergie. Plusieurs seuils de dangers sont définis, pour la perforation et pour l'effondrement de toitures, tandis que les secteurs les plus dangereux de l'île sont indiqués à partir d'un SIG [système d'information géographique] intégrant les résultats du modèle.

Abstract

When volcanoes erupt explosively they inject large amounts of particles of various size (microns to meters) and shape into the atmosphere that eventually deposit back to the ground (i.e., tephra). Numerical models for the transport and dispersal of volcanic particles are important for both the assessment of associated hazards and the understanding of eruptive dynamics. The largest particles (blocks and bombs) are typically decoupled from the gas phase at an early stage and follow independent parabolic trajectories. Lapilli and ash ($< 64\ mm$) are typically transported within a vertical buoyant plume that eventually spreads horizontally (i.e. umbrella cloud) at the level of neutral buoyancy. The coarsest lapilli and ash particles sediment back to the ground within hours, whereas the finest particles (fine ash) can be suspended in the atmosphere for days or weeks.

Studies of total grainsize distributions of explosive eruptions provide important insights into eruption dynamics and fragmentation mechanisms and are necessary to numerical simulations of particle transport and dispersal. Nonetheless, total grainsize distributions are difficult to constrain mainly due to poor preservation of tephra deposits. Based on quantitative comparisons of field data and numerical simulations we have shown how the tephra deposits of large explosive eruptions should be sampled at least up to 100-300 km from the vent in order to derive complete grainsize distributions that are not depleted in fines.

Many tephra dispersal models already exist in the volcanic literature, but important aspects of particle transport and sedimentation still require better parameterizations. Cellular Automata and Lattice Boltzmann models provide simple numerical solutions to very complicated physical systems and can also be easily implemented by adding new physical processes. In particular, Cellular Automata (CA) has been shown to be more computationally efficient than Lattice Boltzmann (LB) for the description of particle transport and dispersal.

We have firstly developed a two-dimensional (2D) CA model with particle release from the plume corner, which has shown good agreement with field observations for large explosive eruptions. In contrast, the description of dispersal from bent-over plumes and of aggregation-driven sedimentation needs a better parameterization. The 2D CA model was then expanded to three dimensions (3D).

In our 3D CA model, particles are released from the vent, are transported within the volcanic plume and are dispersed through the atmosphere. Particle diffusion is described based on a random velocity which corresponds to the velocity fluctuations of turbulence. The implementation of plume dynamics significantly improves the description of particle in proximal area ($<$ 50 km from vent). CA strategies combine advantages of both Lagrangian and Eulerian methods as they can both track particle trajectories (as Lagrangian models) and be easy to parallelize (as Eulerian models).

Ballistic trajectories are modeled in three dimensions based on a Discrete Event Simulation (DES) method. Multiparticle simulations have been implemented that include particle-particle collisions. We have shown how collision between particles can either increase or decrease travel distance. Ballistics represent a significant volcanic hazard due to their high velocities and temperatures, which can damage vegetation and infrastructures. Our DES model has been used to assess the ballistic hazard for Vulcano island (Italy) based on probability maps and energy distributions. Various hazardous thresholds were defined for both roof penetration and roof collapse and indications of the most dangerous areas on the island have been given based on the implementation of model results within the Geographical Information System platform.

Chapter 1

Introduction

Volcanic eruptions are one of the most dramatic natural phenomena and can significantly affect the life of people living close to an active volcano. When a volcano erupts explosively, particles, which are mostly fragments of magma and of rocks (lithics) are emitted from the crater within a mixture of gas. These particles are called tephra regardless of the size of particles.

The large particles (generally > c. 10 mm) are ejected to the atmosphere and are decoupled from the gas phase at an early stage of transport and follow independent parabolic trajectories. These large particles are called ballistic bombs or blocks.

Numerical model for the transport and dispersal of volcanic particles are important for both hazard assessment and understanding of eruption dynamics. Tephra and gas form volcanic plumes. Two types of volcanic plumes are mainly recognized; strong plume and weak plume (Carey and Sparks, 1986 [24]; Bonadonna and Phillips, 2003 [13]) respective to the strength of the wind when the characteristic plume velocity is much greater or much smaller than the wind speed, respectively. Well developed strong plumes consist of a gas thrust region, a convective region and an umbrella cloud (Woods, 1988 [139]). Gas thrust region is momentum dominated region and convective region is where the buoyancy due to the thermal effect dominates. If the plume material is significantly hotter than the ambient fluid, the convective plume rises because of the buoyancy. The buoyant rise stops at the height of neutral buoyancy where the plume starts spreading horizontally. When the vertical plume velocity is significantly lower than wind velocity, the plume is bent over in its convective region and spreads laterally at the neutral buoyancy level. Thus proximal sedimentation is strongly affected by plume dynamics.

Volcanic plumes are described as multiphase (gas and solid particles) turbulent flows. Vortices are observed in all volcanic plumes (Ernst et al, 1994 [43]; Chakrabortory et al, 2009 [27]) and particles are affected by turbulent fluctuations. Particles behavior due to the turbulent fluctuations are often modeled as particle diffusion (Thomson, 1987 [118]; Roberts and Webster, 2002 [95]). Particle transport in the atmosphere is often modeled as advection-diffusion and sedimentation process (Costa et al. 2006 [35]; Bonadonna et al., 2005a [15];

Macedonio et al., 2005 [70]; Searcy et al, 1998 [102]; Dacre et al, 2011; [37]; Stohl et al, 2011 [110]). Particles are advected by the wind and dispersed by the turbulent diffusion. Sedimentation velocity is respective to particle density and particle size.

Many numerical models with Lagrangian method (Draxler and Hess, 1998 [39]; Dacre et al, 2011; [37]; Stohl et al, 2011 [110]) and Eulerian method (Costa et al. 2006 [35]; Bonadonna et al., 2005a [15]) already exist. Lagrangian models can track each particle and randomness of the particle path is applied to simulate diffusion. However it is difficult to parallelize the code because there is no spatial grid. Eulerian models calculate the concentration of particles at each grid and can not track each particle. In contrast to Lagrangian model, its advantage is easy to parallelize the code as it is based on spatial grid. Cellular Automata (CA) and Lattice Boltzmann (LB) method is widely used to simulate advection-diffusion processes (Masselot and Chopard, 1997 [72]; Dupuis and Choaprd, 2000 [41] for CA,and Guo et al, 1999 [52]; Suga, 2006 [111];Ginzburg, 2005 [51]; Chopard et al, 2008 [31] for LB), while they were not used to implement the transport of volcanic particles. Both CA and LB is easy to parallelize and especially CA can track each particle and thus it has advantages of both Lagrangian and Eulerian method.

Ballistic particles are sometimes used to estimate the plume ejection velocity by calibrating the distance from vent (Rosi et al., 2006 [97]; Write et al., 2007 [142]). Nonetheless particle-particle interaction such as collisions between particles affects particle trajectory and have been observed both in the natural system and laboratory experiments (Alatorre-Ibargüengoitia pers. communication). Sophisticated models of ballistic trajectory already exist but can only simulate the trajectory of single particle.(Wilson 1972 [133]; Fagents and Wilson 1993 [46]; Bower and Woods, 1996 [18]; Alatorre-Ibargüengoitia and Delgado-Granados, 2006 [1]). The model of Saunderson(2008) [98]) is multiparticle model in two-dimensional but does not account for the particle distribution on the ground.

Hazard assessment based on probability distribution is applied in many type of volcanic hazards (Connor et al 2001 [33]; Bonadonna et al 2005a [15]; Felpeto et al, 2007[47]) but it is rare for ballistics. Alatorre-Ibargüengoitia et al, (2006) [2] presented the hazard map for ballistic impact but the simulation is based on a single particle model.

Contents of this thesis With my PhD thesis I have applied dedicated numerical strategies to both tephra dispersal and sedimentation of ballistic projectiles.

The influence of the source term (i.e., plume height and grainsize distribution) and meteorological conditions (i.e., wind speed and tropopause height) on particle sedimentation are presented in **Chapter 2**. Chapter 2 also discusses the representative sampling distance in order to obtain a comprehensive total grainsize distribution.

Numerical modeling of tephra transport is presented in **Chapter 3-5**. Basic theory of Cellular Automata (CA) and Lattice Boltzmann (LB) method is presented in **Chapter 3**. Besides, the computation efficiency of CA and LB is compared. Comparison of CA and LB model is published as Tsunematsu et al, (2011) [122]. As a result, we have decided to use multiparticle CA for the simulation of tephra transport.

In **Chapter 4**, two-dimensional tephra transport model with CA is presented. This primary model is implemented with particle release from the plume corner. Good agreement with field observation with strong plume is shown. In contrast, the deposition of particles from the bent-over plume and sedimentation with aggregated particles are necessary to be described with better approach.

Three-dimensional tephra transport model is described in **Chapter 5**. Plume velocity field is included in the simulation and it has improved the description of deposition particles around proximal area ($< 50\ km$ from vent). Particle diffusion due to turbulent fluctuations are implemented by the random velocity and the value of diffusion is derived from the theory of turbulent fluctuations.

Numerical model of ballistics based on the Discrete Event Simulation (DES) method is presented in **Chapter 6**. Multiparticle simulations are implemented with and without the particle-particle collisions. How collisions affect the travel distance of particles is shown and the model advantages are discussed.

As an application to the practical usage, the probability map of ballistic impacts in Vulcano island (Italy) is presented in **Chapter 7**. The probabilities based on the energy class related to the roof penetration and collapse are analyzed and overlaid on the map with Geographical Information System (GIS).

Chapter 2

Grain size features of two large eruptions from Cotopaxi volcano (Ecuador) and implications for the calculation of the total grain-size distribution

2.1 Introduction

The source term of a volcanic event is crucial to the understanding of the associated dynamics and hazards (Bonadonna et al., 2011 [17]). In particular, erupted volume, plume height, mass eruption rate, duration and initial grainsize distribution are all fundamental physical parameters that need to be determined in order to characterize an explosive eruption (e.g. Pyle 1989 [89]; Fierstein and Nathenson 1992 [48]; Carey and Sparks 1986 [24]; Wilson and Walker 1987 [136]). Amongst them, the initial grainsize distribution is one of the most critical to derive (e.g. Bonadonna and Houghton 2005 [12], Walker 1980 [128]; Murrow et al. 1980 [77]; Carey and Sigurdsson 1982 [25]; Parfitt 1998 [83]), but is necessary to investigate fragmentation mechanisms (e.g. Kaminski and Jaupart 1998) and to forecast the spreading and sedimentation of associated volcanic clouds with obvious hazard implications (e.g. Bonadonna et al., 2005 [15] ; Costa et al. 2006 [35]; Textor et al., 2006 a [116], b [117]; Stohl et al., 2011 [110]; Draxler et. al., 1997 [39]; Iwasaki et al., 1998 [60]; Dacre et al., 2011 [37]).

When a volcano erupts explosively, particles of various sizes, shape and composition are injected into the atmosphere and then eventually sediment back to the ground or stay suspended for days depending on their terminal velocity. These particles are called tephra (Thorarnisson 1944 [119]). Tephra deposits are typically sampled in various locations for thickness and grainsize and then individual grainsize distributions are integrated together to derive the initial grainsize distribution (see Bonadonna and Houghton, 2005 [12] for a review on different techniques used to derive the initial grainsize distribution). Bonadonna and Houghton,(2005) [12] have shown how the Voronoi tessellation represents a robust statistical tool to describe not uniform distributions (e.g. Okabe et al., 1992 [82]). Nonetheless, all techniques are strongly dependent on the deposit exposure as they can only combine information of the deposit that is preserved but they cannot extrapolate for parts of the deposit that are eroded away. In addition, Inman (1952) [59] introduced two parameters to quantify the main characteristics of distributions: Md_ϕ and σ_ϕ. Md_ϕ is the 50th percentile of a distribution, while σ_ϕ is the half distance of ϕ between the points of 16 wt% and 84 wt % levels. Thus Md_ϕ represents the average grainsize and σ_ϕ its standard deviation. Walker (1971) [127] showed how the relation between Md_ϕ and σ_ϕ provides important insights into particle transport and allows for fallout deposits and flow deposits to be distinguished. Walker (1973) [126] has also suggested the use of certain grainsize parameters for the classification of explosive eruptions: D and F, where D is the area of the isopach line corresponding to 0.01 T_{max}, and F is the weight percentage of particles <1 mm at the distance where thickness is $0.01T_{max}$.

In this chapter we present the results of grainsize analysis carried out on the tephra deposits associated with two large Plinian eruptions of Cotopaxi volcano characterized by different textural features (i.e., Layer 3 and Layer 5; Barberi et al. 1995 [4]; Costantini 2010 [36]). The last 2000 years of Cotopaxi activity produced 22 tephra deposits with mostly uniform composition (basaltic-andesite to andesite) (Barberi et al., 1995 [4]). However, six of these tephra deposits are characterized by black scoria, six are characterized by white pumices and the rest is characterized by yellow to grey lapilli. Column heights vary between 28 and 39 km, with the highest columns being associated with grey and black scoria. Layer 3 (820±80 years B.P) and Layer 5 (1,180±80 years B.P.) are the best preserved tephra deposits associated with these different explosive events and are associated with white pumices and black scorias respectively (Fig.2.1). In fact, even though they are characterized by similar silica content (62wt% and 58wt% in SiO2 respectively; Barberi et al., 1995 [4]), they show completely different clast microtexture (Costantini 2010 [36]). Biass and Bonadonna (2011) [8] have characterized most physical parameters of these two eruptions (i.e., plume height, mass eruption rate, erupted mass and eruption duration). Here we investigate the grainsize features of the associated deposits and explore if clasts with very different clast mictotexture are characterized by different dispersal. We also compare this dispersal with tephra deposits from other explosive eruptions.

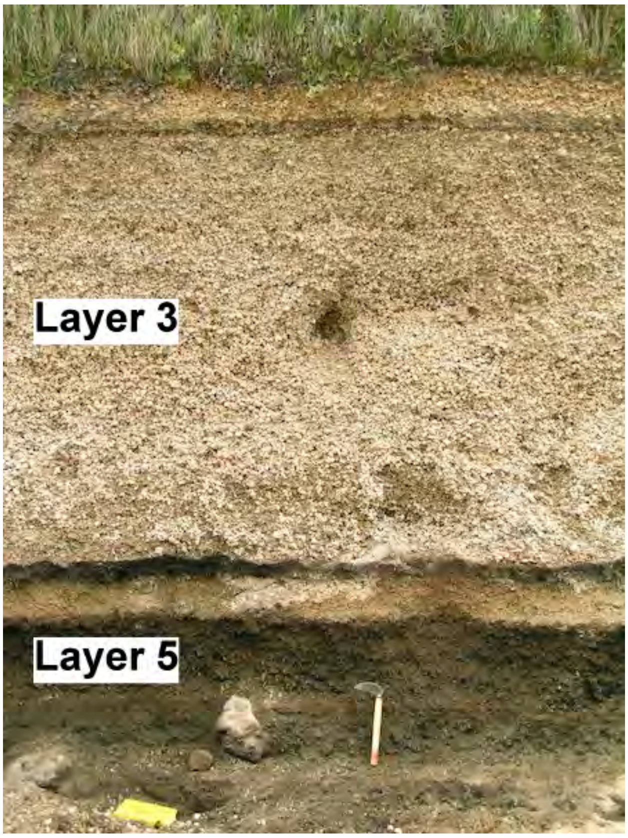

Fig. 2.1: Photo of Layer 3 and Layer 5 at outcrops CP001 (in maps of Fig. 2.2 and 2.3) of Cotopaxi volcano. Thickness of Layer 3 is 179 cm and thickness of Layer 5 is 27.5 cm.

2.2 Method

We sampled Layer 3 and Layer 5 at 33 outcrops. However, due to logistic reasons, grainsize could only be analyzed at 13 outcrops for Layer 3 and 23 outcrops for Layer 5. Samples were dry-sieved in the sedimentology lab of the University of Geneva. The fraction $< 63\ \mu m$ (4ϕ) was analyzed using the CILAS laser diffraction analyzer (http://www.cilas.com/granulometrie.html). The deposit density and thickness was also measured at each outcrop.

2.3 Tephra distribution and Physical Characterization

Isopach maps Isopach maps for Layer 3 and Layer 5 are shown in Fig. 2.2 and Fig. 2.3 respectively. Layer 3 is clearly elongated to north-west direction while Layer 5 shows a more concentric shape. This implies that particle dispersal of Layer 3 was more affected by wind advection than particle dispersal of Layer 5.

Plume height By compiling isopleth maps and using the model of Carey and Sparks (1986) [24] and Pyle (1989) [89], Biass and Bonadonna (2011) [8] reported the plume height in the range from 21 km to 27 km from the crater for Layer 3 and 20-28 km for Layer 5. The plume height derived based on the geometric mean of the 5 largest clast was considered to be the best for the application of the model of Carey and Sparks (1986) [24] and resulted in values of 23.1 km for Layer 3 and 26.1 km for Layer 5.

Erupted volume Erupted volumes were determined by Biass and Bonadonna (2011) [8] based on exponential fitting (Pyle, 1989 [89]), power-law fitting (Bonadonna and Houghton, 2005 [12]) and inversion of observed mass loading using the analytical model TEPHRA2 (Connor and Connor, 2006 [34]). The range of the volume varies from 0.6 to 2.4 km^3 for Layer 3 and 0.2 to 0.5 km^3 for Layer 5. Biass and Bonadonna, (2011) [8] concluded that the inversion technique gives the most reliable values: 2.4 km^3 for Layer 3 and 0.5 km^3 for Layer 5. This range of values corresponds to a Volcanic Explosive Index (VEI) 5 for Layer 3 and 4 for Layer 5.

Mass eruption rate Mass eruption rate (MER) was calculated by Biass and Bonadonna (2011) [8] from the plume height based on the model of Wilson and Walker (1987) [136]. The range of values is $1.4 - 7.6 \times 10^7$

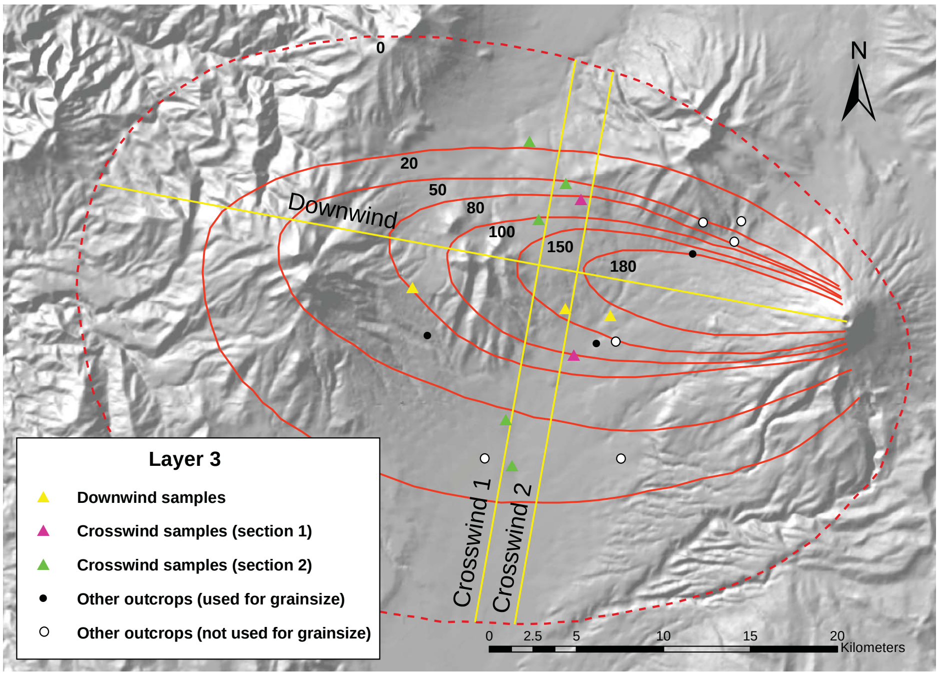

Fig. 2.2: Isopach map for Layer 3 (cm). Yellow triangles indicate the samples along the downwind axis. Pink triangles indicate the samples along the crosswind section 1 (15.7 km from the vent). Green triangles indicate the samples along the crosswind section 2 (18.0 km from the vent). Black circles indicate other samples considered in the calculation of the total grainsize distribution. Empty circles indicate outcrops used to compile the isopach maps but that were not considered in the calculation of total grainsize.

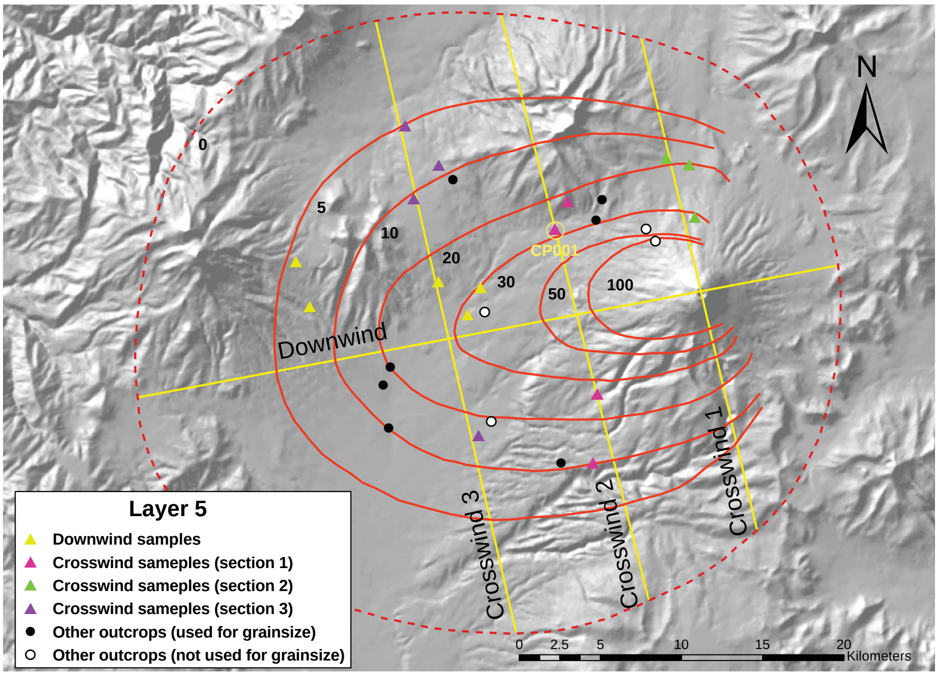

Fig. 2.3: Isopach map for Layer 5 (cm). Yellow triangles indicate the samples along the downwind axis. Pink triangles indicate the samples along the crosswind section 1 (0 km from the vent). Green triangles indicate the samples along the crosswind section 2 (7.3 km from the vent). Violet triangles indicate the samples along the crosswind section 3 (14.7 km from the vent). Black circles indicate other samples considered in the calculation of the total grainsize distribution. Empty circles indicate outcrops used to compile the isopach maps but that were not considered in the calculation of total grainsize.

Table 2.1: Summary of physical parameters for Layer 3 and Layer 5. Plume height, erupted volume, mass eruption rate and duration are from Biass and Bonadonna (2011) [8] [8]. Wind velocity is obtained with this work by using the result from Biass and Bonadonna (2011) [8].

	Layer 3	**Layer 5**
Plume height	23 ± 1 km	26 ± 1 km
Erupted volume	2.4 km^3	0.5 km^3
Mass eruption rate	$4.0 \pm 0.9 \times 10^7$ kg/s	$5.9 \pm 0.7 \times 10^7$ kg/s
Erupted mass	1.7×10^{12} kg	0.6×10^{12} kg
Duration(empirical)	295 ± 155 min	80 ± 21 min
Duration(analytical)	570 ± 195 min	134 ± 25 min
Maximum wind velocity	28 m/s	21 m/s

kg/s and $1.0 - 8.0 \times 10^7$ kg/s for Layer 5. The MER associated with the plume height derived from the 3/5 A technique (i.e., arithmetic mean of the three axis of the 5 largest clasts) are $4.9 \pm 1.2 \times 10^7$ kg/s for Layer 3 and $5.0 \pm 1.9 \times 10^7$ kg/s for Layer 5.

Erupted mass Erupted mass of 1.7 ± 10^{12} kg for Layer 3 and 0.6 ± 10^{12} kg for Layer 5 were obtained by multiplying the erupted volume by the bulk deposit densities measured in the field (i.e., 700 ± 24 kg/m^3 and 950 ± 85 kg/m^3 for Layer 3 and Layer 5 respectively).

Duration Eruption duration was calculated by Biass and Bonadonna (2011) [8] dividing the erupted mass by the MER. Mean duration of Layer 3 eruption is 295 ± 155 min for mass obtained based on empirical method and 570 ± 195 min for mass derived based on inversion. Mean duration of Layer 5 eruption is 80 ± 21 min and 134 ± 25 min for empirical and analytical techniques respectively.

Wind velocity According to the model of Carey and Sparks (1986) [24], maximum wind velocity at the tropopause can be derived from downwind (DW) and crosswind (CW) range of isopleth maps. From Biass and Bonadonna (2011) [8], DW and CW range of 3/5A (arithmetic mean of the threes axis of the five largest clasts) technique is 23.3 km (DW) and 10.8(CW) for Layer 3 and 20.3 km (DW) and 11.0 (CW) for Layer 5. These values correspond to wind velocity of 28 m/s and 21 m/s.
All physical parameters obtained from Biass and Bonadonna, (2011) [8] and from this work are summarized in Table 2.1.

2.4 Results

2.4.1 Trend of grainsize distribution along dispersal axis

Iso-Mdϕ maps are shown in Fig 2.4(a) and 2.4(b) for Layer 3 and Layer 5 respectively. Direction of elongation is similar to isopachs for both layers. Grainsize variations along the downwind direction for both Layers are shown in Fig. 2.5. Md_{ϕ} of particle size clearly decreases with distance from the vent at a similar rate for Layer 3 and 5 (Fig. 2.5 a). However, Layer 3 is always coarser than Layer 5 at a given distance from the vent because it was affected by a stronger wind. The amount of ash (particles $<2\ mm$) also increases with distance from the vent for both Layer 3 and 5 (Fig. 2.5 c). In contrast, sorting does not show any particular trend with distance from the vent and it varies between 1.3 and 1.7 (Fig. 2.5 b). Grainsize variations along crosswind direction for Layer 3 and Layer 5 are shown in Fig. 2.6 and Fig. 2.7 respectively. Grainsize along crosswind (CW) 1 is coarser than grainsize along CW2 for Layer 3 (Fig. 2.6a and 2.6c). However, both Md_{ϕ} and σ_{ϕ} do not show a clear crosswind trend for Layer 3, probably due to the lack of data (Fig. 2.6b). Crosswind variation shows a clearer trend for Layer 5 (Fig. 2.7). In fact, CW1, CW2 and CW3 show a clear decrease of grainsize with distance from the dispersal axis (Figs 2.7 a and 2.7 c). However, grainsize along CW1 is comparable to CW3 and finer than CW2 (Fig. 2.7 a). Sorting does not show a clear crosswind trend (Fig. 2.7 b). The comparison of two crosswind sections with a similar distance from the vent (CW1 for Layer 3, 15.7 km from vent, and CW3 for Layer 5, 14.7 km from the vent) shows a very similar crosswind grainsize variation for Layer 3 and 5 (Fig. 2.8), being associated with a similar plume height.

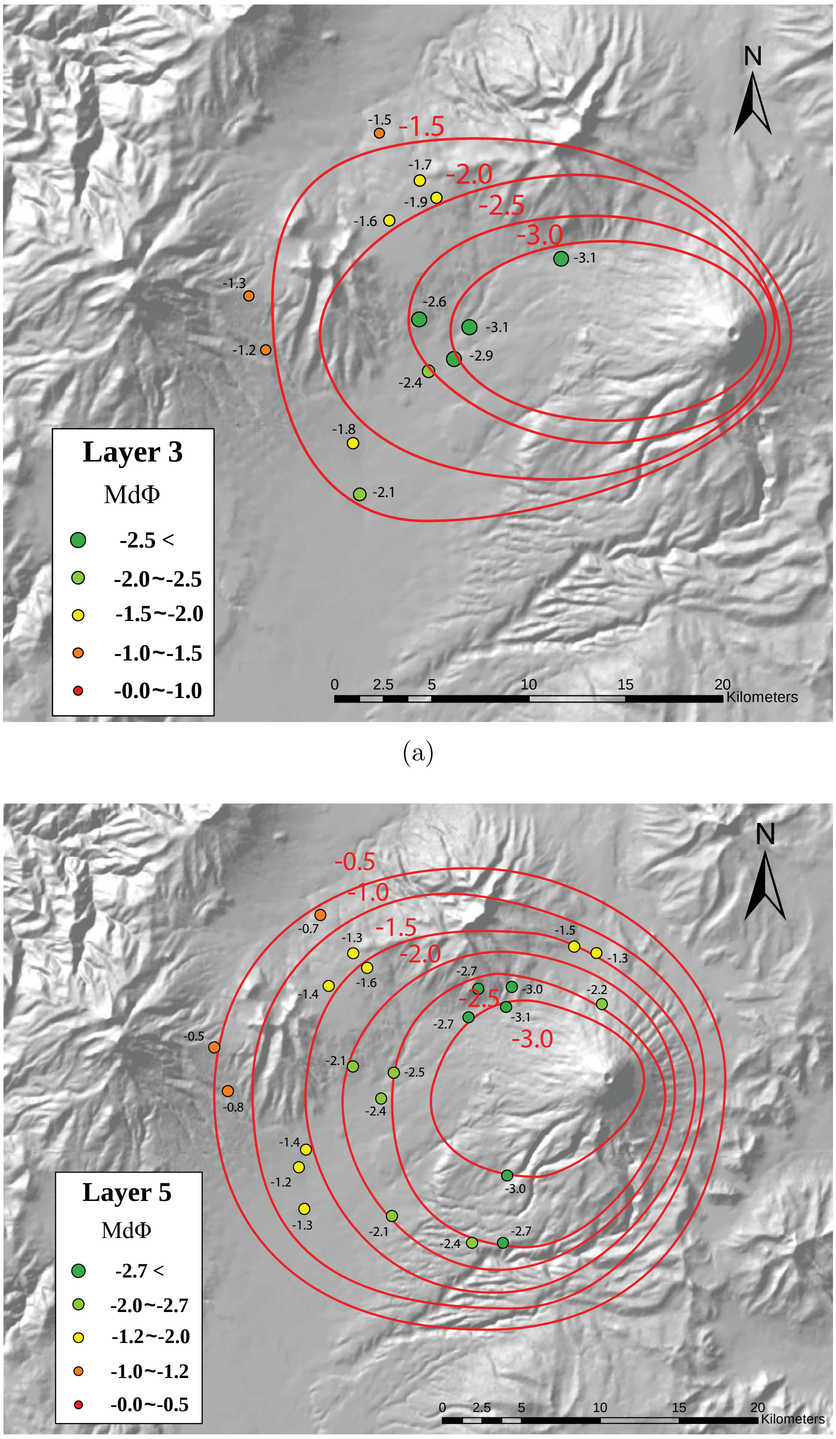

(a)

(b)

Fig. 2.4: (a)IsoMdϕ map for Layer 3. Numbers in figure (red) shows Mdϕ. Points are outcrops where we took samples for grainsize analysis. Colors show the range of Md*phi* value (refer legend). (b) IsoMdϕ map for Layer 5. Numbers in figure (red) shows Mdϕ. Points are outcrops where we took samples for grainsize analysis. Colors show the range of Md*phi* value (refer legend).

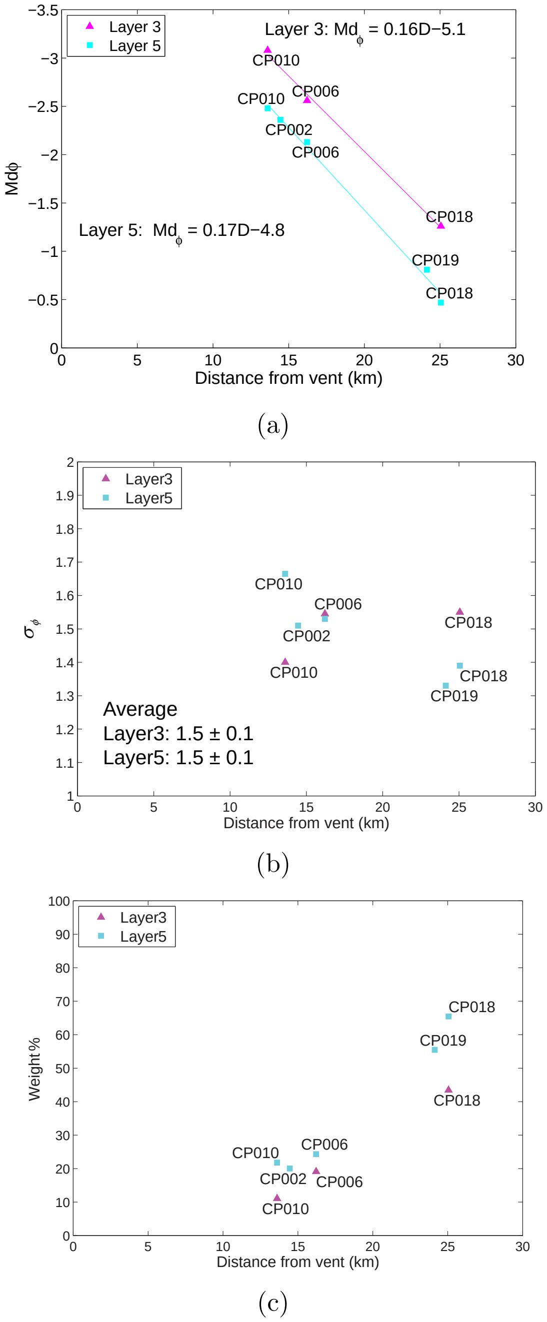

(a)

(b)

(c)

Fig. 2.5: (a) Median grain size, (b) sorting and (c) weight fraction of ash (i.e. particles 0ϕ) along downwind axis for both Layer 3 and Layer 5 ($\phi = -log_2 d$, where d is the particle diameter in mm). Numbers in box of figure (b) indicate the average of σ_ϕ standard deviation for each Layer. Equations in the figure (a) shows the line trend.

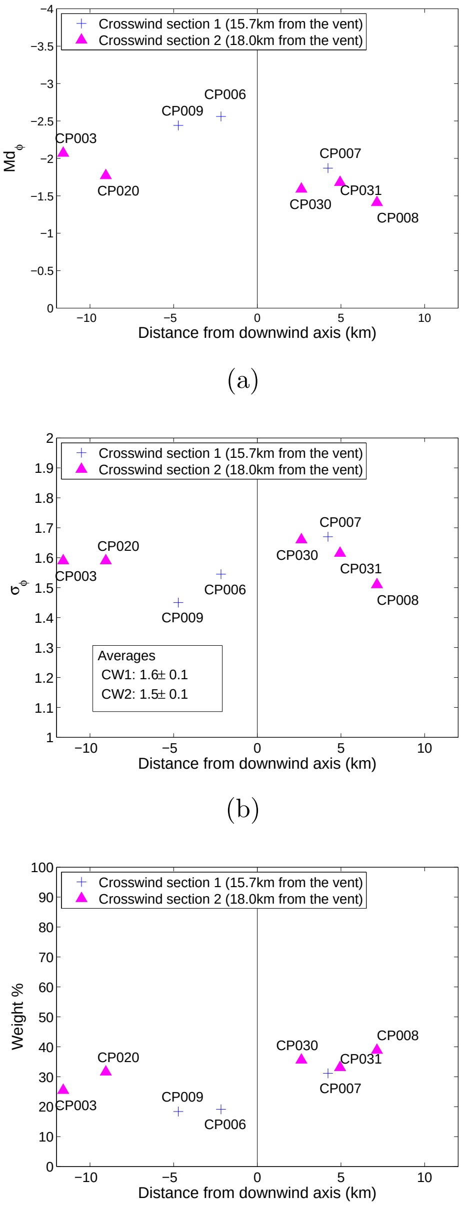

(a)

(b)

(c)

Fig. 2.6: (a) Median grain size, (b) sorting and (c) weight fraction of ash (i.e. particles $\leq 0\phi$) along the two crosswind sections of Layer 3 ($\phi = -log_2 d$, where d is the particle diameter in mm). Crosswind section 1 is 15.7 km from the vent. Crosswind section 2 is 18.0 km from the vent (Fig. 2.2). Numbers in box of figure (b) indicate the average of $\sigma_\phi\pm$ standard deviation for each Layer.

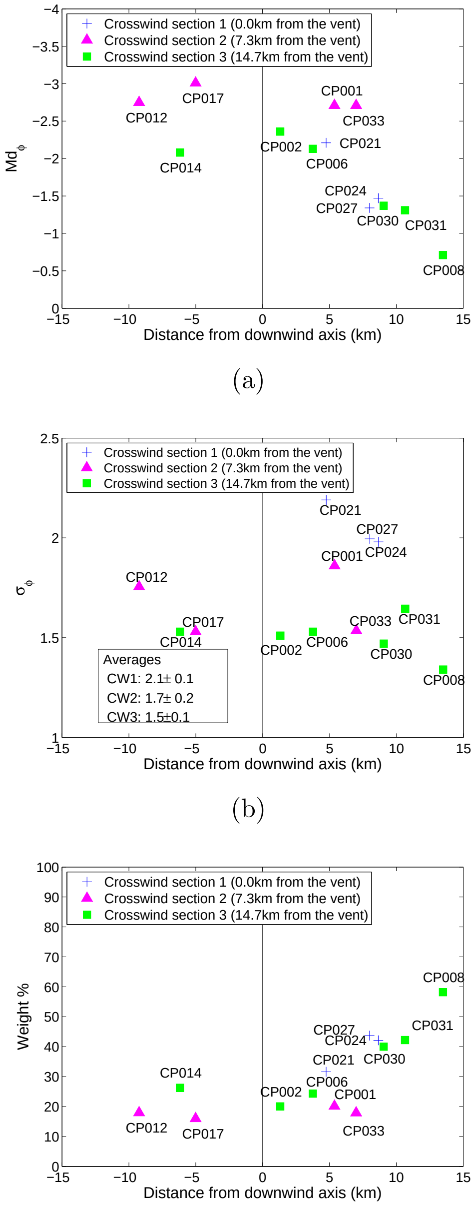

(a)

(b)

(c)

Fig. 2.7: (a) Median grain size, (b) sorting and (c) weight fraction of ash (i.e. particles $\leq 0\phi$) along two crosswind sections of Layer 5 ($\phi = -log_2 d$, where d is the particle diameter in mm). Crosswind section 1 is 0.0 km from the vent. Crosswind section 2 is 7.3 km from the vent. Crosswind section 3 is 14.7 m from the vent (Fig. 2.3). Numbers in box of figure (b) indicate the average of $\sigma_\phi \pm$ standard deviation for each Layer.

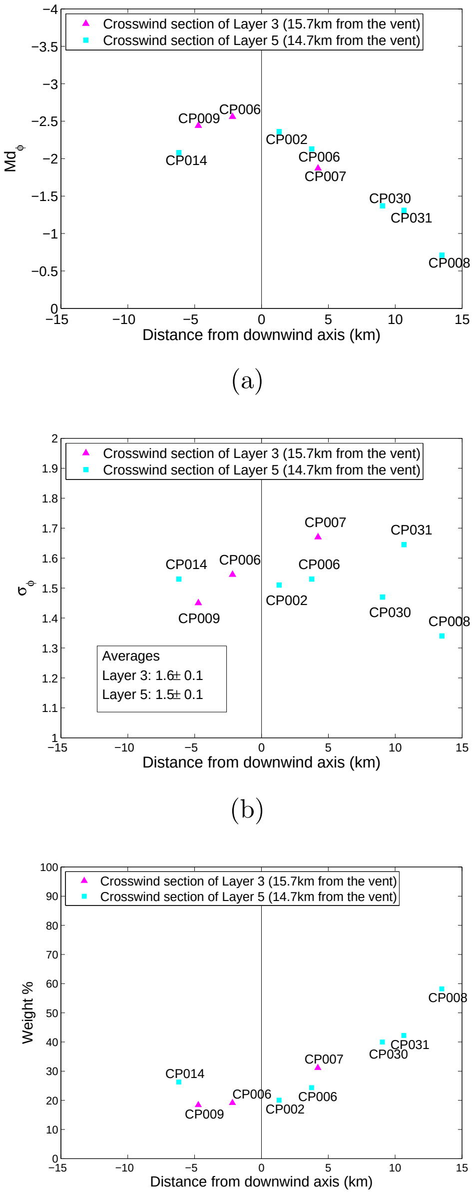

(a)

(b)

(c)

Fig. 2.8: Comparison of (a) median grain size, (b) sorting and (c) of ash (i.e. particles $\leq 0\phi$) for Layer 3 and Layer 5 along a crosswind section at a similar distance from vent. Crosswind section of Layer 3 is 15.7 km from the vent (crosswind section 1 of Layer 3). Crosswind section of Layer 5 is 14.7 km (crosswind section 3 of Layer 5). Numbers in box of figure (b) indicate the average of $\sigma_\phi\pm$ standard deviation for each Layer.

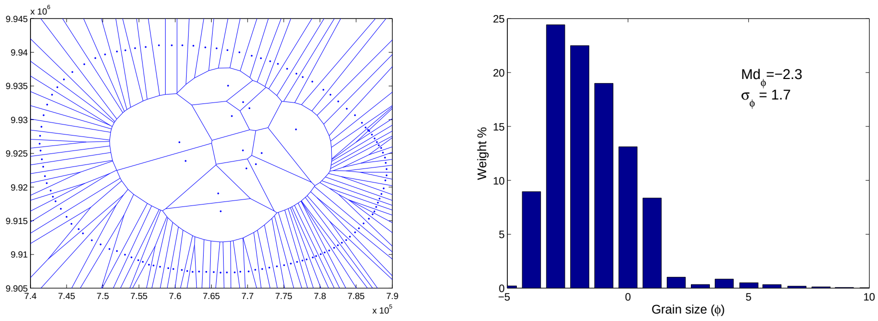

(a) (b)

Fig. 2.9: (a) Diagram showing the Voronoi tessellation and (b) the total grain size distribution calculated by using the Voronoi Tessellation technique for Layer 3.

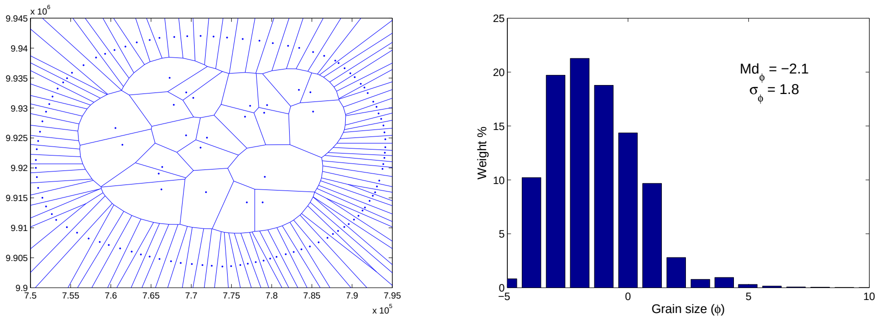

(a) (b)

Fig. 2.10: (a) Diagram showing the Voronoi tessellation and (b) the total grain size distribution calculated by using the Voronoi Tessellation technique for Layer 5.

2.4.2 Total grain size distribution

Total grain size distribution (TGSD) is calculated applying the Voronoi tessellation method of Bonadonna and Houghton (2005). Various sample distributions and various zero lines, which are considered as the lines of zero tephra load, are applied in order to assess the sensitivity of the technique. Layer 3 and Layer 5 have very similar unimodal total grainsize distributions (Fig. 2.9 and 2.10; Md_{ϕ} is about 2.1 to 2.3 ϕ and sorting is about 1.7 and 1.8). Tables 2.2 and 2.3 show how the total grainsize distribution derived based on downwind samples only, does not diverge significantly from the total grainsize distribution derived based on the whole deposit (i.e., discrepancies within 10% for both Layers). Tables 2.4 and 2.4 show that the choice of the

Table 2.2: Median and sorting of total grain size distribution for Layer 3. "All points" are total grain size calculated from all points sampled for Layer 3 (all points in Fig. 2.2 except the empty circles). "DW" is the total grain size calculated considering only samples along the downwind axis. "DW+CW1" is the total grain size calculated from the points of downwind axis and crosswind section 1 (15.7km from the vent). "DW+CW2" is the total grain size calculated from the points of downwind axis and crosswind section 2 (18.0km from the vent). "DW+CW1+CW2" is the total grain size calculated from the samples along the downwind axis, crosswind section 1 and crosswind section 2. "Error" is the percentage of difference of Md_ϕ from "All points".

	All points	DW	DW+ CW1	DW+ CW2	DW+ CW1+CW2
Number of points	14	3	6	8	11
Md_ϕ	-2.3	-2.3	-2.2	-2.2	-2.2
σ_ϕ	1.7	1.7	1.7	1.7	1.7
Error (%)	-	0.0	4.3	4.3	4.3

zero line does not significantly affect the final result for total grainsize distribution determined using the Voronoi Tessellation technique (Bonadonna and Houghton 2005 [12]) (discrepancies within 5% for both Layers).

Table 2.3: Median and sorting of total grain size distribution for Layer 5. "All points" are total grain size calculated from all points sampled for Layer 5 (all points in Fig. 2.3 except the empty circles). "DW" is the total grain size calculated only samples alone the downwind axis. "DW+CW1" is the total grain size calculated from the samples along the downwind axis and along crosswind section 1 (0.0km from the vent). "DW+CW2" is the total grain size calculated from the samples along the downwind axis and along crosswind section 2 (7.3km from the vent). "DW+CW3" is the total grain size calculated from the samples along the downwind axis and along crosswind section 3 (14.7 km from the vent). "DW+CW1+CW2" is the total grain size calculated from the samples along the downwind axis and along crosswind section 1 and 2. "DW+CW1+CW2+CW3" is the total grain size calculated from the samples along the downwind axis and all cross wind sections. "Error" is the percentage of difference of Md_ϕ from "All points".

	All points	DW	DW+ CW1	DW+ CW2	DW+ CW3	DW+ CW2+CW3	DW+CW1 +CW2+CW3
Number of points	24	5	8	9	11	15	16
Md_ϕ	-2.1	-2.2	-2.0	-2.3	-1.9	-2.2	-2.1
σ_ϕ	1.8	1.7	1.8	1.7	1.6	1.7	1.8
Error (%)	-	4.8	4.8	9.5	9.5	4.8	0.0

Table 2.4: Changes of median and sorting of total grain size distribution for Layer 3 by changing the zero-mass line in the Voronoi Tessellation technique. "Zero line 1" is the line of zero-thickness of Layer 3 shown in the isopach map of Fig. 2.2 (dashed line). "Zero line 2" and "Zero line 3" are lines traced 5km and 10km further out from Zero line 1 respectively. "Error" is the percentage of difference of Md_ϕ from Zero line 1.

	Zero line 1	**Zero line 2**	**Zero line 3**
Md_ϕ	-2.3	-2.3	-2.4
σ_ϕ	1.7	1.7	1.7
Error (%)	-	0.0	4.3

Table 2.5: Changes of median and sorting of total grain size distribution for Layer 5 by changing the zero-mass line in the Voronoi Tessellation technique. "Zero line 1" is the line of zero-thickness of Layer 3 shown in the isopach map of Fig. 2.3 (dashed line). "Zero line 2" and "Zero line 3" are lines traced 5km and 10km further out from Zero line 1 respectively. "Error" is the percentage of difference of Md_ϕ from Zero line 1

	Zero line 1	**Zero line 2**	**Zero line 3**
Md_ϕ	-2.1	-2.0	-2.0
σ_ϕ	1.8	1.9	1.9
Error (%)	-	4.8	4.8

Table 2.6: Eruption parameters and total grain size distributions for compared eruptions. 1, Eruption parameters of Askja D 1875 are from Carey and Houghton, (2010) [23] except plume height. Plume height is from Carey and Sparks (1986) [24]. Total grain size data is from Sparks et al., (1981) [106]. 2, Eruption parameters of Cotopaxi Layer 3 and Layer 5 are from Biass and Bonadonna, (2011) [8] and total grain size is from this work. 3, Eruption parameters and total grain size data of Pululagua are from Volentik et al., 2010 [125]. 4, Eruption parameters and total grain size data are from Rose et al., 2008. [96] 5, Eruption parameters are from Bonadonna et al., 2005 and total grain size data are from Bonadonna and Houghton 2005. [12]

	Total plume height above vent (km)	Wind velocity at tropopause (m/s)	Total mass (kg)	Mass discharge rate (kg/s)	Duration	Total grain size distribution	
						Md_ϕ	σ_ϕ
Askja 1875D[1]	26	28	5.0×10^{11}	2.5×10^{7}	6 h	-2.3	4.2
Cotopaxi Layer 3[2]	23	28	$1.4 - 1.7 \times 10^{12}$	4.0×10^{7}	4.9h-9.5h	-2.3	1.7
Cotopaxi Layer 5[2]	26	21	$0.6 - 1.1 \times 10^{12}$	5.9×10^{7}	0.5h-1.3h	-2.1	1.8
Pululagua 2450BP[3]	24.5	0	$1.6 - 5.0 \times 10^{11}$	$6.2 - 18.0 \times 10^{7}$	0.8h-3h	0.2	1.9
Fuego 1974[4]	15	9	5.8×10^{10}	3.0×10^{6}	5h	-0.8	2.5
Ruapehu 1996[5]	6	36	5×10^{9}	2.0×10^{5}	6.5h	-0.8	2.4

2.4.3 Comparison with other eruptions

In order to study the relative characteristics of Cotopaxi Layer 3 and Layer 5 eruptions, thinning trend, Md_ϕ, σ_ϕ trend along the downwind axis are compared with other eruptions. For this comparison, two Plinian eruptions (Askja 1875D and Pululagua 2450BP) and two subplinian eruptions (Fuego 1974 and Ruapehu 1996) were chosen. Pululagua eruption is a rare case which occurred in no-wind condition. Eruption parameters and Md_ϕ, σ_ϕ of total grainsize distribution are shown in table 2.6.

Thinning trends are plotted both versus square root of isopach area (Fig. 2.11 (a)) and versus distance along downwind axis (Fig. 2.11 (b)). The plot of

Table 2.7: Absolute value of exponents of power law fitting for a) Thickness vs square root of area, b) Thickness vs distance and c) Md_ϕ vs distance. Md_ϕ is coverted to the value in mm for the calculation of exponent.

	a) Thickness vs $(\mathrm{Area})^{1/2}$	b) Thickness vs Distance	c) Md_ϕ vs Distance
Askja 1875 D	1.2	1.1	1.2
Cotopaxi Layer 3	1.8	1.5	2.1
Cotopaxi Layer 5	2.1	2.0	2.2
Pululagua 2450BP	1.7	1.6	1.9
Fuego 1974	2.1	2.6	1.1
Ruapehu 1996	2.0	1.5	0.6

thickness versus square root of area was firstly introduced by Pyle (1989) [89] in order to normalize all deposits to a no-wind condition and allow for a better comparison. However, the plot of distance from vent is useful to investigate particle advection.

Plinian eruptions and subplinian eruptions have clear difference in both plots of thinning trend (Fig. 2.11). Thickness of Plinian eruptions is always larger than thickness of subplinian eruptions. Cotopaxi Layer3 and Layer5 eruptions show similar thickness with other Plinian eruptions. Askja shows similar trend with other Plinian eruptions in proximal area while it shows slower decrease in distal area particularly in the plot of thickness vs. distance (Fig. 2.11 (b)) . In subplinian eruptions, Ruapehu shows rapid decrease in proximal area and slower decrease in distal area.

Comparison of grainsize variations of Md_ϕ and σ_ϕ is shown in Fig. 2.12. The difference of Plinian eruptions and subplinian eruptions are clear in Md_ϕ plot(2.12 (a)). Md_ϕ of Cotopaxi Layer 3 and Layer 5 shows the trend between Askja and Pululagua eruptions. In Md_ϕ variation, both Plinian and subplinian eruptions show the slower decreas in distal area (Askja and Ruapehu eruptions).

Thinning and Md_ϕ trends are compared (Fig. 2.13 and Table 2.7). Exponents in Table 2.7 are calculated with the equations as follows:

$$Thickness = A \times ((Area)^{1/2})^{-B} \tag{2.1}$$

$$Thickness = C \times (Distance)^{-D} \tag{2.2}$$

$$Md_\phi = E \times (Distance)^{-F} \tag{2.3}$$

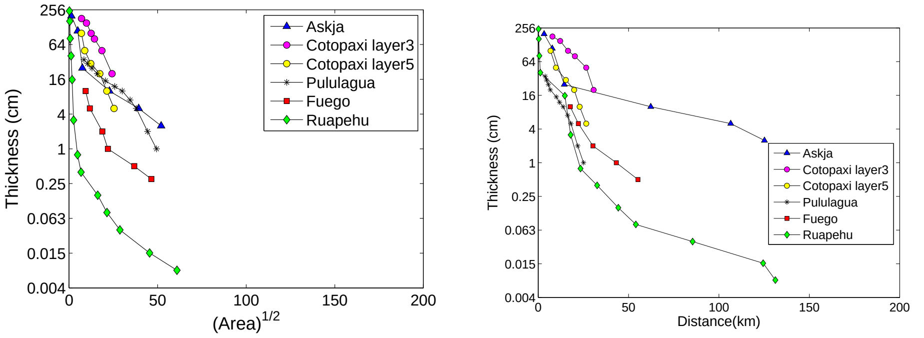

(a) (b)

Fig. 2.11: Thinning trends of compared eruptions. a) Thickness variation versus square root of area. b) Thickness variation versus distance for compared eruptions. Axis of thickness is in log_2 scale for the comparison with grainsize data that are based on ϕ unit ($\phi = -log_2 d$, where d is the particle diameter in mm).

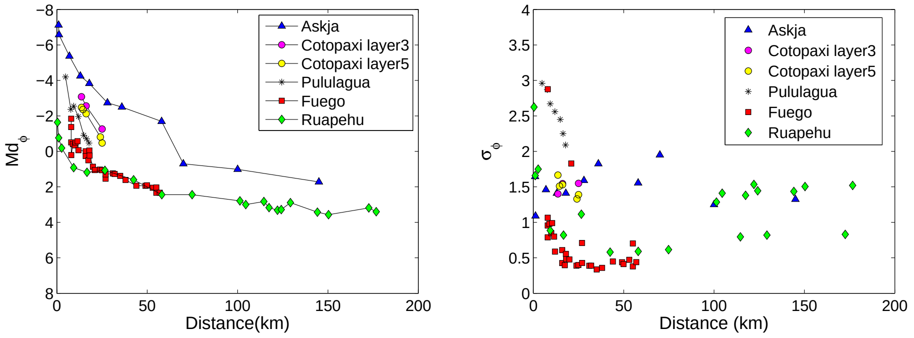

(a) (b)

Fig. 2.12: Grainsize variation for compared eruptions a)Md_ϕ versus downwind distance b) σ_ϕ variation versus downwind distance.

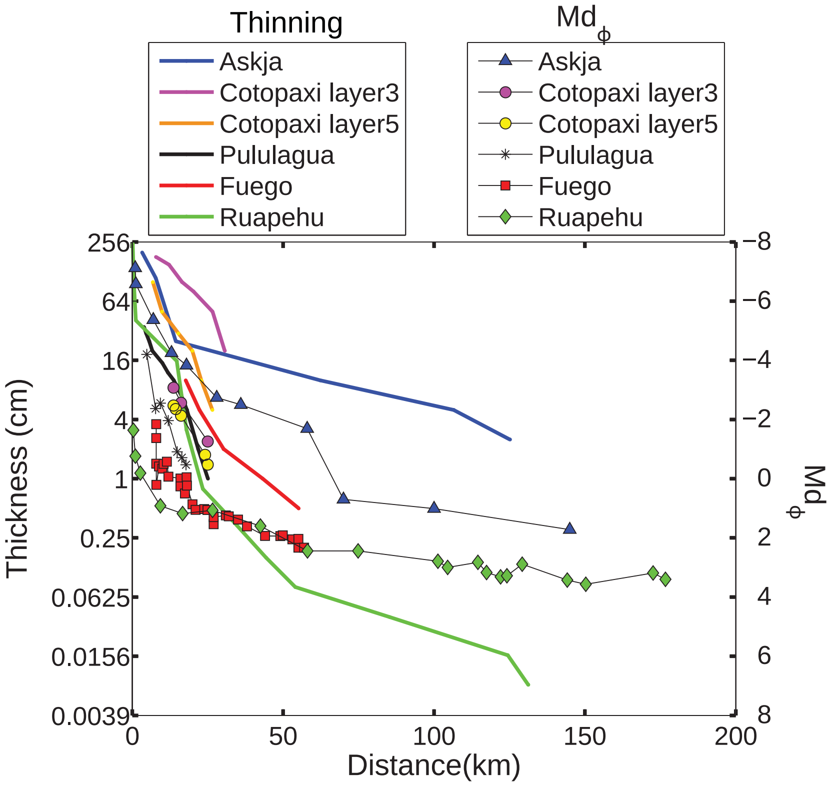

Fig. 2.13: Comparison of thinning and Md_ϕ variation of all eruptions.

Here, thickness is in cm, square root of area is in km, Md_ϕ is in mm, and distance is in km. The values shown in the table 2.7 are B, D and F in eq. (2.1), (2.2) and (2.3) respectively.

Power-law exponents of thinning trends (Table 2.7 a and b) show higher value for subplinian eruptions (i.e., Fuego, Ruapehu) than Plinian eruptions (i.e., Askja, Cotopaxi, Pululagua) on a semilog plot of $\sqrt{Area}$. Nonetheless, the exponent for Ruapehu on a semilog plot of distance from the vent is lower than some Plinian eruptions because it is affected by the stronger wind which results into a more gradual thinning than Fuego. There is no strong relation between power low exponent of Md_ϕ and eruptive style (Fig.2.13):

2.4.4 Numerical investigations

Simple numerical simulations with Lagrangian method have been implemented for plume heights 30km and three different wind velocity (10m/s, 20m/s and 30m/s in maximum) in order to investigate the effect of plume and wind on tephra transport. In the simulations, particles are transported by the velocity field which consists of plume velocity profile (from Woods, 1988 [139]), velocity of umbrella cloud (from Bonadonna and Phillips, 2003 [13]), and wind velocity profile (from Bonadonna and Phillips, 2003 [13]). Wind velocity profile depends on the height of tropopause. Umbrella cloud is considered to exist between the total plume height and the height of neutral buoyancy level (H_b) where the air density and the plume density are in balance. The neutral buoyancy level is defined by comparing the density of air and the bulk density of plume from the result of Woods(1988) [139] model. Settling velocity of particles are calculated by the model of Bonadonna and Phillips(2003) [13] assuming spherical particles for simplicity. With the simple simulations, diffusion is not included and the deposition points are only one for each grainsize. As the value of many input parameters of plume model is not known, the 1D simulations have been implemented for a suitable range of input parameters (initial velocity, plume radius at vent, gas mass fraction at vent, plume temperature at vent) (Table 2.8). From many results of plume velocity profile, the averaged velocity profiles of plumes have been derived.

The results of Lagrangian simulations are shown for particles $> 3\ \phi$ ($125 \mu m$) because particles $< 3\ \phi$ produce aggreagates (Schumacher,1994 [100]; Sparks et al, 1997 [108]). Particles travel farther when the wind velocity is higher (Fig. 2.14). Especially, fine particles are transported to the umbrella cloud region by vertical plume velocity and they travel horizontally by the velocity of umbrella cloud region. This horizontal transport due to umbrella cloud make the travel distance of smaller particles longer. Wind velocity above the

Table 2.8: Parameters and their value used in the 1D simulation of plume profile.

Parameter	**Range of value**
Initial velocity	10-400 (m/s)
Plume radius at vent	20-200 (m)
Gas mass fraction at vent	0.01-0.05
Plume temperature at vent	1100-1300 (K)

tropopause is constant to a value of 10% of the maximum velocity (Carey and Sparks, 1986 [24]). The results in Fig. 2.14 show that particle trajectories are similar above the tropopause height but vary under the tropopause due to different wind velocity. Some particles rise to the top of the plume with wind velocity 10m/s and 20m/s. However, no particles of 3 ϕ reach the top of the plume with wind velocity 30m/s.

Simple simulations with Lagrangian method have been implemented for the case-study Plinian eruptions (Askja 1875D, Cotopaxi Layer 3, Cotopaxi Layer 5 and Pululagua)(Fig. 2.16). Wind velocity profiles of Askja 1875D, Cotopaxi Layer 3 and Cotopaxi Layer 5 are shown in Fig. 2.15. Particles are widely transported under the tropopause for Askja 1875D and Cotopaxi Layer 3 and Cotopaxi Layer 5. In contrast, particles fall vertically without horizontal transport under the tropopause for Pululagua 2450BP because Pululagua 2450BP eruption is simulated in no-wind condition. Finest particle (3 ϕ) travels farther in Cotopaxi Layer 3 eruption than in Askja 1875D eruption though their plume height and wind velocity is similar (Table 2.6) as a result of the position of the tropopause.

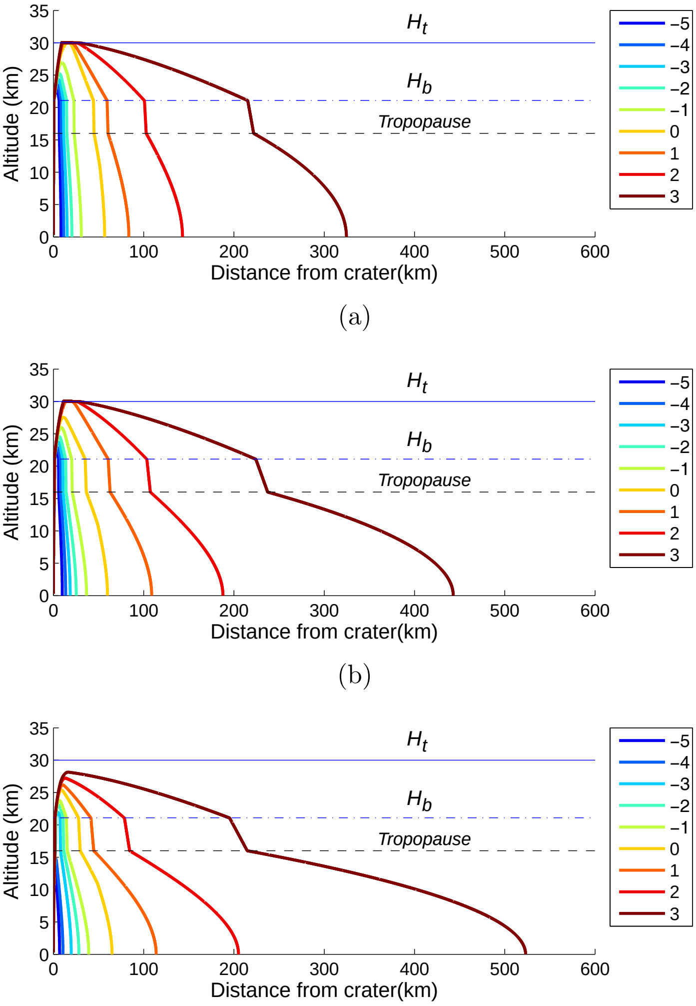

(a)

(b)

(c)

Fig. 2.14: Particle trajectories calculated with simple Lagrangian method for total plume height 30km. Legends show the grainsize in ϕ. Hoirzontal blue line shows the total plume height 30km. Horizontal dash-dot line shows the neutral buoyancy height of the plume (H_b) 21.1km. Horizontal dashed line shows the tropopause height of Cotopaxi volcano 16km. (a) Wind velocity 10 m/s, (b) Wind velocity 20 m/s and (c) Wind velocity 30 m/s.

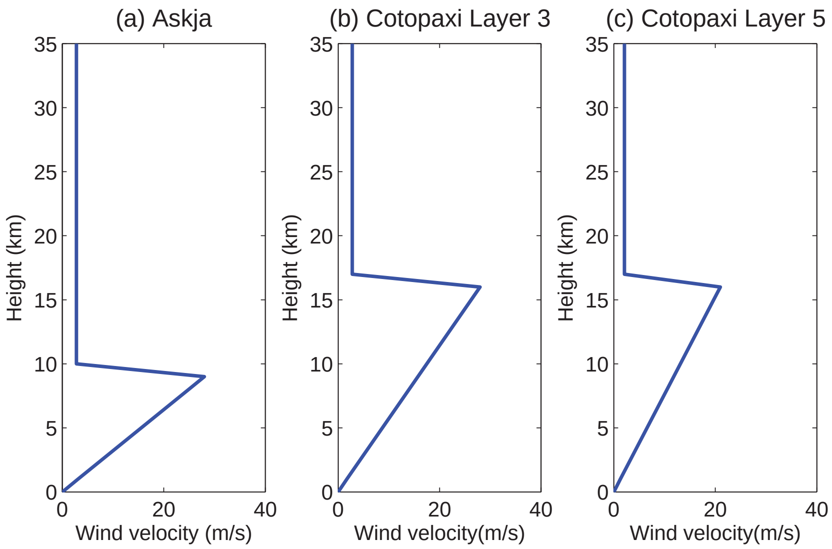

Fig. 2.15: Wind velocity profile for (a) Askja 1875D, (b) Cotopaxi Layer 3 and (c) Cotopaxi Layer 5. Tropopause height is 9km at Askja volcano and 16km at Cotopaxi volcano.

2.5 Discussion

2.5.1 Trend of grainsize distribution along dispersal axis

Grainsize distribution in the downwind direction is a result of both wind advection and plume height (e.g., Carey and Sparks, 1986 [24]). In fact, the coarser grainsize of Layer 3 at each given distance from the vent with respect to Layer 5 is considered as an effect of stronger wind because their total grainsize distribution and plume height are similar (Fig. 2.9 and Fig. 2.10). In contrast, sorting does not show any particular trend and is similar for both eruptions at any distance from the vent. Given that the sorting of particles is related to the effect of wind and atmospheric diffusion, a similar value of sorting implies a similar diffusion during transport. The effect of wind on sorting can be better observed when eruptions occurred with wind and with no wind are compared (e.g. Ruapehu versus Pululagua in Fig. 2.12). In fact, the sorting of the Pululagua deposit is significantly worse than any other eruptions considered, and has a stronger dependence with distance from vent. Nonetheless, the effect of wind on the sorting trend of the two Cotopaxi Layers is not evident.

The similarity of crosswind variation for Layer 3 and Layer 5 (Fig. 2.12)

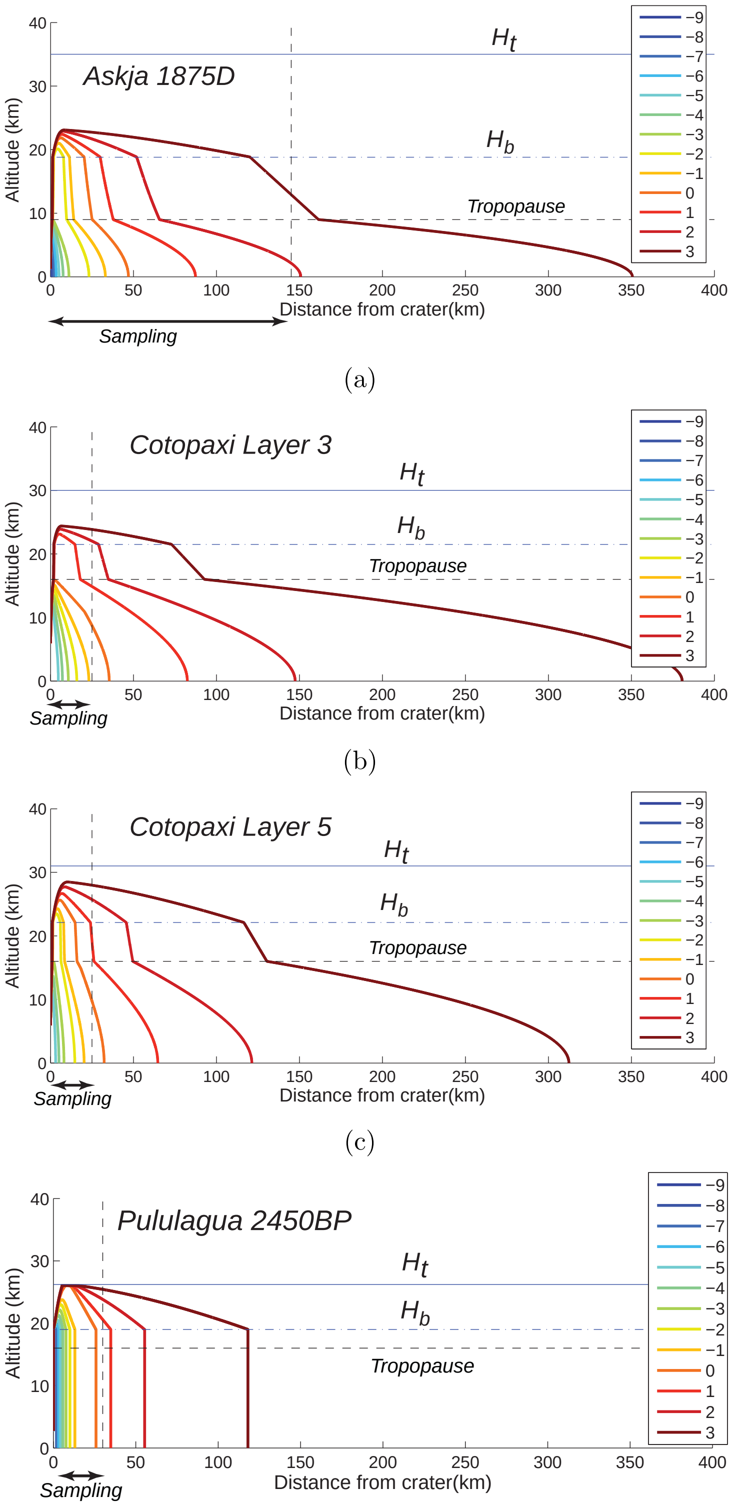

(a)

(b)

(c)

(d)

Fig. 2.16: Particle trajectories calculated with simple Lagrangian method for (a) Askja 1875D (b) Cotopaxi Layer 3, (c) Cotopaxi Layer 5 and (d) Pululagua 2450BP eruptions. Legends show the grainsize in ϕ. Horizontal dash-dot line shows the neutral buoyancy height of the plume (H_b) . Horizontal dashed line shows the tropopause height. Vertical dashed line shows the sample limit of each eruptions.

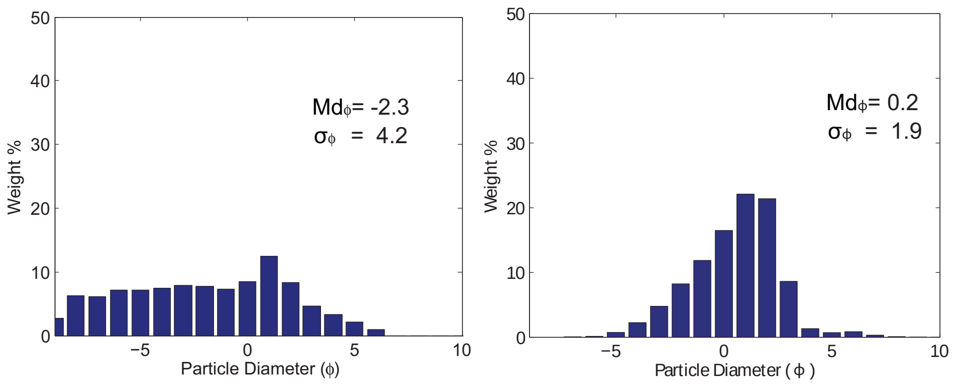

(a) (b)

Fig. 2.17: Total grainsize distributions for (a) Askja 1875D and (b) Pululagua 2450BP eruptions.

is consistent with a similar plume height (Biass and Bonadonna, 2011 [8]). In fact, the crosswind variation of grainsize is considered to be mainly related to the spreading of the umbrella cloud, which depends on the plume height. However, the sorting shows no particular trend even in the crosswind direction, as a possible evidence of good mixing within the umbrella cloud.

2.5.2 Influence of data availability of the determination of Total grainsize distribution

We obtained similar total grainsize distribution for Layer 3 and Layer 5 eruptions by applying the Voronoi tessellation method of Bonadonna and Houghton (2005) [12]. This could be related to a similar plume height and, therefore, a similar mass eruption rate and explosivity of the two eruptions. Nonetheless, the exposure of the deposits is not good enough to infer critical information on magma fragmentation and eruption dynamics (e.g. lack of the fine fraction that was probably eroded away). The Voronoi technique has been tested for sensitivity by using different subsets of the same datasets (table 2.2 and 2.3) and different positions of the line of zero mass loading required for the calculation (table 2.4 and table 2.5). Our results show that the calculation of the total grainsize distribution based only on points along the dispersal axis (3 points) is very similar to the total grainsize distribution based on the whole deposit (14 points). The addition of the crosswind sections does not seem to improve the calculation for Layer 3 (table 2.2). This could be due to both the fact that the downwind axis retain most information on grainsize or that the crosswind data are not enough to affect the calculation. However, the calculations done on Layer 5 (table 2.3) confirm that the grainsize information retained along the DW axis is enough to derive a complete grainsize distribution on only a few points (e.g., 5 points on the DW axis vs 24 points of the total deposit; table 2.3). In contrast, the small discrepancy associated with the use of different zero lines (within 5%) confirms that the Voronoi is a robust technique for the calculation of total grainsize distribution based on a non uniform distribution of points.

2.5.3 Comparison with other eruptions

Thinning, Md_ϕ and σ_ϕ variations with distance from the vent are compared for different eruptions of different styles and that occurred in different meteorological conditions, i.e. wind and no wind (Fig. 2.11 and 2.12). The first feature that can be observed is that the thinning of the Ruapehu deposit decreases very fast in proximal-medial area with respect to the other eruptions considered. This is mainly due to the fact that the Ruapehu eruption occurred in conditions of strong winds that significantly affected the plume dynamics producing a bent-over plume. Sedimentation from bent-over plumes is enhanced in proximal and medial areas (Bonadonna et al. 2005 [16]). In addition, Plinian eruptions are characterized by thicker deposition than subplinian eruptions. (Fig. 2.11).

The plots of Fig. 2.11(a) show the spreading area regardless of the circular or elongated shape of isopachs, while the plots of Fig. 2.11(b) depends on the shape of isopachs. For example, the plots Askja 1875D and Pululagua 2450BP has similar trend in Fig. 2.11(a). However, the isopach of Askja 1875D shows the strong elongation of isopachs due to the wind , which results in a the slower decrease of both thinning and Md_ϕ. In fact, the wind velocity of Askja 1875D is 28 m/s, but Pululagua 2450BP is considered to be no-wind eruption.

Main difference of Plinian eruptions and subplinian eruptions is that the thickness of Plinian eruption is always larger than thickness of subplinian eruptions Fig. 2.11. This is because of the larger amount of mass discharge rate (MDR) and erupted mass in Plinian eruptions.

MDR of Plinian eruptions (Askja 1875D, two eruptions of Cotopaxi and Pululagua 2450BP) are all in order of 10^7 and their plume heights are all in the range of 24-26 km. On the other hand, MDR of subplinian eruptions are in order of 10^5-10^6 and their plume heights are lower than 15 km. Variations of Md_ϕ with distance from vent are similar for Plinian and subplinian eruptions. However, at any given distance, Plinian deposits are coarser than subplinian deposits (Fig. 2.13). This could result in coarser grainsize distribution in cases when the sampling distance is not representative of the sedimentation of all size classes.

2.5.4 Numerical investigations

In order to investigate the effect of height and wind on particle transport and grainsize variations with distance from vent, simple numerical simulations with Lagrangian method are implemented. For these simulations, wind profile which varies in vertical direction and is constant in horizontal direction is used. The wind profile is constant in horizontal direction until ∼100 km. However, it is assumed to be constant for all the simulation area in order to obtain representative sampling distance.

Simulations with the same plume height with different wind velocities show that the wind velocity is a main factor of the horizontal transport. Simulations with the case-study eruptions show how the tropopause height affects the space of wind advection and it indirectly affects the travel distance. For example, Cotopaxi volcano is located close to the equator with a higher tropopause (16km) than the tropopause of Askja volcano (9km). Consequently, particles of Cotopaxi Layer 3 travel farther than Askja 1875D even though their plume height and maximum wind velocity is similar. In fact, particles are advected by stronger wind under the tropopause for Cotopaxi volcano than Askja volcano. Even in no-wind conditions, particles travel horizontally due to the velocity field of umbrella cloud for Pululagua 2450BP eruption. If particles go up to the umbrella cloud effectively, travel distance of particles becomes longer. Therefore, finer particles travel much farther than larger particles for Plinian eruptions.

Another interesting aspect of numerical investigations is that the sampling distance of our case-study eruptions is smaller than the travel distance of 3ϕ particle (Fig. 2.16). The representative sample distance should be the distance of the deposition point of $3\ \phi$ class because particles $< 3\ \phi$ aggregate. As an example, representative sampling distance for Askja and Cotopaxi Layer 3 and Layer 5 is 350km. Nonetheless, the three deposits were sampled only to a distance of 145km and 25km from the vent respectively due to poor exposure. For Pululagua 2450BP eruption, the representative sampling distance is 120km as this is no-wind eruptions, while the sampling distance was 30km (Volentik et al, 2010 [125]). A shorter sampling distance than the representative sampling distance results in a depletion of fines (Fig. 2.9, 2.10 and 2.17).

2.6 Conclusions

Physical parameters and grainsize distributions of Layer 3 and Layer 5 eruptions of Cotopaxi volcano are obtained for understanding dynamics of tephra transport. Furthermore, thinning trend and grainsize variations along DW axis are compared with other eruptions and we investigated the effect of plume heights and wind velocity by implementing simple numerical simulation. The conclusions of this study are as follows.

1. Md_ϕ variation with distance from vent depends on plume height and wind transport.

2. Similar plume heights generate similar variations of Md_ϕ for similar magma composition in the CW direction regardless of the wind advection.

3. Total grainsize distributions are similar for both Cotopaxi Layers analyzed.

4. Calculation of total grainsize distribution depends mainly on DW points and is not very sensitive to CW points. As a result, effective sampling for the characterization of total grainsize distribution should focus on DW direction.

5. Zeroline of total grainsize does not affect the result of the total grainsize distribution based on the Voronoi tessellation method.

6. Both thinning trend and grainsize variation show the clear differences for Plinian and subplinian eruptions, with Plinian eruptions are characterized by thick layer and coarser deposits at any given distance. This result in coarser total grainsize distribution in cases when the actual sampling distance is shorter than the representative sampling distance.

7. Power law exponents of thinning trend of Plinian eruotions on semilog plots of $\sqrt{Area}$ are larger than for subplinian eruptions. Power law exponents of thinning of weak plumes on a semilog plot of distance from vent are lower than for Plinian eruptions because of the more gradual thinning in distal area due to strong wind.

8. Numerical simulations show how total grainsize distributions are depleted in fines when sampling areas are not representative of the sedimentation of all particle sizes.

9. In the case of Askja 1875D and Cotopaxi Layer 3 and Layer 5, representative sampling distance is around 350km from the vent. For Pululagua 2450BP, the representative sampling distance is shorter (i.e. around 120km) because sedimentation was not affected by wind.
10. According to our numerical investigation, transport of particles are affected by the tropopause height.

Chapter 3

Introduction for numerical model of tephra transport

3.1 Introduction

One of the main goals of this project is to develop a reliable numerical model of tephra transport. Cellular automata method (CA) or lattice Boltzmann method (LB) is not used in the former models of tephra transport.

Both Eulerian and Lagrangian models for tephra transport are suggested (e.g. Searcy et al. 1998 [102]; Bonadonna et al., 2005a [15]; Costa et al. 2006 [35]; Textor et al., 2006 a, b [116, 117]; Stohl et al., 2011 [110]; Draxler et al., 1997 [39]; Iwasaki et al., 1998 [60]; D'Amours et al., 2010 [38]; Dacre et al., 2011 [37]; Webley, 2011 [130]). Tephra transport is modeled as an advection-diffusion process (Costa et al. 2006 [35]; Bonadonna et al., 2005a [15]; Macedonio et al., 2005 [70]).

In general, the Eulerian models solve differential equations of particle concentration by descretizing time and space. On the other hand, tephra transport with Lagrangian method uses many particles to produce diffusion of concentration stochastically. To have a grid size in Eulerian model is an advantage because it is easy to apply wind velocity based on grid points. Moreover, it is also easy to parallelize the code with the space grid. While it requires much memory, as we need wide calculation area for simulating tephra transport. Calculation efficiency of Lagrangian models do not depend on the calculation area, but it depends mainly on the number of particles. In order to calculate concentration in distal area, Lagrangian models need a very large number of particles (Scollo et al.,2010 [101]) As it does not use grids, the parallelization of the code is not easy. We have decided to apply the advection-diffusion model of Cellular Automata method (CA) and lattice Boltzmann method (LB) to tephra transport because they were not used in the former models of tephra transport and these two methods may simulate well the tephra transport by advection-diffusion approach.

The lattice Boltzmann method (LB) is widely used for advection-diffusion process(Guo et al, 1999 [52]; Suga 2006 [111]; Ginzburg 2005 [51]; Chopard et al., 2008 [31]). However its numerical stability and accuracy depend on calculation parameters. In Suga (2006) [111] the stability of the LB advection-diffusion is shown to depend on the Peclet number.

An alternative to the LB approach is the multiparticle Cellular Automata (CA) model designed to describe the transport of passive scalar point particles in a given velocity field $\vec{u}(\vec{u}, t)$. This model has been successfully used in [72, 41] to model snow or sand transport and validated on several non-trivial examples of snow accumulation by wind and sand erosion around submarine pipelines.

We have found that the application of CA to the description of tephra transport is more efficient than the application of LB. Details are shown in following sections (from section 3.2) at this chapter.

As a first step towards a numerical tephra transport model, a simple two-dimensional (2D) multiparticle CA for advection-diffusion is developed in Chapter 4. Three-dimensional (3D) tephra transport model is shown in Chapter 5. Where we have expanded 2D model to 3D model, we have focused on two points: the characterization of the source term and the diffusion implementation.

Our model includes the plume velocity field as a source term and we have modeled particle diffusion by stochastic rule of random velocity. Further more, we have applied the value of diffusion coefficient according to the dynamics of turbulence. These two characteristics have successfully reproduced ground sedimentation of volcanic eruptions.

In the following sections of this chapter, the basic concept of CA and LB is introduced (section 3.2). The methods of advection-diffusion simulation with CA and LB are shown (section 3.3 and 3.4 respectively). From section 3.5 to section 3.9, we compare the two methods. This part is published as Tsunematsu et al, (2011) [122]. The CA advection-diffusion model obeys an anisotropic advection-diffusion equation. However, this unwanted anisotropy only introduces a small error for systems with high Peclet numbers, as it is the case in tephra transport. In addition, we show that the unconditional stability of the CA model allows us to choose a coarser discretization than with the LB model. As a result, computations of tephra transport with the CA model can be faster and less memory consuming than with the LB model, yet for a comparable accuracy.

3.2 Introduction of Cellular Automata and Lattice Boltzmann method

3.2.1 Cellular Automata method

Cellular Automata method (CA) is a numerical method to describe a physical system in which space and time are discrete (Chopard et al., 2002 [30]). Nowadays, it is widely applied to scientific and other problems such as simulating traffic (Nagel and Schreckenberg, 1992 [78]; Chopard et al., 1996 [29]), chemical reaction (Kier et al., 2005 [62]), biology (Edlestein-Keshet,1988 [42]), and crystallization (Chahoud et al., 2000 [26]; Reiter 2005).

The definition is to have cells, which represent a discretized space, and states which express the situation of each cell. The states are updated according to the rule and they are propagated to the neighbor sites. CA is based on an idealized, virtual and microscopic world, while the macroscopic behavior of the world emerges eventually. Normally it is easier to implement than using partial differential equation (PDE). For example, to have the advection-diffusion process, PDE-based numerical models approach the discretized PDE and obtain the computer solution (Fig. 3.1). On the other hand, CA-based models implement relatively simple rule and obtain the solution directly from the computer model.

As an extension of CA, Lattice Gas Automata method (LGA) is suggested to simulate the gas behavior from the molecular dynamics. At first, Hardy, Pomeau and de Pazzis (1971) suggested the model with two-dimensional (2D) square lattice. This model is called HPP which named after the three inventors of the model (Fig. 3.2). Then, Frisch, Hasslacher and Pomeau (1986) [50] suggested another model considering isotropy and applying hexagonal lattice in 2D. This model is called FHP. To update the states of LGA, there are two steps; collision and propagation.

FHP reproduces almost correct hydrodynamic behavior such as Navier-Stokes equation. Both HPP and FHP consider 0 or 1 particle at each site, and thus a state at each cell only needs four bits per site for FHP. For example, a state at iteration t and site $\vec{r}$ is written as $s(\vec{r}, t) = (1, 0, 1, 1)$. This is called exclusion principle (Chopard and Droz, 1998 [28]). LGA with many particles at each site (without exclusion principle) is called *multiparticle models* (Chopard and Droz, 1998 [28]).

By modifying the rule of HPP, random walks are reproduced easily(Chopard, et al., 2002 [30]). If each particle at a cell selects its new direction randomly, the random change of directions reflects probabilistic evolution of the system. This probabilistic rule in microscopic scale corresponds to a diffusion process

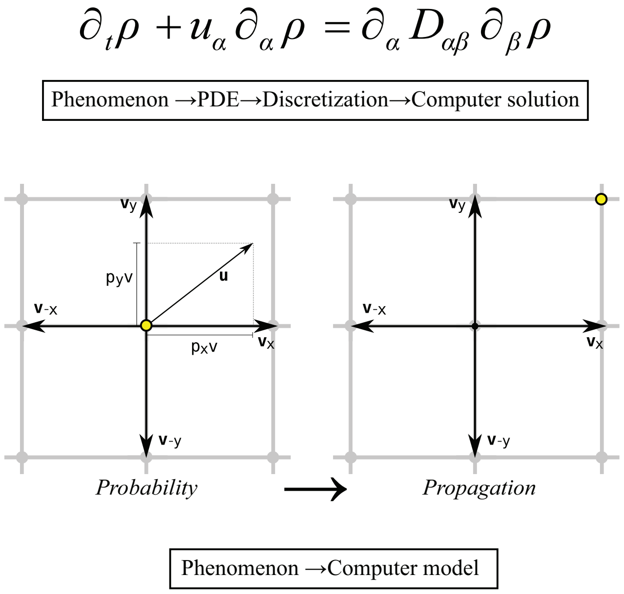

Fig. 3.1: The solution process for advection-diffusion problem for a general numerical approach with discretization of PDE (top)or and with CA (bottom). The left of the bottom: a particle at the center site has probability due to the velocity $\vec{u}$. The right of the bottom: the particle jump to the top-right site according to the probability (propagation process).

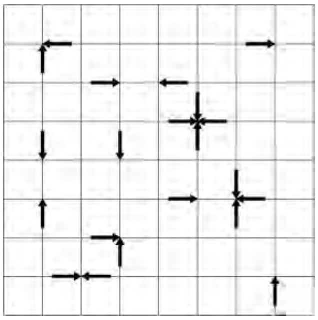

Fig. 3.2: Example of a configuration of HPP particles (Chopard, et al., 2002 [30]).

in macroscopic world.

3.2.2 Lattice Boltzmann method

Inspired by LGA, lattice Boltzmann method (LB) is developed to describe fluid motions. The states are no longer 0/1 but the quantity at each site is described by a distribution function f_i which is interpreted as a density distribution of particles. LB is widely applied to geosciences (Sukop and Thorne 2006 [112]; Llewellin 2010a [69] and b [45]; Huber et al., 2010 [58]), medical studies (Hirabayashi et al., 2004 [55]; Bernsdorf et al., 2006 [5]) and engineering field (Neuhierl and Rank, 2006 [91]; Moriyama and Inamuro, 2011 [74]) and so on.

As the same as LGA, LB has two steps for the update of state. Collision step of LB is written as;

$$f_i^{out}(\vec{r},t) = f_i^{in}(\vec{r},t) + \Omega_i(f_i^{in}(\vec{r},t)) \tag{3.1}$$

And a propagation step is;

$$f_i(\vec{r} + \Delta t\vec{v}_i, t + \Delta t) = f_i^{out} \tag{3.2}$$

where Ω is called collision term. f_i^{out} is the distribution of the next step which is calculated from the current distribution and propagated to the next site. Index i denotes the lattice direction at each site. The physical values density ρ and velocity $\vec{u}$ are calculated by summing the distribution function f_i.

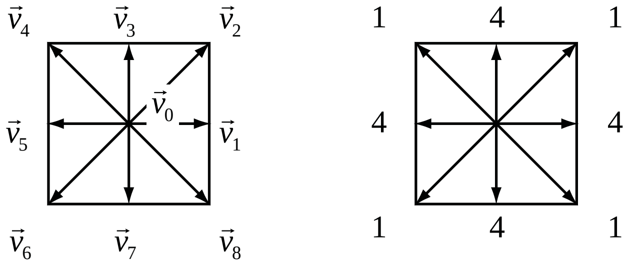

Fig. 3.3: The D2Q9 lattice with nine propagation speed. Right: the ratio of the weights associated with direction. The diagonal directions have a weight four times smaller than the main directions. Left: numbering of propagation speed. $\vec{v}_0$ is the propagation speed of a center point (Chopard et al, 2002 [30]).

$$\begin{aligned} \rho &= \sum_{i=0}^{z} f_i \\ \vec{u} &= \frac{1}{\rho} \sum_{i=0}^{z} f_i \vec{v}_i \end{aligned} \tag{3.3}$$

$\vec{v}_i$ is a propagation speed and it is defined by the lattice geometry (Fig. 3.3). In general, we name the lattice with "DnQm"(Qian et al, 1992 [90]). n is a number of dimension and m is a number of propagation speeds. For instance, the lattice of Fig. 3.3 is in two dimensions and there are nine vectors of propagation speed. Therefore, this lattice is called "D2Q9" lattice.

For this example in two dimensions, the vectors of propagation speeds are defined as;

$$\begin{aligned} v_0 = \begin{pmatrix} 0 \\ 0 \end{pmatrix}, v_1 = \begin{pmatrix} 1 \\ 0 \end{pmatrix}, v_2 = \begin{pmatrix} 1 \\ 1 \end{pmatrix}, v_3 = \begin{pmatrix} 0 \\ 1 \end{pmatrix}, v_4 = \begin{pmatrix} -1 \\ 1 \end{pmatrix}, \\ v_5 = \begin{pmatrix} -1 \\ 0 \end{pmatrix}, v_6 = \begin{pmatrix} -1 \\ -1 \end{pmatrix}, v_7 = \begin{pmatrix} 0 \\ -1 \end{pmatrix}, v_8 = \begin{pmatrix} 1 \\ -1 \end{pmatrix}. \end{aligned} \tag{3.4}$$

In the BGK model by Bhatnagar, Gross, Krook (1954) [6], the collision term is further decomposed by f_i and f^{eq}, where f^{eq} is called local equilibrium distribution. Collision term is calculated as follows.

$$\Omega_i = \omega \left(f_i^{eq} \left(\rho, \vec{u} \right) - f_i \right) \tag{3.5}$$

where $\omega = 1/\tau$ is the inverse of relaxation time τ. This τ is related to the kinematic viscosity ν for a fluid as;

$$\nu = c_s^2 \Delta t \left(\tau - 1/2\right). \tag{3.6}$$

This Δt is a calculation time step.
To simulate viscous fluid with Navier-Stokes equation, equilibrium distribution f^{eq} is taken as;

$$f_i^{eq} = t_i \rho \left[1 + \frac{\vec{v_i}\vec{u}}{c_s^2} + \frac{1}{2c_s^4} Q_{i\alpha\beta} u_\alpha u_\beta \right]. \tag{3.7}$$

Here, $Q_{i\alpha\beta} = u_{i\alpha} u_{i\beta} - c_s^2 \delta_{\alpha\beta}$ (We follow Einstein summation convention over repeated Greek indices and $\delta_{\alpha\beta}$), c_s is interpreted as the speed of sound because the pressure p is related to the density ρ through the ideal gas relation $p = \rho c_s^2$.
The weight t_i is expressed as follows;

$$\sum_i t_i v_{i\alpha} v_{i\beta} = c_s^2 \delta_{\alpha\beta}. \tag{3.8}$$

For D2Q9 model (Fig. 3.3), t_i is taken as $t_0 = 4/9$, $t_1 = t_3 = t_5 = t_7 = 1/9$, and $t_2 = t_4 = t_6 = t_8 = 1/36$.
In summary, the BGK model with collision and propagation steps in microscopic world simulates viscous fluid which is described by Navier-Stokes equation in macroscopic world. The mathematical proof is carried out by so-called *Chapman-Enskog expansion*(Chopard and Droz 1998 [28]; Chopard et al., 2002 [30]; Latt, 2007 [65]).
Boundary conditions are important for CA and LB, and especially LB is sensitive to the distribution f_i of the limit of computational domain. Since we do not know the value of f_i outside of the domain, we have to specify the value of f_i at the boundary. The boundary conditions are explained in Chopard et al (2002) [30]; Latt et al (2008) [66]).
The equations shown in this section(eq. (3.1) to (3.8)) are equations for viscous fluid following Navier-Stokes equation. Those for advection-diffusion process are explained in section 3.4.

3.3 The multiparticle Cellular Automata transport model

The snow and sand transport model proposed in [72, 41] is a stochastic multiparticle cellular automata (CA). Each cell contains an arbitrary number of point particles which move to a nearest neighbor cell according to a given advecting field $\vec{u}(\vec{r},t)$. The particles keep their discrete nature all along the process. If needed additional interactions (such as aggregation) between grains that meet on the same lattice site can be added. As far as passive transport is concerned, the effect of $\vec{u}$ is to give a velocity $\vec{v}_i$ to each of the particle, where $\vec{v}_i$ is a discrete velocity chosen randomly in a set of possible values. The fact that the particles are restricted to move on a lattice introduces a numerical diffusion in the model.

For the sake of illustration we consider here the two-dimensional case. Let us define $\rho(\vec{r},t)$ as the probability to find, at time t, a point particle at spatial location $\vec{r}$ on the lattice. Let us also consider a D2Q9 topology for which the velocity vectors $\vec{v}_i$ $(i = 0, \dots 8\ )$ are defined as

$$\vec{v}_0 = (0,0) \quad \vec{v}_1 = (v,0) \quad \vec{v}_2 = (0,v) \quad \vec{v}_3 = (-v,0) \quad \vec{v}_4 = (0,-v) \tag{3.9}$$

and

$$\vec{v}_5 = (v,v) \quad \vec{v}_6 = (-v,v) \quad \vec{v}_7 = (-v,-v) \quad \vec{v}_8 = (v,-v) \tag{3.10}$$

where v is $v = (\Delta x/\Delta t)$, with Δx the lattice spacing and Δt the time step.

We also define $p_i(\vec{r},t)$ as the probability that a particle at position $\vec{r}$ and time t jumps to its nearest neighbor with velocity v_i and reach, at time $t+\Delta t$ the site $\vec{r} + \Delta t\vec{v}_i$.

With these definition the CA transport model can be written as

$$\rho(\vec{r},t+\Delta t) = p_0(\vec{r},t)\rho(\vec{r},t) + \sum_{i\geq 1} p_i(\vec{r} - \Delta t\vec{v}_i,t)\rho(\vec{r} - \Delta t\vec{v}_i,t) \tag{3.11}$$

This equation simply states that the probability to find a particle in $\vec{r}$ at time $t + \Delta t$ is due to the particles at time t that did not move away from r (this happens with probability p_0), plus all the particles reaching r from the neighobors.

Let assume that $\vec{u}(\vec{r},t)$ is in the quadrant spanned by lattice velocities v_i and v_{i+1}. Due to the action of the advecting field, the particle can have four possible behaviors. It stays still, or moves to $\vec{r}+\vec{v}_i$, $\vec{r}+\vec{v}_{i+1}$ or $\vec{r}+\vec{v}_i+\vec{v}_{i+1} = \vec{r}+\vec{v}_{i+4}$. The probability of each of these movements is determined by the projection of $\vec{u}$ on $\vec{v}_i$ and $\vec{v}_{i+1}$.

Therefore the probabilities $p_i(\vec{r},t)$ are built from the advection speed

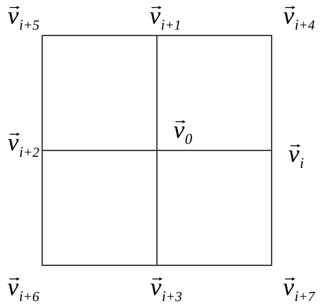

Fig. 3.4: Lattice and propagation speed of multiparticle CA model. $i = 0 - 3$ are perpendicular directions and $i = 4 - 7$ are diagonal directions.

$\vec{u}(\vec{r}, t)$ as follows

$$\begin{aligned}
p_i &= \frac{\vec{u}\cdot\vec{v}_i}{v^2}\left(1 - \frac{\vec{u}\cdot\vec{v}_{i+1}}{v^2}\right) \\
p_{i+1} &= \frac{\vec{u}\cdot\vec{v}_{i+1}}{v^2}\left(1 - \frac{\vec{u}\cdot\vec{v}_i}{v^2}\right) \\
p_0 &= \left(1 - \frac{\vec{u}\cdot\vec{v}_i}{v^2}\right)\left(1 - \frac{\vec{u}\cdot\vec{v}_{i+1}}{v^2}\right) \\
p_{i+4} &= \frac{\vec{u}\cdot\vec{v}_i}{v^2}\frac{\vec{u}\cdot\vec{v}_{i+1}}{v^2}
\end{aligned} \tag{3.12}$$

The other p_j are zero for $j \neq i, i+1, i+4$. From the above equation it is easy to check that $p_0 + p_i + p_{i+1} + p_{i+4} = 1$. Numbering of indices is show in Fig. 3.4.

3.4 The advection-diffusion model with Lattice Boltzmann method

In this section, a model of advection-diffusion with lattice Boltzmann method (LB) is introduced. Advection diffusion equation is generally written as

$$\partial_t \rho + \nabla(\vec{u}\rho) = D\nabla^2\rho. \tag{3.13}$$

where D is the diffusion coefficient and ρ is the density of particles. To calculate the density at each time and step, distribution functions are summed up

$\rho = \sum f_i$ as the same as viscous flow case (section 3.2.2). The difference between the simulation of viscous flow and the simulation of advection-diffusion is only the equation of local equilibrium f^{eq} part (Chopard et al, 2009 [31]).

$$f_i^{eq} = t_i \rho \left[1 + \frac{\vec{v}_i \vec{u}}{c_s^2} \right]. \tag{3.14}$$

If u is the velocity of fluid flow, a term $\frac{1}{2c_s^4} Q_{i\alpha\beta} u_\alpha u_\beta$ is to be added to eq. 3.14. With this term, eq. 3.14 is the same as eq. 3.7 of viscous flow. Main difference is that we give the advection velocity u in advection-diffusion simulation.

With these methods, diffusion coefficient D emerges as

$$D = c_s^2 \Delta t \left(\tau - \frac{1}{2} \right). \tag{3.15}$$

To simulate advection-diffusion, we also need to specify the value of f_i at the boundary. Here, I introduce two types of boundary condition; *Bounce Back*, and *Absorbing* boundary conditions. Actually, a periodic boundary condition is often used for fluid flow (Wolf-gradlow 2000 [138]), but it is not appropriate as the particles which go out from one side of the boundary come into the calculation area again.

Bounce Back, a very popular way to impose a boundary with zero velocity (no-slip condition), is one possibility for the advection-diffusion. We need to redefine the collision operator of LB on the boundary cells,

$$f_i^{out} = f_{opp(i)}^{in} \tag{3.16}$$

where *opp*(i) is the direction of opposite propagation speed. For example, with the D2Q9 lattice in Fig.3.3,

$$v_{opp(0)} = v_0, v_{opp(1)} = v_5, v_{opp(2)} = v_6, v_{opp(3)} = v_7, v_{opp(4)} = v_8. \tag{3.17}$$

Absorbing boundary condition is to impose the boundary where particles are disappear like they are absorbed by the surrounding wall. For the implementation, we need to simply set f_i at boundary zero.

$$f_i = 0 \tag{3.18}$$

In fact, the *Bounce Back* condition affects the particle concentration as the distribution reflects at the boundary. This is not appropriate for our particle transport, as we consider semi-infinite atmosphere for the calculation domain and particle do not reflect at the boundary. Therefore, we applied *Absorbing* condition which can reproduce condition that the particles go out from the boundary and never come back inside by the reflection.

3.5 The anisotropic advection-diffusion equation of CA

We now derive the PDE of multiparticle CA associated with (3.11), in two dimensions and for a constant $\vec{u} = (u_x, u_y)$. Let us call $\vec{v}_1$

and $\vec{v}_2$ the two lattice velocities that define the quadrant in which $\vec{u}$ lies. According to our notation, the diagonal velocity is labeled $\vec{v}_5 = \vec{v}_1 + \vec{v}_2$.

The probability $\rho(\vec{r}, t)$ is given by (3.11) which, with our notation, reduces to

$$\rho(\vec{r}, t+\Delta t) = p_0\rho(\vec{r}, t) + p_1\rho(\vec{r} - \vec{v}_1\Delta t, t) + p_2\rho(\vec{r} - \vec{v}_2\Delta t, t) + p_5\rho(\vec{r} - \vec{v}_5\Delta t, t) \tag{3.19}$$

A Taylor expansion up to order $\mathcal{O}(\Delta t^2)$ gives

$$\partial_t\rho + \frac{\Delta t}{2}\partial_t^2\rho = -\sum_{i=1,2,5} p_i v_{ia}\partial_a\rho + \frac{\Delta t}{2}\sum_{i=1,2,5} p_i v_{ia} v_{i\beta}\partial_a\partial_\beta\rho \tag{3.20}$$

where indices a and β refer to the spatial components of $\vec{v}_i$ and we used the Einstein summation convention over repeated greek indices.

The quantity $\sum_{i=1,2,5} p_i\vec{v}_i$ is easily calculated using expressions (3.12)

$$\begin{aligned} p_1\vec{v}_1 + p_2\vec{v}_2 + p_5\vec{v}_5 &= \frac{\vec{u}\cdot\vec{v}_1}{v^2}\left(1 - \frac{\vec{u}\cdot\vec{v}_2}{v^2}\right)\vec{v}_1 + \frac{\vec{u}\cdot\vec{v}_2}{v^2}\left(1 - \frac{\vec{u}\cdot\vec{v}_1}{v^2}\right)\vec{v}_2 \\ &\quad + \frac{\vec{u}\cdot\vec{v}_1}{v^2}\frac{\vec{u}\cdot\vec{v}_2}{v^2}(\vec{v}_1 + \vec{v}_2) \\ &= \frac{\vec{u}\cdot\vec{v}_1}{v^2}\vec{v}_1 + \frac{\vec{u}\cdot\vec{v}_2}{v^2}\vec{v}_2 \\ &= \vec{u} \end{aligned} \tag{3.21}$$

because $\vec{v}_1$ and $\vec{v}_2$ are orthogonal vectors. Note that this result is valid for any orientation of the coordinate axes.

The other term to be computed in (3.20) is $\sum_{i=1,2,5} p_i v_{ia} v_{i\beta}$. Due to the expression of p_i in terms of $\vec{v}_i$, it produces terms like $\sum_{i=1,2,5} v_{ia} v_{i\beta} v_{i\gamma}$ which actually depends on the choice of the orientation of coordinate system (i.e. the specific value of the components of the $\vec{v}_i$'s). This term is thus not invariant under rotation. We shall compute it for the specific choice of orientation given in (3.9) and (3.10). Thus $\vec{v}_1$ has only a x-component and

$\vec{v}_2$ a y-component. Therefore

$$\begin{aligned}\frac{\Delta t}{2}\sum_{i=1,2,5} p_i v_{ia} v_{i\beta}\partial_a\partial_\beta\rho &= \frac{\Delta t v^2}{2}\left[\frac{u_x}{v^2}\left(1-\frac{u_y}{v}\right)\partial_x^2+\frac{u_y}{v^2}\left(1-\frac{u_x}{v}\right)\partial_y^2\right.\\ &\left.+\frac{u_y}{v^2}\frac{u_x}{v}\left(\partial_x^2+2\partial_x\partial_y+\partial_y^2\right)\right]\rho\\ &= \frac{\Delta t v^2}{2}\left[\frac{u_x}{v}\partial_x^2+\frac{u_y}{v}\partial_y^2+2\frac{u_x u_y}{v^2}\partial_x\partial_y\right]\rho\\ &= \frac{\Delta t v^2}{2}\partial_x\left(\frac{u_x}{v}\partial_x+\frac{u_x u_y}{v^2}\partial_y\right)\rho+\frac{\Delta t v^2}{2}\partial_y\left(\frac{u_x u_y}{v^2}\partial_x+\frac{u_y}{v}\partial_y\right)\rho\end{aligned} \tag{3.22}$$

Then we can write

$$\frac{\Delta t}{2}\sum_{i=1,2,5} p_i v_{ia} v_{i\beta}\partial_a\partial_\beta\rho = \partial_a d_{a\beta}\partial_\beta\rho \tag{3.23}$$

where the matrix $d_{a\beta}$ is defined as

$$d = \frac{\Delta t v^2}{2}\begin{pmatrix}\frac{u_x}{v} & \frac{u_x u_y}{v^2}\\ \frac{u_x u_y}{v^2} & \frac{u_y}{v}\end{pmatrix} \tag{3.24}$$

We can now rewrite (3.20) using (3.21), (3.23) and (3.24). It becomes

$$\partial_t\rho+\frac{\Delta t}{2}\partial_t^2\rho = -u_a\partial_a\rho+\partial_a d_{a\beta}\partial_\beta\rho \tag{3.25}$$

In order to eliminate the second order time derivative in this equation we first differentiate it with respect to time. Neglecting derivatives of 3rd order, the time-derivative of (3.25) gives

$$\partial_t^2\rho = -u_a\partial_a\partial_t\rho \tag{3.26}$$

And, similarly, $\partial_a\partial_t\rho$ is obtained by a spatial derivative of (3.25), again discarding 3rd order derivatives

$$\partial_a\partial_t\rho = -\partial_a u_\beta\partial_\beta\rho \tag{3.27}$$

where we have paid attention to change the name of the summation index. Combining the last two equations gives

$$\frac{\Delta t}{2}\partial_t^2\rho = \frac{\Delta t}{2}u_a\partial_a u_\beta\partial_\beta\rho = \frac{1}{2}v^2\Delta t\partial_a\frac{u_a}{v}\frac{u_\beta}{v}\partial_\beta\rho = \partial_a f_{a\beta}\partial_\beta\rho \tag{3.28}$$

where $f_{a\beta}$ is a lattice contribution to the diffusion matrix whose expression is

$$f = \frac{\Delta t v^2}{2} \begin{pmatrix} \frac{u_x^2}{v^2} & \frac{u_x u_y}{v^2} \\ \frac{u_x u_y}{v^2} & \frac{u_y^2}{v^2} \end{pmatrix} \tag{3.29}$$

Finally, using (3.28), eq. (3.25) becomes

$$\partial_t \rho + u_a \partial_a \rho = \partial_a (d_{a\beta} - f_{a\beta}) \partial_\beta \rho \tag{3.30}$$

or, with the diffusion matrix $D_{a\beta} = d_{a\beta} - f_{a\beta}$

$$D = \frac{\Delta t v^2}{2} \begin{pmatrix} \frac{u_x}{v} - \frac{u_x^2}{v^2} & 0 \\ 0 & \frac{u_y}{v} - \frac{u_y^2}{v^2} \end{pmatrix} \tag{3.31}$$

the advection-diffusion equation corresponding to the 2D multiparticle CA model is

$$\partial_t \rho + u_a \partial_a \rho = \partial_a D_{a\beta} \partial_\beta \rho \tag{3.32}$$

We observe that D is anisotropic, even though the lattice diffusion has removed the non-diagonal contributions. This is clearly an unwanted feature of the model as it reflects a non invariance under a rotation of the coordinate axes.

3.6 Numerical validation

3.6.1 Anisotropic advection-diffusion

We shall first verify numerically that our CA model obeys eq. (3.32). The general solution of an anisotropic advection diffusion

$$\partial_t \rho + u_a \partial_a \rho = \partial_a D_{a\beta} \partial_\beta \rho \tag{3.33}$$

is

$$\rho(\vec{r}, t) = \sum_{\vec{k}} A_{\vec{k}} e^{-(k_a D_{a\beta} k_\beta) t} e^{i\vec{k}(\vec{r} - \vec{u}t)} \tag{3.34}$$

where $\vec{k}$ denotes all the possible wave vectors. For a discrete periodic system of size $L_x = N_x \Delta x$ and $L_y = N_y \Delta x$, the acceptable $\vec{k}$s are

$$\vec{k} = 2\pi \left(\frac{n_x}{L_x}, \frac{n_y}{L_y}\right)$$

with $n_x \in \{0, 1, \ldots N_x - 1\}$ and $n_y \in \{0, 1, \ldots N_y - 1\}$.

N_x	Δt	ε
10	0.1	21.3e-4
20	0.05	6.2e-04
40	0.025	1.73e-04
80	0.0125	0.46e-04

Table 3.1: Value of the error between the analytical expression and the numerical simulation for different discretization level. Here $\Delta x = L/N_x$, $N_x = N_y$, $L = 1$, $T = 1$, $u_x = 0.7v$, $u_y = 0.1v$, and $v = \Delta x/\Delta t$. Note that, when refining the grid we have refined the time accordingly.

Here we consider the case of a periodic system of size $L_x = L_y = 1$, in some physical units that we simulate until time $t = 1$, also in some physical units. We choose $N_x = N_y = 20$ and $\Delta t = 0.05$ (in the same units as t). We take $\vec{u} = (0.7, 0.1)v$ where $v = \Delta x/\Delta t$ and $\Delta x = L/N_x$. As an initial condition we take $\rho(\vec{r}, 0) = \cos(\vec{k}\cdot\vec{r})$, for $\vec{k} = (2\pi/L)(1, 1)$. We observe a very good agreement between simulation and theory, showing that our analytical derivation is correct. Actually it can be checked that the CA obeys eq. (3.32) up to second order in the lattice spacing Δx. Table 3.1 gives the error

$$\varepsilon \equiv \frac{1}{N_x^2}\sum_{\vec{r}} |\rho(\vec{r}, t) - \rho_{th}(\vec{r}, t)|$$

as a function of the discretization. We observe a reduction of the error by a factor 4 as Δx decreases by a factor 2.

3.6.2 Effective diffusion

Since our model produces an anisotropic diffusion, we may want to know which isotropic diffusion coefficient approximates it. A natural solution is to define an effective diffusion coefficient which is the average of D_{xx} and D_{yy}. So we define

$$\begin{aligned} \bar{D} &= \frac{1}{2}\left(D_{xx} + D_{yy}\right) \\ &= \frac{\Delta t v^2}{4}\left[\frac{u_x}{v} + \frac{u_y}{v} - \frac{u_x^2}{v^2} - \frac{u_y^2}{v^2}\right] \end{aligned} \tag{3.35}$$

We shall now study the behavior of our model is the case of a symmetrical and localized initial condition given by

$$\rho(\vec{r}, 0) = a \exp\left(-\frac{(x - L/2)^2 + (y - L/2)^2}{2b^2}\right)$$

where a and b are some parameters.

The time evolution of such an initial condition, subject to an advection-diffusion process, is from Suga (2006) [111]

$$\rho(\vec{r},0) = \frac{ab^2}{b^2+2\bar{D}t}\exp\left(-\frac{(x-L/2-u_xt)^2+(y-L/2-u_yt)^2}{2b^2+4\bar{D}t}\right) \tag{3.36}$$

Note that this solution assumes an infinitely large system. With a finite computational domain, t should be chosen small enough so that the boundary conditions do not play a role.

We now consider a numerical experiment in which our CA model shows its undesired anisotropic diffusion due to the fact that $u_x \neq u_y$. In order to estimate the importance of this model artifact, we compare the result of a numerical simulation with the prediction of (eq. 3.36).

We choose $L = 1$, $N_x = 40$, $t = 0.4$, $\Delta t = 0.025$, $a = 1$ and $b = 2\Delta x$. Different advecting speeds are considered. When $\vec{u}$ is along the diagonal of the lattice, the diffusion tensor D reduces to a scalar value and the CA model is isotropic. Otherwise, D has two different components and the situation is anisotropic.

To compare the CA model with the theoretical solution of an isotropic advection-diffusion with effective diffusion $\bar{D}$, we consider the error ε defined as

$$\varepsilon \equiv \frac{\sum_{\vec{r}} |\rho_{th}(\vec{r},t) - \rho(\vec{r},t)|}{\sum_{\vec{r}} \rho_{th}(\vec{r},t)} \tag{3.37}$$

As opposed to Suga (2006) [111] we no longer normalize the error by N_x^2 because ρ is localized in a small region of the space. With our choice of parameter, the N_x^2 normalization would artificially decrease the error by a factor $64 = N_x^2/\sum_{\vec{r}}\rho_{th}(\vec{r},t) = 1600/25$.

Table 3.2 summarizes our results and quantifies the importance of the undesired anisotropy of the model. For high Peclet number, the accuracy of the CA model is then pretty good. The Peclet number is computed as $Pe = uL/\bar{D} = 4N_x/(1-(u/v))$.

Note that the error we obtain here are comparable in magnitude with those reported in Suga (2006) [111], not even taking into account the difference of normalization. Therefore, in the anisotropic case, the CA model performs only slightly worse than the D2Q9 LB model (and better than the D2Q5).

	Pe	$\vec{u}/v$	t	ε
aniostropic	377	$(0.1, 0.7)$	0.4	0.1
isotropic	377	$(0.7, 0.7)$	0.4	0.025
isotropic	11314	$(0.99, 0.99)$	0.2	0.0033
anisotropic	16000	$(0.99, 0)$	0.2	0.0064

Table 3.2: Value of the error between the analytical expression and the numerical simulation for different Peclet number and either an anisotropic or an isotropic situation. Here $L = 1$, $\Delta x = L/N_x$, $N_x = N_y$, $\Delta t = 0.025$ and $v = \Delta x/\Delta t$.

3.7 Boundary effect

Generally, boundaries affect the result of numerical calculation especially continuous material. To avoid the effect of boundaries, it is necessary to take enough calculation area. However, the wider the calculation area is, the more memory is needed. Therefore, it is compromise between having large calculation area and having the error from the effect of boundary. To study the boundary effect, numerical experiments are done with CA and LB, and their results are compared.

Calculation conditions are presented in Table 3.3, and the snap shot of them are in Fig. 3.5 c and d. The results of calculations are compared with the analytical solution of eq. (3.36) and the relative errors (eq. 3.37) are calculated for each method (Fig. 3.5 a and b).

Errors decrease with the time but they start to increase when the centers of density are close to the boundary of calculation area. The time of the transition from decrease to increase of the error is around 170 seconds for LB and it is 190 seconds for CA (Fig. 3.5 c and d). This implies CA has more sustainable region without having errors due to the boundary.

I also investigated how long the calculation is sustainable when the calculation changed and “maxtime” of stable calculation without the effect of boundary for each size of calculation area is plotted for both method (Fig. 3.5). Plots are linearly aligned, and linear regression for each method is done. The equations of the regression are shown in Fig. 3.7 as well.

Although the slopes are almost the same (0.48 for CA and 0.47 for LB), the CA has always larger maxtime.

Table 3.3: Calculation condition for the comparison of CA and LB boundary effect

Δx	1 (m)
Δt	0.1 (s)
NX	400
u	0.1 (m/s)
D	0.45 (m^2/s)
Pe	888.89
t	170 (s)

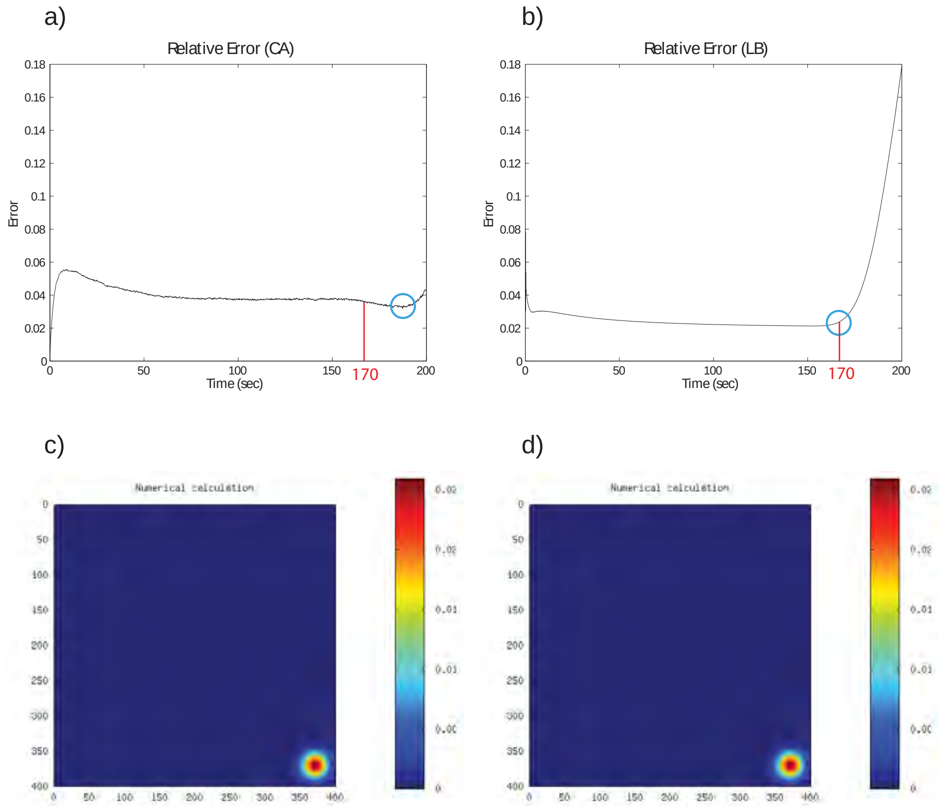

Fig. 3.5: Comparison of boundary effect of CA and LB method. Calculation conditions are summerised in Table 3.3. a) snap shot of numerical simulation for advection-diffusion close to the boundary for CA, b) snap shot of numerical simulation for advection-diffusion close to the boundary for LB, c) changes of relative error with time for CA and b) changes of relative error with time for LB. The point of relative error starting to grow is marked with blue circle, and the red line shows the 170 seconds, the time when LB relative error starting to grow.

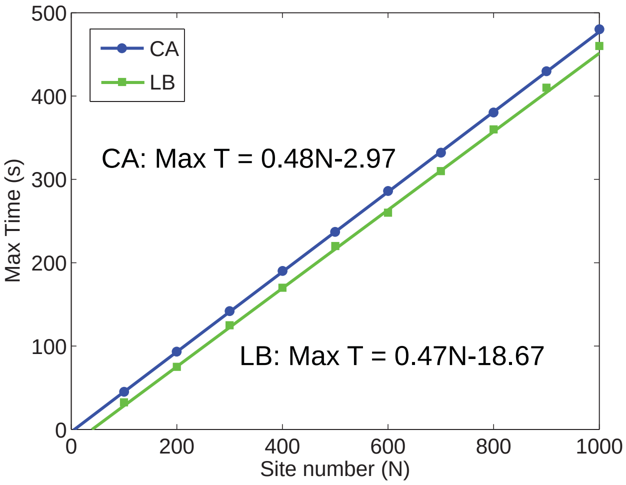

Fig. 3.6: Maximum time of calculation without having a error due to the boundary effect. Equations are the results of linear regression of plots for each method. MaxT is the maxtime, N is the site number.

3.8 Stability Analysis and Calculation Efficiency

When running either the CA or the LB simulations, the cell size Δx and time step Δt should be chosen as large as possible in order to reduce the computational time and memory requirement. However, accuracy and stability constraints set a limit to the maximum value we can choose. We will show that the LB model is more constrained than the CA.

To specify the physical parameters of the problem, we choose the example of the Askja volcano 1875 D eruption [106]. During this eruption, volcanic plume reached the 26 km height (Carey and Sparks, 1986 [24]) and with some dynamics of volcanic plumes, the height of the bottom of the umbrella cloud (H_{cb}) where tephra start to fallout, can be estimated to 14.6 km. Grain size distribution of the tephra on the ground is observed in the field after the eruption from around the vent to 200 km far from the vent. Therefore, the calculation domain should be 14.6 km×200 km. Wind velocity model is suggested by Bonadonna and Phillips (2003) [13]: it varies with height and the maximum wind is 28 m/s at the height of tropopause. However, we can use the constant wind velocity 25 m/s for simplicity. The particle terminal velocity depends on the altitude. It is given in Bonadonna and Phillips (2003) [13], assuming a spherical particle model. The travel time of a particle until sedimentation on the ground (i.e. the duration of the

Table 3.4: Parameters of tephra transport (Askja 1875D eruption)

Parameter	**Value**	**unit**
Width	200	km
Height	14.6	km
Duration	80000	s
Windlocity Velocity	25	m/s
Mean grain size	-2.3	ϕ
Mean velocity	27	m/s
Diffuion coefficient	100	m^2

.

simulation) can be estimated without diffusion. For the smallest particles, it is around 80000 seconds. Grain-size analysis of the ground sediments is done by (Sparks et al., 1981 [106]). In this report, grain size varies from -9ϕ to 4ϕ (ϕ is defined as $\phi = -\log_2 d$, where d is particle diameter in mm). The average grain size is -2.3ϕ. The mean terminal velocity of the mean grain size is around 5 m/s. Therefore, the mean advection speed is the vector sum of terminal velocity and windvelocity which is 27 m/s. Diffusion coefficient of tephra fall range from $\approx 5 \times 10^{-5}$ to $\approx 100\ m^2/s$ vertically, and from ≈ 100 to $\approx 10^4\ m^2/s$ horizontally ([35]). As an applicable value for both horizontal and vertical directions, we can choose the diffusion coefficient $D = 100\ m^2/s$. All the parameters of tephra transport are listed in Table 3.4.

We have analyzed the stability of LB model by numerical experiments corresponding to the Askja 1875 D eruption. From the definition of Courant number $\gamma = u\frac{\Delta t}{\Delta x}$ (u is the advection speed), Δx can be written as follows.

$$\Delta x = \frac{u\Delta t}{\gamma} \tag{3.38}$$

The diffusion coefficient of the LB advection-diffusion model is reported for instance in Guo et al, (1999) [52], Suga (2006) [111] and Chopard et al, (2008) [31].

$$\bar{D} = \frac{1}{2}\frac{\Delta x^2}{\Delta t}\left(\tau - \frac{1}{2}\right) \tag{3.39}$$

From equation (3.38) and (3.39), we can derive the relationship between γ and Δx for LB advection-diffusion model.

$$\gamma = \frac{u\Delta x}{2D}\left(\tau - \frac{1}{2}\right) \tag{3.40}$$

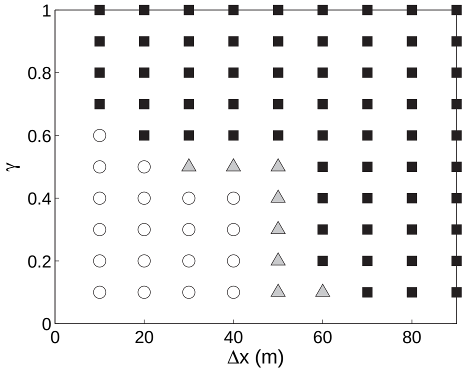

Fig. 3.7: Result of stability analysis. Squares are unstable points. Triangles are stable but the sum of the density has negative value. Circles are stable points. Among these points, we can find the maximum Δx and maximum γ which is $\Delta x = 40$ and $\gamma = 0.4$.

In our numerical experiment we used a terminal velocity which varies with the height [13], which put extra constraints on the stability of the LB model compare to Suga (2006) [111]. Figure 3.7 shows the measured stability region in the $\Delta x - \gamma$ plane.

The maximum γ and Δx are chosen within the clearly stable region of figure 3.7. The maximum cell size Δx and time step Δt are then found to be

$$\Delta x = 40m,\ \Delta t = 0.59s(LB) \tag{3.41}$$

For the CA model, the effective diffusion coefficient is obtained by transforming eq. (3.35).

$$D = \frac{\Delta t v^2}{2}\left(\frac{u}{v}\right)\left(1{-}\frac{u}{v}\right) \tag{3.42}$$

By substituting Courant number $\gamma = u\frac{\Delta t}{\Delta x}$ we can get

$$D = \frac{\Delta x}{2} u\,(1{-}\gamma)\,, \qquad \Delta x = \frac{2D}{u(1{-}\gamma)} \tag{3.43}$$

The CA simulation is unconditionally stable but it is necessary to have $\gamma < 1$ all over the calculation. Therefore, we chose $\gamma = 0.96$, Δx=400m and Δt=$\frac{\gamma\Delta x}{u}$=1.92.

$$\Delta x = 400m,\ \Delta t = 1.92s(CA) \tag{3.44}$$

Table 3.5: Parameters of calculation

		LB	**CA**
Δx	Cell Size	40	400
Δt	Time step	0.59	1.92
N_{site}	Number of site	1.83×10^6	1.8×10^4
I	Number of iteration	1.36×10^5	4.17×10^4
P	Number of particle		10^5
Q	Number of velocities	4 (D2Q4)	
G	Number of grain-size class	13	13

.

We thus observe that the cell size Δx is 10 times larger than that of LB model and the time step Δt is about 3 times longer than in the LB model.

With the above choice of Δx and Δt we can analyze the computational efficiency of both solvers.

LB efficiency In each site of LB model, we have $Q = 4$ distribution functions with a D2Q4 model (table 3.5). Moreover, in a view of future study adding the aggregation process, we should keep the information of all $G = 13$ grain-size classes. Therefore memory usage of LB model is proportional to $N_{site} \times Q \times G$, where $N_{site} = 1.8 \times 10^6$. The number of iterations is $I = T/\Delta t = 1.36 \times 10^5$, where T is the total simulation time.

$$Memory \propto N_{site} \times Q \times G = 1.83 \times 10^6 \times 4 \times 13 = 9.51 \times 10^7$$
$$CPUtime \propto N_{site} \times I \times G = 1.83 \times 10^6 \times 1.36 \times 10^5 \times 13 = 3.23 \times 10^{12}$$

CA efficiency In the CA model, the memory scales as $N_{site} \times G$ because, for each class of grain size, we only need to store an integer value corresponding to the number of particles of that size.

For the particle movement, different types of update schemes can be considered [72, 41]. The slowest one requires to move each particle one by one, according to random numbers. In that case, the CPU time grows as $N_{site} + P$ where here $P = 10^5$ is the total number of transported particles and $N_{site} = 1.8 \times 10^4$ is the number of site of the CA lattice. In a faster updated scheme, the particles are moved by blocks, assuming a Gaussian ditribution for the choice of directions [72]. In this case, the CPU time scales as $N_{site} \times G$. Note that both approaches keep the discrete nature of the particles all along the process and include fluctuations.

But a much faster way is to simulated the CA dynamics directly with eq. (3.11), according to the local values of the p_i's. Then the calculation

Table 3.6: Comparison of calculation efficiency

	LB	**CA**
Memory	9.51×10^7	2.34×10^5
CPU time	3.23×10^{12}	9.76×10^9

.

time goes as the total number of site $N_{site} \times G$ multiplied by the number of iterations $I = 4.17 \times 10^4$.

$$Memory \propto N_{site} \times G = 1.8 \times 10^4 \times 13 = 2.34 \times 10^5$$

$$CPUtime \propto N_{site} \times G \times I = 1.8 \times 10^4 \times 13 \times 4.17 \times 10^4 = 9.76 \times 10^9$$

The result of the comparison shown in Table 3.6. We observe that both memory and CPU time are two orders of magnitude larger for the LB model. For high Peclet numbers, the intrinsic anisotropy of the CA model is negligible and we can conclude that, for tephra transport, the CA approach is computationally more appropriate than the LB, at least if we use eq. (3.11) to update the density of transported particles. As to accuracy, our observation (not shown here) is that both the CA and LB model give consistent results which are well within the precision limits of the field observations.

3.9 Conclusions of CA and LB comparison

We compared two numerical models for advection-diffusion-sedimentation: a multiparticle CA and a LB model. We gave a mathematical description of the CA model and showed that, up to second order in time and space, it simulates an advection process with anisotropic diffusion. However, for high Peclet numbers, the behavior of the model can be well approximated by an effective isotropic diffusion coefficient.

We determined the parameters of the LB model that give the fastest simulation of the transport of tephra in the 1875 eruption of the Askja volcano. Due to numerical stability constraints, the mesh size and time step of the LB method must be much smaller than that for the CA model, which is unconditionally stable. This causes an increase of about two orders of magnitude in the time and space complexity of the LB method as compared to the CA method. In terms of accuracy, both methods are of the same level, in spite of the difference in the space and time discretization.

Chapter 4

A simple model of tephra transport

4.1 Introduction

This chapter is a first step in applying CA for tephra transport, we perform numerical simulations for the tephra transport in the atmosphere from the height H_{cb} (Fig. 4.1) of both strong and weak plumes (Fig. 4.1). The part of the work in this chapter is published as Tsunematsu et al, (2008) [121].
As it is introduced in Chapter 1, interesting topics of tephra transport are the weak plume and the aggregation.
Tephra and gas form an eruption column above the crater, called the plume. Volcanic plumes can be described as multiphase (gas and solid particle) turbulent flows (Bonadonna et al, 2005a [16]). The physics of the plume has been discussed in Woods (1998) [139]. A well-developed eruption column typically consists of a gas thrust region, a convective region and an umbrella region (Fig. 4.1). The injection momentum dominates the gas thrust region, thus, the eruption column rises against gravity. The convective region is where buoyancy force dominates.
The uppermost region (i.e. umbrella cloud) is characterized by lateral intrusion into the atmosphere, at the level of neutral buoyancy where the ascending plume has the same density as the surrounding atmosphere (H_b).
Tephra particles are transported first in the eruption column. Some of them fall during the ascent when terminal velocity exceeds rising speed of the column. Particles which can reach the top of the plume are carried in the spreading current and will fall out at the base of the umbrella cloud (H_{cb}). Tephra are transported in the atmosphere by wind and finally deposit on the ground. Observed tephra deposit shows some diffusion in grain size distribution (Bonadonna and Houghton, 2005 [12], Sparks et al, 1981 [106],Carey and Sigurdsson, 1982 [25]).
Generally, the thickness of tephra deposits decreases with the distance from the crater(Bursik et al, 1992a [21],Bonadonna et al, 1998 [14]). However, sometimes, anomalous thickening occurs: high thickness tephra deposit ap-

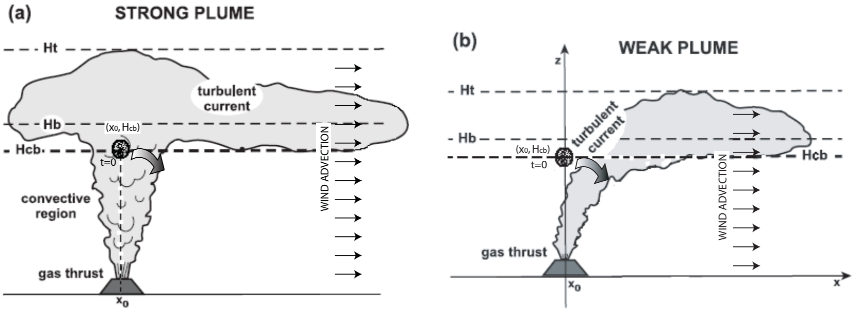

Fig. 4.1: Sketch of plume features. The eruption column is classified into gas thrust region, convective region and umbrella region, from bottom to top. H_t is the total height of the eruption column. H_b is the neutral buoyancy level. H_{cb} is the base of spreading current. At time $t = 0$, we disperse all particles from the point (x_0, H_{cb}). Relatively large particles fall out from the plume during the ascent.

pear at certain distances from the crater. Observations of anomalous thickening suggest that this phenomenon is mainly related to fine particles aggregation(Bonadonna et al, 1998 [14]). As a result, due to their larger size, aggregates will fall faster than the finer particles they are made of. Aggregation is believed to happen within any eruption plumes characterized by fine particles.

Study of tephra fallout progressed in the last two decades and many models have been developed showing agreement with field data(Carey and Sigurdsson, 1982 [25],Bursik et al, 1992a [21], Bonadonna et al, 1998 [14], Suzuki, 1983 [113],Bonadonna and Phillips [13], Bonadonna et al, 2005a [15]). However, there are still fundamental processes that need to be parametrized and numerically described in order to provide comprehensive and reliable forecasting of tephra deposition. Considering the diffusion of tephra particles and microscopic aggregation, it is useful to use a CA method which can implement both microscopic and macroscopic aspects of particle transport.

This chapter is a first step in applying CA for tephra transport, we perform numerical simulations for the tephra transport in the atmosphere from the height H_{cb} (Fig. 4.1) of both strong and weak plumes (Fig. 1). We show the good agreement between the result of numerical simulation and field data in the case of sedimentation from strong plumes and no aggregation (i.e. 1875 eruption of Askja volcano, Iceland). On the other hand, we observe significant discrepancies in the case of sedimentation from weak plumes (i.e. 17 June 1996 eruption of Ruapehu volcano, New Zealand) and when aggregation processes play an important role in particle sedimentation (i.e. 18 May 1980 eruption of Mt St Helens, USA). This suggests that, in order to produce a comprehensive numerical model for tephra dispersal, the CA method needs to be implemented to take into account the dynamics of weak plumes and particle aggregation.

4.2 Tephra transport model

Process of tephra transport can be investigated in two areas: Umbrella cloud (turbulent current) and the atmosphere under the umbrella cloud (Fig. 4.1). The simplest way to compute tephra transport is ballistic calculation (BA). BA is the simple Lagrangian simulation without diffusion effect. Particles are transported only by wind and settling velocity.

$$\dot{\mathbf{r}} = \mathbf{u}_{wind} + \mathbf{u}_{settling} \tag{4.1}$$

In BA, particles starting from the same point with the same size and the same density reach the same point on the ground. On the other hand, if there is some diffusion, particles disperse in the atmosphere and deposit at different places. A multiparticle CA approach can be devised to account for such a dispersion. We evaluate the difference between CA and BA by comparing the result of the two methods. In our numerical experiments, all tephra begin to disperse from the point (x_0, H_{cb}) at time $t = 0$, in a two-dimensional domain (Fig. 4.1).

Tephra is transported horizontally in the atmosphere by the wind which we assume to be of velocity u_x for the whole simulation domain. The vertical velocity u_y is set to the terminal velocity u_t of each particle (i.e. the speed which the particle reaches due to the balance of gravity, buoyancy and friction forces). u_t depends on atmospheric characteristics and, more specifically, on the vertical location of the particle. We compute the terminal velocity as a function of the Reynolds number, as described in [13].

4.2.1 Cellular Automata Tephra Transport Model

To simulate the transport of tephra particles according to the velocity field described above, we use the CA model defined in [28] which was also successfully applied to snow and sediment transport [71, 40]. This model is easy to implement and allow the tracking of individual particles. This property is important to implement the aggregation rules. At each lattice site lies a population of particles subject to a velocity vector $\mathbf{u}$. Ideally, the particles would follow this velocity in the classical way $\mathbf{r}(t + \Delta t) = \mathbf{r}(t) + \mathbf{u}\Delta t$, where Δt is the CA discrete time step. However, except for velocity fields parallel to lattice directions with an intensity equals to $\frac{dx}{dt}$ (where Δx is the distance

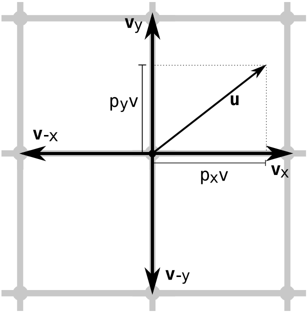

Fig. 4.2: Probabilistic rule of particle transport. The gray lines represents the lattice. The four possible velocity vectors $\mathbf{v}_i$ and the true velocity $\mathbf{u}$ are indicated with black arrows.

between two lattice sites), this would lead the particles off-lattice. In order to constrain the particles on the lattice, we use a probabilistic scheme.
We associate to each lattice direction i a probability p_i proportional to the projection of $\mathbf{u}$ onto the velocity vectors $\mathbf{v}_i$ of norm $v = (\Delta x/\Delta t)$. In a 2D case, the four directions are $i = \pm x$ and $i = \pm y$, as illustrated in Fig. 4.2 and the p_i are obtained as

$$\begin{aligned} p_x &= \max\left(0, \frac{\mathbf{v}_x \cdot \mathbf{u}}{v^2}\right) & p_{-x} &= \max\left(0, \frac{-\mathbf{v}_x \cdot \mathbf{u}}{v^2}\right) \\ p_y &= \max\left(0, \frac{\mathbf{v}_y \cdot \mathbf{u}}{v^2}\right) & p_{-y} &= \max\left(0, \frac{-\mathbf{v}_y \cdot \mathbf{u}}{v^2}\right) \end{aligned} \tag{4.2}$$

To have $p_i \leq 1$, the lattice must be chosen so that $u < v$ at every site.
Note that if $p_x > 0$ then $p_{-x} = 0$ and vice versa. The same holds for p_y and p_{-y}. Thus, from now on, we assume that p_x and p_y are positive.
To update the system, two independent random numbers $q_x, q_y \in [0, 1]$ are drawn per particle at each time step. If $q_x < p_x$ then the particle moves along the $\mathbf{v}_x$ direction. Similarly, if $q_y < p_y$, the particle moves along $\mathbf{v}_y$. Thus the particle will move to $\mathbf{r} + (\Delta x, 0)$ with probability $p = q_x(1 - q_y)$, to $\mathbf{r} + (0, \Delta x)$ with $p = (1 - q_x)q_y$, to $\mathbf{r} + (\Delta x, \Delta x)$ with $p = q_x q_y$ and stay at rest with $p = (1 - q_x)(1 - q_y)$. This is an algorithm of stochastic particle transport with probability p and random number q.
It has been showed in [28] that, when the velocity field is constant across the lattice, the average velocity $\langle \mathbf{v} \rangle$ following from the above rules is equal to $\mathbf{u}$. Here we evaluate the dispersion of the trajectory.
For n time steps, the particle trajectory is:

$$\mathbf{r}(n\Delta t) = \mathbf{r}_0 + \mathbf{v}(t_1)\Delta t + \mathbf{v}(t_2)\Delta t + \cdots + \mathbf{v}(t_n)\Delta t = \mathbf{r}_0 + \Delta t \sum_i \mathbf{v}_(t_i) \tag{4.3}$$

where $\mathbf{v}(t_i) \in \{0, \mathbf{v}_{\pm x}, \mathbf{v}_{\pm y}\}$ is the random velocity variable at step t_i. On average the above eq. reads

$$\langle \mathbf{r}(n\Delta t)\rangle = \mathbf{r}_0 + \Delta t \sum_i \langle \mathbf{v}(t_i)\rangle = r_0 + n\mathbf{u}\Delta t \tag{4.4}$$

Using eq. 4.2, it is possible to evaluate the dispersion in function of $\mathbf{u}$:

$$\langle \mathbf{v}^2\rangle - \langle \mathbf{v}\rangle^2 = u_x\left(\frac{\Delta x}{\Delta t} - u_x\right) + u_y\left(\frac{\Delta x}{\Delta t} - u_y\right) \tag{4.5}$$

This shows that the dispersion is minimal when $\mathbf{u}$ would lead the particle close to a lattice site and maximal when it would lead the particle between sites. Therefore, although D is not constant when $\mathbf{u}$ is not constant, the lattice can be adjusted to control the maximum dispersion.

4.2.2 Parameters and Eruptions

We apply the BA and CA models to two types of volcanic plumes; strong plumes and weak plumes. (Fig. 4.1) When the characteristic plume velocity is much greater than wind velocity, eruptive columns develop as a strong plumes. Strong plumes typically rise above the tropopause developing a horizontal umbrella cloud spreading laterally around the level of neutral buoyancy, whereas weak plumes typically develop in the troposphere following a bent-over trajectory as a result of the strong wind advection (Fig. 4.1b). Due to this inclined plume trajectory between the vent and the neutral buoyancy level, particle sedimentation in proximal area of weak plumes is more intense than for strong plumes. Table 1 shows the eruption and simulation parameters used to described the case study considered in this work (i.e. 1875 eruption of Askja volcano, Iceland; 17 June 1996 eruption of Ruapehu volcano, New Zealand; 18 May 1980 eruption of Mt St Helens, USA) As described above, the Askja and Mt St Helens plumes developed as strong plumes, whereas the Ruapehu plume was bent-over by a strong wind. In addition, the tephra deposit associated with the Mt St Helens eruption shows a double maximum of thickness because mostly consists of volcanic ash (diameter between 2mm and 1 micron) and therefore was significantly affected by aggregation processes. In contrast, both Askja and Ruapehu plume are characterized by coarser particle sizes and therefore were not significantly affected by particle aggregation.

Table 4.1: *Case studies. Askja: Askja 1875. Mt. St. Helens: 18 May 1980 eruption of Mt. St. Helens. CA parameters are presented below the separation line.*

	Askja	**Ruapehu**	**Mt. St. Helens**
Type of sedimentation	No aggregation	No aggregation	With aggregation
H_t [km]	26	8.5	16
H_{cb} [km]	14.6	4.8	9
Wind velocity [m/s]	25	24	32
Particle size (Φ)	-3 to 6	-8 to 14	-3 to 9
References	Sparks et al. (1981) [106]	Bonadonna and Houghton (2005) [12]	Carey and Sigurdsson (1982) [25]
Δx [m]	500	500	500
Δt [s]	16.6	4.167	12.5
Duration [s]	10^5	10^5	10^5

4.3 Results and Discussion

We first compare the CA to the classical BA (Fig. 4.3). The results of both approaches are in the same range but the average of CA for each class of particle sizes deviates from the BA predictions. The CA probabilistic model behaves in average like BA only when the velocity field is constant.[1] Numerical experiments with a uniform terminal velocity (data not shown) confirm this point. In our case, however, the terminal velocity u_y varies with the particle height.

Up to the above discrepancy, CA results show a good agreement between observed and calculated distances of particle deposition for Askja volcano (no aggregation). However, Ruapehu simulation results deviate from field data close to the crater. The area which is characterized by this discrepancy corresponds to the bent-over region. In Bonadonna and Phillips (2003)[13], they show that a transition between the bent-over region and the horizontal spreading at 27 km from the crater. Therefore, the incompatibilities must be attributed to the fact that the particles are dispersed from a lower level than H_{CB} close to the crater.

In contrast, the observed deposition distances of the fine particles are smaller than those computed for Mt. St. Helens volcano which produced an anoma-

---

[1] Layered wind velocity profile is used in Chap 5.

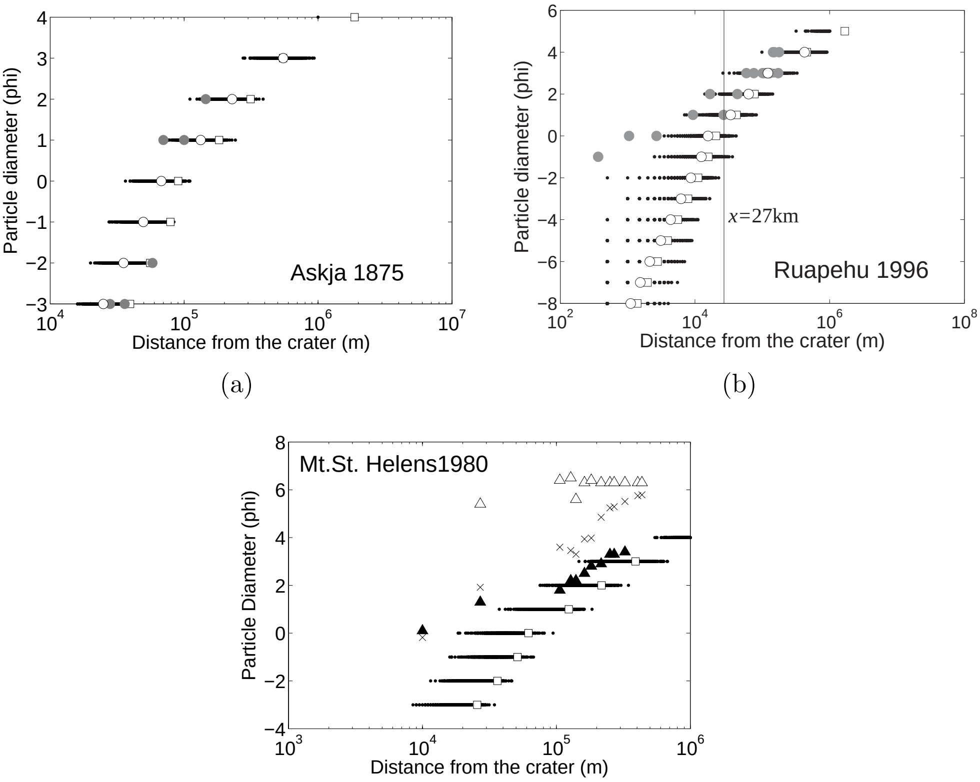

(a) (b)

(c)

Fig. 4.3: Observed and computed deposition distances for different particle sizes for (a) Askja 1875 and (b)Ruapehu 1996, and (c)Mt.St.Helens 1980. CA results are shown as black dots (which make black lines as there are many points), the average of CA for each class as white circles, and BA results as white squares. Field data of grain size mean are shown as gray circle for Askja. For Mt. St. Helens, field data in coarse mode are shown as black triangles, field data in fine mode are shown as white triangles and grain size in mean mode are shown as crosses. Distance is in log scale.Field data represents the mode of individual GS distribution collected at different distances from the vent for both Askja [106] and Mt. St. Helens[25].

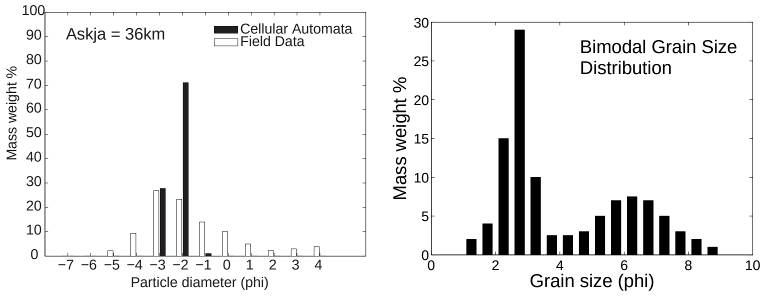

(a)

(b)

Fig. 4.4: (a) Histogram of grain size distribution of a tephra sample collected at 36km from the crater for the deposit of Askja 1875. The values shown in this figure are normalized by the total mass at the distance. Result of CA calculation is shown with black bar and the field data is shown with white bar. (b) Example of bimodal grain size of a tephra sample collected 182km from the crater

lous thickening at about 300km ENE from the vent and therefore was significantly affected by particle aggregation. Fig. 4.3 (a) shows the grain size distribution at the distance of 182km from the crater as an example. In fact, tephra deposits affected by aggregation processes are typically characterized by bimodal distribution where the coarse particle mode represents the population of particles that fell individually, whereas the fine particle mode represents the population of particles that fell as aggregates. The discrepancy between observed and calculated distances of Mt. St. Helens is therefore due to the fact that the fine particles fell as larger aggregates and thus deposited closer to the vent than expected. According to [13], most particles of diameter $d < 125 \times 10^{-3} mm$ (i.e. $\Phi = -\log(d) > 3$) are likely to fall as dry or wet aggregates. Eventually most aggregates break when impacting the ground, therefore releasing their fine particles and producing a bimodal grain size distribution as in Fig. 4.3.

In conclusion, we have shown that a multiparticle CA model is sufficient for describing simple tephra transport from strong plumes without aggregation (e.g. Askja eruption). However, in order to describe sedimentation controlled by aggregation processes (e.g. Mt. St Helens eruption), and turbulent in the eruption column (e.g. Ruapehu eruption), it is necessary to continue our study and improve our model.

Chapter 5

Advanced model of tephra transport (3D)

5.1 Introduction

We developed two-dimensional (2D) numerical models of tephra transport with multiple Cellular Automata method (CA) by releasing the volcanic particles from one point source (Chapter 4) at the bottom of spreading current. However, it is not realistic as particles travel in the plume and fallout from the edge or the bottom of spreading current (Bonadonna and Phillips, 2003 [13]). The source term, such as erupted volume, plume height, mass eruption rate, duration and initial grainsize distribution are significant inputs for the tephra transport model (Bonadonna et al., 2011 [17]). In the process of extending our multiparticle CA model from two dimension (2D) to three dimension (3D), the model of source term is improved as a result of comparison between CA model and Lattice Boltzmann model (Chapter 3)
In some existing tephra transport models, source term is one point (Searcy et al., 1998 [102]; Macedonio et al., 2005 [70]), a line along one vertical line over the crater (Bonadonna et al., 2005a [15]; Dacre et al., 2011 [37]; Stohl et al., 2011 [110]), or a set of discrete points in a region around a line above the crater (Costa, 2006 [35] and Folch et al, 2009 [49]) However, it is difficult to identify the source term during the eruption. For the operational requirement, Stohl et al, (2011) [110] have determined the source term by implementing inversion simulations. By simulating more than 6000 different scenarios, the mass emission rate is derived as a function of time and height. These models are practical, but they do not take into account the dynamics of volcanic plumes. Other models describe the three-dimensional dynamics of volcanic plumes but are computationally very heavy (e.g. ATHAM Oberhuber et al, 1998 [81])
Models of volcanic plumes are studied from 1950's. Morton et al., (1956) [76] suggested one-dimensional buoyant plume model. Turner(1980 [124], 1986 [123]) followed Morton's model to identify the entrainment effect of turbulent jet. Wilson (1976) [134], Wilson et al, (1978) [137] and Wilson and Walker

(1987) [136] considered the relationship between energy of eruption and the plume heights.
Sparks (1986) [104] applied the model of Morton et al., (1956) [76] to volcanic plumes and compared with real plume of Mount St. Helens eruption. Then, Woods (1988) [139] included thermal effect and presented superbuoyancy region where the plume's velocity increases with height because of the buoyancy due to the thermal effect although the former models suggested monotonic decrease of velocity with height. Up to this point, the plume models are in steady-state. Later on, not only three-dimensional models but also unsteady models are suggested (Neri and Macedonio, 1996 [79]; Neri et al 2003 [80]; Carazzo et al, 2008 [22]; Suzuki et al, 2005 [115]).
The effect of plume on tephra transport is considered by Bursik et al (1992a,b) [20], [21] Sparks et al, (1992) [107], Ernst et al., (1996) [44], Bonadonna and Phillips, (2003) [13] and Bonadonna et al., (2005) [16].
In Chapter 4, we also studied the effect of plume for both strong plume and weak plume. We showed that the simulation result of weak plume case does not agree with the observed ground deposition. It is possible to simulate the three-dimensional turbulent plumes. In fact, ATHAM (Oberhuber et al, 1998 [81]; Textor et al., 2006 a [116],b [117]) implemented three-dimensional (3D) plume and dispersion of particles. However, the implementation of 3D plume with tephra transport is not practical because of the heavy computation. In our model, the 1D steady-state model of Woods (1988) [139] and Carey and Sparks (1986) [24] is applied for the calculation of velocity field produced by strong plume. For weak plume, there is no appropriate model to simulate velocity profile of weak plumes although many numerical models are suggested. For example, a model in 1D (Bursik, 2001 [19]) is too simple to simulate the trajectory of weak plume because of the complicated turbulent feature of the weak plume such as bifurcate vorticity (Bonadonna et al, 2005 [16]). In this chapter, we only focus on strong plumes as a source term of tephra transport.
Another issue of tephra transport models is the effective "diffusion". Diffusion does not have collective view of tephra transport models. Tiesi et al., 2006 [120] pointed out that the atmospheric diffusion is parameterized differently in different models but is typically difficult to describe because of the poor understanding of diffusion dynamics in the atmosphere. Furthermore, Costa and Bonadonna (in Press) [11] reported as a result of case study of tephra dispersal models that there is a large discrepancy of diffusion coefficient calculated with different models.

Especially there are large gap in the treatment of turbulence. Some models ignore the atmospheric turbulence (Bonadonna et al., 1998[14]; Bursik et al., 1992a [21]; Sparks et al., 1992[107]) while some models are treated atmo-

spheric turbulence as it is not negligible (Bursik et al., 1992b [20]; Suzuki, 1983 [113]; Morrison and Webster 2005 [75]).
We treat turbulence as a main cause of diffusion because Robert and Webster, (2002) [95] and Thomson, (1987) [118] pointed that turbulence diffusion is more effective than molecular diffusion.

Turbulence in tephra transport field is classified into two types; (1) volcanic plume and (2) atmospheric turbulence. Volcanic plume is ejected with jet and rise with the buoyancy which is promoted by the entrainment of the air. In contrast, atmospheric turbulence is complicated with various effects such as wind, thermal instability, ground roughness and so on. Nevertheless main cause of the turbulence is horizontal wind flow. Thus, two sources of turbulence are fundamentally different and we treat them separately. We describe turbulence using different diffusion coefficients for atmosphere and volcanic plume. Technically, in our previous CA model, diffusion is controlled by grid size and time step in two-dimensional multiparticle CA model (Chapter 3). However, diffusion coefficient can vary depending on the situation. To control diffusion coefficient more flexibly, we added random velocity and produce the diffusion by the stochastic rule (section 5.2.2).

5.2 Model

5.2.1 Velocity field

Tephra are ejected from the crater and transport in the atmosphere. To simulate the transport of tephra, we consider the transport field as a space above the ground. We ignore the topography around the volcano and assume the ground height as a see level except the crater.

In our model, particles are released from the crater and they are transported in the velocity field defined as follows. To simulate with multiparticle Cellular Automata (CA) model, the advection velocities and random velocities are given. The velocity fields for both advection and random velocities are shown in Fig. 5.1. Both velocity field are classified into three regions; (1) plume, (2) umbrella cloud and (3) atmosphere. We define that plume is only a column part of the volcanic plume from the crater height to the neutral buoyancy height (H_b). Umbrella cloud is the region higher than H_b until the total plume height (H_t). Atmosphere is all space above the ground except the plume and umbrella cloud.

Advection velocity is a sum of velocity vector of wind velocity (u_w), plume velocity (u_p), settling velocity of particles (u_s) and spreading velocity of umbrella cloud (u_b). In each region, advection velocity is given as;

(1) Plume: $\mathbf{u} = \mathbf{u}_w + \mathbf{u}_p + \mathbf{u}_s$

(2) Umbrella cloud: $\mathbf{u} = \mathbf{u}_w + \mathbf{u}_b + \mathbf{u}_s$

(3) Atmosphere: $\mathbf{u} = \mathbf{u}_w + \mathbf{u}_s \ldots$

Random velocity in umbrella cloud (2) is given only for the vertical direction because the spreading velocity (u_b) includes the turbulent effect. In region (1) and (3), the random velocity $\mathbf{u}_r$ is given as the sum of horizontal and vertical random velocities.

(1) Plume: $\mathbf{u}_r = \mathbf{u}_{rph} + \mathbf{u}_{rpv}$

(2) Umbrella cloud: $\mathbf{u}_r = \mathbf{u}_{rav}$

(3) Atmosphere: $\mathbf{u}_r = \mathbf{u}_{rah} + \mathbf{u}_{rav}$

where index h and v represents horizontal and vertical components respectively and p and a represents the plume and atmospheric region.

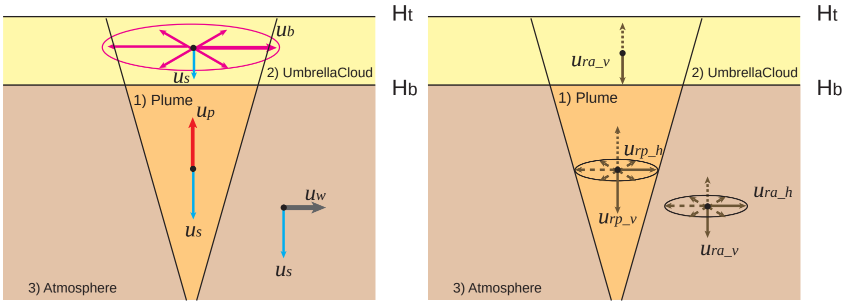

(a) (b)

Fig. 5.1: Velocity field of (a) advection velocity and (b) random velocity.

5.2.2 Tephra transport with multiparticle Cellular Automata method

In our 2D model, we have implemented advection-diffusion process by advection velocity and a diffusion which is a numerical artifact. The value of diffusion in our former model only depends on propagation speed v (defined as $v = \Delta x/\Delta t$, Δx is grid size and Δt is time step) and advection velocity $\mathbf{u}$ (sum of wind velocity $\mathbf{u}_w$ and settling velocity $\mathbf{u}_s$). With this method, it is impossible to vary the value of diffusion with location. As the value

Table 5.1: Parameters for modeling

Title	Notation
Diffusion coefficient	D
Concentration of particles	C
Standard deviation	σ
Probability to jump to next site	p
Total velocity	$\mathbf{u}_{tot}$
Advection velocity	$\mathbf{u}$
Random velocity	$\mathbf{u}_r$
Coefficient of random velocity	R
Direction angle of random velocity	θ_a
Propagation speed	$v = (\Delta x/\Delta t)$
Grid size	Δx
Time step	Δt
Iteration number	t
Distance of particle movement for one iteration	δx
Plume radius	L
Half radius of plume	b
Plume vertical velocity along center line	U_c
Plume vertical velocity	u_p
Particle settling velocity	u_s
Wind velocity	u_w
Velocity of spreading current	u_b

of diffusion can be different in the volcanic plume and outside of the plume (section 5.2.5), it is required to vary the value of diffusion coefficient with location. To vary the value of diffusion, we added random velocity $\mathbf{u}_r$ for each particle at each site.

Random velocity $\mathbf{u}_r$ has the magnitude u_r proportional to the propagation velocity and thus it is written as

$$u_r = Rv \tag{5.1}$$

where R is a coefficient of random velocity and v is propagation speed. For the 2D case, random velocity is given with constant magnitude of velocity u_r and random direction θ_a. Direction angle θ_a is chosen from the uniform distribution $\theta_a = \mathcal{U}(0, 2\pi)$. R is defined by the diffusion condition of each site. Then, the transport of each particle at each site is calculated with the sum of these velocities $\mathbf{u}_{tot}$ (Fig. 5.2) as

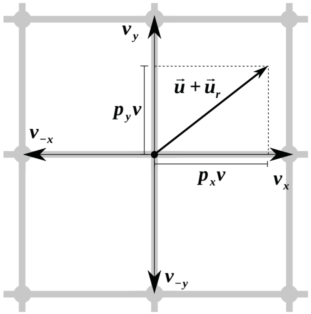

Fig. 5.2: Lattice of the tephra transport model with CA. At each lattice for each particle, advection velocity $\mathbf{u}$ and random velocity $\mathbf{u}_r$ are given.

$$\mathbf{u}_{tot} = \mathbf{u} + \mathbf{u}_r. \tag{5.2}$$

This total velocity $\mathbf{u}_{tot}$ is given to the simulator. The condition is that $\mathbf{u}+\mathbf{u}_r$ is smaller than propagation velocity $\mathbf{v}$ (Fig. 5.2). Considering that the diffusion in the atmosphere and in volcanic plumes is due to the turbulence, $\mathbf{u}_{tot}$ is connected to the velocity of turbulence as follows.
Generally, characteristics of turbulence are fully described by the mean flow and the associated fluctuations through the Reynolds decomposition:

$$u = \langle u \rangle + u' \tag{5.3}$$

Likewise, the concentration C is decomposed into a mean and fluctuation fields:

$$C = \langle C \rangle + C' \tag{5.4}$$

Advection-diffusion equation is generally written as

$$\frac{\partial C}{\partial t} + u_i \frac{\partial C}{\partial x_i} = D \frac{\partial^2 C}{\partial x_i \partial x_i}. \tag{5.5}$$

where u_i is the velocity. Here, we use the Einstein summation convention for repeated indices. x and t denotes the distance and time respectively.
In our model, advection velocity $\mathbf{u}$ is interpreted as mean velocity $\langle u \rangle$, and random velocity $\mathbf{u}_r$ is interpreted as fluctuations u'. By applying this velocity (eq. 5.3), we can reproduce concentration of particles of turbulence C which is dispersed by turbulent diffusion. To interpret diffusion coefficient with turbulence, the advection-diffusion equation (eq. 5.5) is transformed by substituting eq.(5.3) and (5.4) into eq. (5.5).

$$\frac{\partial \langle C\rangle}{\partial t} + \left\langle u_i \frac{\partial C}{\partial x_i} \right\rangle = D\frac{\partial^2 \langle C\rangle}{\partial x_i \partial x_i}. \tag{5.6}$$

In this equation, the second term on the left hand side can again be decomposed as

$$\begin{aligned} \left\langle u_i \frac{\partial C}{\partial x_i} \right\rangle &= \left\langle (\langle u_i\rangle + u_i')\frac{\partial \langle C\rangle}{\partial x_i} + (\langle u_i\rangle + u_i')\frac{\partial C'}{\partial x_i} \right\rangle \\ &= \langle u_i\rangle \frac{\partial \langle C\rangle}{\partial x_i} + \left\langle u_i' \frac{\partial C'}{\partial x_i} \right\rangle. \end{aligned} \tag{5.7}$$

With this decomposition, eq. (5.6) is transformed as,

$$\frac{\partial \langle C\rangle}{\partial t} + \langle u_i\rangle \frac{\partial_i \langle C\rangle}{\partial x_i} = D\frac{\partial^2 \langle C\rangle}{\partial x_i \partial x_i} - \left\langle u_i' \frac{\partial C'}{\partial x_i} \right\rangle \tag{5.8}$$

The second term of the right hand side of this equation is the term which leads to a closure problem. (Closure problem is a problem with a number of equations to solve is less than number of unknowns. Consequently, with the absence of information, the set of equations cannot be solved.) To solve this equation, we have to model this term with known values. In this case, the simplest model is the so-called turbulent diffusivity which consists of the physical molecular diffusive effects by considering an additional diffusivity D_t associated with the turbulent nature of the flow. Then eq. (5.8) for the mean concentration is re-written as

$$\frac{\partial \langle C\rangle}{\partial t} + \langle u_i\rangle \frac{\partial_i \langle C\rangle}{\partial x_i} = D\frac{\partial^2 \langle C\rangle}{\partial x_i \partial x_i} + D_t \frac{\partial^2 \langle C\rangle}{\partial x_i \partial x_i} \tag{5.9}$$

Finally we obtain the modeled advection-diffusion equation.

$$\frac{\partial \langle C\rangle}{\partial t} + \langle u_i\rangle \frac{\partial \langle C\rangle}{\partial x_i} = (D + D_t)\frac{\partial^2 \langle C\rangle}{\partial x_i \partial x_i} \tag{5.10}$$

Here, D is the molecular diffusion and D_t is a diffusion due to turbulence. In our model, $D + D_t$ is modeled as all by turbulence because the diffusion of particles in the air is mainly affected by the turbulence of ambient fluid and the effect of molecular diffusion is very small and can be neglected (Thomson 1987 [118]).

Diffusion coefficient produced only with the advection velocity is shown in Chapter 3. Here, the diffusion coefficient produced by the random velocity is introduced. For the derivation, diffusion is considered in two dimensions. Variance σ^2 is related to the diffusion coefficient as

$$\sigma = \sqrt{2Dt} \tag{5.11}$$

where σ is standard deviation. Variance of particle distribution is based on the distance of particles.

$$\begin{aligned} \sigma^2(t) &= \langle |\mathbf{r}(t) - \mathbf{r}_0|^2 \rangle \\ &= \langle (x(t) - x_0)^2 \rangle + \langle (y(t) - y_0)^2 \rangle \\ &= \sigma_{xx} + \sigma_{yy} \end{aligned} \tag{5.12}$$

where $r(t) = (x(t), y(t))$ is the current location at time iteration t. $r_0 = (x_0, y_0)$ is the location of starting point. We define $x_0 = y_0 = 0$ here. σ_{xx}^2 and σ_{yy}^2 is variance of x and y direction respectively. $x(t)$ and $y(t)$ is written with the starting location x_0 and y_0 and the summation of displacement until iteration t.

$$\begin{aligned} x(t) &= x_0 + \sum_{i=1}^{t} \delta x(i) \\ y(t) &= y_0 + \sum_{i=1}^{t} \delta y(i) \end{aligned} \tag{5.13}$$

i is an index of time iteration. δx and δy is displacements of each iteration. Here, we consider only x direction because x and y are symmetric. As $x_0 = 0$, variance of x direction σ_{xx} is

$$\begin{aligned} \sigma_{xx}^2 &= \langle x(t)^2 \rangle = \left\langle \left(x_0 + \sum_{i=1}^{t} \delta x(i) \right)^2 \right\rangle \\ &= \left\langle x_0^2 + 2x_0 \sum_{i=1}^{t} \delta x(i) + \sum_{i=1}^{t} \sum_{j=1}^{t} \delta x(i) \delta x(j) \right\rangle \\ &= \left\langle \sum_{i=1}^{t} \sum_{j=1}^{t} \delta x(i) \delta x(j) \right\rangle \end{aligned} \tag{5.14}$$

where j is also an index of iteration. Eq. (5.15) is divided into twp conditions when $i = j$ and $i \neq j$.

$$\begin{aligned}\sigma_{xx}^2 &= \sum_{i=1}^{t}\sum_{j=1}^{t}\langle \delta x(i)\delta x(j)\rangle \qquad (5.15)\\ &= \sum_{i\neq j}\left\langle \delta x(i)^2\delta x(j)^2\right\rangle + \sum_{i=j}\left\langle \delta x(i)^2\right\rangle\end{aligned}$$

When $i \neq j$ first term of eq. (5.16) is 0 because of the independent random variable.

$$\sum_{i\neq j}\langle \delta x(i)\delta x(j)\rangle = 0 \qquad (5.16)$$

When $i = j$, second term of eq. (5.16) is the product of sum of displacement as

$$\begin{aligned}\sum_{i=j}\left\langle \delta x(i)^2\right\rangle &= \sum_{i=1}^{t}\left\langle \delta x(i)^2\right\rangle \qquad (5.17)\\ &= \langle \delta x^2\rangle t\end{aligned}$$

where δx^2 is expressed as the product of grid size Δx and the probability to jump to its neighborhood site p.

$$\delta x^2 = \begin{cases} (\Delta x)^2 & p \\ 0 & (1-2p) \\ (-\Delta x)^2 & p \end{cases} \qquad (5.18)$$

Finally, we obtain the equation of variance in x direction as a function of probability p.

$$\begin{aligned}\sigma_{xx}^2 &= \left(p\Delta x^2 + 0 + p\Delta x^2\right)t \qquad (5.19)\\ &= 2p\Delta x^2 t\end{aligned}$$

The probability p depends on the random velocity u_r. As a x component of random velocity is $u_r cos\theta$, probability p is written as an integral of all direction θ from $-\pi/2$ to $\pi/2$.

$$\begin{aligned}p(\mathbf{u}_r) &= \frac{1}{2\pi}\int_{-\pi/2}^{\pi/2}\left(\frac{u_r\cos\theta}{v}\right)d\theta \qquad (5.20)\\ &= \frac{u_r}{\pi v}\end{aligned}$$

Therefore, variance σ_{xx} is obtained as

$$\sigma_{xx}^2 = \frac{2u_r \Delta x^2 t}{\pi v} \tag{5.21}$$

From the relationship between diffusion coefficient D and standard deviation σ eq. (5.11), diffusion coefficient of x direction D_{xx} is

$$D_{xx} = \frac{u_r \Delta x^2}{\pi v}. \tag{5.22}$$

The same as variance σ^2 (eq. 5.13, diffusion coefficient D is a sum of diffusion coefficient of x and y direction D_{xx} and D_{yy}, and $D_x x = D_{yy}$ because they are symmetric. Therefore the diffusion coefficient of our model produced by random velocity u_r is

$$D = \frac{D_{xx} + D_{yy}}{2} = \frac{1}{2}\left(\frac{u_r \Delta x^2}{\pi v} + \frac{u_r \Delta x^2}{\pi v}\right) = \frac{u_r \Delta x^2}{\pi v}. \tag{5.23}$$

5.2.3 Numerical experiments of diffusion production with random velocity

In the simulation of tephra transport, diffusion is produced by the random velocity u_r as explained in section 5.2.2. However, analytical description has not been compared with simulation result. To verify the analytical solution of diffusion (eq. 5.23), we have implemented the numerical experiments with random velocity in two dimensions. Variance σ_{xx}^2 is calculated from the results of particle distribution dispersed only with the random velocity (Fig. 5.3). In this experiments, $\Delta x = 100$, and time step $\Delta t = 1$ are applied. And the value of random velocity u_r is varied as $0.01v$, $0.05v$, $0.1v$, $0.5v$ and $1.0v$, where v is propagation speed ($\Delta x / \Delta t$).

The variance σ_{xx}^2 linearly increases with time (Fig. 5.4 a). The rate of increase D_{xx} are plotted versus random velocity u_r in Fig. 5.4 (b) (black dots). D_{xx} increases with u_r (Fig. 5.4 b). In Fig. 5.4 (b), the blue line shows the relationship between D_{xx} and random velocity u_r calculated from eq. (5.22). This analytical solution agrees well with the results of numerical experiments. Therefore, analytical solution eq. (5.22) is verified.

5.2.4 Model of source term

In our 2D model, particles are released from one point at certain height in the atmosphere, (Chapter 4). To improve the source term, the plume velocity field is applied in our 3D model.

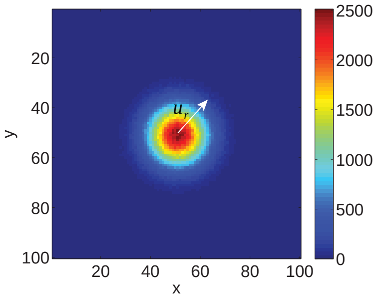

Fig. 5.3: Snapshot of numerical experiments with diffusion due to random velocity u_r.

The plume is divided into two parts when the model of source term is considered: volcanic column and umbrella cloud. Volcanic column reflects gas thrust region and buoyancy driven region of Woods (1988) [139]. These two parts are divided by the neutral buoyancy height H_b (Sparks 1986 [104]; Woods 1988 [139]) and the different velocity fields are applied to two regions. The velocity of the column part is calculated by expanding one dimensional (1D) steady-state profile to 3D. The model of Woods (1988) [139] is applied to calculate 1D steady-state profile assuming the plume has only vertical component of the velocity (see Appendix A for details). Equations and algorithms of the calculation of this model is presented in Appendix A. With this simulation, we have obtained the plume velocity profile and the radius of the plume (Fig. 5.5).

The initial conditions of the 1D plume model are not totally clear and we only know the range of the values (Table 5.2). To search the appropriate input parameters(Fig. 5.6 1), Monte Carlo simulation is implemented. Simulation results are calibrated by the total plume height H_T which is derived from the model of Carey and Sparks (1986) [24]. With the obtained input parameters, again we implement Monte Carlo simulation to derive the plume velocity profiles (Fig. 5.6 2). By averaging these velocity profiles, 1D plume velocity field is defined for each case-study eruption.

Then, the velocity of the center line U_c at each height is expanded to the horizontal plane by the Gaussian distribution (Fig. 5.7) proposed by Sparks (1986) [104] as

$$u_p(r, z) = U_c(z)e^{r^2/b^2}. \tag{5.24}$$

where, U_c is the plume vertical velocity on the center axis and U_v is the vertical velocity at the point of distance x from the center line. As Sparks

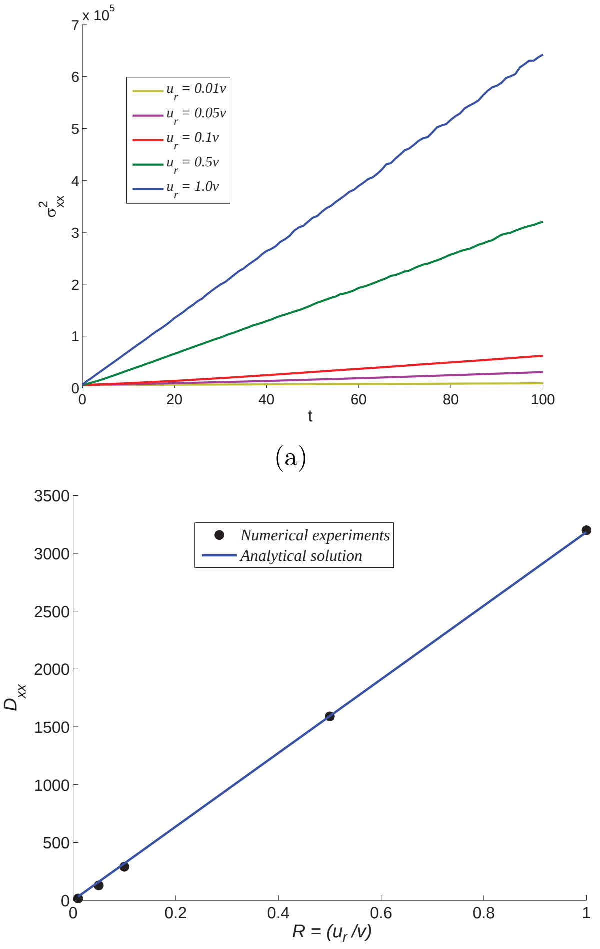

(a)

(b)

Fig. 5.4: (a) Time variation of variance $\sigma^2 = \langle x^2 \rangle - \langle x \rangle^2$ with different random velocity u_r. (b) Diffusion of x direction D_{xx} calculated from the results of numerical experiments (black dots) versus random velocity u_r and analytical solution of eq. (5.22)(blue line)

.

Table 5.2: Input parameters and their range of values for 1D plume model.

Parameter	**Notation**	**Range of value**
Ejection velocity	u_0	10-400 (m/s)
Plume radius at vent	l_0	20-200 (m)
Gas mass fraction at vent	n_0	0.01-0.05
Plume temperature at vent	θ_0	1100-1300 (K)

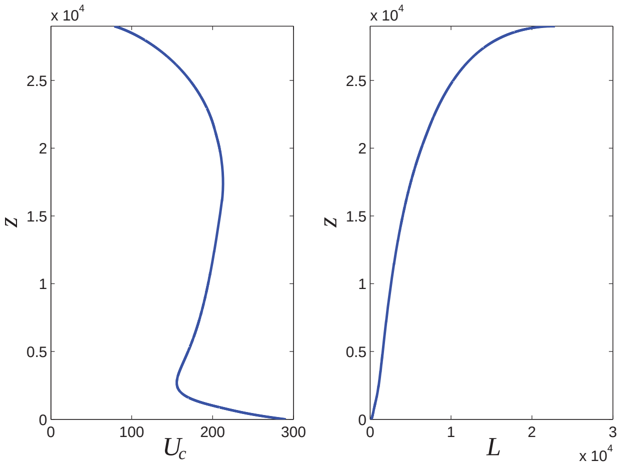

Fig. 5.5: An example of results from the 1D steady-state plume model. Left hand side is the velocity profile along the centerline of plume U_c. Right hand side is the plume radius L.

and Wilson (1982) [105] found that the $2b$ is a visible edge, the plume radius L in Woods (1988) [139] is linked to b as $b = L/2$.

1D steady-state plume models of Woods (1988) [139] do not describe the thermal disequilibrium (Woods and Bursik, 1991 [140]) and unsteadiness of certain volcanic process (Scase, 2009 [99]). We ignore disequilibrium because we do not know the value. Also we do not take into account for unsteadiness for simplicity.

The umbrella cloud of volcanic plumes is considered to spread as a gravity current radially (Fig. 5.8) (Bursik et al., 1992 [20]; Sparks et al., 1997 [108]; Suzuki and Koyaguchi, 2009 [114]).

In our model, the velocity profile of spreading current of umbrella cloud is calculated by the model of Bonadonna and Phillips (2003) [13] whose formulation is derived from the gravity current dynamics and includes also the Brunt-Väisälä frequency N. The equaion of spreading velocity u_b is written as

$$u_b = \sqrt{\frac{\lambda N Q}{\varepsilon r}} \frac{\mathbf{r}}{r} \tag{5.25}$$

where λ is shape factor for a gravitationally spreading plume and Q is volumetric flux.$\frac{\mathbf{r}}{r}$ is a unit vector of direction of $\mathbf{r}$. ε is a value related to the shape of spreading cloud and is determined with

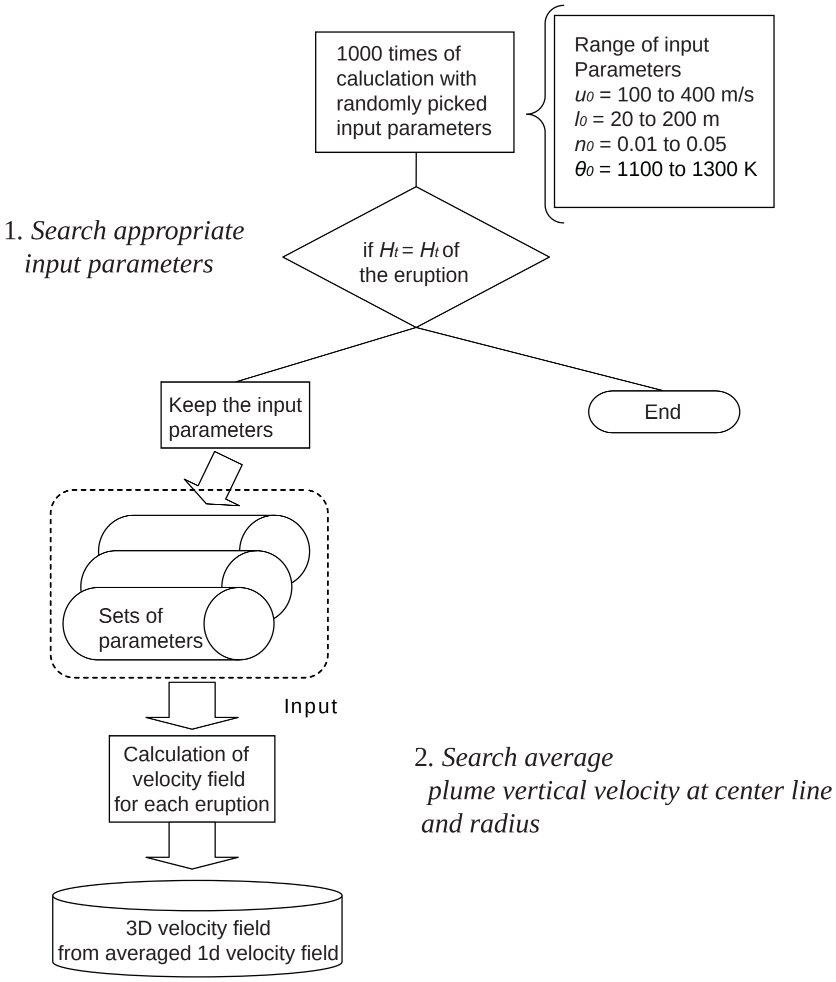

Fig. 5.6: Flow chart for Monte Carlo simulation to obtain the averaged velocity profile of 1D steady-state plume model.

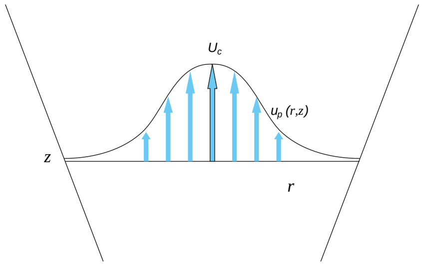

Fig. 5.7: Illustration of plume center velocity U_c and plume velocity u_p. r is the distance from the centerline in horizontal plane.

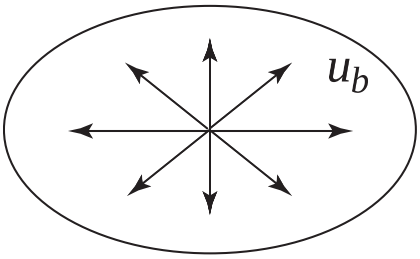

Fig. 5.8: Radial velocity of umbrella cloud.

$$\varepsilon = 2\pi\sqrt{\frac{2-e^2}{2(1+e)^2}}.$$

where, e is a eccentricity which corresponds to the shape of spreadng cloud. It is 0 when the shape is a complete circle and it is 1 when the shape is a line. For our calculation, e is set as 0.5 which corrsponds to an ellipse for windy case even though u_b transport particles radially and e is set as 0.0 for no wind case. Volume flux Q (m^3/s) is related to the total plume height H_t by eq. (6) of Bursik et al., (1992a) [21]. This equation is re-written as a function of H_t

$$Q = \left(\frac{H_t}{0.287}\right)^{5.2632}. \tag{5.26}$$

The value of λ is set to 0.8 in Bonadonna and Phillips (2003) [13] from the work of Woods and Kienle (1994) [141]. Recently, this value is studied by the numerical experiments and Suzuki and Koyaguchi (2009) [114] defined this value for the two different specific heat of pyloclast C_{vs}. We applied λ =0.15 for our simulation because 0.15 is common for the the value ranges which are C_{vs} = 0.15-0.22 for 1100 (J/(kg K)) and C_{vs} = 0.10 to 0.15 for 1617 (J/(kg K)).

For simplicity of calculation, Brunt-Väisälä frequency N is taken 0.01 s^{-1} for the troposphere and 0.02 s^{-1} for the lower stratosphere as the same as Bonadonna and Phillips (2003) [13].

5.2.5 Diffusion due to turbulence

The main sources of turbulence in a tephra transport field are volcanic plumes (e.g. Morton et al., 1956 [76]; Suzuki et al., 2005 [115]; Carazzo et al, 2008 [22]), wind shear and convection of atmospheric boundary layer (Webster et al., 2003 [131]; Morison and Webster 2005 [75]).

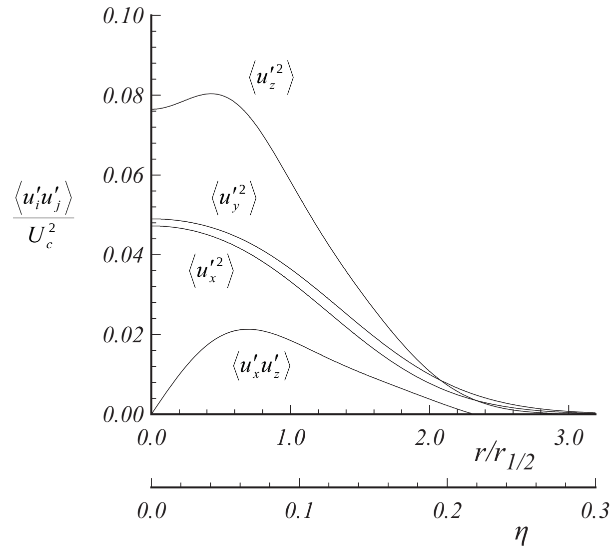

Fig. 5.9: Profiles of Reynolds stress in the self-similar round jet: curve fit to the LDA data of Hussein et al., (1994)[53].

Intensity of turbulence is identified with the production $\mathcal{P}$, which is derived from the Navier-Stokes equation to obtain kinetic energy (Pope 2000 [88]). Production term of the turbulence is written as

$$\mathcal{P} = -\langle u'_i u'_j \rangle \frac{\partial \langle u_i \rangle}{\partial x_j}. \tag{5.27}$$

In this equation, u'_i and u'_j are fluctuation velocities. $\langle u'_i u'_j \rangle$ is called Reynolds stress tensor and $\frac{\partial \langle u_i \rangle}{\partial x_j}$ is the shear stress. As the Reynolds stress comes directly from the fluctuations, we want to know the value of Reynolds stress. Hussein et al., (1994) [53] measured profiles of Reynolds stress tensor in the self-similar round jet (Fig. 5.9). According to Fig. 5.9, the component of the Reynolds stress along the direction of the mean flow (here, the root mean square fluctuations in the z-direction) is approximately twice larger than the other components.

Round jet is similar to the volcanic plume in the aspect of having a jet and vertical rise of the plume. The main difference between round jet and volcanic plume is that the volcanic plume is very hot and therefore strong thermal effects affect the dynamics of the turbulence flow. On the contrary, the round jet is subject to strictly no thermal effects. However, in classical approaches to volcanic plumes, self-similarity is assumed because of the strong anisoropy

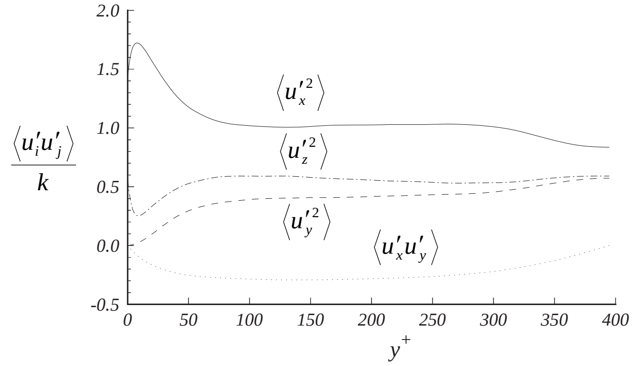

Fig. 5.10: Profiles of Reynolds stress normalized by the turbulent kinetic energy from DNS of channel flow at Re = 13,750 (Kim et al., 1987)[63]

of the flow in the z direction (Morton et al.,1956 [76]).
Assuming that the distribution of the fluctuations of volcanic plumes is similar to the one of the round jet, we use a diffusivity twice larger in the direction of mean velocity than in the other components. In volcanic plume, the direction of mean velocity is vertical because the plume rises vertically.

As the sum of advection velocity and random velocity($\mathbf{u} + \mathbf{u}_r$) is given at each cell, random velocity plays a role of fluctuations in our model. Therefore, to reproduce the diffusion described above, we apply twice larger random velocity in z direction than x and y direction;

$$\mathbf{u}_{rp} = \begin{pmatrix} R_{dp}v \\ R_{dp}v \\ 2R_{dp}v \end{pmatrix} \tag{5.28}$$

where R_{dp} is a coefficient of random velocity in the volcanic plume and v is propagation speed ($v = \Delta x / \Delta t$).
Cases of wall-bounded flows have been extensively studied are reported in all classical monographs on Turbulence (e.g. Pope, 2000 [88]). The Reynolds stress in the mean direction is approximately twice larger than the other components in this case as well (Fig. 5.10, Kim et al., 1987[63]). Although the atmosphere is complex in many respects, we assume the wind flow as a horizontal and constant flow for simplicity. Accordingly, we apply twice larger random velocity in x and y direction than z direction;

$$\mathbf{u}_{ra} = \begin{pmatrix} R_{da}v \\ R_{da}v \\ 0.5R_{da}v \end{pmatrix} \tag{5.29}$$

where R_{da} is a coefficient of random velocity in the atmosphere.
Now, we have the diffusion relationship among the three components for both the volcanic plume and the atmosphere. However, absolute value of diffusion is still missing. To identify the value of diffusion, we calibrated the diffusion value from the results of simulation and the observed ground deposition.

5.2.6 Algorithm of CA multiparticle model

With our CA multiparticle model, we can track position and properties of each particle. Algorithm 1 shows how the particles are defined in the program. If the particle size ϕ and its density ρ_p are given, diameter and mass of the particle is calculated inside the program. These properties are kept until the particle deposit on the ground, thus the output can be not only the particle number but also the distribution of particle size and mass.

Algorithm 1 Algorithm of **Particle**(ϕ, *density*).Definition of each particle including all properties of particle.

```
  double density
  double diameter ← calculate from $\phi$
  double mass ← calculate from diameter and density
```

Beginning of the simulation, all types of velocity is calculated (Algorithm 3) and the particles are initialized. For the initialization, particles are added in the List of particles at given cell (Algorithm 2). In this algorithm, *Particles* is the list of *Particle*s which is made before (Algorithm 1).

Algorithm 2 Algorithm of **addParticle**(ϕ, $density, numP, x, y, z$). To add particles to the list of *Particles*. *Particle* in this figure is a particle defined before (Algorithm 1).

```
  add numP particles ($\phi$, density) to the list of $Particles(x, y, z)$
```

Then, main iteration of simulation starts (Algorithm 3). The iteration is implemented to the time, location of cell (x, y, z) and particles at the cell. The "*currentParticle*" is chosen from the list of "*Particles*" at each cell. For this "*currentParticle*", probabilities of jumping to the next site are calculated. The next site of particles $(ix + \delta x, iy + \delta y, iz + \delta z)$ is decided by using the random number which is chosen from 0 to 1 $(random = \mathcal{U}(0, 1))$. The list of particles at next time step is "*nextParticles*", and the *currentparticle* is added to the "*nextParticles*" with new site calculated from the probability and random number. At the end of each time step, "*nextParticles*" is swapped with "*Particles*".

Algorithm 3 Algorithm of **Simulation**(). Simulation with multiparticle CA.

```
prepare Wind velocity $\mathbf{u}_w$
prepare Spreading velocity in umbrella cloud region $\mathbf{u}_b$
prepare Plume (column part) velocity $\mathbf{u}_p$
prepare Settling velocity $\mathbf{u}_s$
prepare Ramdom velocity $\mathbf{u}_r$
Velocities are summed up and make $\mathbf{u}_{tot}$ (eq. 5.2).
initialize $Particles$
for $it \leftarrow 1$ to maxtime do
    clear $nextParticle$
    for $iz \leftarrow 1$ to $Nz$ do
        for $iy \leftarrow 1$ to $Ny$ do
            for $ix \leftarrow 1$ to $Nx$ do
                for $ip \leftarrow 0$ to $NP$ (at this cell) do
                    $nextX \leftarrow 0$
                    $nextY \leftarrow 0$
                    $nextZ \leftarrow 0$
                    $currentParticle \leftarrow Particles(ip)$
                    $p_x \leftarrow u_x/v$
                    $p_y \leftarrow u_y/v$
                    $p_z \leftarrow u_z/v$
                    update probabilities $p_i$ $(i \in [1, Q])$ $\{Q = 9 \because \text{D2Q9 model}\}$
                    for $i \leftarrow 1$ to $Q$ do
                        random number $RNG \leftarrow \mathcal{U}(0, 1)$
                        if $p_i > RNG$ then
                            $\delta x \leftarrow \delta x + v_{ix}$
                            $\delta y \leftarrow \delta y + v_{iy}$
                            $\delta z \leftarrow \delta z + v_{iz}$
                        end if
                    end for
                    $nextX \leftarrow ix + \delta x$
                    $nextY \leftarrow iy + \delta y$
                    $nextZ \leftarrow iz + \delta z$
                    $nextParticles(nextX, nextY, nextZ) \leftarrow currentParticle$
                end for
            end for
        end for
    end for
    $Particles \leftarrow nextParticles$
end for
```

5.2.7 Lagrangian on grid method

The multiparticle CA model works fine with windy cases. However, it shows axes dependency when there is no wind and radial velocity is dominant in the umbrella cloud. To avoid such a grid dependency, we propose a modification of the multiparticle CA model. The idea of this new method is to add extra degrees of freedom to the particles storing their deviation from a grid point to their actual position (off-grid). Thus, this method can track the particles even they are in between grid points. We call this method "*Lagrangian on grid*" method. This method have the benefit of Eulerian method which is easy to parallelize, and also have a same accuracy as Lagrangian method.

Particles are transported in a Lagrangian manner with $\mathbf{r_i} = \mathbf{r_{i-1}} + \mathbf{v} \cdot \Delta t$, where $\mathbf{r_i}$ is the position of particle at step i and $\mathbf{v}$ is a velocity and Δt is a time step. When the displacement is smaller than the grid size, the value of deviation from the grid point is stored in a variable *storage*, different for each particle. When the cumulated displacement in *storage* becomes larger than the grid size, the particle moves to the next site. It means that the index of particle position increments and the simulator subtracts the grid size Δx from the value in *storage.* The algorithm implementing the main iteration of this method is shown in Algorithm 4.

Diffusion coefficient with Lagrangian on grid model In order to produce a value of diffusion due to turbulence, a random velocity is applied for each point and each time step. The random velocity $\mathbf{u}_r$ is the same as in the multiparticle Cellular Automata method, in eq. (5.1).

For the derivation of the diffusion constant in this new model, the position vector is expressed with complex numbers as

$$\mathbf{u}_r = u_r(cos\theta_a + isin\theta_a) = u_r e^{i\theta_a}.$$

Diffusion coefficient and variance are related throuh eq. (5.11). The value of the variance can be computed as the average of the square of travel distance minus the square of averaged travel distance ($\sigma^2 = \langle \delta x^2 \rangle - \langle \delta x \rangle^2$). With the expression in terms of complex numbers, the average travel distance $\langle \delta x \rangle$ is

$$\langle \delta x \rangle = u_r \Delta t \sum_{t=0}^{T} \langle e^{i\theta_a(t)} \rangle = \int_0^{2\pi} \frac{d\theta_a}{2\pi} e^{i\theta} = \left[-ie^{i\theta_a} \right]_0^{2\pi} = 0. \tag{5.30}$$

Algorithm 4 Algorithm of the main iteration of "Lagrangian on Grid" method.

```
for $iz \leftarrow 1$ to $Nz$ do
  for $iY \leftarrow 1$ to $NY$ do
    for $ix \leftarrow 1$ to $Nx$ do
      for $ip \leftarrow 1$ to $NP$ do
        $nextstorageX \leftarrow storageX + vx \cdot dt$
        $nextstorageY \leftarrow storageY + vy \cdot dt$
        $nextstorageZ \leftarrow storageZ + vz \cdot dt$
        — Increment or No increment? (*)—
        if $|nextstorageX| > dx$ and $nextstorageX >= 0$ then
          $nextX \leftarrow ix + 1$ //Increment (+)
          $nextstorageX \leftarrow nextstorageX - dx$
        else if $|storageX| > dx$ and $nextstorageX < 0$ then
          $nextX \leftarrow ix - 1$ //Increment (-)
          $nextstorageX \leftarrow nextstorageX + dx$
        else
          $nextX \leftarrow ix$ //No increment
        end if
        —Repeat * for y and z direction —
        — Calculation of exact position —
        $px \leftarrow nextX \cdot \Delta x + nextStorageX$
        $py \leftarrow nextY \cdot dx + nextStorageY$
        $pz \leftarrow nextZ \cdot dx + nextStorageZ$
        — Calculation of velocity —
        $\mathbf{v} \leftarrow getVelocity(px, py, pz, \phi)$
        — Set Parameters to the attribute of particle —
        $currentParticle.index \leftarrow (nextX, nextY, nextZ)$
        $currentParticle.velocity \leftarrow \mathbf{v}$
        $currentParticle.storage \leftarrow (nextstorageX, nextstorageY, nextstorageZ)$
        $currentParticle.position \leftarrow (px, py, pz)$
      end for
    end for
  end for
end for
```

The next step is to derive the average of square of travel distance.

$$\begin{aligned}\langle\delta x^2\rangle &= \langle u_r\Delta t\sum_{t=0}^{T} e^{i\theta_a(t)}\cdot u_r\Delta t\sum_{t'=0}^{T} e^{i\theta_a(t')}\rangle \\ &= u_r^2\Delta t^2\sum_{t,t'=0}^{T}\langle e^{i[\theta_a(t)-\theta_a(t')]}\rangle \\ &= u_r^2\Delta t^2\left[\sum_{t=t'}\langle e^{i\theta_a(t)}e^{-i\theta_a(t')}\rangle+\sum_{t=0}^{T}\langle e^{i[\theta_a(t)-\theta_a(t)]}\rangle\right]\end{aligned} \tag{5.31}$$

In this equation, both the 1st term and the exponent of e in the second term become zero. Then, the average of square of travel distance is simply

$$\begin{aligned}\langle\delta x^2\rangle &= u_r^2\Delta t^2\sum_{t=0}^{T}\langle 1\rangle \\ &= u_r^2\Delta t\cdot t\end{aligned} \tag{5.32}$$

From eq. (5.30) and eq. (5.33), variance is described as

$$\sigma^2=\langle\delta x^2\rangle-\langle\delta x\rangle^2=u_r^2\Delta t\cdot t. \tag{5.33}$$

Finally, diffusion coefficient is obtained as

$$D=\frac{\sigma^2}{2t}=\frac{u_r^2\Delta t}{2}. \tag{5.34}$$

This diffusion coefficient can also be used by the fully Lagrangian method because the random velocity u_r does not depend on the grid size. The equation shows that we can control diffusion by tuning the amplitude of the random velocity u_r or by tuning the time step Δt.

5.3 Results

5.3.1 Input parameters

The parameters of our model are summarized in Table 5.3. Simulations of tephra transport in 3D are implemented for four case-study eruptions; Askja 1875 D eruption (Sparks et al, 1981 [106]), Cotopaxi Layer 3 and Layer 5 eruptions (Biass and Bonadonna, 2011 [8]), and Pululagua 2450 BP eruption (Volentik et al, 2010 [125]).

Table 5.3: Model and parameters. Notation, references of models and rangeof values. * Values of random velocity for diffusion coefficient are discussed in section 5.4.

Type	**Title**	**Notation**	**Input/Calculate**	**Value**
Advection velocity	Wind velocity	u_w	Input	Table.5.6
	Maximum wind velocity at tropopause	u_{wmax}	Input	Table.5.6
	Settling velocity	u_s	Calculate	eq.(5.35)
	Plume velocity	u_p	Input	Table 5.2 and Appendix A
	Spreading velocity of umbrella cloud	u_b	Calculate	eq. (5.25)
Random velocity	Random velocity	$\mathbf{u}_r$	-	-
	Random velocity for atmosphere	$\mathbf{u}_{ra}$	Calculate	eq. (5.29)
	Random velocity for plume	$\mathbf{u}_{rp}$	Calculate	eq. (5.28)
	Coefficient of random velocity for atmosphere	R_{da}	Input	*
	Coefficient of random velocity for plume	R_{dp}	Input	*
Heights	Total plume height	H_t	Input	Table 5.5
	Crater height	H_c	Input	Table 5.5
	Height of tropopause	H_{trop}	Input	Table 5.6
	Height of neutral buoyancy level	H_b	Input	Table 5.5
Grain size	Grain size	Φ	Input	Fig. 5.12
	Number of particles for each class	$N_{p\phi}$	Input	10^6
	Density of particles for each class	ρ_ϕ	Input	Table 5.4; Fig. 5.11
	Weight percent of particles for each class	W_ϕ	Input	References of Fig. 5.12

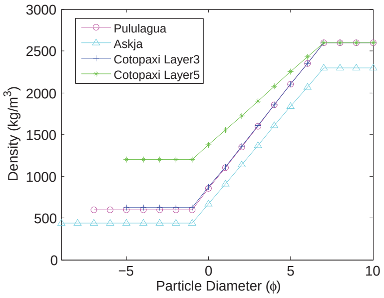

Fig. 5.11: Density distributions for Pululagua, Askja, Cotopaxi Layer3 and Cotopaxi Layer5 eruptions. Linear interpolation applied this calculation is model by Bonadonna and Phillips (2003) [13]

.

Table 5.4: Pumice(or Scoria) and magmatic density for sample eruptions (unit:kg/m^3) *1:Costantini (2010), *2: Bonadonna and Phillips (2003), *3: Decided by considering similar value of Cotopaxi. Details are in the text.*4: Papale and Rosi (2006).

	Pulualgua	**Askja**	**Cotopaxi Layer3**	**Cotopaxi Layer5**
Pumice (or Scoria) density	600^{*3}	440 ^{*2}	620 ^{*1}	1200 ^{*1}
Magmatic density	2500^{*4}	2300	2600	2600

As this model is based on multiparticle CA, we can follow all the particle properties such as grain size (ϕ) and density (ρ_ϕ). Mass of particles is calculated from the size and the density assuming that all particles are spherical. Grain size data are obtained from Sparks et al (1981) [106] for Askja 1875D eruption, Chapter 2 for Cotopaxi Layer 3 and 5 eruptions and Volentik et al(2010) [125] for Pululagua 2450 BP eruption. Density distribution is calculated with the model of Bonadonna and Phillips (2003) [13] by assuming linear trend from -1 ϕ to 7 ϕ (Fig. 5.11). The density values of pumice (or scoria) and magmatic density are used for the value for coarser particles < -1ϕ and the value for finer particles > 7ϕ and these values are presented in table 5.4.

The total grainsize of all eruptions are shown in Fig. 5.12.

The velocity fields of plume are calculated as it is described in section 5.2.4

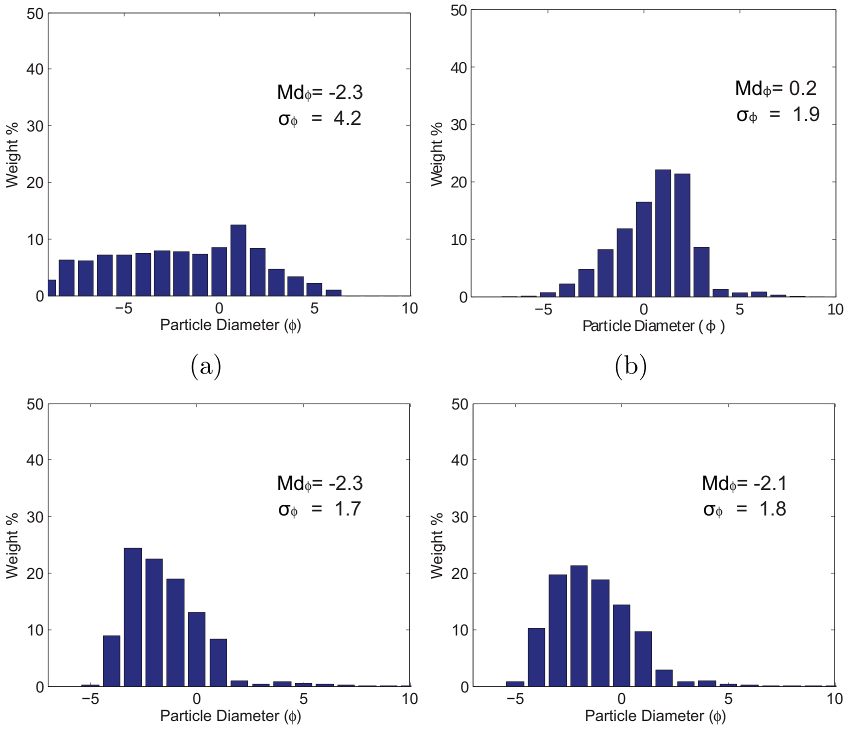

(a) (b)

(c) (d)

Fig. 5.12: Total grainsize distributions for (a) Askja 1875 D (Sparks et al. 1981 [106]), (b) Pululagua 2450BP [125], (c) Cotopaxi Layer3 (chapter 2), (d) Cotopaxi Layer 5 eruptions(chapter 2).

Table 5.5: Plume related heights

	Askja 1875D	**Cotopaxi L3**	**Cotopaxi L5**	**Pululagua 2450BP**
Total plume height (H_t)	26km	23km	26km	24.5km
Height of neutral buoyancy level (H_b)	18km	16km	16km	16.5km
Crater height	1km	6km	6km	2.5km

and Appendix A. Total plume height is a parameter which is obtained from the model of Carey and Sparks (1986) [24]. By using the total plume height, the velocity profiles are obtained by Monte Carlo simulation (Fig. 5.6). Neutral buoyancy height (H_b) is defined by comparing density of plume and air density from the calculation results. Total plume heights (H_t), neutral buoyancy heights (H_b) and crater height (H_c) of each sample eruptions are shown in Table 5.5.

Wind velocity is assumed to vary only with height and the distribution of wind velocity is defined by the wind model II of Bonadonna and Phillips (2003) [13](i.e. model of Carey and Sparks, 1986 [24]). To calculate the wind velocity profile, tropopause height is required for each location as the wind is maximum at the tropopause. Tropopause height mainly changes with latitude. Hoinka (1998) [56] suggested the model of calculating the pressure at the tropopause depending on the latitude. The pressure of the tropopause is converted to the height above sea level by the relationship between atmospheric pressure and height (Wallace and Hobbs 2006 [129]). By using maximum wind velocity obtained from referenced studies and the tropopause height, the wind velocity profiles are obtained. These values are summarized in Table 5.6.

Settling velocity is calculated by the equation of giving the terminal velocity of particles, assumed to be spherical, although real particles can strongly deviate from spheres (Wilson and Hunag, 1979 [135]) with very different settling velocities (Pfeiffer et al, 2005 [85]). Bonadonna and Phillips (2003) [13]

Table 5.6: Parameters related to the wind velocity

	Askja	**Cotopaxi L3**	**Cotopaxi L5**	**Pululagua**
Lattitude	N65:03	N00:68		N00:04
Pressure at Tropopause	320 hPa	115hPa		115hPa
Height of Tropopause	9km	16km		16km
Maximum wind velocity at Tropopause	$26m/s$	$28m/s$	$21m/s$	$0m/s$
Reference of maximum wind velocity	Carey and Sparks (1986) [24]	Chap2	Chap 2	Volentik et al,(2010) [125]

modified the equation from Kunii and Levenspiel, (1969) [64].

$$\begin{aligned} u_s &= \tfrac{gd^2(\rho_p-\rho_a)}{18\mu} && \text{for } Re < 6 \\ u_s &= d\left[\tfrac{4g^2(\rho_p-\rho_a)^2}{225\rho_a}\right]^{\frac{1}{3}} && \text{for } 6 < Re < 500 \\ u_s &= \left[\tfrac{3.1gd(\rho_p-\rho_a)}{\rho_a}\right]^{\frac{1}{2}} && \text{for } 500 < Re < 200,000 \end{aligned} \tag{5.35}$$

where, g is gravity acceleration , d is particle diameter, ρ_p is particle density, ρ_a is air density and μ is dynamic viscosity of air.

5.3.2 Qualitative results

Our tephra transport model is implemented in three dimensions for sample eruptions (Pululagua 2450BP, Askja 1875D, Cotopaxi Layer3 and Cotopaxi Layer 5) and the particle distribution in the atmosphere and on the ground are obtained. In order to see how our model works, the images of particle trajectories for Cotopaxi Layer3 eruption case are shown in Fig. 5.14. This image presents the points where particles have passed until the indicated time for three classes of grainsize. The coarsest particle class (-5ϕ) forms a mushroom like feature in 300s and it becomes like a hanging bell after 600s. This feature change shows the particles suspending at 300s and later starting to fallout at 600s. Finer particle classes (-1ϕ and 2ϕ) have also a mushroom like feature and their cap parts are clearer than the feature of coarser classes.

Fig. 5.13: A plume of Grímsvötn volcano in Iceland on 21 May, 2011. The plume reached 11 kilometers (6.8 miles), according to the Icelandic meteorological institute. (http://www.theatlantic.com/infocus/2011/05/grimsvotn-volcano-erupts-in-iceland/100071/, Last visit: 16 December, 2011)

Particles of -1ϕ and 2ϕ are affected by the wind and the shapes are elongated to the downwind direction.

These mushroom like shapes are produced by the plume velocity field which raises the particles upper around the crater, and makes them to spread in the umrella cloud where there is a cap of mushroom. These shapes are similar to the shape of strong plumes (e.g. Fig. 5.13).

To see the trajectory of each particle, the trajectories of five particles are shown in three classes (-5 ϕ, -1ϕ and 2ϕ) of grainsize until 300 seconds (Fig. 5.15). In these figures, five particles have totally different trajectories. This shows the effect of the stochastic rule of our model. However, even though each particle behaves differently, the movement of all particles produces the plume with mushroom like shape such as those shown in Fig. 5.14 and described above.

5.3.3 Results for source term improvement

We have implemented the velocity profile of volcanic plumes for improving the source term. In order to show the improvement of the ground deposition by including the velocity profile of the plume, simple Lagrangian simulations have been implemented with and without the velocity profile obtained by expanding 1D steady-state plume model to 3D.
The trajectories of the particles simulated by the Lagrangian simulation for

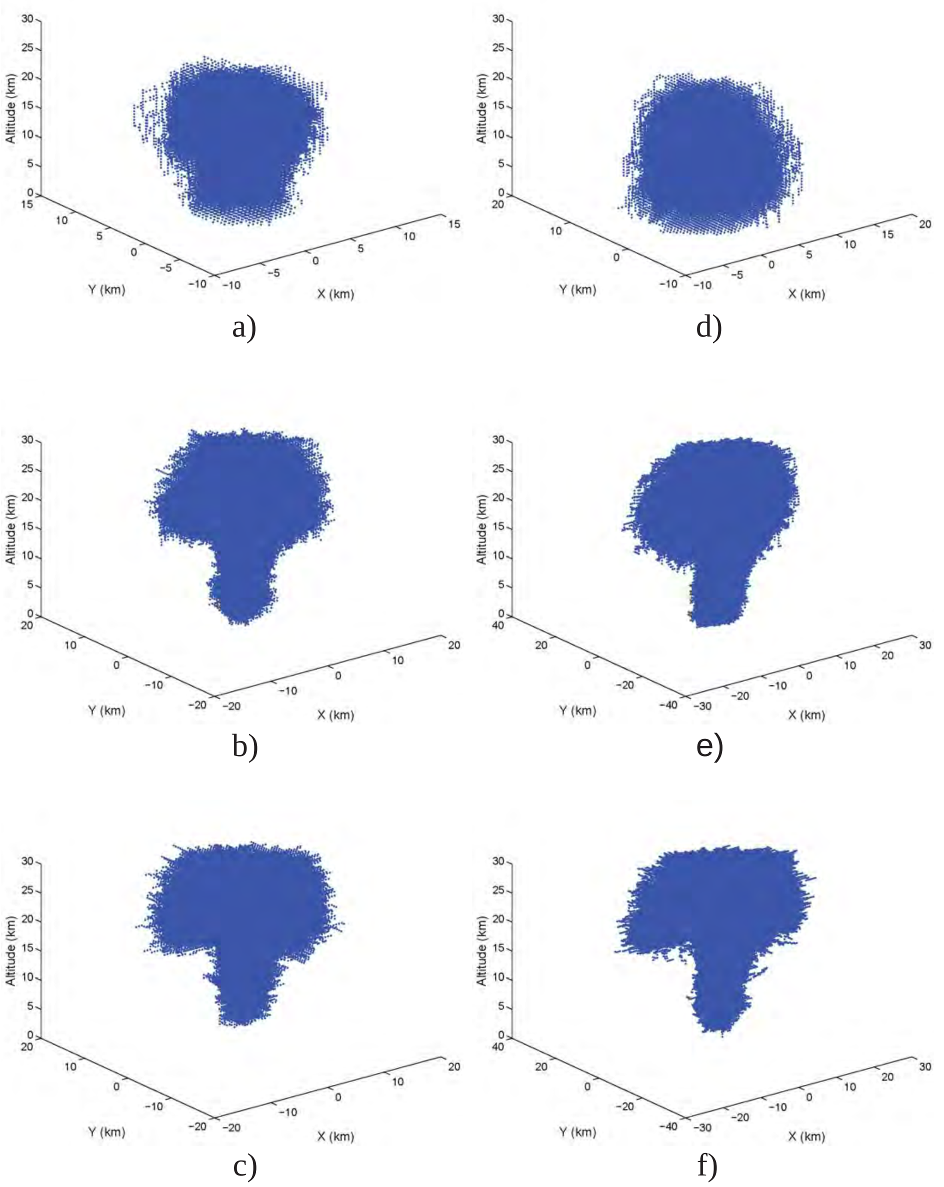

a) d)

b) e)

c) f)

Fig. 5.14: Cumulative particle trajectories of all the partilce for (a)-5ϕ in 300s. (b) -1ϕ in 300s. (c) 2ϕ in 300s. (d)-5ϕ in 600s. (e) -1ϕ in 600s. (f) 2ϕ in 600s. Downwind direction is diagonal direction of x and y. Example of Cotopaxi layer 3 case.

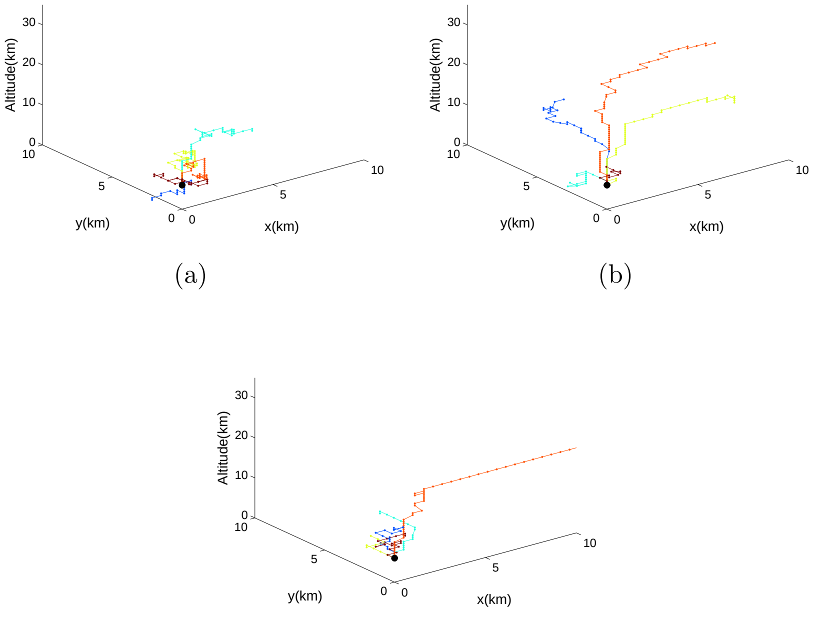

(a)

(b)

(c)

Fig. 5.15: Five particle trajectories in 300s for (a) -5ϕ, (b) -1ϕ, (c) 2ϕ. Color difference corresponds the particle discrimination. Example of Cotopaxi Layer 3 case.

both cases with and without plume velocity profiles are shown in Fig. 5.16. As this is a Lagrangian simulation without diffusion, only one particle of each grainsize is considered. For the case with the velocity profile of plume, particles are released from the vent (at the vent height), and they sediment on the ground which is assumed to be at the sea level for simplicity. For the case without the plume velocity, particles are released from one point at the neutral buoyancy height (H_b). To transport the particles without the plume velocity, particles are advected only by the wind in the horizontal direction. The particles of Pululagua 2450BP eruption, which is considered to have occurred in no-wind condition, fall at the crater. Therefore the trajectories are shown only for the case with plume velocity profile for Pululagua 2450BP eruption.

According to Fig. 5.16, fine particles travel longer distance in simulations with the plume velocity profile than in the simulation without the plume velocity profile. For example, particles $> -2\phi$ in the case with the plume velocity profile traveled farther than in the case without the plume velocity profile for Askja 1875D (Fig. 5.16a and b). This is because finer particles $> -2\phi$ arrive at H_b and they are advected by the spreading of the umbrella cloud.

The comparison of the Md_ϕ of ground deposition between simulations and field observations are shown in Fig. 5.17. The plots show the slower increase of the case with plume velocity profile than the case without the plume velocity profile. For Askja 1875D eruption, fitted curve of field observations show slower increase than simulation results for both with and without plume velocity profile. The field observations are closer to the result of simulation with and without the plume velocity profile(Fig. 5.17 (a)). Besides, simulation results with the plume velocity profile show the slower increase than the simulation results without the plume velocity profile. For Pululagua 2450BP case, grainsize distributions can not be calculated without plume velocity (Fig. 5.17 (d))because it erupted in no-wind condition and there is no advection speed except the velocity of spreading current.

5.3.4 Results of parameter work for diffusion values

The values of the diffusion coefficient have not been identified although we have defined the relationship of random velocities in three directions (x,y and z). In eq. (5.28) and (5.29), the value of R_{dp} and R_{da} is not defined. To define these values, numerical experiments are carried out.

The results of numerical experiments of random velocity for the diffusion due to the plume are shown in Fig. 5.18. The conditions of the Pululagua 2450BP eruption are applied for this simulation because this case is con-

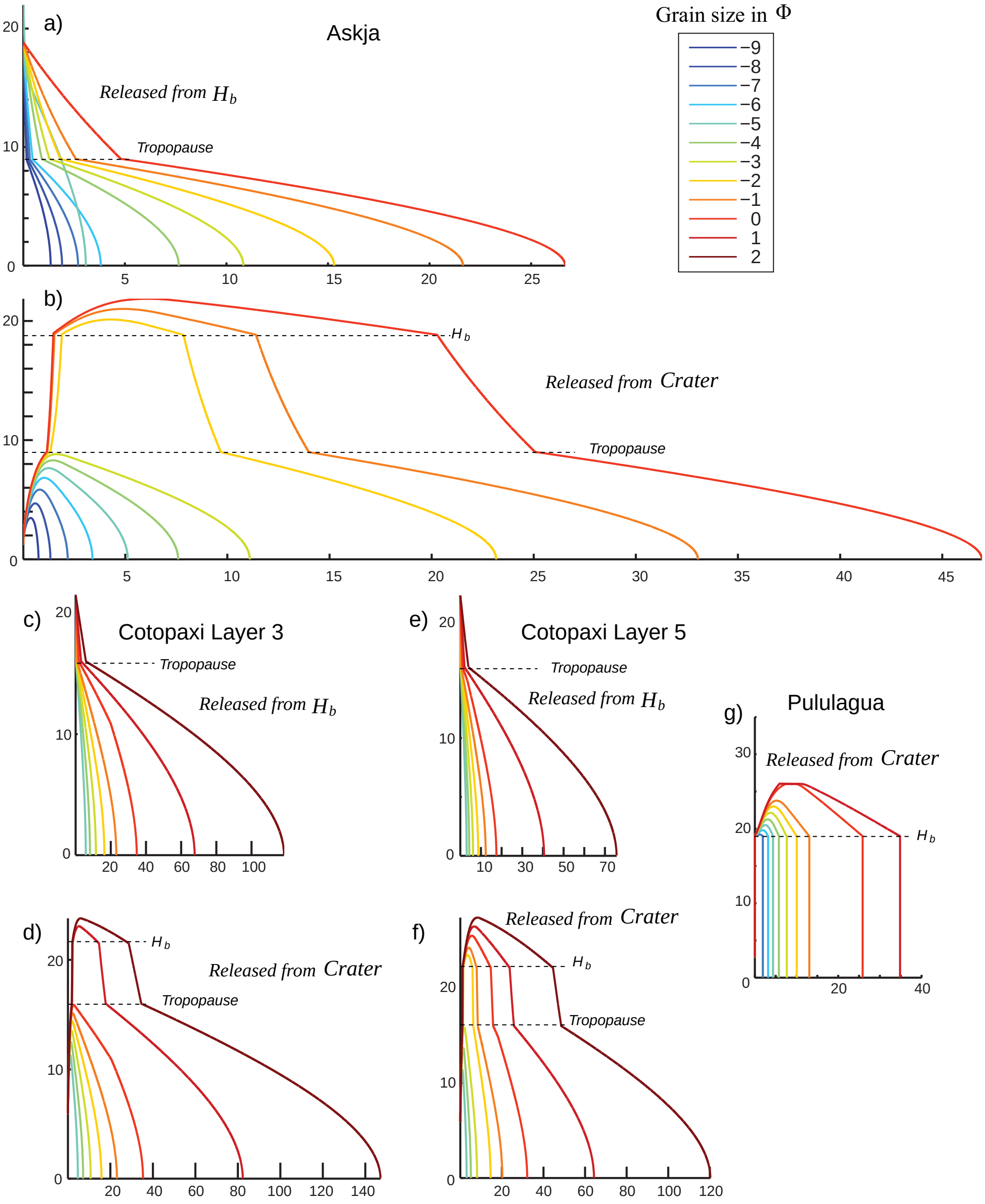

Fig. 5.16: Trajectory of Lagrangian calculation for particle released from one point at H_b and from the crater with velocity field of plume. Horizontal axes show the distance (km) of downwind direction and vertical axes show the height above sea level (km). (a) Simulation of one point release at the level of H_b without the plume velocity field for Askja 1875D, (b) Simulation of vent release with the velocity profile of plume for Askja 1875D, (c) Simulation of one point release at the level of H_b without the plume velocity field for Cotopaxi Layer3, (d) Simulation of vent release with the velocity profile of plume for Cotopaxi Layer3, (e) Simulation of one point release at the level of H_b without the plume velocity field for Cotopaxi Layer5, (f) Simulation of vent release with the velocity profile of plume for Cotopaxi Layer5 and (g) Simulation of vent release with the velocity profile of plume for Pululagua.

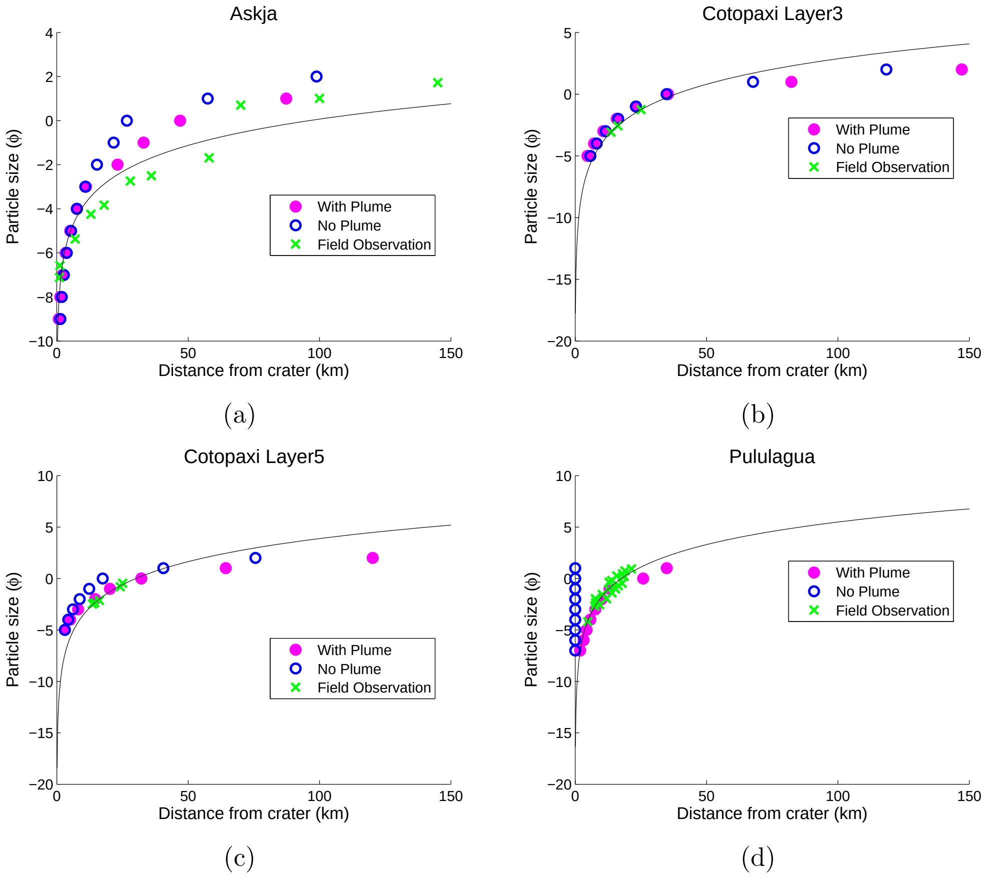

(a) (b) (c) (d)

Fig. 5.17: Simulated median of the ground deposition with plume (pink filled circle) and with no plume (blue circle), and $Md\phi$ of field observation (green cross) for (a) Askja 1875D, (b) Cotopaxi Layer 3, (c)Cotopaxi Layer 5 and (d) Pululagua 2450BP. Black line shows the powerlaw fitting of the data points of field observation.

sidered as no-wind case (section 2.4.3 in chapter 2) and thus there is no effect of the particle sorting due to the wind. Md_ϕ of the field observation are also plotted for the comparison. Points from the numerical experiments in the case of $R_{dp} = 0.09$ covers observed data points (Fig. 5.18 c), while some points from the field observation are not in the range of the results of numerical experiments.

The results of numerical experiments of random velocity for the diffusion due to the atmospheric turbulence are shown in Fig. 5.19. The conditions of the Pululagua 2450BP eruption are also applied for this simulation. Plots of numerical simulation is flatter as the random velocity increases and it agrees better when the random velocity is smaller.

5.3.5 Validation of the model

Our model can also describe mass of deposition on the ground (mass/area). To validate it, simulation results of mass per unit area data (MPA) are compared with the field data. For this comparison, Lagrangian on grid model is implemented to obtain the mass of deposition.

MPA of field data is calculated by multiplying the data of thickness by the deposit density.

$$M_o(x, y) = H(x, y) \cdot \rho_o(x, y)$$

where M_o is MPA obtained from field data, H is the thickness of the layer of eruption and ρ_o is the bulk density of outcrop at the point (x, y). We utilized MPA of Pululagua 2450 BP, Cotopaxi Layer 3 and Cotopaxi Layer 5 eruptions. The values of density of these eruptions are considered constant for every observed point(Biass and Bonadonna 2011 [8]). MPA of simulation result is calculated with

$$M_s(x, y) = \sum_i M^i\,(x, y) = \sum_i \frac{n^i(x, y) \cdot w^i \cdot M_{Total}}{N^i_{sim}}.$$

where M_s is mass of all particles in site (x, y), i is the index of grainsize class, n^i is the number of particles at class i, w^i is the weight percent of grainsize class i of total grainsize distribution, M_{Total} is total mass of each eruption, and N^i_{sim} is the number of particles released for each grainsize class in the simulation.

Before showing the simulation result of MPA, particle trajectory in the air with Lagrangian on grid model is checked (Fig. 5.20 and 5.21). These are trajectories of particles cumulated at each time step. Trajectories of coarse particles (-5ϕ) shows similar feature with time and they fall around crater,

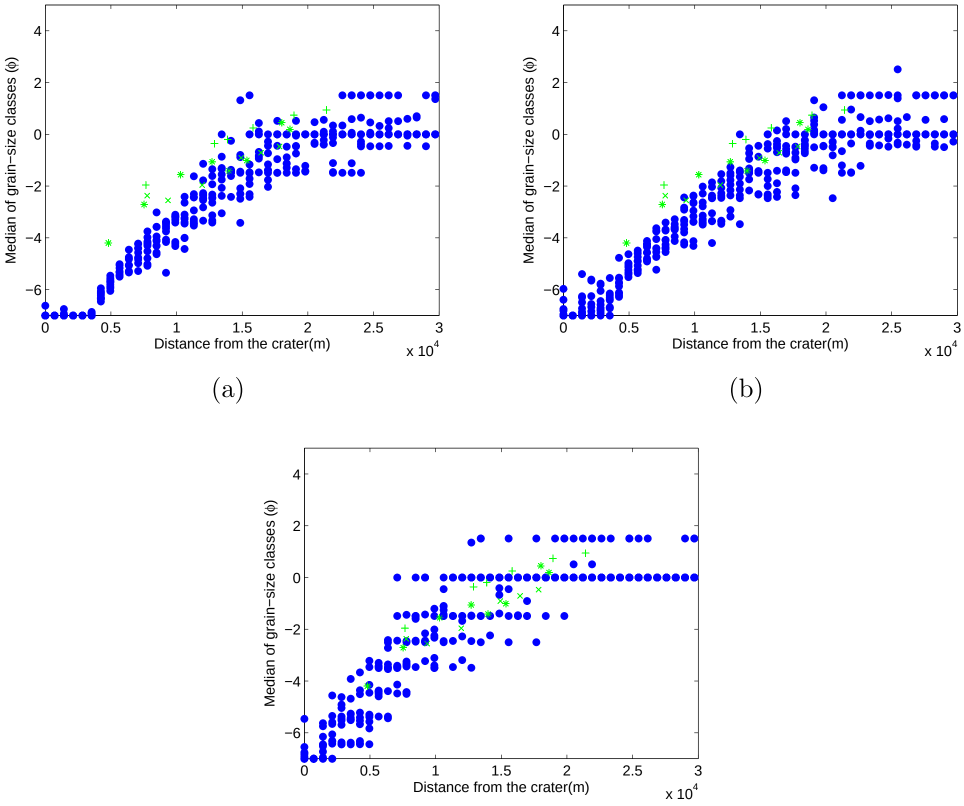

(a)

(b)

(c)

Fig. 5.18: Results of numerical experiments for the random velocity for the plume. Random velocity for the atmosphere is fixed $R_{da} = 0.0$. Median values of the grainsize distribution of the deposition on the ground are plotted. The results of the ten times calculation are shown in the same plots for all cases. (a) $R_{dp} = 0.01$,(b) $R_{dp} = 0.05$ and (c) $R_{dp} = 0.09$. Green points are Md_ϕ of field observation and blue points are simulation results

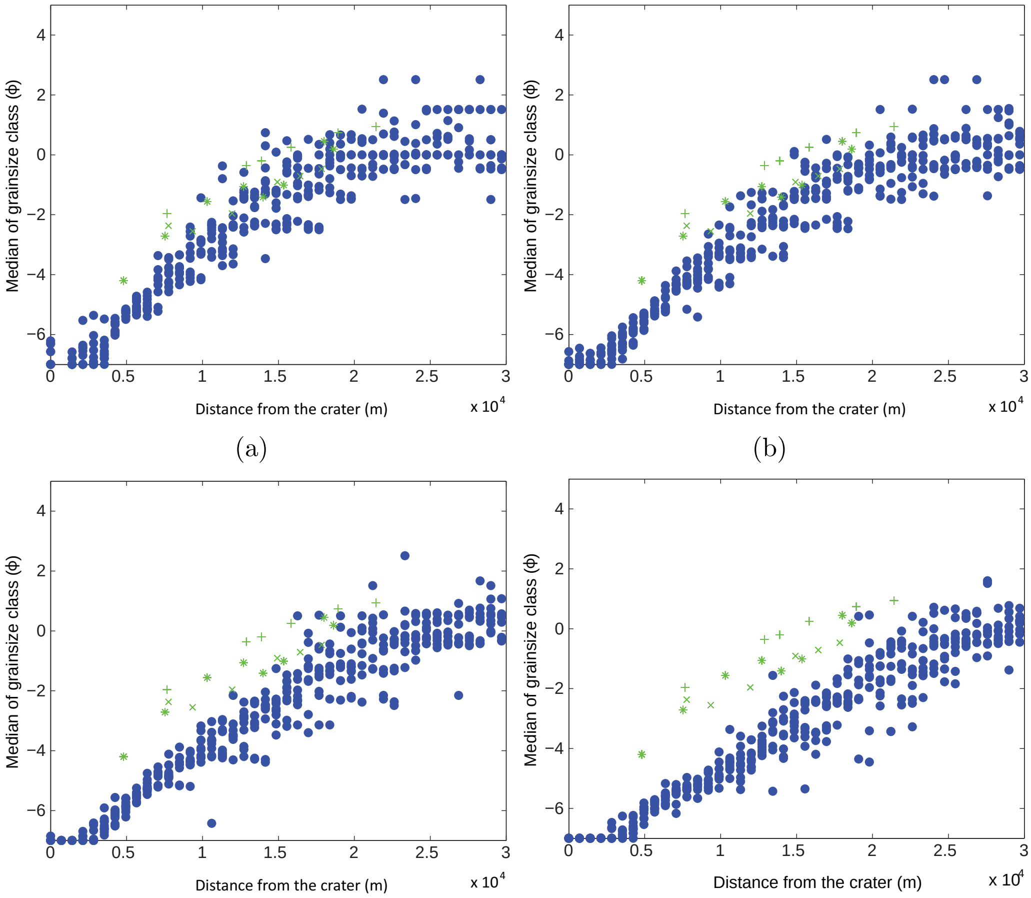

(a) (b)

(c) (d)

Fig. 5.19: Results of numerical experiments for the random velocity for the atmosphere. Random velocity for the plume is fixed $R_{dp} = 0.05$. Median values of the grainsize distribution of the deposition on the ground are plotted. The results of the ten times calculation are shown in the same plots for all cases. (a) $R_{da} = 0.00$, (b) $R_{da} = 0.01$,(c) $R_{da} = 0.05$ and (d) $R_{da} = 0.09$. Green points are Md_{ϕ} of field observation and blue points are simulation results

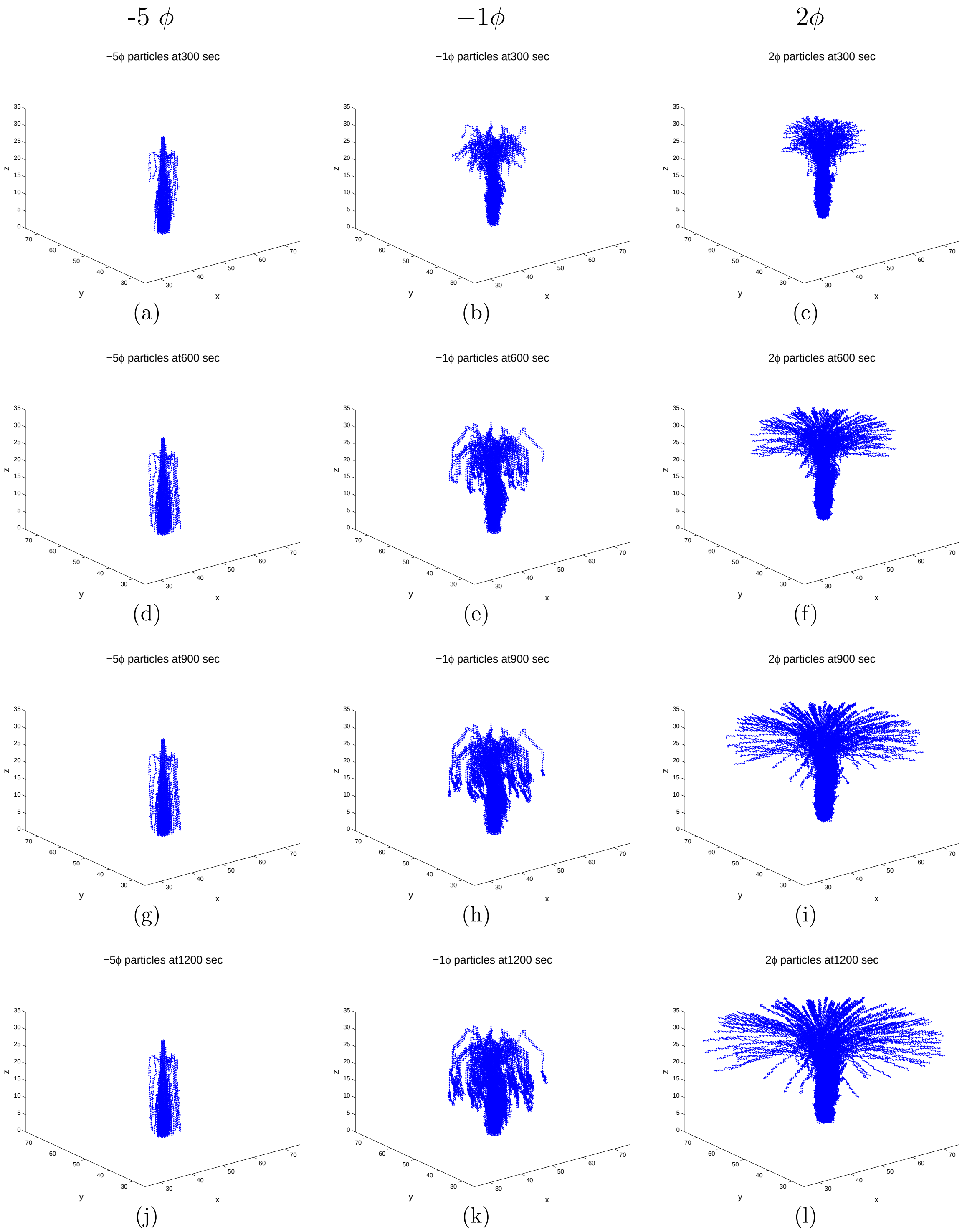

Fig. 5.20: Cumulative particle trajectories of all particles for each class with Lagrangian on grid method at time 300, 600, 900 and 1200 seconds.(a),(d),(g), (j) is the time evolution of -5 ϕ particles and (b),(e),(h),(k) is the time evolution of -1ϕ and (c),(f),(i),(l) is the time evolution of 2ϕ particles.

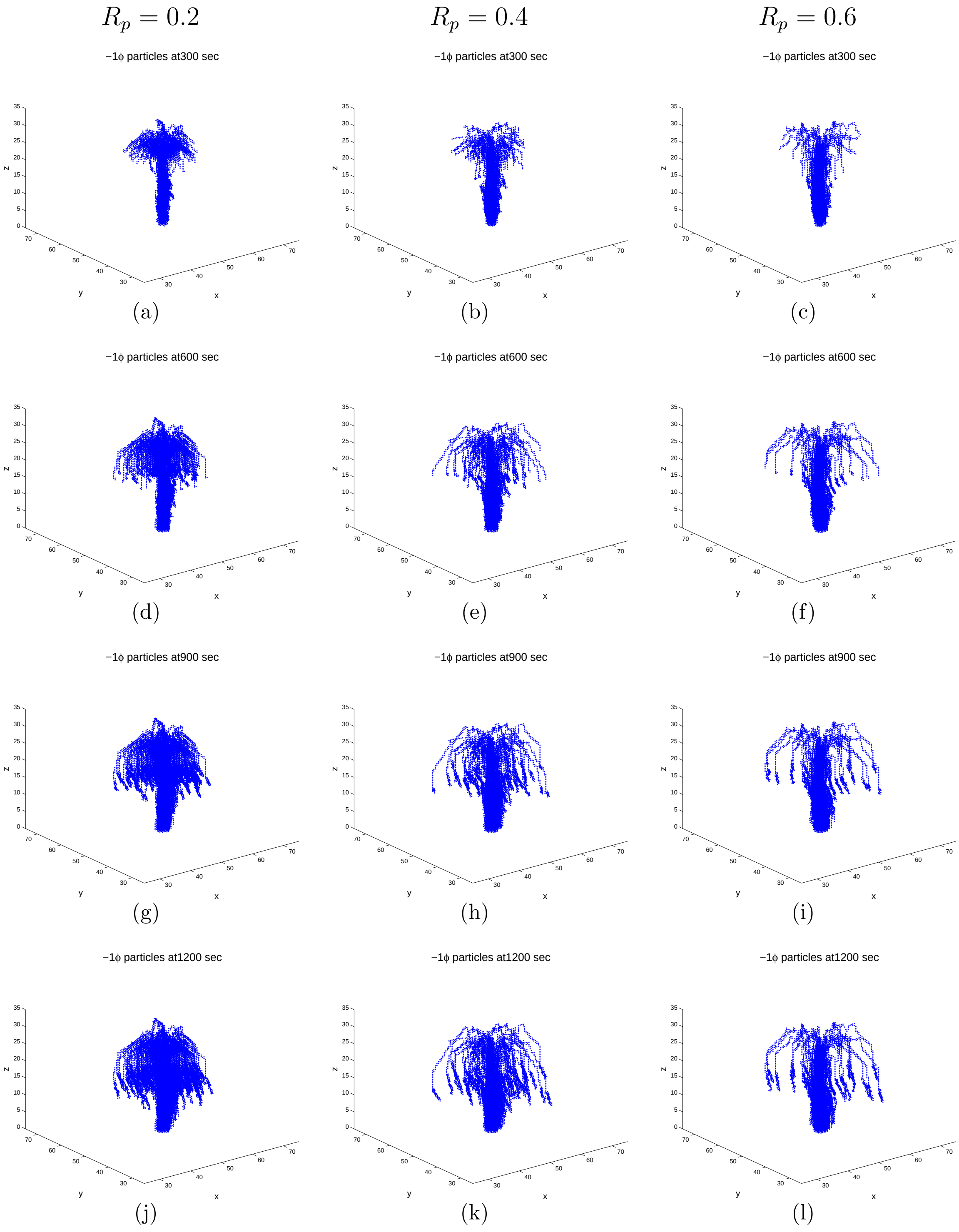

(a) (b) (c)
(d) (e) (f)
(g) (h) (i)
(j) (k) (l)

Fig. 5.21: Cumulative particle trajectories of all the particles of grainsize class -1ϕ calculated with Lagrangian on grid method at time 300, 600, 900 and 1200 seconds. (a),(d),(g),(j) is the time evolution when random velocity is given with ratio ($R_p =$) 0.2 ($u_r = R_p \frac{\Delta x}{\Delta t}$) and (b),(e),(h),(k) is the time evolution when random velocity is given with ratio 0.4 and (c),(f),(i),(l) is the time evolution when random velocity is given with ratio 0.6.

while trajectories of finer particles show the lateral displacement around umbrella cloud. Especially 2ϕ particles widely spreads for radial and horizontal directions. Particle trajectories also show variation with different diffusion produced by random velocity. Fig. 5.21 shows that the lateral spreading around umbrella cloud is larger if the diffusion (random velocity) is larger.

To compare simulation and observation, randome velocity is varied from 0.05 $\frac{\Delta x}{\Delta t}$ to 0.8 $\frac{\Delta x}{\Delta t}$. Input value of random velocities and particle numbers of simulation cases are shown in Table 5.7.

In Fig. 5.22, 5.23 and 5.24, values of MPA on the ground by varying plume random velocity are shown. Graphs of simulated MPA versus observed MPA are also shown. MPA value is compared for each outcrop point. To quantify the correlation of the result from simulation and observation, misfit function (MF) is calculated with the equation

$$MF = \sum^{N_o} \frac{|M_{sim} - M_{obs}|}{N_o} \tag{5.36}$$

where N_o is the number of outcrops observed for each eruption. M_{sim} is MPA for each point obtained from simulation and M_{obs} is MPA for each point obtained from observation.
Misfit functions for simulation cases with the variation in plume random velocity and in atmospheric random velocity are shown in Fig. 5.25(a) and (b).

MPA of windy case (Cotopaxi Layer 3 and Cotopaxi Layer 5 erutions) show the maximum which deviates to downwind direction. Then, contourlines of MPA (isomass line) show that the mass decrease with the distance from the crater. In the results of simulations with various plume random velocity (R_p), deposition is less elongated when R_p is larger for windy case, but the difference in elongation is not clear from the map. On the contrary, misfit function varies significantly. In Cotopaxi Layer 3 case, largest value of misfit function is 2245.50. This error means more than 2 m difference in thickness because the density of this layer is around 700 kg/m^3. For Cotopaxi Layer 3 eruption, misfit function is smallest when R_p is 0.6. For Cotopaxi Layer 5, misfit function is smallest when R_p is 0.4. However, values of misfit function do not show wide variation from $R_p = 0.2$ to $R_p = 0.8$. For Pululagua 2450BP eruption, misfit function is minimum when $R_p = 0.05$ although the variation of MPA in the figures of simulated MPA versus observed MPA or contour maps do not show large variation.
In the results of simulations with various atmospheric random velocity (R_a), isomass lines expands in the crosswind direction as R_a increases. Misfit function becomes smallest when R_a is 0.05 for all eruptions.

Table 5.7: Simulation cases for MPA comparison with observed data. Other input parameters are described in section 5.3.1.

Eruption	Ra	Rp	particle number
Cotopaxi Layer 3	0.1	0.05	100000
Cotopaxi Layer 3	0.1	0.2	100000
Cotopaxi Layer 3	0.1	0.4	100000
Cotopaxi Layer 3	0.1	0.6	100000
Cotopaxi Layer 3	0.1	0.8	100000
Cotopaxi Layer 3	0.05	0.6	100000
Cotopaxi Layer 3	0.2	0.6	100000
Cotopaxi Layer 3	0.4	0.6	100000
Cotopaxi Layer 3	0.6	0.6	100000
Cotopaxi Layer 3	0.8	0.6	100000
Cotopaxi Layer 5	0.1	0.05	100000
Cotopaxi Layer 5	0.1	0.2	100000
Cotopaxi Layer 5	0.1	0.4	100000
Cotopaxi Layer 5	0.1	0.6	100000
Cotopaxi Layer 5	0.1	0.8	100000
Cotopaxi Layer 5	0.05	0.6	100000
Cotopaxi Layer 5	0.2	0.6	100000
Cotopaxi Layer 5	0.4	0.6	100000
Cotopaxi Layer 5	0.6	0.6	100000
Cotopaxi Layer 5	0.8	0.6	100000
Pululagua 2450BP	0.1	0.05	400000
Pululagua 2450BP	0.1	0.2	400000
Pululagua 2450BP	0.1	0.4	400000
Pululagua 2450BP	0.1	0.6	400000
Pululagua 2450BP	0.1	0.8	400000
Pululagua 2450BP	0.05	0.1	400000
Pululagua 2450BP	0.2	0.1	400000
Pululagua 2450BP	0.4	0.1	400000
Pululagua 2450BP	0.6	0.1	400000
Pululagua 2450BP	0.8	0.1	400000

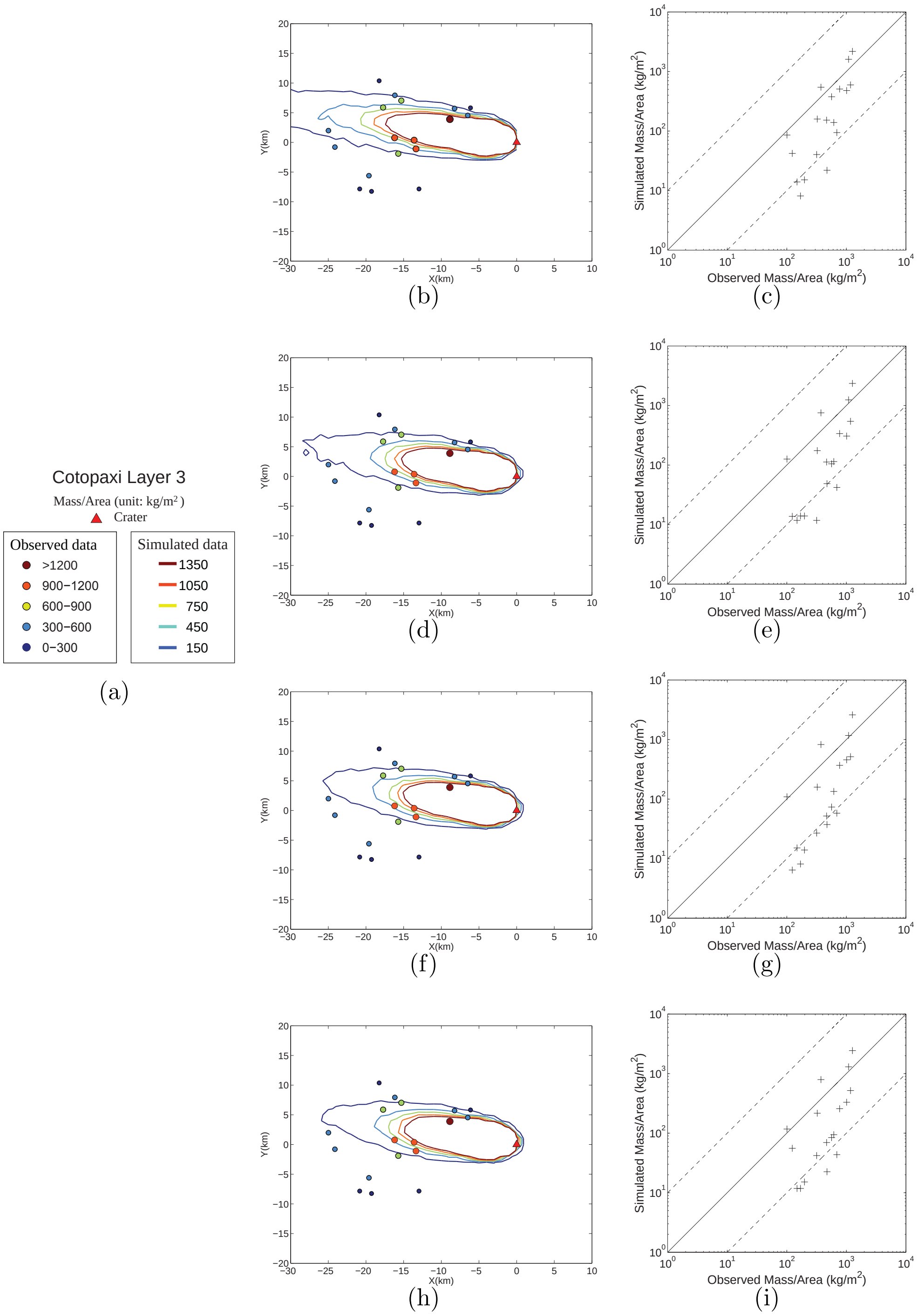

(a) (b) (c) (d) (e) (f) (g) (h) (i)

Fig. 5.22: Contour map of MPA (kg/m^2) (isolines) and observed ground accumulation (colored circles) for Cotopaxi Layer 3 eruption.(left side) Simulated MPA versus observed MPA (right side). Plume random velocity is given with the ratio $R_p = 0.2$ for (b) and (c), $R_p = 0.4$ for (d) and (e), $R_p = 0.6$ for (f) and (g), and $R_p = 0.8$ for (h) and (i). Color of lines and points show the range of value which is shown in legend. Here, atmospheric random velocity is fixed with $R_a = 0.1$

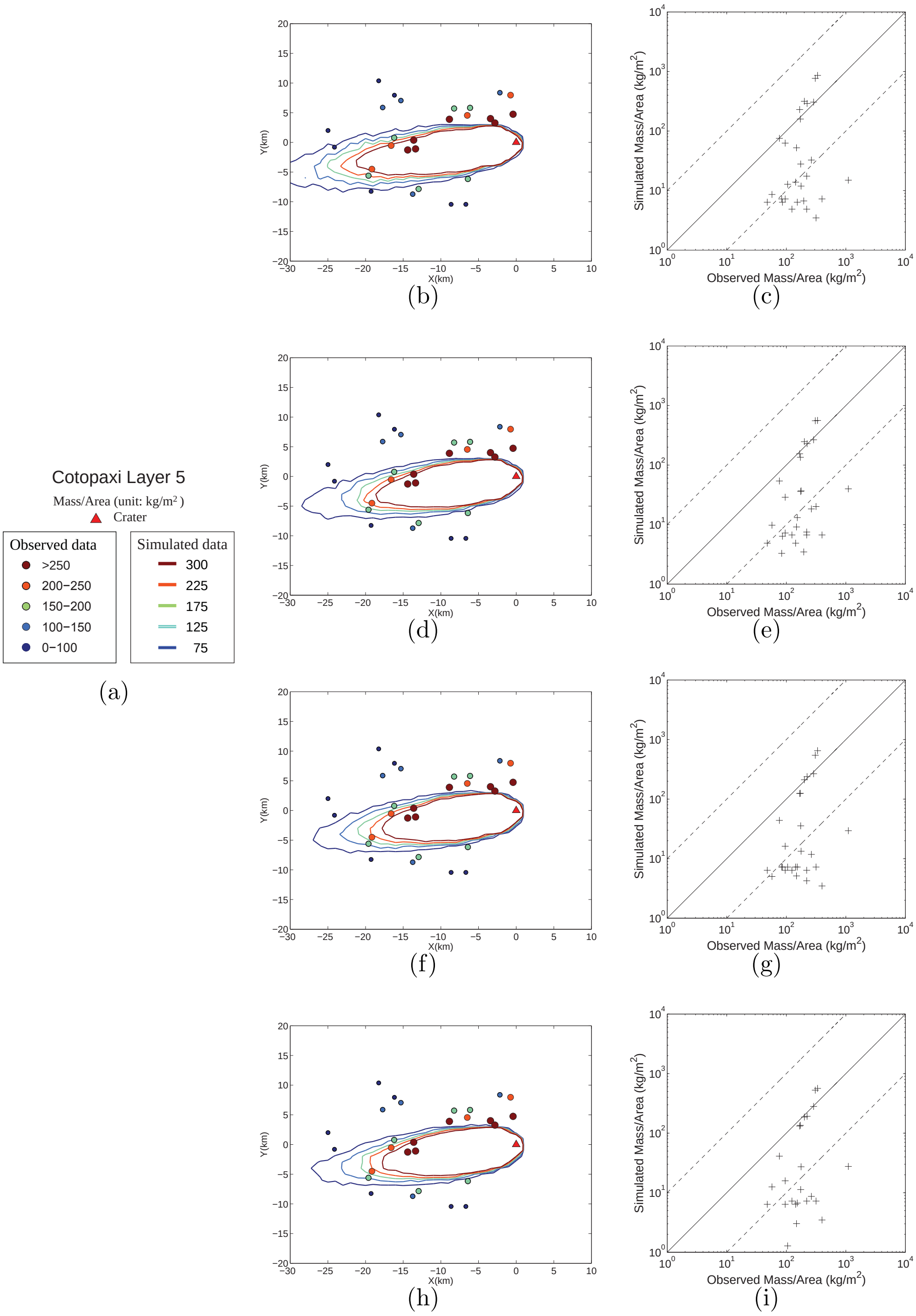

(a) (b) (c) (d) (e) (f) (g) (h) (i)

Fig. 5.23: Contour map of MPA (kg/m^2) (isolines) and observed ground accumulation (colored circles) for Cotopaxi Layer 5 eruption.(left side) Simulated MPA versus observed MPA (right side). Plume random velocity is given with the ratio $R_p = 0.2$ for (b) and (c), $R_p = 0.4$ for (d) and (e), $R_p = 0.6$ for (f) and (g), and $R_p = 0.8$ for (h) and (i). Color of lines and points show the range of value which is shown in legend. Here, atmospheric random velocity is fixed with $R_a = 0.1$

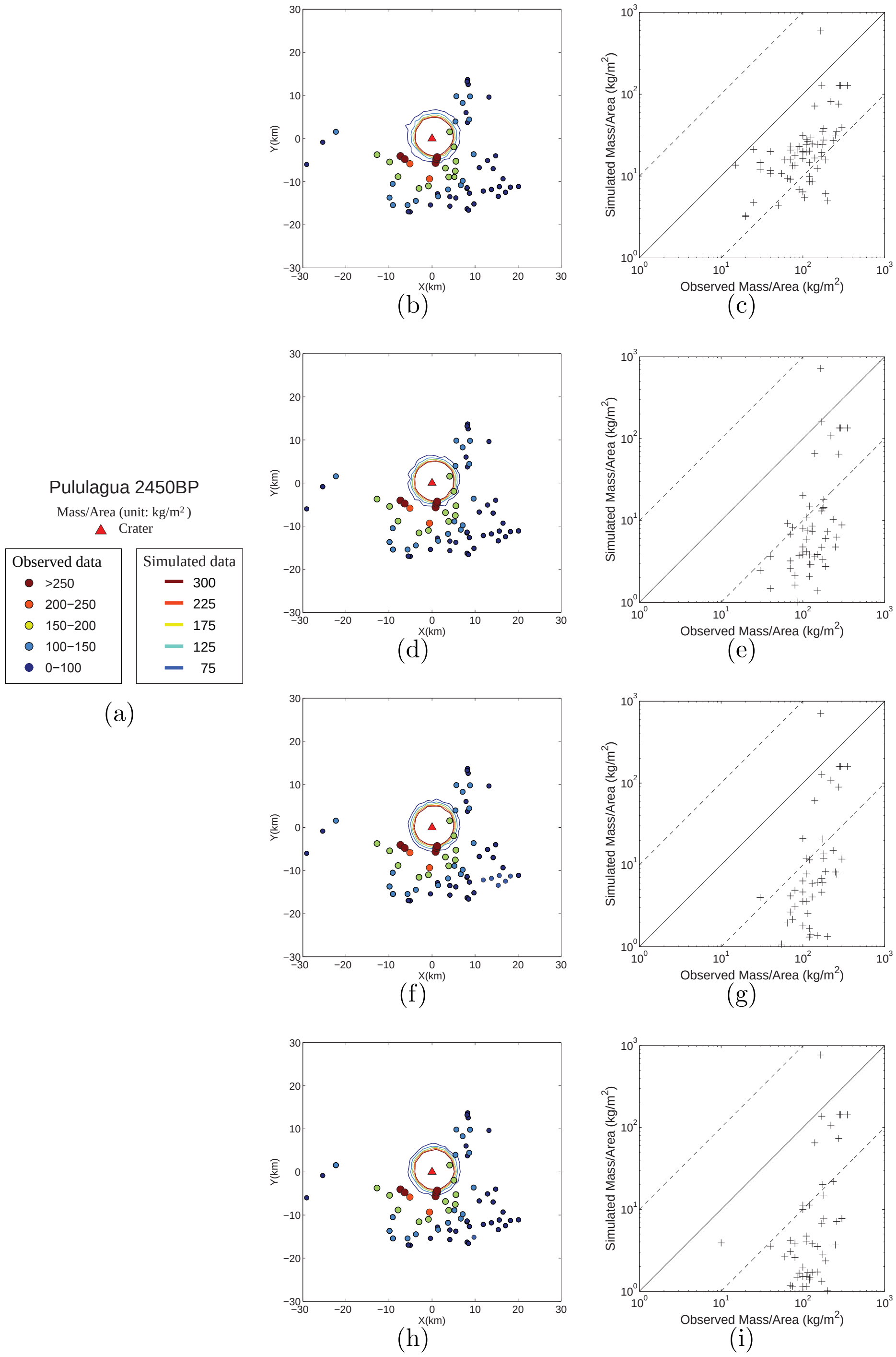

(a) (b) (c) (d) (e) (f) (g) (h) (i)

Fig. 5.24: Contour map of MPA (kg/m^2) (isolines) and observed ground accumulation (colored circles) for Pululagua 2450BP eruption.(left side) Simulated MPA versus observed MPA (right side). Plume random velocity is given with the ratio $R_p = 0.2$ for (b) and (c), $R_p = 0.4$ for (d) and (e), $R_p = 0.6$ for (f) and (g), and $R_p = 0.8$ for (h) and (i). Color of lines and points show the range of value which is shown in legend. Here, atmospheric random velocity is fixed with $R_a = 0.1$

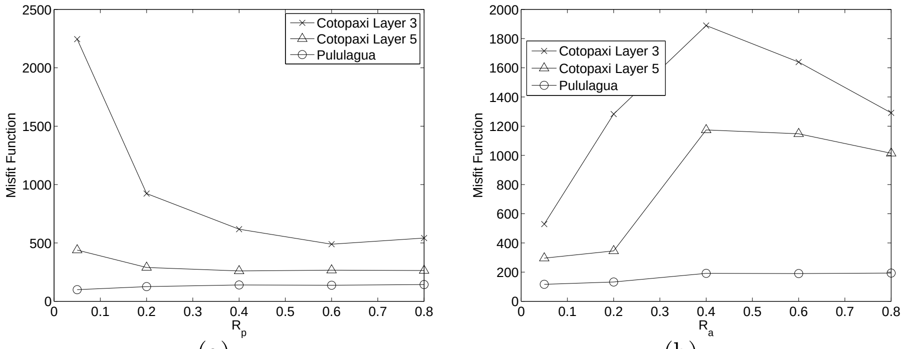

(a) (b)

Fig. 5.25: Misfit function with variation of (a)Plume random velocity (R_p) and (b) atmospheric random velocity(R_a).

5.4 Discussion

Improvement of source term In our former model in two dimensions, particles are released at one point from the neutral buoyancy height of plume (H_b) and some models of tephra transport release the particles from one line above the crater (Stohl et al., 2011 [110]; Dacre et al., 2011 [37]). To improve the source term, we have applied velocity profiles of volcanic plumes calculated by one-dimensional plume model by Woods (1988) [139] and expanded to three dimensions. In Fig. 5.14, plume shape is described as trajectories of all particles. Especially the trajectories of fine particles (-1ϕ and 2ϕ) show the mushroom like shape of plumes which is closer to the visible plume shape when the eruptions occur (Fig. 5.13).

For the simple Lagrangian simulation without diffusion, the simulation case with the velocity profiles of volcanic plumes show better agreement with the field observation (Fig. 5.17). Especially, the results of simulation improves ground deposition in proximal area. This implies the plume velocity profiles improves the ground deposition in proximal area where the hazards due to volcanic ash. Therefore, our model can contribute to forecast or predict the ground deposition of tephra around volcano.

In the reality of the forecasting of tephra dispersal during the volcanic crisis, source term is not well defined. The grainsize of particles and input parameters of one-dimensional plume model such as temperature of plume and ejection velocity are unclear. In our model, Monte Carlo simulations are implemented to calculate the plume velocity profile and calibrate it by the plume total height in order to have appropriate values of input parameters. Stohl et al., (2011) [110] suggested the inversion simulation with Lagrangian

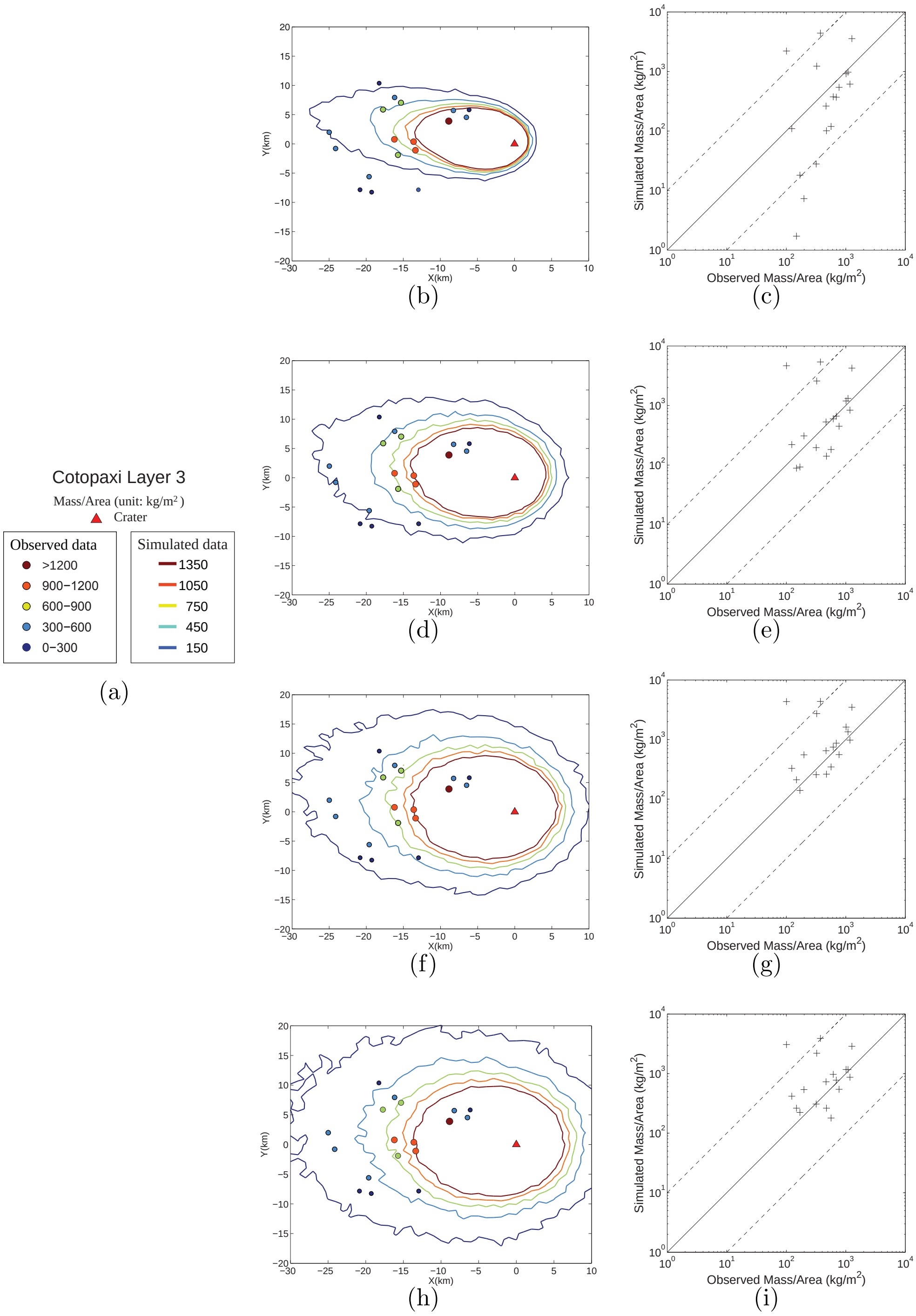

(a) (b) (c) (d) (e) (f) (g) (h) (i)

Fig. 5.26: Contour map of MPA (kg/m^2) (isolines) and observed ground accumulation (colored circles) for Cotopaxi Layer 3 eruption.(left side) Simulated MPA versus observed MPA (right side). Atmospheric random velocity is given with the ratio $R_a = 0.2$ for (b) and (c), $R_a = 0.4$ for (d) and (e), $R_a = 0.6$ for (f) and (g), and $R_a = 0.8$ for (h) and (i). Color of lines and points show the range of value which is shown in legend. Here, plume random velocity is fixed with $R_p = 0.6$.

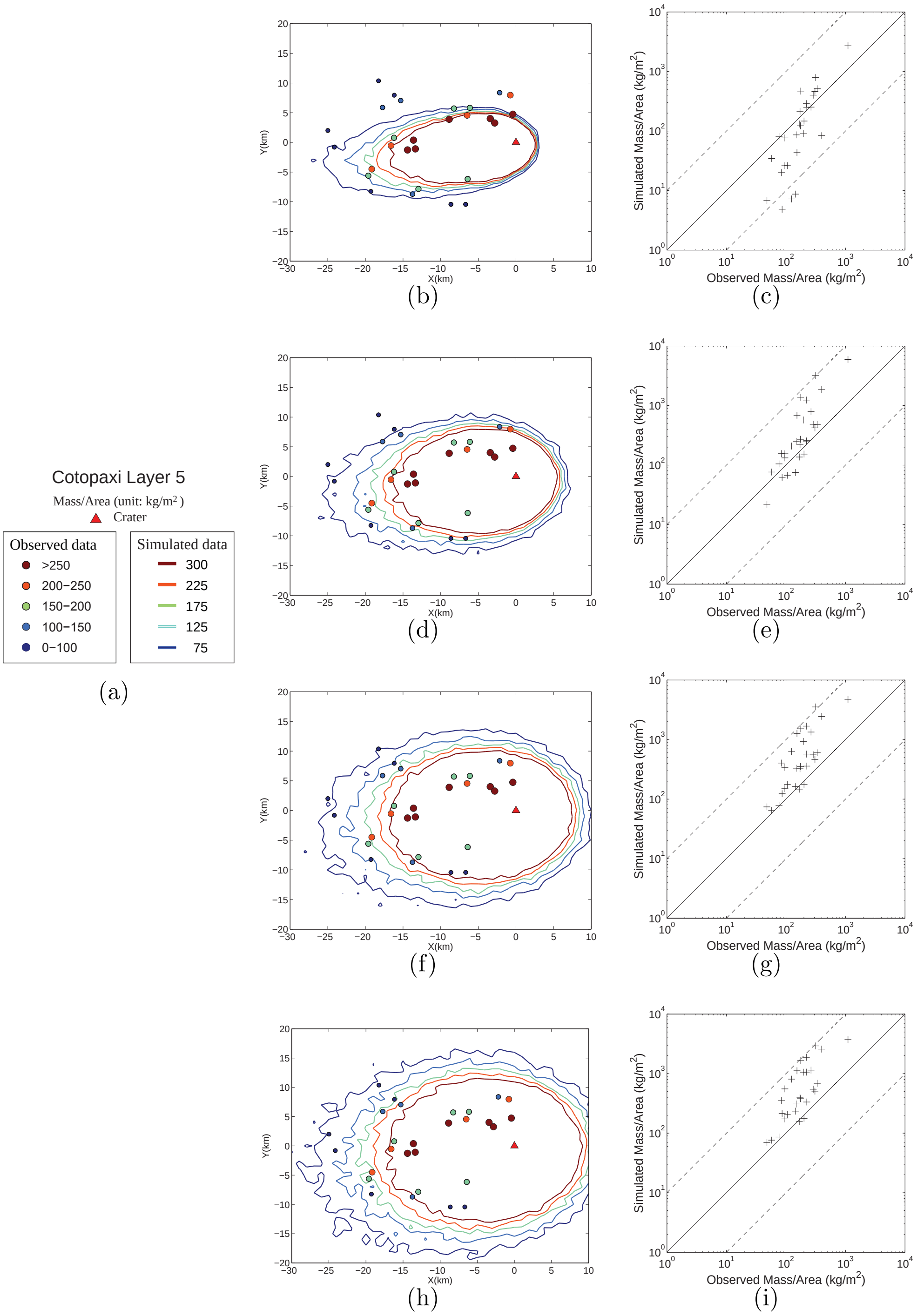

Fig. 5.27: Contour map of MPA (kg/m^2) (isolines) and observed ground accumulation (colored circles) for Cotopaxi Layer 5 eruption.(left side) Simulated MPA versus observed MPA (right side). Atmospheric random velocity is given with the ratio $R_a = 0.2$ for (b) and (c), $R_a = 0.4$ for (d) and (e), $R_a = 0.6$ for (f) and (g), and $R_a = 0.8$ for (h) and (i). Color of lines and points show the range of value which is shown in legend. Here, plume random velocity is fixed with $R_p = 0.6$.

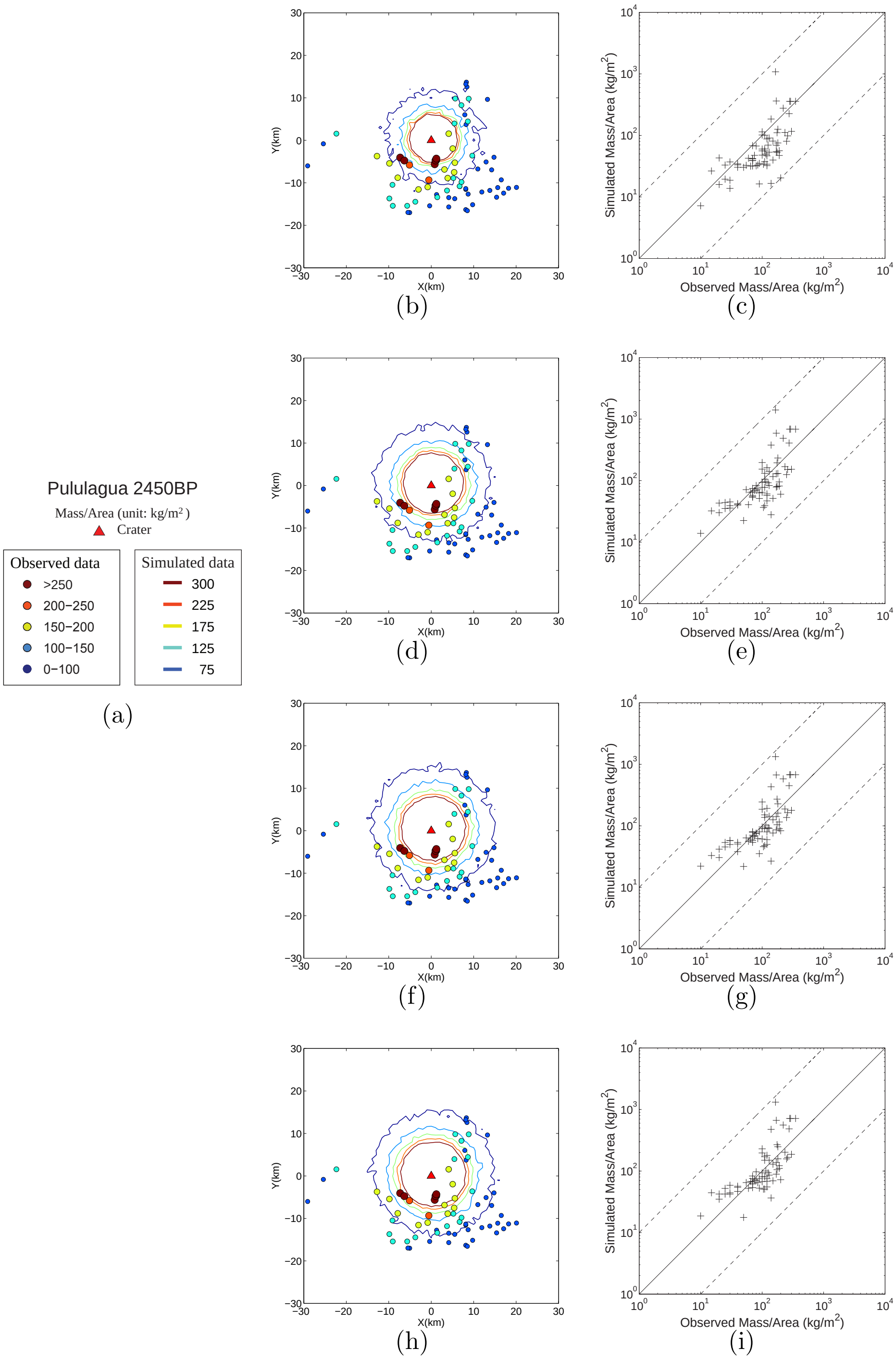

(a) (b) (c) (d) (e) (f) (g) (h) (i)

Fig. 5.28: Contour map of MPA (kg/m^2) (isolines) and observed ground accumulation (colored circles) for Pululagua 2450BP eruption.(left side) Simulated MPA versus observed MPA (right side). Atmospheric random velocity is given with the ratio $R_a = 0.2$ for (b) and (c), $ra = 0.4$ for (d) and (e), $R_a = 0.6$ for (f) and (g), and $R_a = 0.8$ for (h) and (i). Color of lines and points show the range of value which is shown in legend. Here, plume random velocity is fixed with $R_p = 0.1$.

model to define the source term. However, it is computationally expensive. For the Monte Carlo simulations with one-dimensional model is not computationally expensive and it only takes a couple or hours to calculate 1000 cases on a standard laptop computer. We can conclude that a stochastic treatment of the source term is practical for operational purposes.

This can be done for all source term parameters (i.e. grainsize, plume height, exit velocity, plume temperature, mass eruptions rate) which can be stochastically sampled out of probability density functions build on past data.

Another approach of defining the source term is to define it by the dynamics of the conduit flow and the magma fragmentation model. Magma fragmentation largely affects grainsize distribution of tephra (Kaminski and Jaupart 1998 [61]). Conduit flow affect the ejection velocity or mass eruption rate and it is strongly related to magma fragmentation (e.g. Houghton and Gonnermann, 2008[57]). Even though it is complicated, it is very useful if we can define the ejection conditions and grainsize distributions from the geodynamical observation before the eruption and calculate using the models of magma fragmentation and conduit flow. So far, it is practical to prepare the parameters and grainsize distribution by compiling the data from the past eruptions and implement the MonteCarlo simulation.

Random velocity and diffusion coefficient According to the parameter work (section 5.3.4), when the random velocity of volcanic plume is $0.09v$, Md_ϕ of numerical experiments and the field observation agree well. This can imply that the plume turbulence is strong and it agrees well when the value of random velocity is large.

When the random velocity of atmosphere is $0.0v$, Md_ϕ of numerical experiments and the field observation agree well. Our model has numerical diffusion only with advection velocity, and it is enough for the atmospheric diffusion. In fact, the value of diffusion in atmosphere is much smaller than that in the volcanic plume. Schlichting (1979) [54] reported the value of turbulent fluctuations in atmosphere 0.0005, and List (1982) [67] reported the value of fluctuations 0.27 or 0.40 in maximum for jet and buoyant plume and respectively. These values also show fluctuations of atmospheric turbulence is much smaller than fluctuations of plumes. (The value of fluctuations are non-dimensional due to the normalization by mean velocity.)

If random velocity is $0.09v$ and $0.0v$ for the plume and the atmosphere respectively, diffusion coefficient is estimated as $1.4 \times 10^4\ m^2/s$ in volcanic plume and $0.0v$ in the atmosphere by assuming the random velocity is only affected the diffusion of particles.

Eq. (3.31) in Chapter 3 also shows the diffusion coefficient emerges only from advection velocity and grid size. This diffusion value depends on the advection velocity. The advection velocity in our model is mainly wind velocity and it varies approximately from 0 to 30 m/s (e.g. maximum wind speed of Cotopaxi Layer 3 eruption is 28 m/s in Table 5.6). With grid size $\Delta x = 500m$ and time step $\Delta t = 1s$, diffusion value due to the advection velocity calculated by eq. (3.31) is from 0 to 7050 m/s^2.
Bonadonna and Costa (in Press) [11] introduced the value of diffusion in horizontal direction as 1 to 8000 m^2/s in the atmosphere by using different tephra transport models such as the model of Bonadonna and Phillips, 2003 [13], TEPHRA2(Bonadonna et al, 2005) [15] and FALL3D (Folch et al. 2009 [49]. These values are similar to the diffusion emerged only from advection velocity in multiparticle CA model. Thus, the combination of random velocity 0.0 m/s and advection velocity produces similar diffusion with the value calculated by other tephra transport models reported in Bonadonna and Costa(in Press) [11].
As the velocity field of the turbulent flow is random (Pope 2000 [88]), it is appropriate to apply the stochastic rule of random velocity to simulate the diffusion of turbulence. The value of diffusion in tephra transport models were not obvious, while our model follows the theory of turbulence (section 5.2.5) to have more reliable model. Additionally, considering the results of particle distribution in the air show the mushroom like plume shape although each particle has absolutely different moving path, we have successfully implemented turbulent characteristics of plumes and atmosphere.
We also tried to have more quantification of comparison with observed data by comparing the value of mass per unit area (MPA) for each outcrop and calculated misfit function with Lagrangian on grid model (section 5.3.5). With this model, diffusion value and random velocity is related by the eq. (5.34). Then, plume diffusion value which makes the misfit function smallest can be obtained as 45000 m^2 for Cotopaxi Layer 3, 20000 m^2 for Cotopaxi Layer 5 and around 300 m^2 for Pululgua 2450 BP eruption. While diffusions of atmospheric random velocity which makes misfit function smallest is around 300 m^2. Clearly, the diffusion is larger for plume. It corresponds to the fact that the turbulence in the plume is stronger than the turbulence in the atmosphere. The value of atmospheric diffusion obtained here is smaller than the value obtained from the literature(Bonadonna and Costa in Press [11]). However, there are many ambiguous parameters for both observation and simulation. To define the diffusion coefficient, we have to be careful with such ambiguities.

Thickness of layers are obtained in the field, and coverted to MPA with the density of outcrops which is also obtained in the field. Thickness data is affected by the erosion of artificial change of the land. Especially, if the eruption is old, it is more likely to have transformation. Moreover, the distribution of outcrops is not in the grid and it depends on accessibility of the field. Outcrop points are sometimes not enough for the statistical analysis. Density variation of outcrops is ignored for our sample eruptions. However, outcrop density varies with the distance from the vent and it depends on the particle compaction. Simulation itself also has ambiguity. Initial parameters of plume velocity such are temperature and exit velocities are often unknown and it is calibrated with Total plume height. Besides, the model of spreading current of umbrella cloud is calibrated by numerical simulation and the parameter λ is defined from the simulation without considering wind. This spreading current is highly turbulent, while spreading velocity is derived by ignoring turbulent effect. In our results, isomass map (b, d, f, h of Fig. 5.22-5.24 and Fig. 5.26-5.28) is more elongated than isopach map in Chap. 2. It is because spreading current is blown by the wind strongly thus it is imporatnt to think umbrella cloud as turbulence. Nevertheless of these uncertainty, our simulation results show good agreements with observed data. Although we have to add more particles to make the isomass map smoother, the model is quite promissing for simulating tephra fall deposits.

For further improvement of our model, in terms of turbulence, the model of turbulence based on the atmospheric dynamics is suggested. The nature of atmosphere is more complicated than wall-bounded flows and the atmosphere has some kinds of instability to produce turbulence (e.g. instability due to the temperature difference in the day and the night). Webster et al., (2003) [131] showed the diffusion coefficient due to the turbulence for the atmospheric boundary layer and free atmosphere separately. Webster's model is based on the meteorological back ground, we can possibly improve our model by applying their turbulent model.

Model advantages and pespectives Our model keeps the sophisticated aspects of Lagrangian model in that the model tracks particles and has the characteristics of the Eulerian model such as the grid base approach. The grid makes easy the parallelization of the codes which significantly improves the computation speed. In fact, the Lagrangian models are not easy to parallelize because they describe particle trajectories without spatial grid. In this study the wind velocity is simplified only depending on the height. However, magnitude of velocity and direction of the wind changes with time. Our results show that particle transport model based on a simple description of wind profile provides a first approximation agreement with field observations. As our model is based on the grid, it is easier to include the wind velocity

field than Lagrangian models.
To verify the model for the dispersion of tephra in the air, the simulation results should be compared with the tephra concentration observed by airplains or satellites. To have the solid model to predict dispersal of tephra in the air is important for the aviation industry which is damaged by the volcanic erutpion if the flights are cancelled.

5.5 Conclusions

1. The 3D multiparticle Cellular Automata method provides an accurate description of the source term which significantly improves the prediction of particle sedimentation with respect to the 2D model.

2. The turbulence field is described by stochastic rule of multiparticle Cellular Automata and it is appropriate because turbulent flow is random.

3. Diffusion coefficient due to the atmospheric turbulence estimated by the parameter work is similar to the value which is reported by other tephra transport models.

4. Diffusion values are calculated based on the turbulent theory for both volcanic plume and atmosphere.

5. Tephra transport model with multiparticle Cellular Automata method holds advantages of both Lagrangian and Eulerian models.

6. Tephra transport model with Lagrangian on grid model also holds advantages of both Lagrangian and Eulerian models. With this model, we obtained good agreements between simulation results and observed data despite the uncertainty of obeserved and simulated data.

Appendix A

One-dimensional steady-state plume model simulation

PLume 1D veloctiy profile along vertical axis (z) is calculated by Woods (1988) [139]. This model is steady-state model and the parameters are solved as a function of z. Model of Woods (1988)[139] consists of two models, model A which is the model of the basal gas thrust region and model B which is the model of convective region. There are seven unknown parameters (summarized in Table A.1. For solve seven parameters, seven equations are necessary and they are presented as follows.

At first, the model equations for each model are presented.

Model A: Gas thrust region

Eq. (16) of [139]: Transfromed mass conservation

$$U\frac{dU}{dz} = -\frac{U^2}{8L}\sqrt{\frac{\alpha}{\beta}} + \frac{g(\alpha-\beta)}{\beta}$$

Eq. (2): Momentum conservation

$$\frac{d}{dz}\left(\beta U^2 L^2\right) = g\left(\alpha-\beta\right)L^2$$

Table A.1: Sveven Unknown Parameters of Woods(1988) model

Title	Notation
Velocity	U
Plume radius	L
Density of plume	β
bulk specific heat of the plume	C_p
Plume bulk temperature	θ
Plume bulk gas constant	R_g
Gas mass fraction in the plume	n

Table A.2: Other Parameters of Woods(1988) model

Title	Notation
Vertical axis	z
Graivity acceleration	g
Atmospheric density	α
Specific heat of the air	C_a
Specific heat of the plume at the vent	C_p
Atmospheric pressure	P
The gas constant for the air (285)	R_a
The gas constant for the plume at the vent ($= R_m$)	R_{g0}
The gas constant for the volcanic gas (462)	R_m
The entrainment constant (0.09)	k

Eq. (8)

$$\frac{d}{dz}\left(C_p\theta\beta UL^2\right) = (C_aT)\frac{d}{dz}\left(\beta UL^2\right) + \frac{U^2}{2}\frac{d}{dz}\left(\beta UL^2\right) - \alpha UL^2 g$$

Eq. (3)

$$\frac{1}{\beta} = (1-n)\frac{1}{\sigma} + \frac{nR_g\theta}{P}$$

Eq. (4)

$$n = 1 + (n_0 - 1)\frac{L_0^2U_0\beta_0}{L^2U\beta}$$

Eq. (5)

$$R_g = R_a + (R_{g0} - R_a)\left(\frac{1-n}{n}\right)\left(\frac{n_0}{1-n_0}\right)$$

Eq. (10)

$$C_p = C_a + (C_{p0} - C_a)\left(\frac{1-n}{1-n_0}\right)$$

Model B: Convective region

Eq. (18): Mass conservation

$$\frac{d}{dz}\left(\beta UL^2\right) = 2kUL\alpha$$

Eq. (2): Momentum conservation

$$\frac{d}{dz}\left(\beta U^2L^2\right) = g\left(\alpha - \beta\right)L^2$$

Eq. (8)

$$\frac{d}{dz}\left(C_p\theta\beta UL^2\right) = \left(C_aT\right)\frac{d}{dz}\left(\beta UL^2\right) + \frac{U^2}{2}\frac{d}{dz}\left(\beta UL^2\right) - \alpha UL^2g$$

Eq. (3)

$$\frac{1}{\beta} = (1-n)\frac{1}{\sigma} + \frac{nR_g\theta}{P}$$

Eq. (4)

$$n = 1 + (n_0 - 1)\frac{L_0^2U_0\beta_0}{L^2U\beta}$$

Eq. (5)

$$R_g = R_a + \left(R_{g0} - R_a\right)\left(\frac{1-n}{n}\right)\left(\frac{n_0}{1-n_0}\right)$$

Eq. (10)

$$C_p = C_a + \left(C_{p0} - C_a\right)\left(\frac{1-n}{1-n_0}\right)$$

Then, differential equations are transformed in order to solve numerically.

Transformation of equations: Model A

From eq. (16)→ U

$$\begin{aligned} U\frac{dU}{dz} &= -\frac{U^2}{8L}\sqrt{\frac{\alpha}{\beta}} + \frac{g(\alpha-\beta)}{\beta} \\ \frac{dU}{dz} &= -\frac{U}{8L}\sqrt{\frac{\alpha}{\beta}} + \frac{g(\alpha-\beta)}{\beta U} \end{aligned} \tag{A.1}$$

From eq. (2) → βUL^2

$$\begin{aligned} \frac{d}{dz}\left(\beta U^2L^2\right) &= g\left(\alpha-\beta\right)L^2 \\ U\frac{d}{dz}\left(\beta UL^2\right) + \left(\beta UL^2\right)\frac{dU}{dz} &= g\left(\alpha-\beta\right)L^2 \\ \frac{d}{dz}\left(\beta UL^2\right) &= \frac{g\left(\alpha-\beta\right)L^2}{U} - \left(\beta L^2\right)\frac{dU}{dz} \end{aligned} \tag{A.2}$$

From eq. (8) → θ

$$\begin{aligned}
\frac{d}{dz}\left(C_p\theta\beta UL^2\right) &= \left(C_aT\right)\frac{d}{dz}\left(\beta UL^2\right)+\frac{U^2}{2}\frac{d}{dz}\left(\beta UL^2\right)-\alpha UL^2g \quad \text{(A.3)}\\
\beta UL^2\frac{d}{dz}\left(C_p\theta\right)+C_p\theta\frac{d}{dz}\left(\beta UL^2\right) &= \left(C_aT\right)\frac{d}{dz}\left(\beta UL^2\right)+\frac{U^2}{2}\frac{d}{dz}\left(\beta UL^2\right)-\alpha UL^2g\\
\beta UL^2\frac{d}{dz}\left(C_p\theta\right) &= \left(C_aT+\frac{U^2}{2}-C_p\theta\right)\frac{d}{dz}\left(\beta UL^2\right)-\alpha UL^2g\\
\frac{d}{dz}\left(C_p\theta\right) &= \frac{1}{\beta UL^2}\left[\left(C_aT+\frac{U^2}{2}-C_p\theta\right)\frac{d}{dz}\left(\beta UL^2\right)-\alpha UL^2g\right]
\end{aligned}$$

Transformation of equations: Model B

The first equation is eq.(18) of Woods(1988).

$$\frac{d}{dz}\left(\beta UL^2\right)=2kUL\alpha \tag{A.4}$$

Second equation is transformed from Eq. (2)

$$\begin{aligned}
\frac{d}{dz}\left(\beta U^2L^2\right) &= g(\alpha-\beta)L^2 \quad \text{(A.5)}\\
\beta UL^2\frac{dU}{dz}+U\frac{d}{dz}\left(\beta UL^2\right) &= g(\alpha-\beta)L^2\\
\beta UL^2\frac{dU}{dz} &= g(\alpha-\beta)L^2-U\frac{d}{dz}\left(\beta UL^2\right)\\
\frac{dU}{dz} &= \frac{1}{\beta UL^2}\left[g(\alpha-\beta)L^2-U\frac{d}{dz}\left(\beta UL^2\right)\right]
\end{aligned}$$

Third equation is the same as model A (eq. A.4).
By solving differential equations, we can obtain U, βULr and $C_p\theta$. Parameters n, R_g, C_p and β are separately calculated from eq. (3), (4), (5) and (10) of Woods(1988) respectively. The rest of calculation is as follows.

- From U, β and βULr, L is obtained.
- From $C_p\theta$ and C_p, θ is obtained.

If parameters U, L, n and θ, are identified, calculation can start.

For model A;

- C_p and $R_g \leftarrow n$.
- $\beta \leftarrow R_g, n, \theta$
- Differential eq. (A.4) and (A.3) $\leftarrow U, \beta, L$

- Differential eq. (A.4) ← C_p, θ, β, U, L

For model B;

- C_p and $R_g \leftarrow n$.
- $\beta \leftarrow R_g, n, \theta$
- Differential eq. (A.4) and (A.6) ← U, β, L
- Differential eq. (A.4) ← C_p, θ, β, U, L

Chapter 6

A new numerical model for the description of ballistics

6.1 Introduction

When a volcano erupts explosively, volcanic particles of various size and shape are ejected from the crater of the volcano. In explosive eruptions, large particles (> c.10 cm) are transported in the air decoupled from the gas phase at the early stage of transport and follow independent parabolic trajectories. These large particles are called ballistic blocks or ballistic bombs.

The study of ballistics are crucial to both understanding of ejection dynamics and hazard assessment. In fact, exit velocity of ballistics is strongly related to the jet phase of volcanic plumes. In addition, the kinetic energy associated with ballistics can significantly damage infrastructures in proximal are.

There are many numerical models describing the trajectory of the individual particles (Wilson ,1972 [133]; Fagents and Wilson, 1993 [46]; Bower and Woods,1996 [18]; Mastin, 2002 [73]; Alatorre-Ibarguëngoitia and Delgado-Granados, 2006 [1]). A numerical model of ballistic trajectories of volcanic bombs was first suggested by Wilson, (1972) [133] which accounted for the effect of drag forces. It was further developed by Fagents and Wilson, (1993) [46] with realistic conditions including the coupling of the explosion and surrounded air for the Vulcanian eruption. Bower and Woods, (1996) [18] considered ballistic trajectories which were accelerated by the gas phase, while taking into account the particle motion through the crater and the atmosphere. Alatorre-Ibarguëngoitia and Delgado-Granados, (2006) [1] measured drag force of ballistic particles due to the shape difference in laboratory experiments. The model of Mastin, (2002) [73] is a system of Graphical User Interface (GUI) with which people can pursuit their own scenario. Saunderson, (2008) [98] suggested the equations of motion with the resistance and total centrifugal terms by using plural particles. All models are two-dimensional and neither the spatial distribution of deposited particles on the ground, nor the effect of particle interaction such as collisions, has been investigated.

We have based our model on observation of strombolian eruptions. Chouet et al., (1974) [32], Blackbur et al.,(1976) [9] and Ripepe et al., (1993) [94] analyzed photos of short exposure time to obtain the trajectory of particles. This approach provided velocity of particles, ejection angles and frequency of bursts. Patrick et al.,(2007) [84] used thermal (Forward Looking Infrared Radiometer) video and obtained the ejection velocity, maximum height of particle during the flight and eruption durations. Unfortunately, obtained velocity and trajectory can not be easily compared with the distribution of deposited particles.

We have applied the value of parameters obtained by the analysis of thermal videos and have investigated possibility of inter-particle collision and the effect of collisions to travel distances.

6.2 Model

6.2.1 Discrete Event Simulation method

To simulate ballistic trajectories, we have built a three-dimensional model of ballistics by using a discrete event simulation (DES) method. In our model, many particles are used in the simulation and collisions between particles are considered. Nonetheless, simulations are quickly executed because DES is applied.

The discrete event simulation system (DES) is known to be the opposite terminology to the continuous time system (Zeigler et al., 1976 [143]). The discrete time system is one in which the state variables change only at a discrete set of points in time. A continuous time system is one in which the state variables change continuously over time (Banks et al., 2010 [3]).

A DES simulator consists of a “state” and a “queue of future events” (Fig. 6.1). A state consists of the current simulation time and the relevant variables of state, which shows a state or condition at the current time, while the queue of future events is a list of discrete events which are expected to occur in future and sorted by the event time. Steps of DES simulation are shown in a flow chart of Fig. 6.2.

At first, states are initialized and a queue is filled with future events which are directly related to the initial state. At the time of initialization, the event queue is filled with exogenous events. Exogenous events are events which are caused by the external effect of the simulated system. On the contrary, events which are caused by the internal effects of the system are called endogenous events. One exogenous event triggers many endogenous

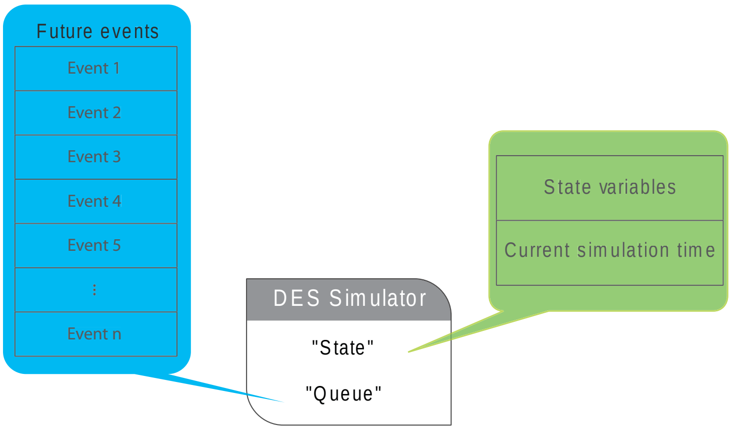

Fig. 6.1: Structure of DES simulator

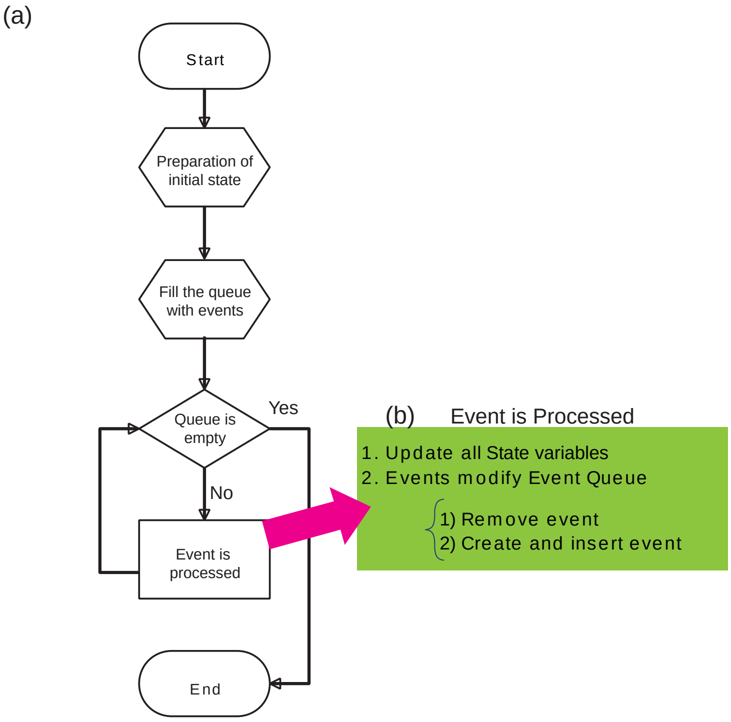

Fig. 6.2: Algorithm of a simple DES simulation system. a) Whole process. b) When the event is processed.

Table 6.1: Notation of parameters for a model of ballistics

Parameter	Value	unit
m	Mass	
R	Radius	
$\mathbf{r}$	Position	
t	Current time	
t_d	deposition time	.
$\mathbf{v}$	Velocity	
$\mathbf{o}$	Ejection position	
$\mathbf{e}$	Unit vector of collision line	
n_b	Number of particles of bursting	
N	Number of all particles	
C_R	Restitution coefficient	

events (Reitman, 1971 [92]).
Events in the queue are processed until the queue becomes empty (Fig. 6.2). When an event is processed, all states are updated and the events in the queue are modified by removing existing events or creating and inserting new events (Fig. 6.2). Simulation time jumps from the time of one event to the time of next event. Finally, simulation ends when the queue is empty.

We have applied this DES approach to our ballistic model. We have assumptions as follows;

1) For the simplicity, we ignore the drag force;
2) The ground where particles deposit is assumed to be flat;
3) Ballistics are spherical particles;
4) Collision with three or more than three particles are ignored.

In this model, states are current time and variables of state which consists of a list of **airborne** particles and a list of **deposited** particles. Besides, each particle includes parameters to express the condition of the particle such as density, diameter, current time, position, velocity (Algorithm. 5). The position and velocity have three components because the simulation is executed in three dimensions.
There are three types of events in our model; **Burst**, **Collision** and **Deposition**.
Burst is an ejection of volcanic particles from the vent to the air. This is an "exogenous" type event because the event itself is not controlled by the model. **Collision** is an inter-particle collision of two airborne particles. **Deposition** is the arrival of a particle on the ground. When the center position

of a particle arrives lower than the altitude of the ground, the particle is recognized to deposit on the ground. The **Collision** and **Deposition** are "endogenous" type events because these events are caused by the movement of particles in the simulated system which are firstly triggered by the exogenous **Burst** event. In between events, trajectories are calculated with fully analytical equations and it makes possible to apply DES to ballistic model.

At first, states are initialized and the queue of events is filled with **Burst** events. The **Burst** events are drawn by initial parameters such as velocity of particles, ejection points and ejection angles. Such parameters can be defined deterministically or stochastically. When we do not know the exact value of initial parameters but we only know the range of value, it is useful to draw the initial parameters stochastically. In this simulator, both deterministic methods and stochastic methods are possible for defining initial parameters. The stochastic method of drawing initial parameters is implemented by the ***BurstGenerator*** and it is explained later in this section.

The structure of the simulator is shown in Algorithm 6 by a pseudocode. Mainly it is the iteration of processing events. For each type of event, the modification of states and event queue is different.

In **Burst** event, trajectories of airborne particles during the period between former event time and current time are calculated at first and the time jumps to current time (Algorithm 7). Then, expected deposition time is calculated and a future **Deposit** event is inserted to the event queue. And the collision is checked and the expected collision times for all pairs of particles are calculated. Then future **Collision** events are also inserted to the event queue. As we know which are airborne particles and which are burst particles, the program checks the collision in burst groups and between burst group and the airborne group separately.

In **Deposit** event, trajectories of all particles are calculated and the time jumps to current time (Algorithm 8). The deposited particles are removed from the list of airborne particles and they are all added to the list of deposited particles. All event related to these deposited particles are removed from the event queue.

In **Collision** event, trajectories of particle1 and particle2, which is a colliding pair, are calculated and the time jumps to the current time (Algorithm 9). Here, the changes in velocity after the collision are calculated. Then the events regarding particle1 and particle2 are removed from the event queue. According to the new velocity after the collision, the expected deposition times are calculated for both particles and the Deposit events are newly added to the event queue. The collisions are checked and the expected collision times are calculated for two colliding particles with all others. Therefore, the number of collision check is done $2N$ times, where N is the number of all particles. For the collision check, the collisions of three or more than three particles are ignored because this model express the timing of two-particle collisions precisely and it is rare to have the three particles in collision exactly at the same time.

Algorithm 5 Algorithm of **DEFINE**.Definition of "Particle" list and "State".

```
Particle{
double density
double diameter
double currentTime
double position[3]
double velocity[3]
}
State{
double Time
List ⟨Particle⟩airborne
List ⟨Particle⟩deposited
}
```

Algorithm 6 Algorithm of **Simulation**. Algorithm of BurstGenerator is shown in Algorithm 10

```
run BurstGenerator            # fill the event queue with BURST events
while event queue is empty do
  if event type = BURST then
    BURST event is processed
  end if
  if event type = DEPOSIT then
    DEPOSIT event is processed
  end if
  if event type = COLLISION then
    COLLISION event is processed
  end if
end while
```

Ultimately, the simulation ends when the queue becomes empty, in other words, all particles deposit on the ground.

In our model, many particles are included to simulate ballistics and it is useful to analyze the phenomena stochastic way. There are random numbers in inputs of stochastic simulation and thus the outputs are analyzed statistically.

Algorithm 7 Algorithm of **BURST**(*time*) event.

```
calculate position and velocity
time joums to currentTime
for j ← 1 to sizeOf(Particles) do
    calculate deposition time
    add DEPOSIT event to eventqueue
end for
for i ← 1 to sizeOf(Particles) do
    for j ← 1 to sizeOf(Particles) do
        check collision of particle(i) and particle(j)
        if There is a collision then
            calculate collision time
            add COLLISION event to eventqueue
        end if
    end for
    for j ← 1 to sizeOf(airborne) do
        check collision of particle(i) and particle(j)
        if There is a collision then
            calculate collision time
            add COLLISION event to eventqueue
        end if
    end for
end for
```

Algorithm 8 Algorithm of **Deposit**(*time*) event.

```
calculate position and velocity
time jumps to currentTime
remove particle from the list of airborme particles
add particle to the list of deposit particles
remove event(particle) from eventqueue
```

Algorithm 9 Algorithm of **Collision**(*time*, *particle*1, *particle*2) event.

```
calculate position and velocity of $particle1$
calculate position and velocity of $particle2$
$time$ jumps to $currentTime$
calculate velocity of $particle1$ and $particle2$ after the collision
remove $event$ of $particle1$ from $eventqueue$
remove $event$ of $particle2$ from $eventqueue$
calculate the new deposit time for $particle1$ to $particle2$
add $deposit$ event of $particle1$ to $eventqueue$
add $deposit$ event of $particle2$ to $eventqueue$
for i ← 1 to sizeOf(airborne) do
  if $particle\ (i)$ is not $particle1$ or $particle\ (i)$ is not $particle2$ then
    check collision of particle $(i)$ and $particle1$
    check collision of particle $(i)$ and $particle2$
    calculate collision time
    add COLLISION event to $eventqueue$
  end if
end for
```

When the simulator runs the ***BurstGenerator*** (Algorithm 6), the initial parameters are drawn. The algorithm of the burst generator is shown in Algorithm 10. Basically, the ***BurstGenerator*** makes a list of burst particles. The number of particles is defined by the random number generator (*RNG*) with the value of average (*avg*) and standard deviation (*stdev*). Each particle has attributes which indicate the condition at the time of burst such as velocities, angles of ejection and ejection points. Each condition is also defined by *RNG* with given *avg* and *stdev.* Input parameters are shown in table 6.2 and the explanation about each parameter is in Table 6.3.

Algorithm 10 Algorithm of *BurstGenerator* drawing initial parameters by applying random number generator (*RNG*). For reproducing Gaussian distribution with RNG, we give the values of average (*avg*) and standard deviation (*stdev*).

```
List ⟨$Event$⟩ burst
read $avg$ and $stdev$ of parameters from the file ”init.txt”
n ← draw number of $particle$s with $RNG$
for j ← 0 to n do
  draw particle with $RNG$
  $burst$ ← add particle $(i)$
end for
```

6.2.2 Model equations

In this section, the expression of ballistics with equations is introduced.

Generally, an equation of motion for the center of mass is written as;

$$F_{drag} + F_{gravity} = m\frac{d\ddot{\mathbf{r}}}{dt} \tag{6.1}$$

In our model, drag force F_{drag} is ignored for simplicity, and the motion is only dependent on the gravity force $F_{gravity}$. By solving this equation with certain conditions, we obtain the expression of particle motion.

Deposition time In this model, the deposition time and the collision time is calculated from a three-dimensional trajectory. To calculate the deposition time, we focus on the equation of motion eq. (6.1) only for a vertical(z) component. The equation of motion is solved with initial velocity v_z and intial height z and we obtain;

$$\frac{1}{2}gt_d^2 + v_z t_d + z = 0 \tag{6.2}$$

The deposition time t_d is calculated by solving this quadratic equation. The right hand side of eq. (6.2) is zero because it is the time when the particles arrive at the ground.

When inter-particle collision happens, the velocity of the particle is updated. As this collision is assumed to be an elastic collision, the velocity after the collision is calculated according to the momentum conservation and the conservation of kinetic energy.

Collision time The collision occurs when two particles meet, that is to say that the distance between trajectory vectors of particle 1 ($\mathbf{r_1}$) and particle 2 ($\mathbf{r_2}$) is smaller than the sum of radii of particle 1 (R_1) and particle 2 (R_2), where subscript 1 and 2 indicate the value of particle 1 and particle 2 of colliding pair respectively.

$$|\mathbf{r}_1 - \mathbf{r}_2| \leq (R_1 + R_2) \tag{6.3}$$

Particle trajectories, which are calculated fully in three dimensions, are expressed with vectors by solving again eq. 6.1 with initial velocity $\mathbf{v}_1$ and $\mathbf{v}_2$ and initial position $\mathbf{o}_1$ and $\mathbf{o}_2$. Here, ’initial” means not only ’ejection” but also the starting time of each event.

$$\begin{aligned}\mathbf{r}_1 &= \frac{1}{2}\mathbf{g}t^2 + \mathbf{v}_1 t + \mathbf{o}_1 \\ \mathbf{r}_2 &= \frac{1}{2}\mathbf{g}t^2 + \mathbf{v}_2 t + \mathbf{o}_2 \end{aligned} \tag{6.4}$$

By substituting eq. (6.4) into eq. (6.3) and the quadratic equation of time t is obtained as follows.

$$\left(\mathbf{v}_1 - \mathbf{v}_2\right)^2 t^2 + 2\left(\mathbf{v}_1 - \mathbf{v}_2\right)\left(\mathbf{o}_1 - \mathbf{o}_2\right)t + \left(\mathbf{o}_1 - \mathbf{o}_2\right)^2 - \left(R_1 + R_2\right)^2 = 0 \tag{6.5}$$

The collision time t_c is a solution of this equation.
Among the two possible solutions of eq. (6.5), we have to select collision time, according to two constraints;

1) It is a future time, which means t is positive.

2) It is the closest time, which means the absolute value of t is smaller than the other one.

The algorithm of selection of the collision time with these constraints is shown in Algorithm 11.

Velocity after the collision The velocity of two colliding particles $\mathbf{v}_1$ and $\mathbf{v}_2$ becomes $\mathbf{v}_1'$ and $\mathbf{v}_2'$ after the collision. The velocities after the collision are shown in Fig. 6.3. At first, the velocity change in three dimensions is split into two orthogonal components: one is along the collision line and the other is orthogonal to the collision line and the tangential direction of contacted surface of two bodies (Wikipedia of Elastic collision [132]).

$$\begin{aligned}\mathbf{v'}_1 &= \mathbf{V}_{1p} + \mathbf{V}_{1o} \\ \mathbf{v'}_2 &= \mathbf{V}_{2p} + \mathbf{V}_{2o}\end{aligned} \tag{6.6}$$

where $\mathbf{v'}_1$ and $\mathbf{v'}_2$ are velocity vectors after the collision of particle 1 and particle 2, and indices p and o indicate the parallel and orthogonal direction of collision line. In the direction of the collision line, the velocity change is the same as in the one-dimensional case and it is calculated with following equations.

$$\begin{aligned}V_1' &= \frac{\left(1 + C_R\right)\left(-\mathbf{v}_1 \cdot \mathbf{e} + \mathbf{v}_2 \cdot \mathbf{e}\right)}{m_1/m_2 + 1} + \mathbf{v}_1 \cdot \mathbf{e} \\ V_2' &= \frac{\left(1 + C_R\right)\left(-\mathbf{v}_2 \cdot \mathbf{e} + \mathbf{v}_1 \cdot \mathbf{e}\right)}{m_2/m_1 + 1} + \mathbf{v}_2 \cdot \mathbf{e}\end{aligned} \tag{6.7}$$

Algorithm 11 Case classification of solutions of quadratic equation for collision time.

```
solve the quadratic equation
if There is no solution then
    There is no collision time
else if There is only one solution then
    if The larger solution $< 0$ then
        There is no collision time # Solution is not valid
    else
        Collision time $\leftarrow$ solution
    end if
else if There is two solutions then
    if The smaller solution $> 0$ then
                                        # Two solutions are valid
        Collisiont time $\leftarrow$ the smaller solution
    else if The larger solution $> 0$ then
        Collisiont time $\leftarrow$ the larger solution
    else
        There is no solution
    end if
end if
```

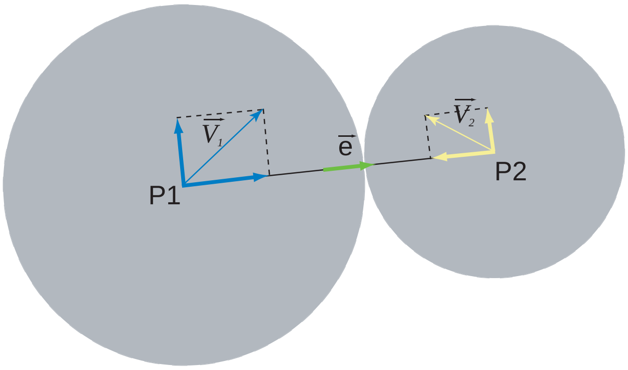

Fig. 6.3: Velocity vectors and unit vector of direction from the center of the particle 1 (P1) to particle 2 (P2)

where $\mathbf{e}$ is the unit vector in the direction of the collision line and scalar products $\mathbf{v}_1 \cdot \mathbf{e}$ and $\mathbf{v}_2 \cdot \mathbf{e}$ are the projection of $\mathbf{V}_1$ and $\mathbf{V}_2$ to the direction of collision line. C_R is the restitution coefficient. Assuming the energy is conserved (elastic collision), we apply restitution coefficient $C_R = 1$[1] The velocity vector along the collision line $\mathbf{V}_{1p}$ and $\mathbf{V}_{2p}$ are obtained by multiplying with unit vector.

$$\begin{aligned} \mathbf{V}_{1p} &= V_1' \cdot \mathbf{e} \\ \mathbf{V}_{2p} &= V_2' \cdot \mathbf{e} \end{aligned} \tag{6.8}$$

In the orthogonal direction of the collision line, the magnitude of velocity does not change before and after the collision.

$$\begin{aligned} \mathbf{V}_{1o} &= \mathbf{V}_1 - (\mathbf{V}_1 \cdot \mathbf{e})\,\mathbf{e} \\ \mathbf{V}_{2o} &= \mathbf{V}_2 - (\mathbf{V}_2 \cdot \mathbf{e})\,\mathbf{e} \end{aligned} \tag{6.9}$$

By substituting eq. (6.7),(6.8) and (6.9) into eq. (6.6), the velocity after the collision is obtained.

6.3 Result

In this section, the parameters of our model are defined. All parameters are summarized in Table 6.2. As the value of most parameters are not exactly clear and only the range of values is known, Gaussian or uniform distribution is applied to most of parameters and the values of parameters are automatically defined by simulator using random generator. Ejection position $\mathbf{r}_e$, burst time t_b, ejection velocity $\mathbf{v_e}$ and particle properties are defined to start simulation (Fig. 6.4). As it is declared in "Particle" list (Algorithm 5), particle properties are density ρ_p and diameter D. The ejection velocity $\mathbf{v_e}$ is identified by the magnitude of velocity v and its direction which is drawn by three angles; rotation angle γ, inclination angle θ and azimuth angle ϕ.
At first the velocity vector $\mathbf{V}$ (velocity vector without rotation of axis) is drawn by using spherical coordinate (Fig. 6.5 a).

$$\mathbf{V} = \begin{pmatrix} V_{ex} \\ V_{ey} \\ V_{ez} \end{pmatrix} = \begin{pmatrix} v \sin\theta \cos\phi \\ v \sin\theta \sin\phi \\ v \cos\theta \end{pmatrix} \tag{6.10}$$

---

[1] The possibility another value of restitution coefficient is discussed in the section 6.4.3.

Table 6.2: Parameter notation, range, distributions and inputs. μ represents average and σ represents standard deviation. $N(\mu,\ \sigma)$ indicates normal (=Gaussian) distribution defined by the mean μ and the standard deviation σ. $u(min,\ max)$ indicates uniform distribution between the minimum *min* and the maximum *max*.

Parameter	**Notation**	**Range**	**Distribution**	**Input**
Particle density (kg/m^3)	ρ_p	$\rho_p \in [0, \infty]$	$\rho_p = \mathcal{N}(\mu_{\rho p}, \sigma^2_{\rho p})$	$\mu_{\rho p}$,$\sigma_{\rho p}$
Particle diameter (m)	$D = 2R$	$D \in [0, \infty]$	$D = \mathcal{N}(\mu_D, \sigma^2_D)$	μ_D,σ_D
Magnitude of Initial velocity (m/s)	$v = \lvert\mathbf{v}_e\rvert$	$v \in [0, \infty]$	$v = \mathcal{N}\left(\mu_v, \sigma^2_v\right)$	μ_v, σ_v
Rotation angle (*degree*, rotation from vertical axis)	γ	$\gamma \in \left[0, \frac{\pi}{2}\right]$	*Deterministic*	γ
Inclination angle (*degree*, from vertical axis)	θ	$\theta \in \left[-\frac{\pi}{2}, \frac{\pi}{2}\right]$	$\theta = \mathcal{N}\left(\mu_\theta, \sigma_\theta\right)$	σ_θ
Azimuth angle (*degree*)	ϕ	$\phi \in [0, 2\pi]$	$\phi = \mathcal{U}(0, 2\pi)$	-
Displacement of ejection points from the vent center (m)	$\mathbf{r}_e = \begin{pmatrix} x_0 \\ y_0 \\ 0 \end{pmatrix}$	$x_0 \in [0, \infty]$, $y_0 \in [0, \infty]$	$x_0 = \mathcal{N}(\mu_r, \sigma^2_r)$ $y_0 = \mathcal{N}(\mu_r, \sigma^2_r)$	σ_r
Number of particles per burst	N_P	$N_p \in [0, \infty]$	$N_p = \mathcal{N}(\mu_{N_P}, \sigma^2_{N_P})$	μ_{N_P}, σ_{N_P}
Time interval between bursts (s)	Δt_b	$\Delta t_l \in [0, \infty]$	$\Delta t_l = \mathcal{N}(\mu_{\Delta t}, \sigma^2_{\Delta t})$	$\mu_{\Delta t}$, $\sigma_{\Delta t}$

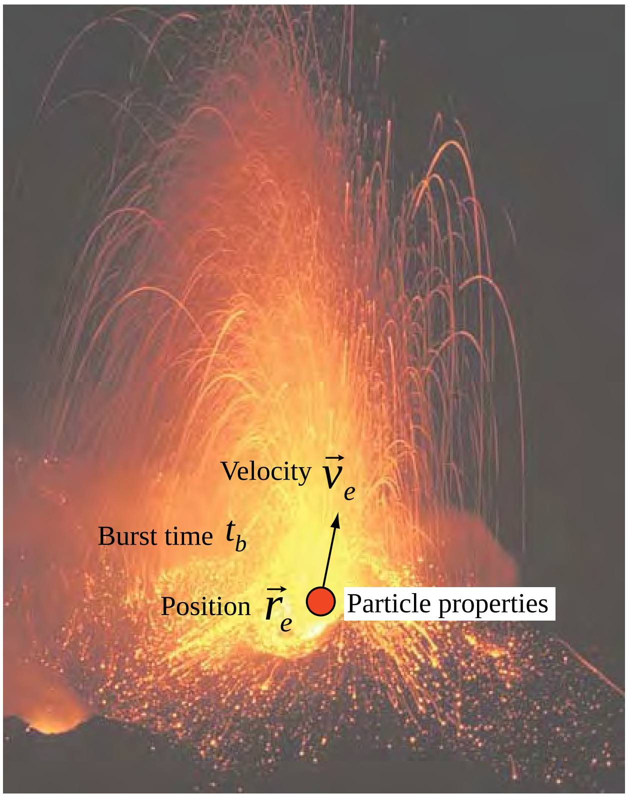

Fig. 6.4: Initial condition of simulation for ballistic trajectories. (Photo is taken from http://www.swisseduc.ch/stromboli/volcano/photos/photo0908-en.html?id=2, Last visit: 30 September 30, 2011)

As particles ejected for any direction around the z axis, angle ϕ is chosen from the uniform distribution in the range of 0 to 2π and this parameter is automatically defined by the simulator. On the contrary, inclination angle is chosen from the Gaussian distribution with the average 0 and standard deviation σ_θ.

The ejection direction is sometimes inclined depending on the vent or conduit shape. Thus, the velocity vector drawn around z axis is rotated around the y axis with the rotation angle γ and we obtain vector of ejection velocity $\mathbf{v}_e$ (Fig. 6.5 a).

$$\mathbf{v}_e = \begin{pmatrix} v_{ex} \\ v_{ey} \\ v_{ez} \end{pmatrix} = \begin{pmatrix} V_{ex}\cos\gamma + V_{ez}\sin\gamma \\ V_{ey} \\ -V_{ex}\sin\gamma + V_{ez}\cos\gamma \end{pmatrix} \tag{6.11}$$

This rotation angle γ is deterministically given based on observations. (Table 6.2).

An ejection position of each particle $\mathbf{r}_e$ is defined by the displacement from the vent center. Since the vent of volcano has area, the ejection position $\mathbf{r}_e$ has x and y components and each component can take the different distribution.

In our model, several particles are launched at the same time and several burst can occur. To describe series of bursts, the number of particles per burst N_P , burst time interval (BTI)Δt_b and the duration of bursts T_b are given as input parameters. The values of N_P can be different for each burst and it is chosen from a Gaussian distribution with average μ_{Np} and standard deviation σ_{Np}. Each burst time t_b is defined by the simulator according to the BTI Δt_b(Fig. 6.5 b) and BTI is also chosen from a Gaussian distribution with $\mu_{\Delta t}$ and$\sigma_{\Delta t}$. The duration of bursts is deterministically given by user.

Values of input parameters are shown in Table 6.3. These values are defined for our statistical analysis from the Stromboli 2008 eruption (Vanderkluysen et al., in Prep).

To study the effect of each parameter, it is possible to use a constant value by setting the standard deviation 0.

6.3.1 Qualitative results

This model can simulate eruptions with or without collision. To simulate the eruption without collision, the simulator ignores collisions even when the particles are close enough to collide (Fig. 6.6 a). For an eruption with collision, the simulator takes account of collisions between particles and calculates velocity change when collision occurs (Fig. 6.6 b). Generally, trajectories of particle of the collision-allowed case show a wider expansion than that of no-collision allowed case.

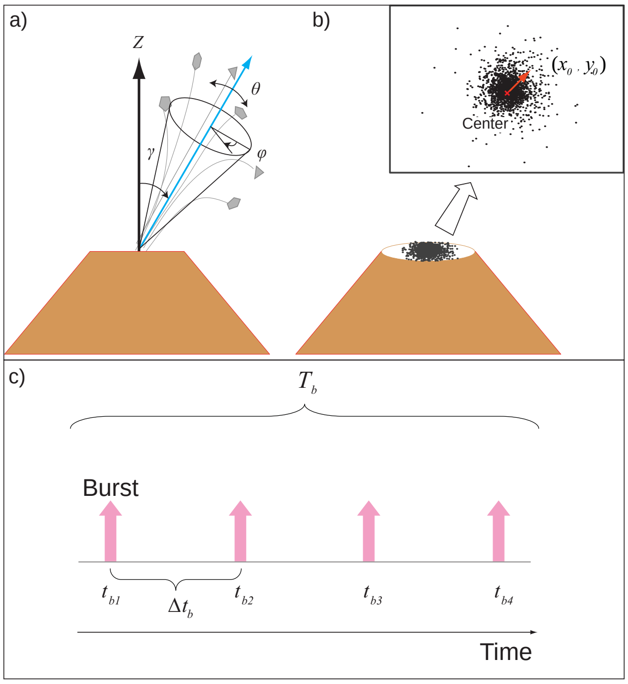

Fig. 6.5: Input parameters. a) Axis angle (γ) and deviation angle (θ). b) Displacement of ejection point from the vent center $r_e = (x_0, y_0, 0)$. c) Total time (T_t) and time of launching (t_{b1}, t_{b2}, t_{b3},...). Δt_l is the interval between launch times. For example, time between t_{b1} and t_{b2} is $\Delta t_{b1} = t_{b2} - t_{b1}$.

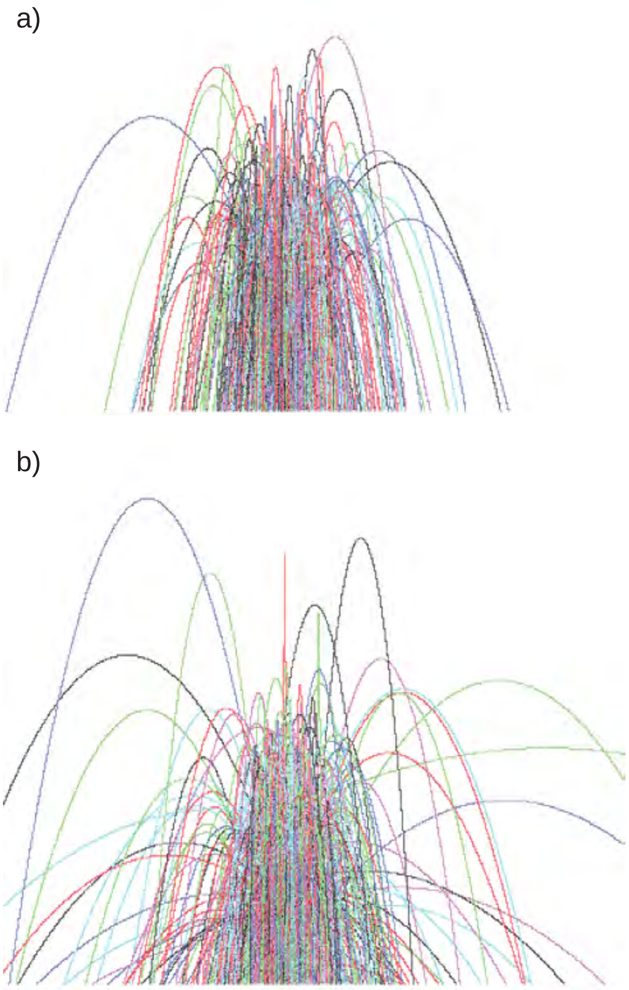

Fig. 6.6: Illustrations of the ballistic trajectories of 1000 particles for a) an eruption with collision and b) an eruption without collision. Color variation shows particle difference.

Table 6.3: Basic values of input parameters for our analysis (Vanderkluysen et al. in Prep.).

Parameter	**Unit**	**Input**	**Value**
Particle density	kg/m^3	$\mu_{\rho p}$ $\sigma_{\rho P}$	1450 500
Particle diameter	m	μ_D σ_D	0.5 0.3
Magnitude ofinitial velocity	m/s	μ_v σ_v	40 10
Standard deviation of inclination angle	$degree$	σ_θ	5
Rotation angle	$degree$	γ	0
Displacement of ejection points from the vent center	m	σ_r	10
Number of particles per launch		μ_{Np} σ_{NP}	20 0
Time interval between launches	s	$\mu_{\Delta t}$ $\sigma_{\Delta t}$	0.1 0
Total launch time	s	T_l	10

Deposition points on the ground are recorded for all particles. To compare the deposition of collision-allowed case and no-collision allowed case, deposition points are plotted in the same figure (Fig. 6.7). In this simulation, particle diameter is set to 1m for all burst particles. Particles in the collision-allowed case have wider distribution than those in the no-collision allowed case. Most of particles that collided in the simulation deposit farther than those which did not collide. However, it can not be quantified from the plot. To evaluate the difference quantitatively, statistical analyses are applied.

Initial condition changes even if the same input parameters are given because the simulator randomly build the intial condition from the Gaussian distribution. Therefore, with the same value of input parameters, the simulation repeated 10 times for each set of input parameters and the average deposition distance is extracted.

In statistical analysis, we count how many collisions occurred in one simulation. We measure deposition distance where 50 %, 75%, 90% and 99% percentiles of particles (Fig. 6.7). Each circle with the number of percentile in Fig. 6.7 shows the distance where the percentage of particles is included inside.

Deposition distances of 50 %, 75%, 90% and 99% percentile are compared 6.8

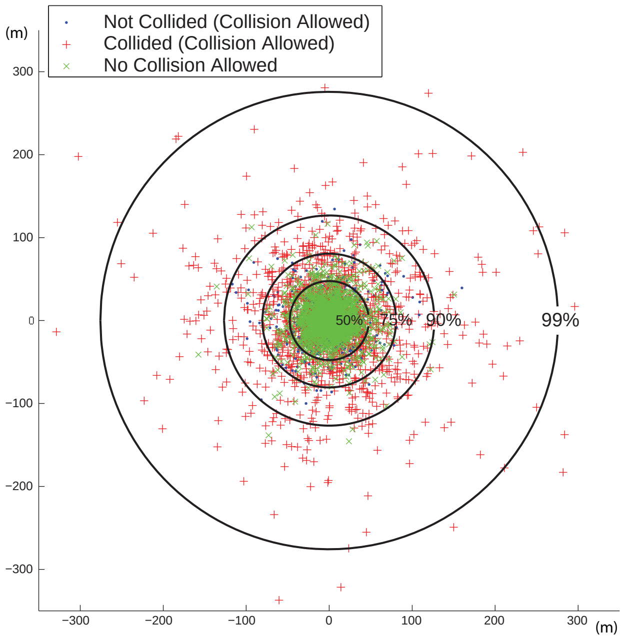

Fig. 6.7: Distribution of deposit particles. (Particle Diameter = 1m, 2000 particles). Every single point corresponds to a deposition point of a single particle. Numbers in the figure show the percentage of number of particles deposited in the circle. The radius of these circles is shown as a deposition distance of 50%, 75%, 90% and 99% percentile in results of statistical analysis. Green crosses are the deposition points of the particles in the case of no-collision-allowed simulation. Blue dots are deposition points of the particles which are not collided even if the collision is allowed in our simulation code. Red crosses are deposition points of the particles which are collided in the case of collision allowed simulation.

between collision-allowed case and no-collision-allowed case (Fig. 6.7). Even though the time interval of bursts changes, deposition distances do not change if a collision does not occur. On the other hand, the deposition distance of the collision-allowed case changes.

6.3.2 Collision Effect

To study how parameters affects deposition distance and collision occurrence, we have done statistical analysis for each parameter. Results of the analysis with different parameters show some influence of collisions on the deposition distances (Appendix C). Through these analyses, we have identified parameters which are effective for the probability of collision and the travel distance of particles. These results are presented as follows.

Total number of particles The role of total number of particles is considered because this parameter is important when collisions are included. Besides, it has not been verified quantitatively so far. Collision number increases with the particle number (Fig. C.1 in Appendix). The deposition distance of an eruption with collision increases with the particle number, while the deposition distance of an eruption without collision does not change. The difference of deposition distance between two cases is maximum for 99% number of particles.

Burst time interval Burst time interval is also important when collision can occur. Deposition distance of collision-allowed case decrease with the time interval while deposition distances of no-collision-allowed case do not change with the time interval (Fig. 6.8 a). Around 10 seconds of interval, the deposition distances of no-collision allowed case and collision-allowed case become almost same. Total number of collisions decreases with the time interval (Fig. 6.8 b). Collisions possibly occur in between particles in different groups which have burst at the different times. The number of collisions in different groups is shown in Fig. 6.8(b). The number of collisions in different groups decreases as the time interval increases. The curve of total number of collision is similar to that of the number of collisions in different group.

Efficient collision to transport particles farther In order to find a condition of efficient collision to make the deposition distance longer, the trajectories of collided pair are illustrated. Especially, a pair of particles which travels farthest among the particle burst in one simulation is chosen (Fig. 6.9). By repeating this kind of illustration, we noticed:

1) A particle which travel farthest collides only once or twice.

2) Difference in particle mass is always large for the pair of particles one of which travels farthest.

According to these two points, we have analyzed (1) the relationship between the number of collisions and the deposition distance for each particle and (2) the relationship between particle mass and the reposition distance.

Collision number and mass for each particle The relationship between number of collisions and deposition distance for each particle is shown in Fig.6.10. The deposition distance decreases as the number of collisions increases and a particle travels farthest only when it collides one time. Particles that collide more than 10 times do not go farther than 200m.

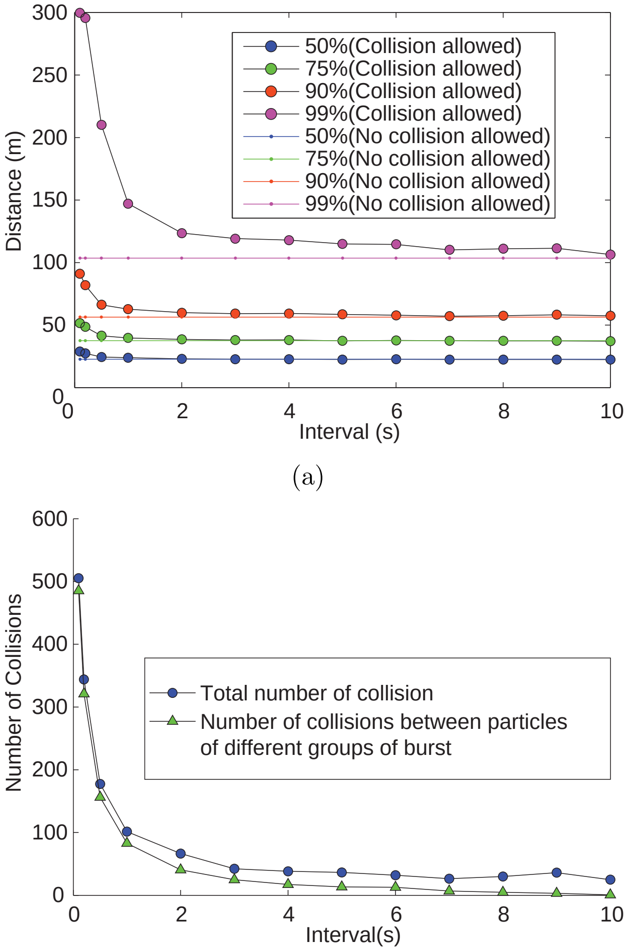

(a)

(b)

Fig. 6.8: (a) Deposition distance versus burst time interval. and (b) Number of collisions versus burst time interval.

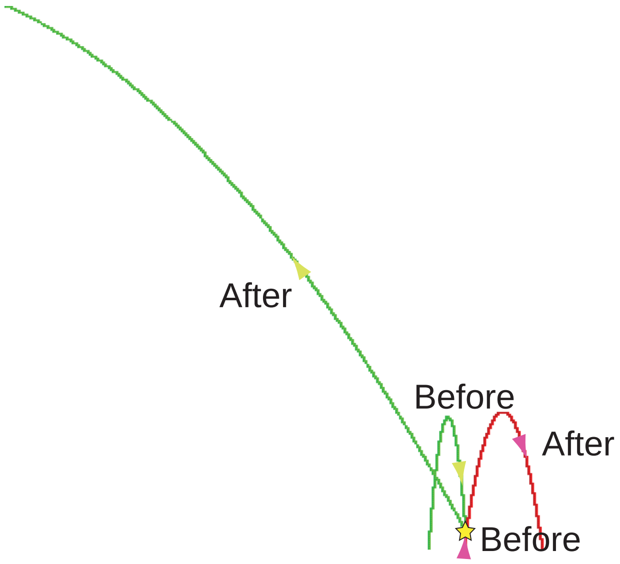

Fig. 6.9: Illustration of trajectories for two-particle collision. Green trajectory is a trajectory of a particle with mass of 2.8 kg, and red trajectory is a trajectory of a particle with mass of 99.9kg. The particle of green trajectory had a velocity of 34.3m/s before the collision and 94.2m/s after the collision. The particle of red trajectory had a velocity of 38.4m/s before the collision and 37.9m/s after the collision.

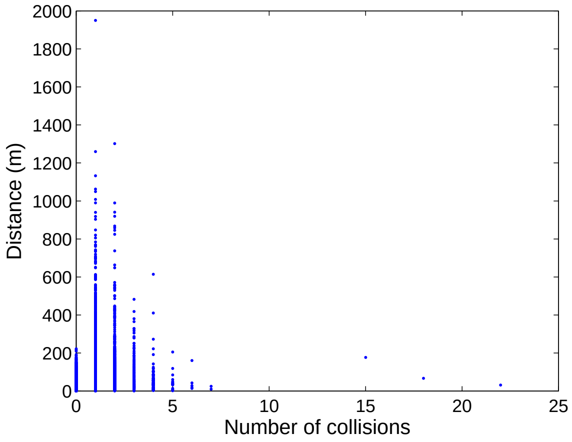

Fig. 6.10: Deposition distance versus number of collisions experienced during one simulation by each particle. The results of ten times simulation are all plotted.

The relationship between particle mass and deposition distance for each particle is shown in Fig.6.11. The deposition distance decreases with particle mass.
Both results are simulated with the input parameters shown in Table6.5 and the results of ten times simulation are all plotted in one graph. The particle that traveled the farthest has collided only one time and has a mass 1.9kg. Travel distance is 1900 m.

6.4 Discussion

We have developed a new model of ballistics based on three dimensions obtained by applying the discrete event method (DES) and taking into account the collisions between particles. The trajectory of particles is calculated fully analytically in between events (See section 6-2: model). The existing models of simulating ballistic trajectory of volcanic eruptions did not include interactions between particles (Wilson,1972 [133]; Fagents and Wilson, 1993 [46]; Ripepe et al., 1993 [94]; Bower and Woods, 1996 [18]; Mastin, 2002 [73]; Alatorre-Ibarguëngoitia and Delgado-Granados, 2006 [1]; Saunderson, 2008 [98]), while our model includes the collisions between particles. Some papers cite ejection velocities of ballistics which are inversely calculated from the deposition distance by assuming the particle has not experienced collision during the flight in the air (e.g. Rosi et al., 2006 [97]; Write et al., 2006 [142]). However, our study shows that the deposition distances are af-

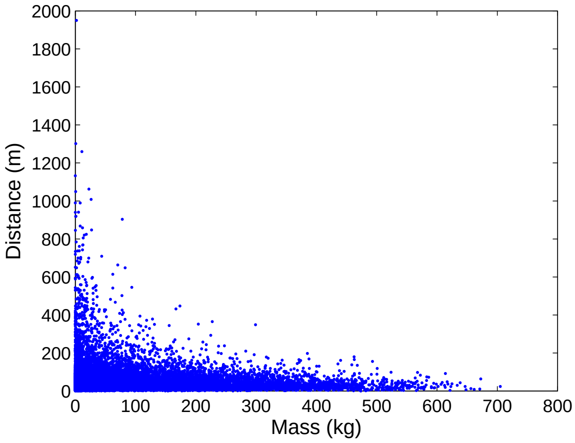

Fig. 6.11: Deposition distance versus mass of each particle during one simulation. The results of ten times simulation are all plotted.

fected by the collision between particles. Therefore, it is important to study what controls the collision between particles and how it affects the deposition distances of ballistics.

6.4.1 Characteristics of this model

The implementation of a model with collisions based on DES is faster than a model based on the continuous time system. The time complexity is highly depend on the number of collision checks. In the models based on the continuous time simulation, the number of collision checks is

$$C_{c\_continuous} = \frac{N\left(N-1\right)}{2} \cdot \frac{T}{\Delta t} \tag{6.12}$$

.

where N is the total number of particles, T is the total simulation time and $\Delta t$is the time step. The collisions must be checked at each time step for each particle pairs. Eventually, the order of time complexity of the model based on continuous system is $O\left(N^2 \frac{T}{\Delta t}\right)$. In the model based on DES, the number of collision checks depends on the event type. For each **Burst** event, the collision checks is done inside a group of bursting particles, then between the bursting particle and airborne particles. Assuming the number of particles per **Burst** is constant, the number of collision checks is

Table 6.4: The number of collision checks in one simulation

	DES	**Continuous System**
Burst	$b\left(\frac{n_b(n_b-1)}{2}+n_b\left(N-n_b\right)\right)$	$\frac{N(N-1)}{2}\cdot\frac{T}{\Delta t}$
Collision	$2c(N-2)$	
Deposit	-	
The order of time complexity	$O\left(cN\right)$	$O\left(N^2\frac{T}{\Delta t}\right)$

$$C_{c\_burst}=b\left(\frac{n_b\left(n_b-1\right)}{2}+n_b\left(N-n_b\right)\right) \tag{6.13}$$

where, b is the number of bursts, n_b is the number of particles in each **Burst** event. The first term in parenthesis is the number of collision checks in the same **Burst**. The second term in parenthesis is the number of the collision checks between the burst particles and airborne particles. For each **Collision** events, the collision check is done between colliding pair of particles and the others. Thus, the number of collision checks is $2(N-2)$ multiplied by the total number of collisions c.

$$C_{c\_DES}=2c(N-2) \tag{6.14}$$

The collision is not checked in the **Deposit** events because particle does not collide with other particles anymore.

Assuming the number of the **Burst** events is much less than that of the **Collision** events, the order of time complexity of the model based on DES is $O\left(cN\right)$. Comparing the time complexity of two models, the time complexity of DES based model is much less than the model based on the continuous system as the time steps has to be small enough to detect the collision and the iteration number of the continuous system $T/\Delta t$ is larger than collision number c. For example, if we consider the time step Δt of continuous system has to be smaller than a period for a particle traveling the distance which is 0.1 of particle diameter for not missing the collision, Δt is follows

$$\Delta t<\frac{0.1D}{v_{fastest}} \tag{6.15}$$

.

Therefore, we can conclude the time complexity of DES based model is smaller than that of the continuous system. The number of collision checks is summarized in Table 6.4. Comparison of the number of collision checks of DES and continuous time system are in Appendix B.

6.4.2 Controlling parameter of collision probability and deposition distances

The model is applied to simulate the ballistic trajectory and the collisions between particles. By the numerical experiment, we have clarified the parameter controlling the collision probability and its influence of travel distance. Here, we discuss the factors which increase collision number. The collisions can either increase or decrease. We also discuss how the collision number effectively increases the travel distance of a particle.

According to the results of analysis (Appendix C), collision number largely changes when the number of particles vary. It is intuitively understandable that the particles have more possibility to collide with other particles when particle concentration in the air is large. Then we are also interested in what kind of collision makes the deposition distance longer and what is the controlling parameter for collision probability and deposition distances.

Time interval is focused as it changes with the eruption style. Strombolian eruption consists of short-lived discrete events (Chouet et al., 1974 [32]; Blackburn et al., 1976 [9]; Patrick et al., 2007 [84]).

Our model can simulate several bursts and the period between different bursts is the time interval. According to the result of our analysis of the time interval, both collision number and deposition distance increase as the time interval decreases. This implies that the collisions between particles in the different group of burst occur when the time interval is shorter than the travel time (a period when particles travel in the air from the ejection point to the ground) of the particles in the first group of burst arriving at the ground.

In our analysis, we choose an average of ejection speed v_e =40m/s and the deposition time of the particle with this v_e is expected to be $t_d = \frac{2v_e}{g} =$ 8.15s in average. In Fig. 6.8, the difference of the distance between collision-allowed case and no-collision-allowed case becomes almost 0 at 10s of the time interval. 10s and 8.15s is not exactly the same, but considering the ejection velocity is drawn with Gaussian distribution, the ejection velocity can be larger than 40m/s and the deposition time sometimes can reach 10s. Therefore, the time interval affects collision probability and it becomes almost 0 when the time interval is a little larger than the average of deposition time.

Some study reported the frequency of eruption but not focusing on the ballistics. Ripepe et al., (1993) [94] reported the mass flux change as a function of time of an eruption in Stromboli volcano (Fig. 6.12). It simulates a kind of the changes in time interval. If these peaks of pulses are the time of burst, burst time interval of ballistics in Stromboli 1985-1986 eruption is around 0.5-2.0 seconds. This is clearly shorter than the travel time when the particle ejected with an initial velocity 40 m/s in average according to our analysis

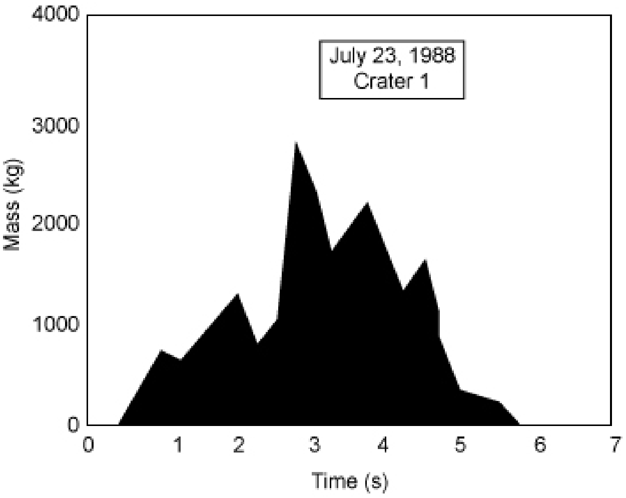

Fig. 6.12: An example of mass flux diagrams reconstructed from the observation of eruption (Modified from Ripepe et al., 1993 [94] Fig.5 a).

on burst time interval (Fig. 6.8). Therefore, it is possible to have collisions. However, these pulses are expressed with mass (Fig. 6.12), and we cannot recognize each particle. More precise observation is required to recognize the time interval for each particle.

The differences in time interval reflect dynamics of conduit flow and magma fragmentation dynamics (Patrick et al., 2007 [84]; Ripepe and Harris 2008 [93]). However, there is no clear model to identify the time intervals from the dynamics of conduit flow and magma fragmentation. The study to identify the time interval from the dynamics of conduit flow and magma fragmentation is required

Another interesting point is whether the deposition distance of particles becomes longer or not, if the particles collide many times. Fig. 6.10 shows that particles deposit farther than 500m only experienced <6 times of collisions. On the contrary, particles with many collisions do not go far. According to Fig. 6.10, particles with more than 10 collisions travel less than 200m. This implies that only a few times of collisions are required to travel far.

If only a few collisions are enough for the longer deposition distance, what makes the particles travel further? To have a hint for the answer of this question, the illustration of the trajectories of a colliding pair of particles are shown in Fig. 6.9. This illustration of particle trajectories indicates that the particle travels further when two particles have a significant difference in mass. One particle travels very far when it collides with another particle which has much larger mass than itself because the larger particle gives much momentum to the smaller particle.

The relationship between the mass and the deposition distance is also investigated (Fig. 6.11). This shows that the particles with smaller mass are tend to travel further. Especially, particles travel $>$ 500m when they have mass $<$ 50kg. In other words, particles with mass $>$ 500kg stay within 100m from the vent. This result also supports the light particles travel further by receiving the large momentum from the heavy particles.

6.4.3 Caveats

Although this model is new and promising, there are some effects which are not included in this model; 1) drag force, 2)wind effect, 3) non-elastic collision and 4) realistic topography. We discuss here how the model can be improved.

Drag force In the isopleth map by Parfitt (1998), the larger particles deposit around the crater and the smaller particles deposit further from the crater. We have two possible factors to such separation; 1) collision between particles, 2) separation by drag force. Considering the wind existence, it is natural to assume that particles are also affected by the air drag.

Moreover, it is presented that the drag force has an important role in ballistics (Wilson ,1972; Fagents and Wilson, 1993; Bower and Woods, 1996; Mastin, 2001; Alatorre-Ibargungoitia and Delgado-Granados, 2006) and to include the drag force in our model is a first priority among the points to be improved.

Mastin, (2001) showed the equations of motion according to the drag force of Sherwood, (1967) which includes a constant drag coefficient C_d and air density ρ_a (eq. 12 of Mastin 2001). These partial differential equations are solved analytically about deposition distance x_d;

$$x_d = \frac{1}{\mu}\ln(\mu v_e \cos\theta t_d + 1) \tag{6.16}$$

$$t_d = \left[\cosh^{-1}\sqrt{1+\frac{\mu}{g}v_e^2\sin^2\theta} + tan^{-1}\left(\sqrt{\frac{\mu}{g}}v_e\sin\theta\right)\right] \tag{6.17}$$

where $\mu = \rho_a C_d A/2m$, ρ_a is the density of the ambient air, A is cross-sectional area of a particle and θ is an ejection angle from the horizontal direction. As the trajectory is written analytically, it is possible to apply DES for the model.

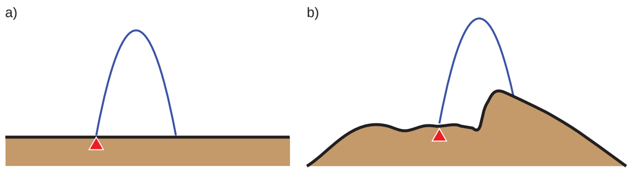

Fig. 6.13: Parabolic trajectories for a) flat and b) non-flat case. Blue lines are the trajectory of particles. Red triangles show the ejection positions.

Wind effect As it is discussed, wind and air drag have a strong relationship. If the wind velocity is the same as the velocity of a particle, the drag force does not affect the movement of the particle. In this case, the velocity difference between wind and particle $\mathbf{v}_{diff} = \mathbf{u}_{wind} - \mathbf{u}_p$ can be substituted into the equation of motion with drag force eq. (6.1). If the wind is not very strong, particles are not affected by the wind. Especially, when the mass of particle is large, the wind effect can be possibly ignored because the acceleration is the force divided by the mass.

Non-elastic collision We have assumed that the collision is elastic, but we do not know if the collisions are elastic or non-elastic. For example, if a particle breaks when it collided with another particle, the energy is not conserved. Also we observe aggregated particles and deformed particles in the field. If we know the restitution coefficient C_R, we can calculate the velocity after the collision from the eq. (6.6). However, the collision in ballistics of volcanic eruption has not been clearly observed. Then, the value of C_R is not restricted. More field and experimental observations are needed.

Realistic topography In this model, we assume that the ground where particles deposit is flat for simplicity. However, deposition distances of particles are affected by the topography. Thus it is a high priority to include the topographic effect in this model. The DES is applicable to our model because the trajectories between events are described analytically. In case the ground is flat, we can analytically calculate the deposition distance because we know the deposition height (Fig. 6.13 a). In case the ground is not flat, we do not know the height of deposition and it has to be checked step by step (Fig. 6.13 b). For this check, we have to use the differential equation with constant time step (Δt) and grid size (Δx) instead of analytical solution. It means that the time complexity is much larger than the DES method only without Δt and Δx. To compromise between the request of the computation speed and the topographic effect, we approximate the ground shape as a geometric shape such as a cone or plane. Then, we project the point on the interpolated shape to the real point on the ground. For instance, assuming the topography is conical shape, the relationship between distance from the center and the height of ground is

$$H = ar \tag{6.18}$$

r is the distance from the center point (the center of the crater), H is the topographic height and a is the inclination of the slope of conical shape.
The equation of trajectory for vertical (z) direction r_z is obtained by solving the eq. 6.1 with initial velocity component v_z and with initial height o_z.

$$r_z = -\frac{1}{2}gt^2 + v_z t + o_z \tag{6.19}$$

As the ground is inclined, according to the equation 6.18.

$$r_z = ar \tag{6.20}$$

r is expressed with the coordinate of x and y.

$$r = \sqrt{x^2 + y^2} = \sqrt{v_x^2 t^2 + v_y^2 t^2} = t\sqrt{v_x^2 + v_y^2} \tag{6.21}$$

By submitting 6.21 into 6.20, and connecting 6.19 and 6.20, we obtain the equation to solve.

$$-\frac{1}{2}gt^2 + v_z t + o_z = at\sqrt{v_x^2 + v_y^2} \tag{6.22}$$

Rearranging this equation in the respect of time t,

$$-\frac{1}{2}gt^2 + \left(v_z + a\sqrt{v_x^2 + v_y^2}\right) t + o_z = 0 \tag{6.23}$$

This quadratic equation can be solved similarly to the equation of deposition (eq. in section of method).
To have more precision, we can project the trajectory of the particle from the point on the conical shape to the point on the real ground. There are mainly three methods to project the trajectory;

1)Vertical projection is to vertically project the deposition point on the conical shape and only estimate the deposition height (Fig. 6.14 A).

2)Linear projection is to project the deposition point by extending the tangential line and estimate deposition point by calculating cross point of linear and the local topography (Fig. 6.14 B).

3) continuing the parabolic trajectory(Fig. 6.14 C).

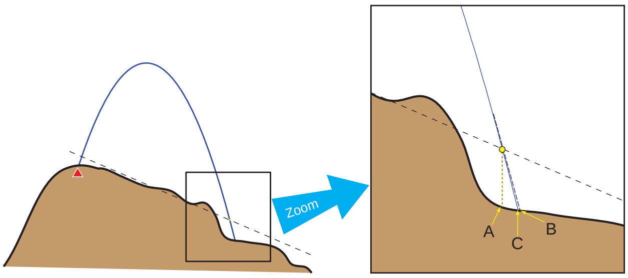

Fig. 6.14: Three types of projection to estimate deposition point in the case of taking account of realistic topography. Red triangle shows the ejection position. Yellow dot shows where the parabola crosses with the line expressed with 6.18.

For the linear projection, we need to apply the continuous time method with constant time step Δt and grid size Δx only to the calculation from the point on the conical shape to the real point. Continuing the parabolic trajectory is also calculated by the continuous time method. Alternatively, bisection method can be used to define the projection point.

6.5 Conclusion

We have implemented three-dimensional ballistic simulations including collision effect. From our analysis of simulation results, we conclude:

1. Collision probability is controlled by time intervals of launch. Most collisions happen between particles ejected in different burst.
2. Only few collisions are enough and necessary to increase travel distance.
3. Collisions can either increase or decrease with travel distance. Only a few collisions are required for particles to travel farther.
4. Mass difference makes particles travel farther due to collision. When the particle mass of collided pair is different, a lighter particle receives larger momentum by a heavier particle.
5. DES model for ballistics is more efficient than a model based on continuous system because of its fast computation

Appendix B

Comparison of number of collision checks

In chapter 6, we have discussed the collision check of our model with Discrete Event Method (DES) is less than continuous time system. Here, the proof of the statement that the number of collision check in DES is less than number of collision check in continuous time system is presented.

Continuous time System Every pair of particles is checked for each time.

$$\frac{N^2 - N}{2}$$

where, N is number of all particles.

Discrete Event Simulation Bursting particles and particles in the air are recognized,

$$\frac{n_b(n_b - 1)}{2} + n_b(N - n_b)$$

where, n_b is number of burst particles Supposing number of checks for continuous system simulation is larger than the numer of DES, following inequation is possibly prooven.

$$\frac{N^2 - N}{2} \geq \frac{n_b(n_b - 1)}{2} + n_b(N - n_b)$$
$$N^2 - N \geq n_b(n_b - 1) + 2n_b(N - n_b)$$
$$N^2 - (2n_b + 1)N + n_b(n_b + 1) \geq 0$$

The solution which satisfy this inequality is

$$N \leq n_b, N \geq n_b + 1$$

.

As n_b and N is positive integer and the N between n_b and $n_b + 1$ does not exist. It means inequality is always true. Therefore, $\frac{N^2-N}{2}$ is always larger than $\frac{n_b(n_b-1)}{2} + n_b(N - n_b)$.
Q.E.D

Appendix C

Report of parameter work of ballistic model

C.1 How to detect the parameter effect

To investigate the effect of parameters, I focused on following six parameters.

1. Total Particle Number
2. Launching Source
3. Particle Diameter
4. Rotation angle
5. Inclination angle
6. Launching Interval

The detail of parameters is in each section. General explanation about input parameters and calculations are;

- Input parameters are set by Gaussian distribution. Our code picks up one value from Gaussian distribution for each particle and each launch. However, for detecting the effect of the parameter, the value is fixed for focused parameters.
- With these parameters, *Number of Collisions* is measured to see how the parameters affect collisions. *Deposition Distance* of collision allowed case and no collision allowed case is measured to see how the collisions make the difference of deposition distance.
- Simulations are implemented with fixed 500 particles and 2000 particles except the investigation of total particle number. In some cases, 5000 particles case is also implemented.

- For each initial condition, 10 times of the simulation were repeated to analyze statistically. Averages of the simulations are plotted in the graphs of *Number of Collisions* and *Deposition Distance.*

- In the plots of *Number of Collisions*, the error bars show the minimum and the maximum value of 10 times of simulation.

- Results of *Number of Collisions* are tried exponential and a power law fittings. Parabolic fittings are also tried for total particle number and rotation angle.

- To see the deposition distance of many particles statistically, the distances of 50%, 75%, 90% and 99% particles fallen on the ground (Fig. 6.7 in main text) are shown in the graphs of *Deposition Distance.* Moreover, deposition distances are shown with the case of "*collision allowed*" and "*no collision allowed*" to see how collisions affect the deposition distance. The difference of the deposition distance between collision allowed case and no collision allowed case shows the effect of collision.

- The simulations of "no collision allowed" case were implemented with Monte Carlo Method as the deposition distances of no collision case are analytically expressed.

C.2 Total Particle Number

As the total particle number controls the concentration of the particles in the air, the effect of Total Particle Number was investigated.
Initial conditions are shown in Table C.1. To fix the total particle number, time interval and the number of particles per launch are fixed. 2, 5, 10, 15, 20, 25, 30 particles per launch make total particle number 200, 500, 1000, 1500, 2000, 2500, 3000.

Discussion for total particle number Number of collisions increases monotonically as the total particle number increases (Fig. C.1). Power law fitting agrees well with the number of collisions and the factor is close to 2 (Table C.2). Therefore parabolic fitting is also tried.
As the collision probability depends on the particle concentration in the air, more collision happens when the particle number increase.
Deposition distance also increase as the total particle number increases when the collision is allowed in our simulation (Fig. C.2). When the collision is

Table C.1: Initial conditions of the simulation for detecting the effect of total particle number. * is changed parameter.

Parameter	**Mean**	**Standard Deviation**
Time interval between bursts (s)	0.1	0
Number of particles per launch	*	
Particle density (kg/m^3)	1450	500
Particle diameter (m)	0.5	0.3
Displacement of the ejection point relative to vent center (m)	0	10
Norm of initial velocity (m/s)	40	10
Deviation angle (degree, from vertical axis)	0	5.0
Total burst time (s)	10	

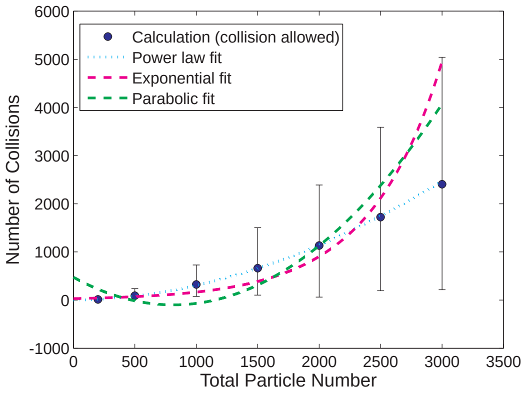

Fig. C.1: The effect of total particle number on number of collisions. Average of ten calculation results are shown in circles, with error bars which shows the range of these calculation results. Power law, exponential and parabolic fittings are tried.

Table C.2: Equations of power law, parabolic and exponential fittings for the plots of number of collisions.

Power law fitting	Parabolic Fitting	Exponential Fitting
$y = 0.0006x^{1.9023}$	$y = 0.002x^2 + 0.109x - 19.855$	$y = 30.299\exp(0.0017)$

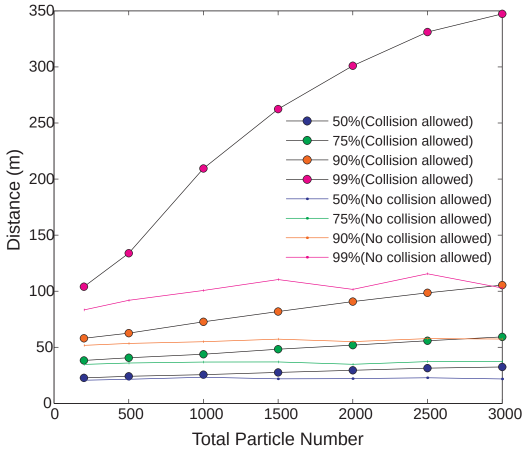

Fig. C.2: Changes in deposition distance of collision allowed case and no collision allowed case with total particle number.

not allowed during the calculation, the deposition distance does not increase with the total particle number. Distance related to the collision effect increase with the total particle number. Maximum difference is around 250m.
In short, total particle number affects the collision and the collisions make the deposition distance much farther.

C.3 Ejection points

As input parameters are defined by Gaussian distribution (Fig. C.3 (a)), each ejection point is chosen from the Gaussian distribution set by the value of mean and standard deviation. Considering the real volcanic setting, launching point has some range. Source of ejection which is called “vent” in the field is a collection of ejection points and the range of ejection area is controlled by the standard deviation of ejection points (Fig. C.3 (b)). Therefore, to see the effect of range of launching area, we have investigated the collision and the deposition distance when the standard deviation of the displacement of the ejection point relative to vent center.

Initial conditions are shown in Table C.3. 10m, 20m, 30m 40m and 50m of standard deviations of ejection points are used.

Discussion of ejection points Number of collisions decreases with the standard deviation of ejection points (Fig. C.4). When the launching source

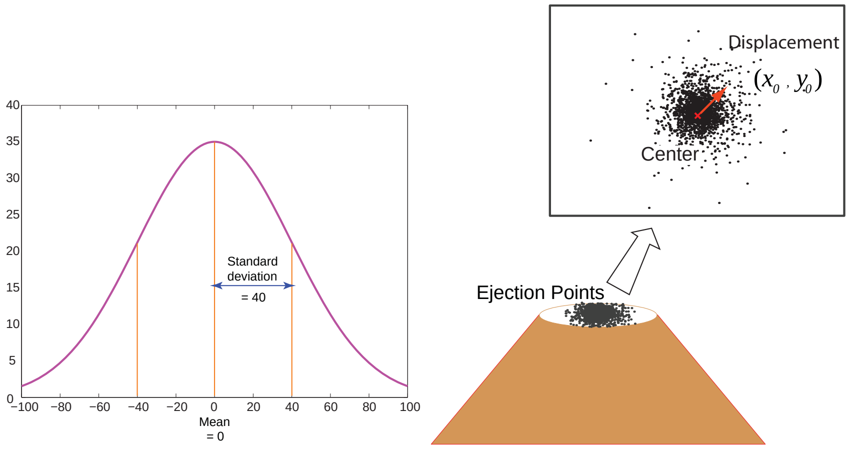

Fig. C.3: (a)Sample of Gaussian distribution with the sample value mean = 0 and standard deviation = 40. For ejection points, vertical axis expresses the number of particles burst at the ejection point. (b)Image of ejection points. At each time of burst, the ejection point is randomly chosen from the Gaussian distribution with mean = 0 (center of launching source) and variable standard deviation shown in following initial conditions.

Table C.3: Initial conditions of the simulation for detecting the effect of the range of launching source. * = 10m, 20m, 30m, 40m, 50m

Parameter	**Mean**	**Standard Deviation**
Time interval between bursts (s)	0.1	0
Number of particles per burst	5 /20	0
Particle density (kg/m^3)	1450	500
Particle diameter (m)	0.5	0.3
Displacement of the launch point relative to vent center (m)	0	*
Norm of initial velocity (m/s)	40	10
Deviation angle (degree, from vertical axis)	0	5.0
Total burst time (s)	10	

Table C.4: Equations of fittings of power law and exponential curves for the plots of number of collisions.

	Power law Fitting	Exponential Fitting
500P	$y = 9940x^{-1.8904}$	$y = 195.89\exp(-0.0763x)$
2000P	$y = 50665x^{-1.5955}$	$y = 1920.6\exp(-0.0643x)$

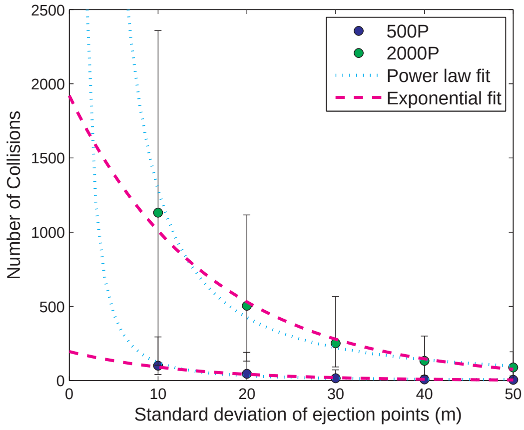

Fig. C.4: The effect of ejection points to number of collision. Average of ten-calculation results are shown in circles, with error bars which shows the range of these calculation results. Fittings are tried with power law and exponential curves.

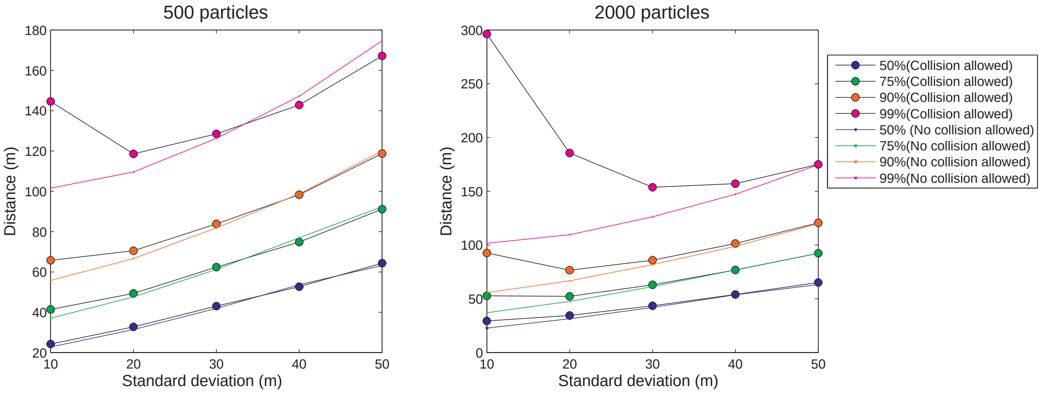

Fig. C.5: Changes in deposition distance of collision allowed case and no collision allowed case with the standard deviation of ejection points.

Table C.5: Initial conditions of the simulation for detecting the effect of the particle size. * = 10cm, 50cm, 100cm, 150cm, 200cm

Parameter	**Mean**	**Standard Deviation**
Time interval between bursts (s)	0.1	0
Number of particles per burst	5 /20	0
Particle density (kg/m^3)	1450	500
Particle diameter (m)	*	0
Displacement of the ejection points relative to vent center (m)	0	10
Norm of initial velocity (m/s)	40	10
Deviation angle (degree, from vertical axis)	0	5.0
Total burst time (s)	10	

becomes larger, particle concentration in the air decrease and the collision probability also decrease. This can be the reason of the monotonically descending curve. In this case, it is difficult to see which fitting agrees better with the plots.

Deposition distances of no collision allowed case increase as the standard deviation of launching source increases (Fig. C.5). This is because if the launching source is larger, the particle deposit farther even if the travel distance is the same.

Deposition distance of collision allowed case decreases once and again increase. This trend is much clearer in 90% and 99% of the deposition distance. When the launching source is smaller, the travel distance due to collision becomes longer. As the launching source becomes bigger, the results of collision allowed case and no collision allowed case becomes closer because of the collision effect decrease as shown in Fig. C.4

C.4 Particle Size

Particle size is the main factor changing the particle concentration in the air. It does not change the travel distance with no collision assumption.

Initial conditions are shown in Table C.5. To see the effect of particle size, particle diameters 10cm, 50cm, 100cm, 150cm, 200cm are used.

Discussion of particle size Number of collisions increases with the particle diameter increases. This is because the particle concentration in the air

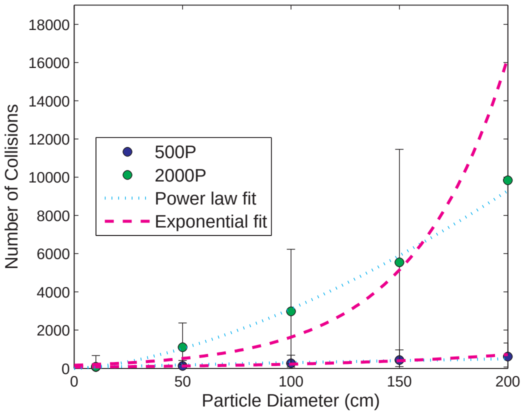

Fig. C.6: The effect of particle size to number of collision. Average of ten-calculation results are shown in circles, with error bars which shows the range of these calculation results. Fittings are tried with power law and exponential curves.

Table C.6: Equations of fittings of power law and exponential curves for the plots of number of collisions.

	Power law Fitting	Exponential Fitting
500P	$y = 9.8734x^{0.7403}$	$y = 66.76\exp(0.0119x)$
2000P	$y = 2.1428x^{1.5807}$	$y = 163.45\exp(0.023x)$

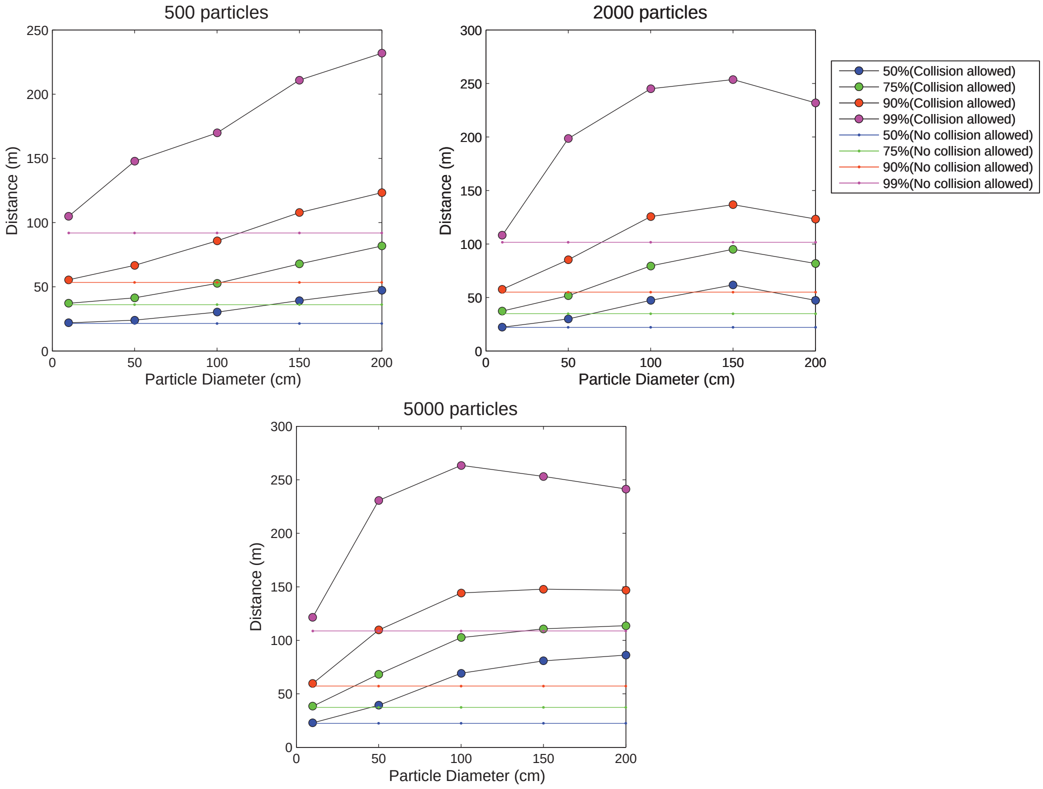

Fig. C.7: Changes in deposition distance of collision allowed case and no collision allowed case with the particle diameter.

increases when the number of particle increases.

Particle diameter does not change the deposition distance of the case of no collision allowed. Deposition distance of collision allowed case increases, but with 2000 and 5000 particles, it decreases again.

The distribution of deposit particles are looked in order to check the reason why deposition distance decreases though number of collisions increases (Fig. C.6). Not so many particles with many collision deposit in the center of the distribution in the case of 1m particles. However, the particles with many collisions deposit in the center are in the case of 2m particles. This means the particles moment is not used to disperse and collision make them stuck in the center are if the particle diameter is large. In fact, the condition of the decrease in the deposition distance is controlled by both particle diameter and the number of particles. As both particle diameter and the number of particles changes the concentration in the air, the concentration in the air must be a main parameter to control the deposition distance of the ballistic bombs.

I compare how many collisions does one particle experience between particle diameter 1m and particle diameter 2m (Fig. C.8). Many of them experienced only small number of collisions ($<$ 10 times of collisions). However several particles experienced many times of collisions. And the maximum number of collisions is larger in 2m particles than 1m particles. Collision affects the deposition distance of only a few numbers of particles, but the maximum deposition distance is changed by only these few number of particles.

Fig. C.9. shows the change in deposition distance as the number of collision increases. Maximum deposition distance decreases as the number of collisions increases in both the case with 1m particles and the case with 2m particles. This implies the particles with extremely many collisions are stuck around the center of launching source. Moreover the maximum deposition distance is made by only few numbers of collisions.

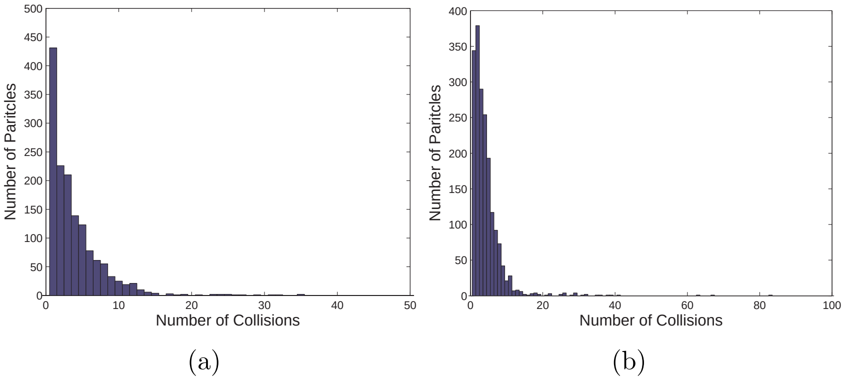

(a) (b)

Fig. C.8: Histogram of Collision number of only collided particle. (a) particle diameter = 1m, and 2000 particles, (b) particle diameter = 2m, and 2000 particles.

C.5 Rotation Angle

It is well known that the particle traveled farthest when it launched with the angle 45 degree. However, it is not clear how the angle of burst affects collision. In real volcanic situation, sometimes we observe the limited range of particle deposition (Fig. C.10 (a)). Therefore, we checked how number of collision and deposition distance is affected by the launching angle. In our code, the rotation angle is changed by rotating the vertical axis (Fig. C.10 b). Initial conditions are shown in Table C.7. Rotation angle is 0, 15, 30, 45, 60 degree.

Discussion of rotation angle Number of collisions is maximum when the axis angle is vertical because the particle launched vertical and they fall down vertically (Fig. 15). Collision decreases as the axis inclines. However, around 30 or 45 degrees, the trend of the collision number is not obvious. In fact the change of the value is much smaller than error value and it is difficult to see the trend. As it was not clear whether the collision number increases or decreases around 30 or 45 degrees, the calculation was implemented also with 5000 particles (Fig. 15 b). The trend is not clear with 5000 particles case, either.

Deposition distance increases as the axis angle increase until 45 degrees and later it decreases again for no collision allowed case (Fig. 16). For collision allowed case, the deposition distance is higher than no collision allowed case around 0 degrees. Later, it approaches to the result of no collision allowed case. This kind of feature is clear in 2000 particles and 5000 particles but it is not clear for 500 particles. It implies 500 particles are not enough to make

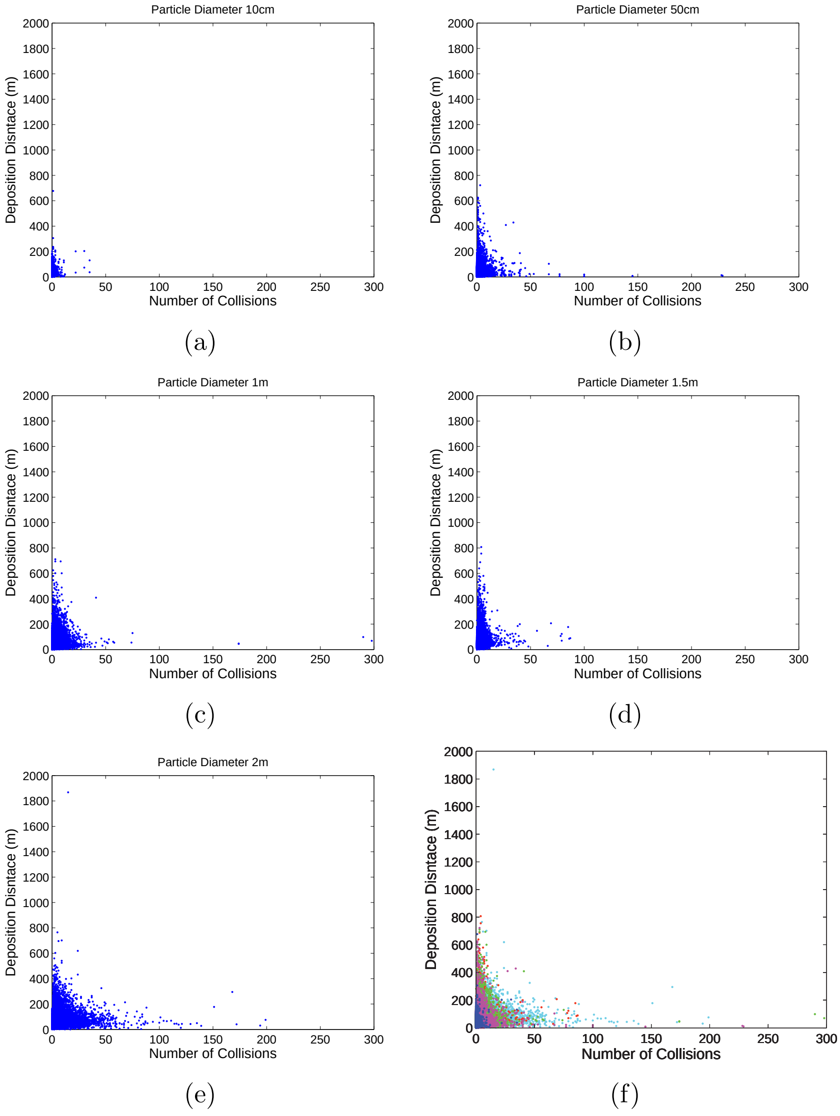

(a) (b) (c) (d) (e) (f)

Fig. C.9: Number of collisions and Deposition distance.

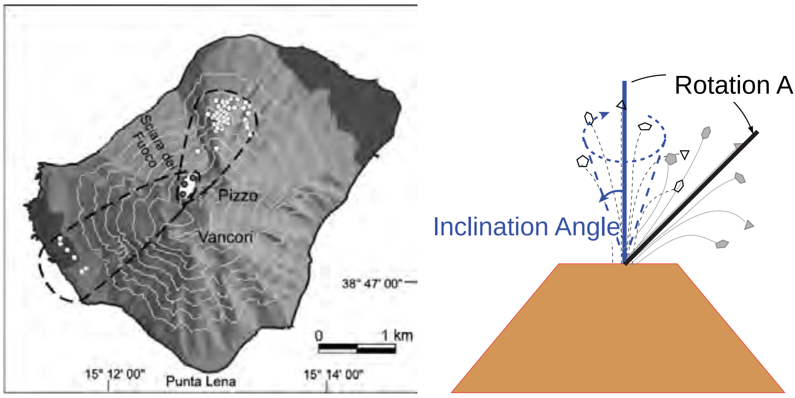

(a) (b)

Fig. C.10: (a) Distribution of impact crater observed on placeStromboli volcano (Rosi et al., 2006). (b) Image of the rotation of launching axis. Rotaion angle is an angle from the vertical axis.

Table C.7: Initial conditions of the simulation for detecting the effect of the rotation angle. * is changed parameter with 0, 15, 30, 45, 60 degree.

Parameter	**Mean**	**Standard Deviation**
Time interval between launches (s)	0.1	0
Number of particles per launch	5 /20	0
Particle density (kg/m^3)	1450	500
Particle diameter (m)	0.5	0.3
Displacement of the launch point relative to vent center (m)	0	10
Norm of initial velocity (m/s)	40	10
Deviation angle (degree, from vertical axis)	0	5.0
Total burst time (s)	10	
Rotation angle (degree)	*	

Table C.8: Equations of fittings of exponential fitting and parabolic fitting for the plots of number of collisions.

	Exponential fitting	Parabolic fitting
500P	$y = 70.818 \exp(-0.024x)$	$y = 0.0214x^2 - 2.2145x + 80.909$
2000P	$y = 878.25 \exp(-0.0147x)$	$y = 0.3875x^2 - 33.396x + 1089.4$

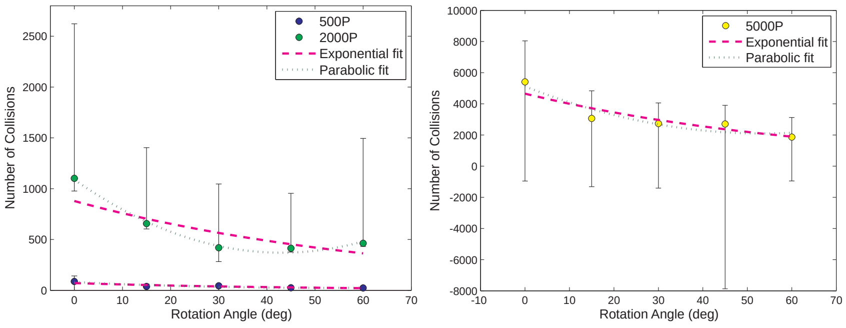

(a) (b)

Fig. C.11: Changes in number of collisions of collision allowed case and no collision allowed case with the axis angle (a) for 500 and 2000 particles, (b) for 5000 particles.

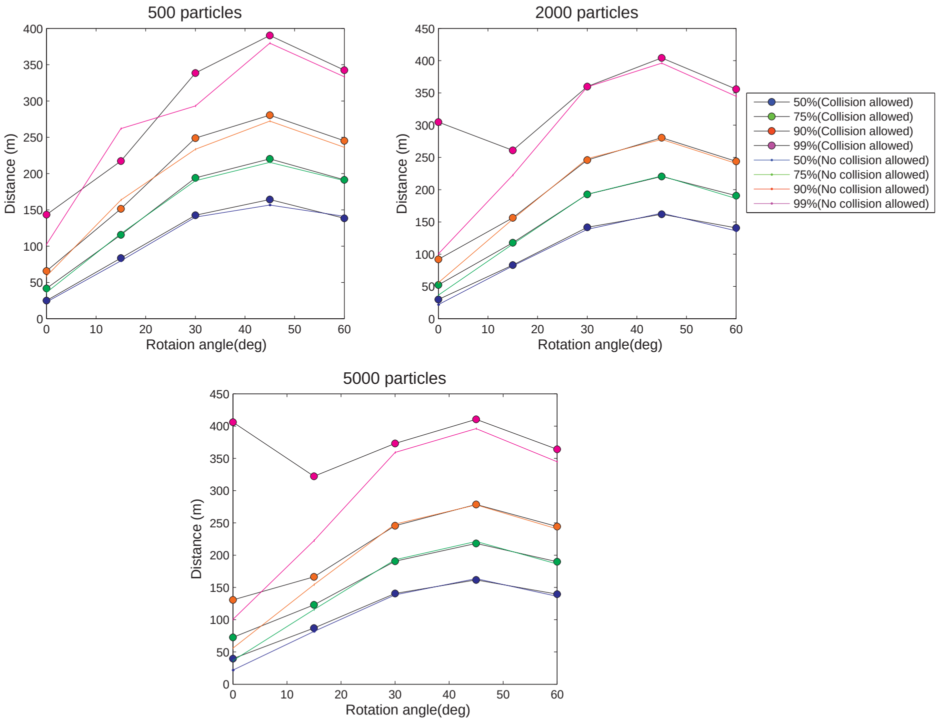

Fig. C.12: Changes in deposition distance of collision allowed case and no collision allowed case with the rotation angle.

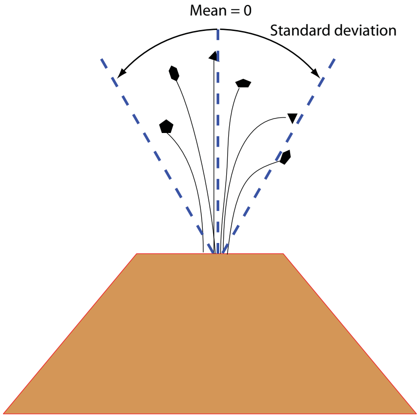

Fig. C.13: Image of the standard deviation of inclination angle. Mean and standard deviation are measured from the vertical axis.

the dense conditions in the air which is enough for particles to collide each other.

C.6 Inclination Angle

Inclination angle is the direction of the initial velocity. It is chosen from the Gaussian distribution defined by mean value and standard deviation. The velocities of horizontal direction (v_h) and vertical direction (v_z) is assigned as

$$\begin{aligned} v_h &= V sin\theta \\ v_z &= V cos\theta \end{aligned} \tag{C.1}$$

where, V is the norm of velocity and θ is the inclination angle. If the standard deviation of inlincation angle is large, the range of the ejection direction is wide.
Initial conditions are shown in Table C.9. Standard deviation of the inclination angles is 5 , 15, 30,45, 60 degrees.

Discussion of inclination angle Number of collisions is large when the standard deviation (STD) is small. It decreases until 30 degrees. However, the changes are not clear for larger value ($>$ 30 degrees) of STD. Number of collisions is minimum when the STD is 30 degrees for 500 particles case

Table C.9: Initial conditions of the simulation for detecting the effect of the inclination angle.

Parameter	**Mean**	**Standard Deviation**
Time interval between bursts (s)	0.1	0
Number of particles per launch	5 /20	0
Particle density (kg/m^3)	1450	500
Particle diameter (m)	0.5	0.3
Displacement of the ejection point relative to vent center (m)	0	10
Norm of initial velocity (m/s)	40	10
Deviation angle (degree, from vertical axis)	0	*
Total burst time (s)	10	

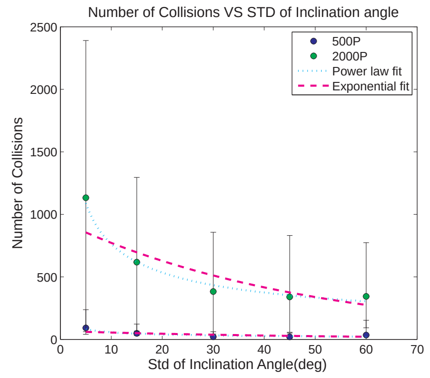

Fig. C.14: Changes in number of collisions of collision allowed case and no collision allowed case with the standard deviation of launching angle.

Table C.10: Equations of fittings of power law and exponential curves for the plots of number of collisions.

	Power law fitting	Exponential fitting
500P	$y = 195.58x^{-0.5381}$	$y = 66.13exp(-0.0192x)$
2000P	$y = 2486x^{-0.5133}$	$y = 948.36exp(-0.0206x)$

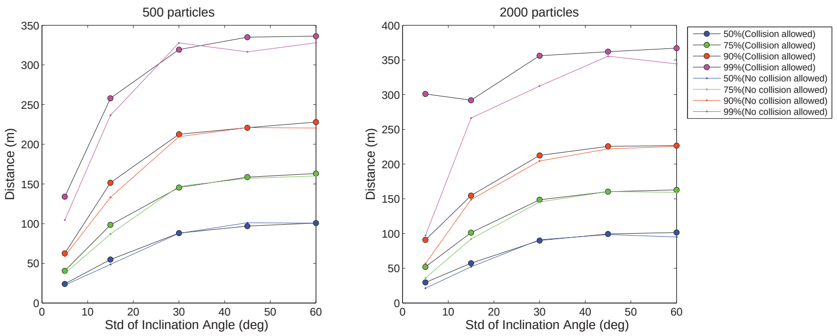

(a) (b)

Fig. C.15: Changes in deposition distance of collision allowed case and no collision allowed case with inclination angle. (a) 500 partciles and (b) 2000 particles are utilized

and 45 degrees for 2000 particles. The difference of values is quite small comparing to error range.

Deposition distance increases until 45 degrees as the STD increases for no collision allowed cases. This trend is the same as the rotation angle but as the mean angle is vertical and most of them are launched vertically, deposition distance does not become so long as the rotation angle calculation. For collision allowed case, deposition distance is much farther when the STD is 15 degree. In larger STD, the value of deposition distance of collision allowed case becomes close to the value of no collision allowed case. This means that the collision effect to deposition distance is visible only in small STD. When the STD is large, concentration is small and the collision does not occur so often. Therefore the distance difference is getting smaller as the STD becomes larger.

C.7 Burst time interval

Several particles burst at the same time and these events are repeated with certain interval. Some observations reported cyclic patterns of bursts (Ripepe et al, 1993 []; Patrick et al, 2007 [84]). To see the effect of time interval of burst, the calculation with intervals of 0.1, 0.2, 0.5, 1.0, 2.0, 3.0, 4.0, 5.0 seconds are implemented.

Initial conditions are shown in Table C.11. To fix the total number of particles, duration of burst varies with time interval. Interval and duration of burst are in Table C.12.

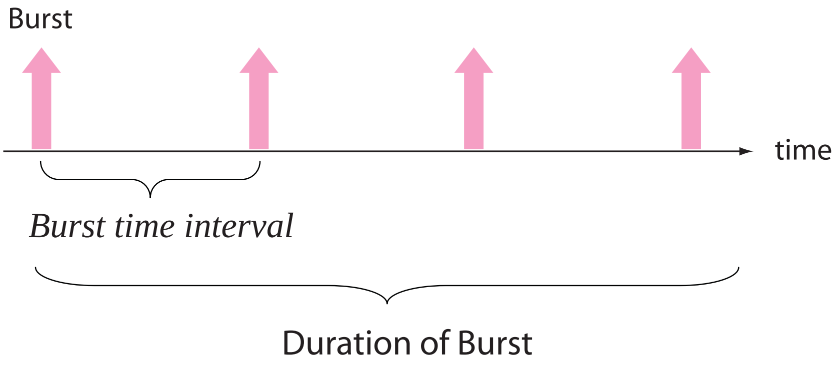

Fig. C.16: Image of particle bursts and its time interval.

Table C.11: Main parameters of initial conditions of the simulation for detecting the effect of the burst interval.

Parameter	**Mean**	**Standard Deviation**
Time interval between bursts (s)	*	0
Number of particles per burst	5 /20	0
Particle density (kg/m^3)	1450	500
Particle diameter (m)	0.5	0.3
Displacement of the ejection points relative to vent center (m)	0	10
Norm of initial velocity (m/s)	40	10
Deviation angle (degree, from vertical axis)	0	5

Table C.12: Burst time interval and total burst time for each case.

Time interval between bursts (s)	Burst duration (s)
0.1	10
0.2	20
0.5	50
1	100
2	200
3	300
4	400
5	500

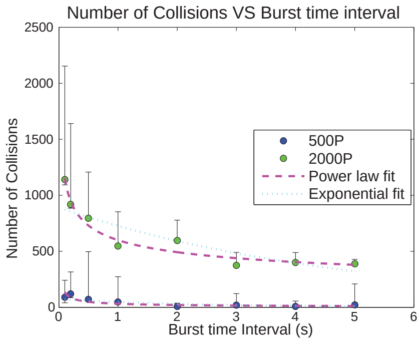

Fig. C.17: Changes in number of collisions of collision allowed case and no collision allowed case with the burst time interval .

Table C.13: Equations of fittings of power law and exponential curves for the plots of number of collisions.

	Power law Fitting	Exponential Fitting
500P	$y = 31.652x^{-0.63}$	$y = 73.705\exp(-0.4353x)$
2000P	$y = 599.42x^{-0.2847}$	$y = 890.79\exp(-0.2039x)$

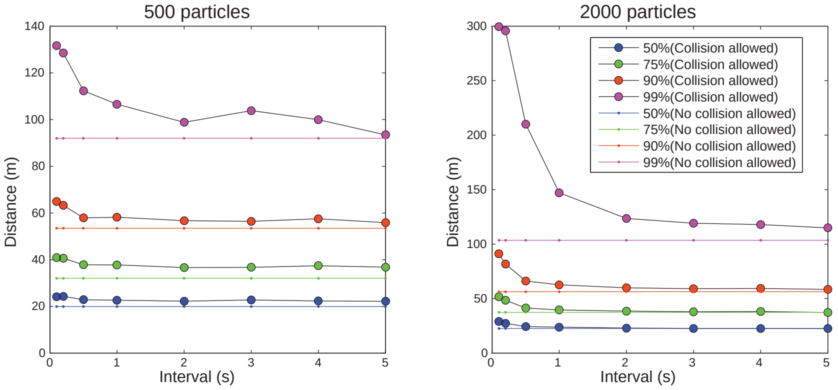

Fig. C.18: Changes in deposition distance of collision allowed case and no collision allowed case with the burst time interval.

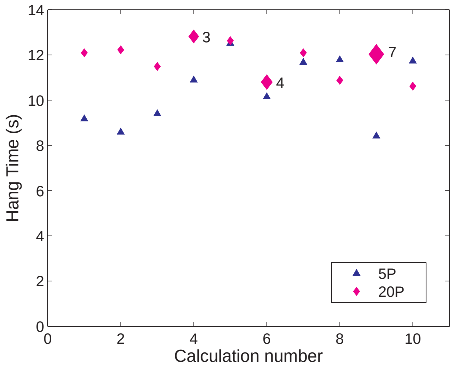

Fig. C.19: Measurement of hang time (from launching to reaching the ground) of only one launching. 10 times of calculation has repeated for both the case of 5 particles per launch and 20 particles per burst. The number in the figure is the number of collisions. There is no collision for the case of 5 particles per burst.

Discussion Number of collision decreases as the burst time interval decreases (Fig. C.17). This implies the collision happens in between the different group of burst. To make sure the collision happens not in the same group, hanging time of the collision is measured (Fig. C.19). Hanging time is around 10 seconds and intervals which are used for calculation is less than half of total hanging time. Moreover, collisions in one burst is also tracked. In most of burst events, collisions are not occurred. Even if collision happens, number of collision of one burst is much smaller than total number of collisions. Therefore, the collisions occur in between different burst groups and number of collisions decreases as the interval increases. This is probably because frequent bursts makes the concentration of particles in the air denser.

Deposition distance of no collision allowed case is not affected by the interval. However, the deposition distance of collision allowed case decreases as interval increases simply because the collision happens more if the launching events are frequent.

Chapter 7

Application of a DES ballistic model to the risk assessment of Vulcano island (Italy)

7.1 Introduction

Most explosive eruptions are characterized by the ejection of ballistic bombs and blocks of various sizes (i.e., projectiles with diameter $> 64mm$) that decouple from the gas phase at early stage and follow independent parabolic trajectories.

Blocks are angular to sub-angular fragments of juvenile or lithic material. Bombs are thrown from vents in a partly molten condition and solidify during flight or shortly after they land. As a result,, they are shaped by drag forces during flight, and if still plastic, their shape can be modified by impact when they hit the ground. Bombs are therefore almost exclusively juvenile. In particular, bread-crust bombs are caused by stretching of the solidified outer shell by expansion of gas within the still-plastic core. They are most commonly produced from magma of intermediate and silicic compositions and they are a very common product of Vulcanian explosions. Both blocks and bombs represent a significant proximal hazard associated with moderate explosions due to their velocity and temperature. In fact, impact of ballistic projectiles can harm people and damage buildings, critical facilities and vegetation.

For example, during the paroxysmal eruption of Stromboli volcano in Italy, 2003, some large blocks (> 1 m) set fire on vegetation (Pistolesi et al, 2008 [86]).

Evaluating the potential damage caused by ballistics during explosive eruptions is crucial to the hazard and risk assesment of proximal to medium area (i.e., $< 20km$ from the vent). Risk assessments of ballistics are based on numerical simulations with hazardous energy thresholds. We have applied our three-dimensional(3D) multiparticle ballistic model (see Chapter 6 for

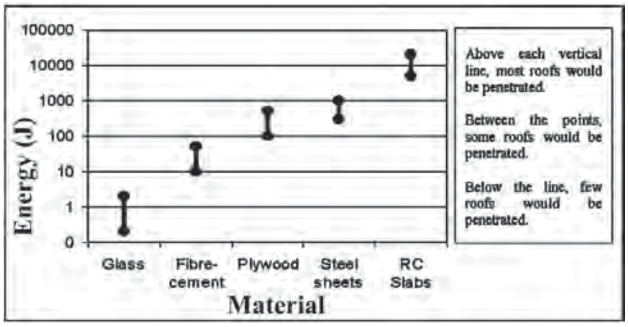

Above each vertical line, most roofs would be penetrated.

Between the points, some roofs would be penetrated.

Below the line, few roofs would be penetrated.

Fig. 7.1: The relationship between impact energy and the damage caused to a range of building materials, based on Blong (1984) [10] and Pomonis et al. (1999) [87]. (Spence(2005) [109])

a detailed description) to the hazard and risk assessment of Vulcano Island (Italy). This model can compute the distribution of ballistics on the ground.

There are two types of roof vulnerability associated with ballistic hazard: penetration and collapse of roof. We have worked with engineers of the École Polytechnique Fédérale de Lausanne (EPFL) in order to identify the hazardous energy thresholds for both collapse and penetration of building roofs. Liu(2010) [68] has presented the theory of the roof collapse. She calculated the deformation angle of the roof by using the theory of Smith and Hetherington (1994) [103]. In this calculation, deformation is treated as a dynamic load and the roof is assumed to be made of elastic material.

Spence et al(2005) [109] introduced the threshold of penetration of the roof by ballistic bombs by compiling the work of Blong (1984) [10] and Pomonis et al., (1999) [87](Fig. 7.1). According to Spence et al, (2005) [109], threshold of RC slab (reinforced concrete) is around 10^4 J.

Vulcano is a volcanic island in Aeolien sea (Fig. 7.2). Main volcanic cone is called La Fossa whose summit altitude is around 350m a.s.l. There are mainly three populated towns in Vulcano: Vulcano Piano, Vulcano Porto and Vulcanello (Fig. 7.2). The population of Vulcano island is only around 700 people during the winter, but it becomes 15000 people during the summer. Most hotels are located in the north part of the island, in the towns of Vulcano Porto and Vulcanello. Ferries are the only way of transportation method to and from the island and the main port is located in Vulcano Porto (i.e., Porto Levante). The port of Gelso and the port of Ponente are mainly designed for evacuation purpose (Fig. 7.2).

In this chapter, we have analyezd the probability distribution of ballistics and discussed the vulnerability of Vulcano Island.

Fig. 7.2: Map of Vulcano island.

7.2 Method

7.2.1 Method of numerical simulation

We have implemented numerical simulations to predict the distribution of ballistics on the ground in case of a Vulcanian eruption with model presented in Chapter 6. This model is based on Discrete event simulation (DES) method and simulates ballistic trajectory with analytical solutions in between events. By simulating ballistic trajectory in three dimensions, we obtain two-dimensional distributions of particles on the ground. In order to have a high computation efficiency, we have considered a simplified topography where the crater area is at the altitude of 350m a.s.l. and the populated area is at the sea level(Fig. 7.3). If a ballistic projectile deposits at a larger distance than the radius of crater area, it is transported to the sea level.

In this model, dragforce is ignored for simplicity and the input parameters are randomly sampled by using a random number generator. Thus the values of average and standard deviation are given to the simulator to draw the values based on a Gaussian distribution. Input parameters are in Table (7.1).Ranges of particle diameter and density are based on field observations (Fig. 7.4 (a) and (b)).

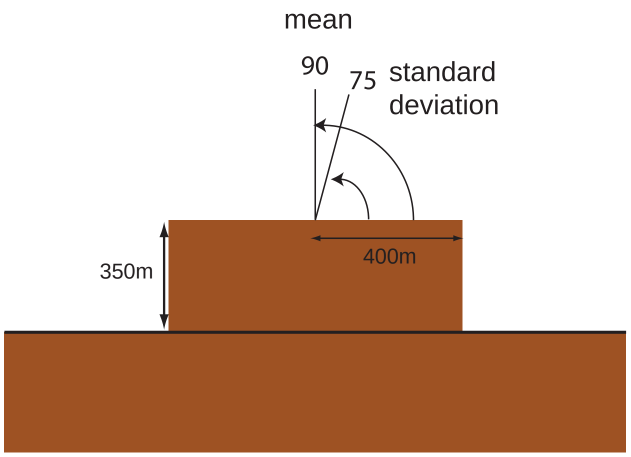

Fig. 7.3: Sketch of crosscut of the model used in the simulations. Mean and standard deviation of ejection angle is also shown (see Table 7.1).

Table 7.1: Input parameters.

Parameter	**Notation**	**Value**
Average of particle density (kg/m^3)	μ_{rho}	2000
Standard deviation of particle density (kg/m^3)	σ_{rho}	500
Average of particle diameter (cm)	μ_d	20
Standard deviation of Particle Diameter (cm)	σ_d	80
Average of ejecting angle(degree)	μ_{θ_e}	90
Standard deviation of ejecting angle (degree)	σ_{θ_e}	75
Standard deviation of ejection point (m)	σ_{r_e}	100
Crater altitude (m)	H_c	350
Radius of crater area (m)	L_c	400

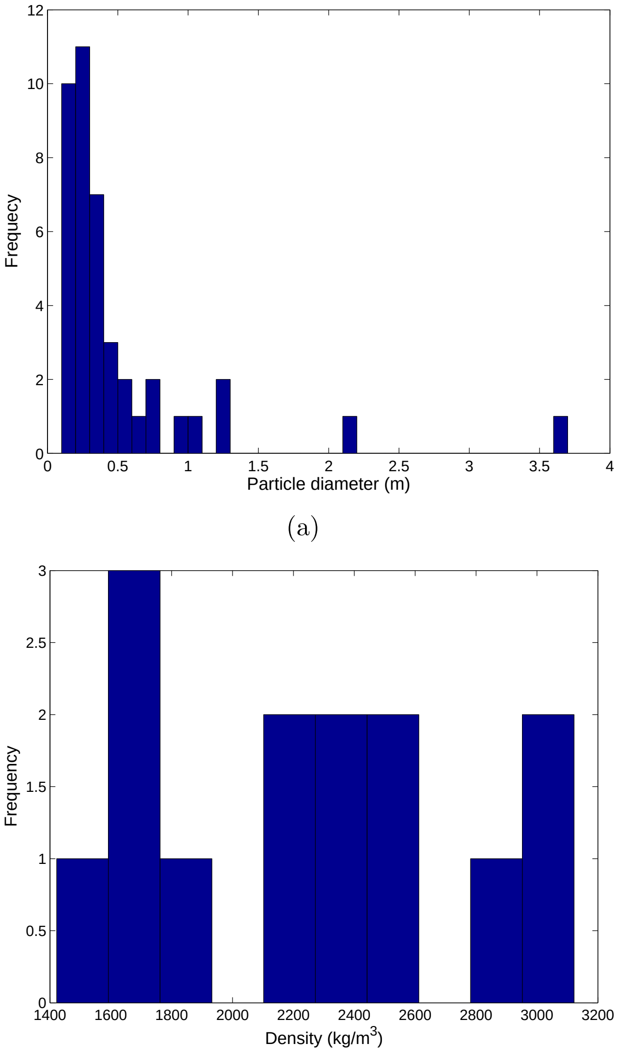

(a)

(b)

Fig. 7.4: Histogram of (a) particle diameter and (b) particle density obtained from the field observations of the 1888-1890 eruption of Vulcano. Ballisitic projectiles were collected based on a uniform grid with 35m-wide cells between 400m and 600m from the crater. Ballistic projectiles were characterized based on their 3 largest axis and their mass. Volume of the projectile has been calculated by assuming ellipsoldal shape. The density is calculated by using the mass and the volume. Diameter of the sample is an average of three axes.

Table 7.2: Velocity and ejection angles of two scenarios

Parameter	**Scenario1**	**Scenario2**
Average of Velocity (m/s)	100	50
Standard deviation of Velocity (m/s)	50	10

From these distributions, we decided to use the average of particle density $\mu_{rho} = 2000\ kg/m^3$ and standard deviation of particle density $\sigma_{rho} = 500\ kg/m^3$. For particle diameter, we applied average $\mu_d = 20\ cm$and standard deviation $\sigma_d = 80\ cm$ (particle diameter $d \leq 0\ cm$ is excluded). Ejection angles are decided according to the crater shape of La Fossa and standard deviation of ejection points is defined based on the crater radius.
We have considered two scenarios of potential Vulcanian eruptions (Table 7.2). The former work of Bianchi (2007) [7] estimated the velocity of the farthest ballistics bomb by fitting the travel distance with the result of simulation of one particle with a software by Mastin(2002) [73]. According to Bianchi (2007) [7] , the particle travel distance of 1558 m can be reached by the ejection velocity of 145 m/s and the ejection angle of 45 degrees (from the vertical axis) or the ejection velocity of 350 m/s and the ejection angle of 75 degrees. However, ejection velocity is normally less than 100 m/s for ballistics (M. Rosi, Personal communication). Furthermore, Bianchi (2007) [7] did not consider particle-particle interaction such as collision. If there are collisions between particles, the travel distance of ballistics can be longer or shorter (Chapter 6). Therefore we have chosen two possible ejection velocities of 100m/s and 50m/s + or - standard deviation (Table 7.2).

7.2.2 Energy thresholds for penetration of roof

According to Spence et al(2005) [109] (Fig. 7.1) , the RC-slabs have thresholds of the penetration around 10^4 J. Other materials have smaller thresholds than RC-slabs(Fig. 7.1). Based on the work of Spence et al. (2005) [109] and on the typical roofs on Vulcano, we have defined four classes of energy (Table 7.3) and the probability of having each class is analyzed from the results of the simulations.

7.2.3 Energy thresholds for roof collapse

Energy thresholds for of roof collapse have been studied in the collaboration with EPFL (Fig. 7.5). Vulnerability has been classified based on the length between beams in the roof. Typical roof in Vulcano consists of concrete with iron beams inside. The roof is stronger when the distance between beams

Table 7.3: Energy class (J) regarding the penetration of roof

Class	**Energy(J)**
Class 1	$E(p) \leq 10^2$
Class 2	$10^2 < E(P) \leq 10^3$
Class 3	$10^3 < E(P) \leq 10^4$
Class 4	$10^4 < E(P)$

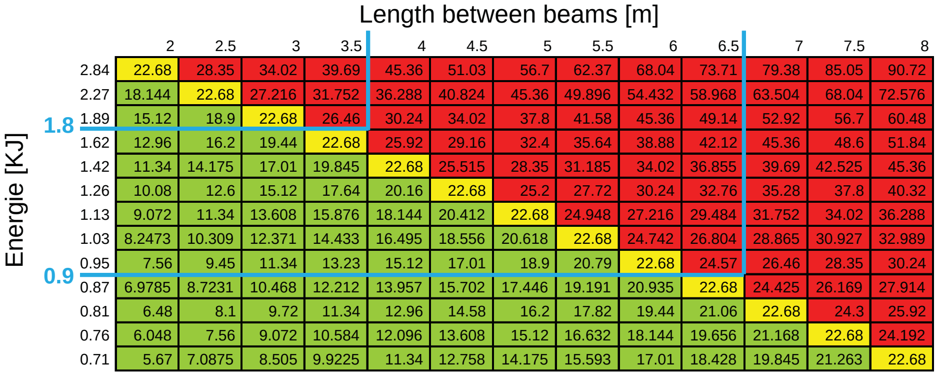

	2	2.5	3	3.5	4	4.5	5	5.5	6	6.5	7	7.5	8
2.84	22.68	28.35	34.02	39.69	45.36	51.03	56.7	62.37	68.04	73.71	79.38	85.05	90.72
2.27	18.144	22.68	27.216	31.752	36.288	40.824	45.36	49.896	54.432	58.968	63.504	68.04	72.576
1.89	15.12	18.9	22.68	26.46	30.24	34.02	37.8	41.58	45.36	49.14	52.92	56.7	60.48
1.62	12.96	16.2	19.44	22.68	25.92	29.16	32.4	35.64	38.88	42.12	45.36	48.6	51.84
1.42	11.34	14.175	17.01	19.845	22.68	25.515	28.35	31.185	34.02	36.855	39.69	42.525	45.36
1.26	10.08	12.6	15.12	17.64	20.16	22.68	25.2	27.72	30.24	32.76	35.28	37.8	40.32
1.13	9.072	11.34	13.608	15.876	18.144	20.412	22.68	24.948	27.216	29.484	31.752	34.02	36.288
1.03	8.2473	10.309	12.371	14.433	16.495	18.556	20.618	22.68	24.742	26.804	28.865	30.927	32.989
0.95	7.56	9.45	11.34	13.23	15.12	17.01	18.9	20.79	22.68	24.57	26.46	28.35	30.24
0.87	6.9785	8.7231	10.468	12.212	13.957	15.702	17.446	19.191	20.935	22.68	24.425	26.169	27.914
0.81	6.48	8.1	9.72	11.34	12.96	14.58	16.2	17.82	19.44	21.06	22.68	24.3	25.92
0.76	6.048	7.56	9.072	10.584	12.096	13.608	15.12	16.632	18.144	19.656	21.168	22.68	24.192
0.71	5.67	7.0875	8.505	9.9225	11.34	12.758	14.175	15.593	17.01	18.428	19.845	21.263	22.68

Fig. 7.5: Threshold of structual collapse derived for typical roofs in Vulcano. Red cells indicate roof collapse. Green cells indicate roof resilience. Yellow cell is the critical structure between collapse and resist. The blue lines show the boundary values for roof collapse used for our hazard assessment.

is smaller because beams support the roof structure. Then vulnerability depends on the distance between beams which is normally 2 to 6 m. Class 1, 2 and 3 indicate collapse of roofs with length between beams of ≥7 m, 4-6.5 m and <3.5 m respectively.

7.2.4 Probability and spatial analysis of vulnerability

The affected area is divided into envelops in the shape of concentric rings around crater for the spatial analysis.

Table 7.4: Energy class (J) for roof collapse

Class	**Energy(J)**	**Length between beams(m)**
Class 1	$E(p) \leq 0.8 \times 10^3$	≤ 7
Class 2	$0.8 \times 10^3 < E(P) \leq 1.9 \times 10^3$	4-6.5
Class 3	$1.9 \times 10^3 < E(P)$	≥ 3.5

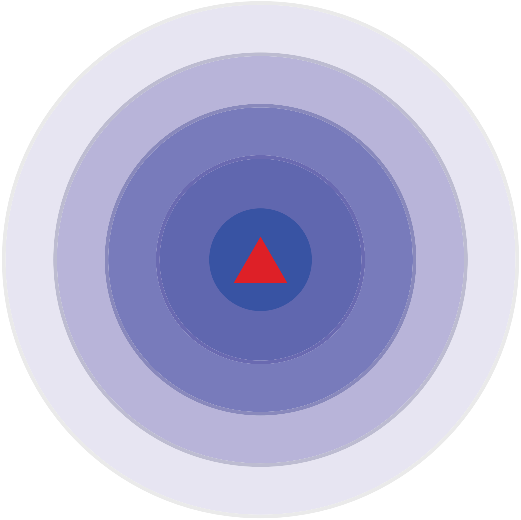

Fig. 7.6: Ring-shaped envelop for probability analysis.

Probability of having each energy class (Table 7.3) is calculated by two approaches.

At first, conditional probability which is the probability of particle being class C knowing that it fell in envelop E $P(C \mid E)$ is calculated.

$$P(C \mid E) = \frac{N_{EC}}{N_E} \tag{7.1}$$

where N_{EC} is the number of particles in each energy class and each envelop and N_E is number of particles in each envelop. Sum of this probability in each envelop is 1.

$$\sum_{i=1}^{TotC} P(C_i \mid E) = \sum_{i=1}^{TotC} \frac{N_{ECi}}{N_E} = 1. \tag{7.2}$$

where $TotC$ is total number of energy classes.

Second, joint probability, which is the probability of having a particle of a certain class in each enevelop normalized by the total number of particles, $P(E, C)$, is calculated by multiplying the probability of having a particle of a given envelop regardless of the energy class $P(E)$, and the probability of having a particle of a certain class in each enevelop $P(E, C)$.

$$\begin{aligned} P(E,C) &= P(E) \times P(C \mid E) \\ &= \frac{N_E}{N_T} \times \frac{N_{EC}}{N_E} \\ &= \frac{N_{EC}}{N_T} \end{aligned} \tag{7.3}$$

where N_T is the total number of particles used in the simulation. Sum of the probabilities for all classes and all envelops is 1.

$$\sum_{i=1}^{TotC} \sum_{j=1}^{TotE} P(E_i, C_j) = \sum_{i=1}^{TotC} \sum_{j=1}^{TotE} \frac{N_{Ei}}{N_T} \times \frac{N_{Cj}}{N_{Ei}} = 1. \tag{7.4}$$

where $TotE$ is total number of enevelops.

These two types of probability are calculated for both roof penetration and roof collapse and overlaid on the map of Vulcano island in the Geographic Information System(GIS).

7.3 Results

7.3.1 Result of simulation

The results of simulations for scenario 1 and 2 are shown in Fig. 7.7 and Fig. 7.8. These figures show the distributions of ballistic particles on the ground. Scenario 1 shows a wider particle distribution than scenario 2 because of the larger ejection velocities. In both scenario 1 and 2 particles with large energy ($> 10^4$ J) deposit far from the vent and particles with smaller energy ($< 10^2$ J) deposit around the crater.

Distributions of energy for each particle are analyzed as a function of the distance from the vent (Fig. 7.9 and Fig. 7.10) because the distribution of particles are approximately axisymmetric (Fig. 7.7 and Fig. 7.8). Curves of averaged energy become smooth as particle number increases for both scenario 1 and 2 (Fig. 7.9 and Fig. 7.10). The averaged particle energy increases with distance from vent and it becomes extremely large at the edge of the distribution (Fig. 7.9 and Fig. 7.10), and this is consistent with the maps of Fig. 7.7 and Fig. 7.8. At around 900m from the vent, there is a peak for scenario 1 (Fig. 7.9) and a depression for scenario 2 (Fig. 7.10). This is possibly due to the effect of simple topography (see discussion in section 7.4). Maximum value of averaged energy is one order of magnitude higher for scenario 1 than scenario 2 (10^6 J for scenario 1 and 10^5 J for scenario 2) because the ejection velocity is higher for scenario 1 (Table 7.2). Besides, distance range of particle distribution is wider for scenario 1 than scenario 2 because of the difference in ejection velocity.

Distributions of energy cumulated in each envelop are analyzed as a function of the distance from the vent (Fig. 7.11 and Fig. 7.12). Curves of averaged energy become smooth as particle number increases for both scenario 1 and 2 (Fig. 7.11 and Fig. 7.12). Cumulative energy decreases with distance from vent (Fig. 7.11 and Fig. 7.12). A depression of curve is recognized around 900 m from vent in scenario 1 (Fig. 7.11). Order of maximum energy is in the same order for scenario 1 and 2 (10^6(J) for 10^3 particles, 10^7 for 10^4 particles, 10^8 for 10^5 particles and 10^9 for 10^6 particles).

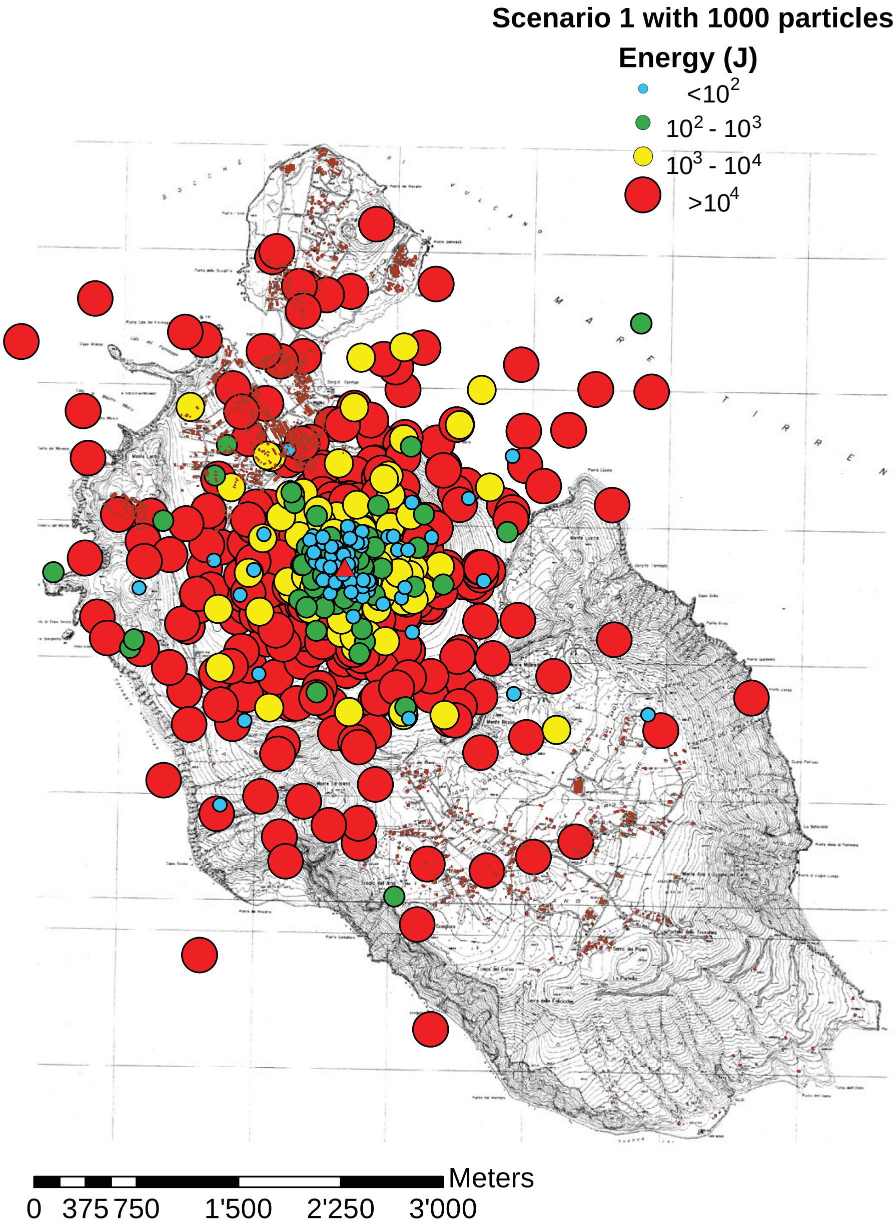

Fig. 7.7: The distribution of ballistic particles scenario 1 with 1000 particles. Color and size of circles show the energy class (J) of ballistics when they arrive at the ground. Red triangle shows the crater location of Fossa. Buildings are shown with filled brown polygons.

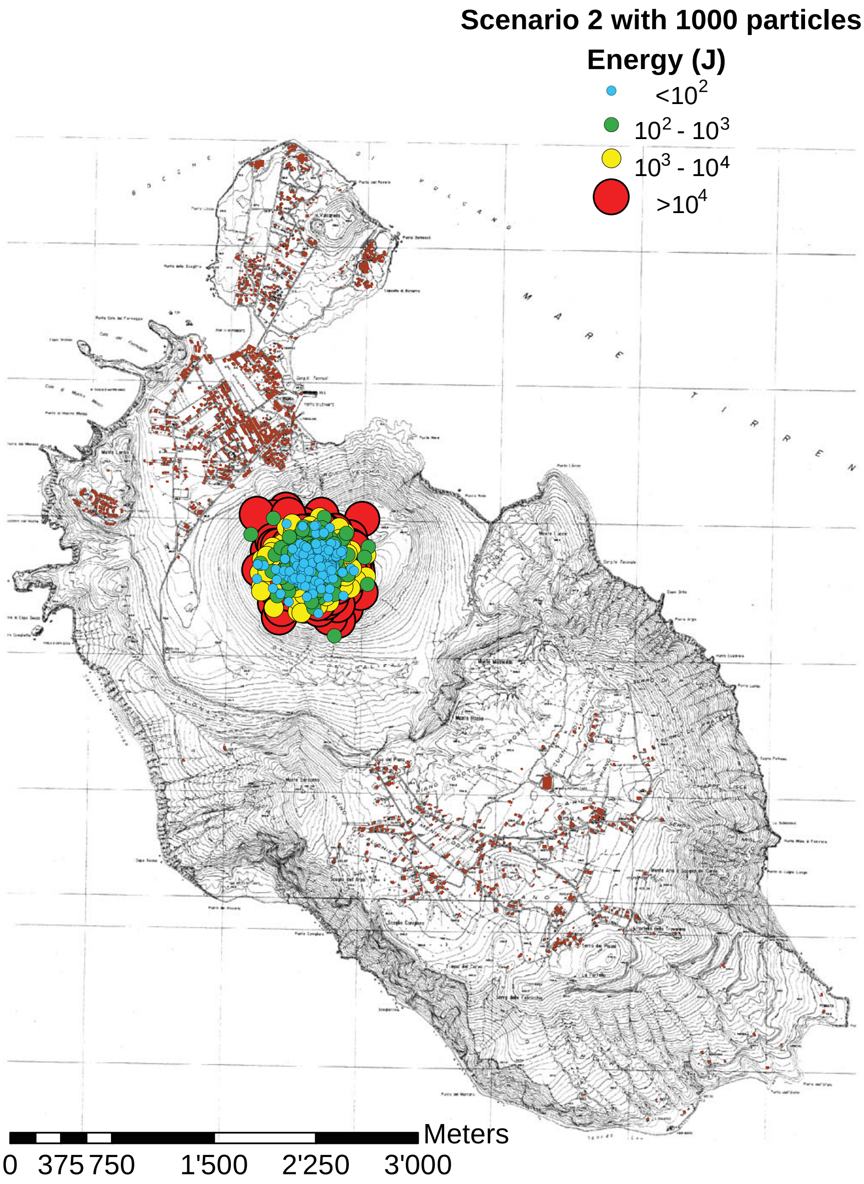

Fig. 7.8: The distribution of ballistic particles scenario 1 with 1000 particles. Color and size of circles show the energy class (J) of ballistics when they arrive at the ground. Red triangle shows the crater location of Fossa. Buildings are shown with filled brown polygons.

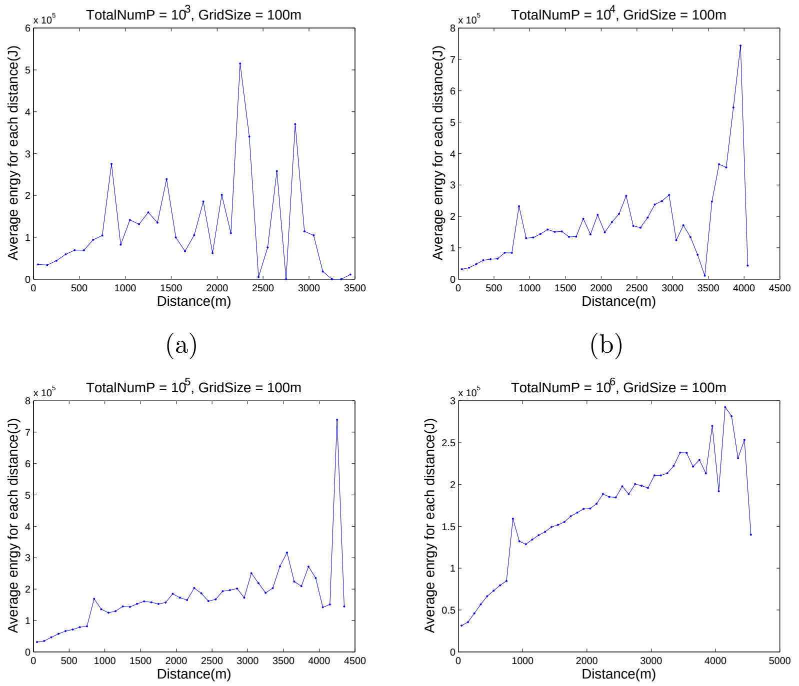

(a) (b)

(c) (d)

Fig. 7.9: Averaged particle energy for each envelop for Scenario 1. Particle number is (a) 10^3 (b)10^4 (c) 10^5 and (d) 10^6.

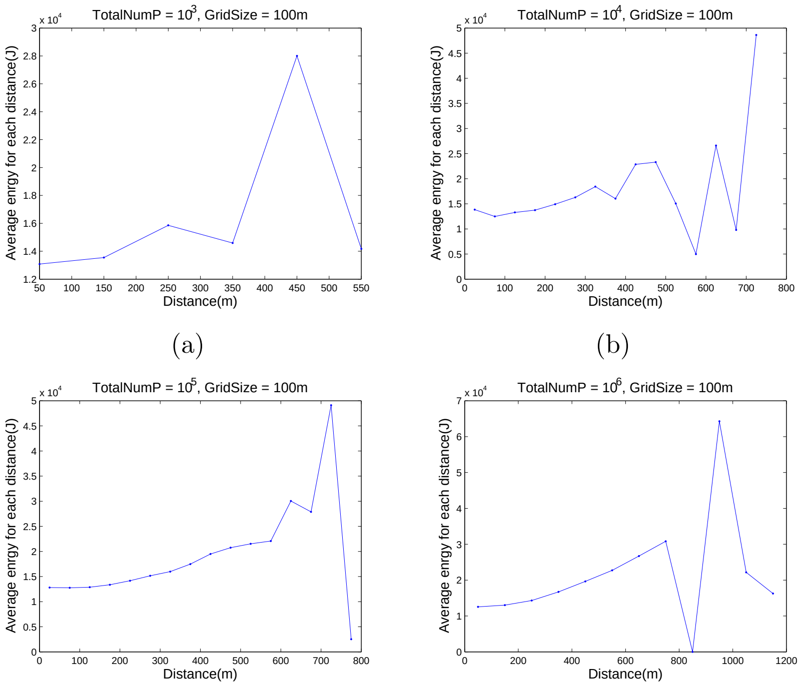

(a) (b)

(c) (d)

Fig. 7.10: Averaged particle energy for each envelop for Scenario 1. Particle number is (a) 10^3 (b)10^4 (c) 10^5 and (d) 10^6.

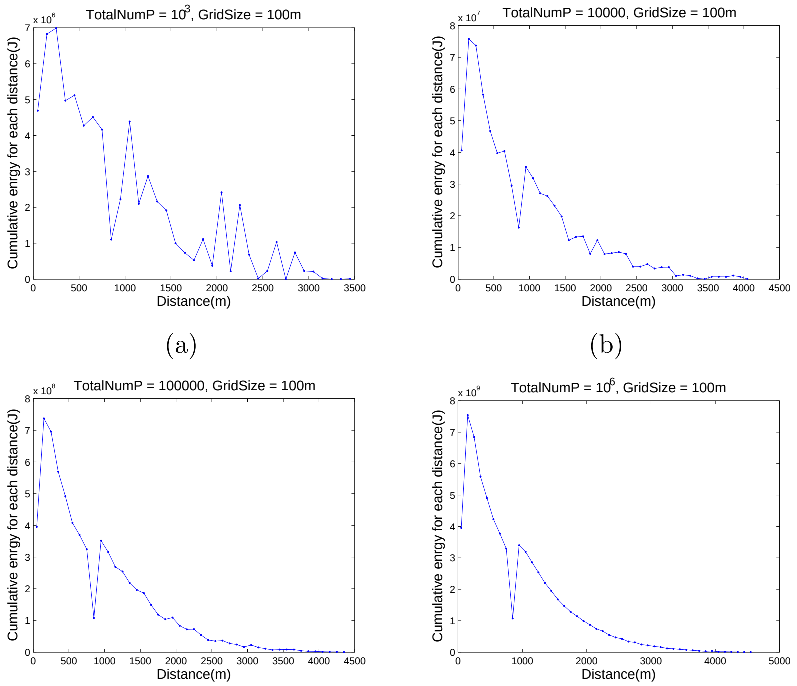

(a)

(b)

(c)

(d)

Fig. 7.11: Energy cumulated for each distance with total number of particles for scenario 1 (a) 10^3 (b)10^4 (c) 10^5 and (d) 10^6.

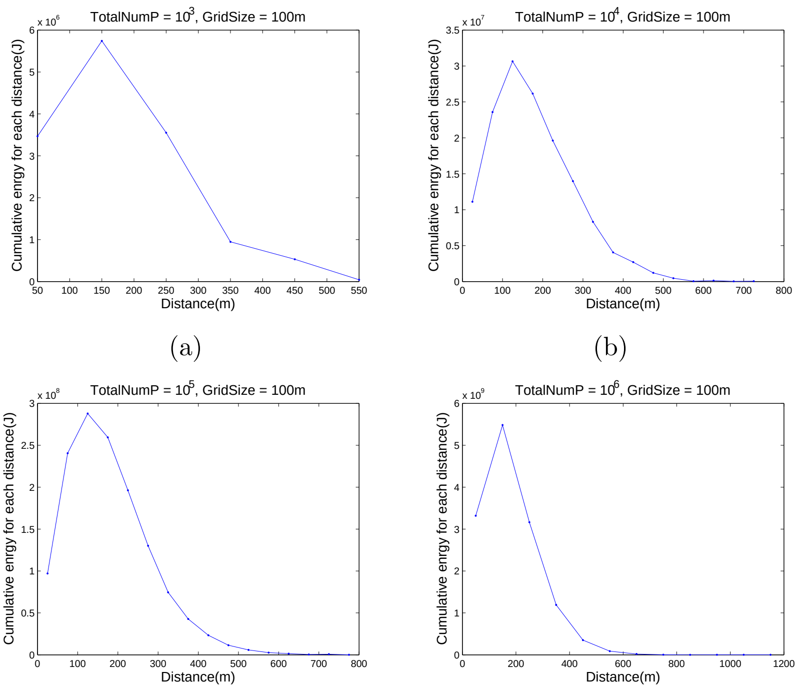

(a) (b)

(c) (d)

Fig. 7.12: Energy cumulated for each distance with total number of particles for scenario 2 (a) 10^3 (b)10^4 (c) 10^5 and (d) 10^6.

7.3.2 Probabilities

Probabilities are analyzed as a function of distance from vent (Fig. 7.13 - Fig. 7.20) for both roof penetration and collapse.

Conditional probabilities ($P(C \mid E)$) for roof penetration are shown in Fig. 7.13 and Fig. 7.14. Curves of averaged energy becomes smooth as particle number increases for both scenario 1 and 2 (Fig. 7.13 and Fig. 7.14). The probability of class 1-3 decreases with distance form vent but the probability of class 4 increases with distance from vent for both scenario 1 and 2 (Fig. 7.13 and Fig. 7.14). However, the probability curve shows the depression around 900m from the vent in scenario 2 with particle number 10^6 (Fig. 7.14 (d)).

Joint probabilities ($P(E, C)$) for roof penetration are shown in Fig. 7.15 and Fig. 7.16. Curves of averaged energy becomes smooth as particle number increases for both scenario 1 and 2 (Fig. 7.15 and Fig. 7.16). The probabilities for all classes decrease with distance from vent for both scenario 1 and 2(Fig. 7.15 and Fig. 7.16). The probability curves of scenario 1 show depressions at 900m from vent(Fig. 7.15). Maximum value of probability is 0.1 for scenario 1 and around 0.18 for scenario 2 (Fig. 7.15 and Fig. 7.16).

Conditional probabilities ($P(C \mid E)$) for roof collapse are shown in Fig. 7.13 and Fig. 7.19 and Fig. 7.20. Curves of averaged energy becomes smooth as particle number increases for both scenario 1 and 2 (Fig. 7.13 and Fig. 7.20). In scenario 2, curve trend changes with the particle number (Fig. 7.20) and the depression in curve around 900m from vent emerges only in the case with 10^6 particles. The probabilities decrease with distance from vent for class 1 and 2, but increase with distance from vent for class 3 for both scenario 1 and 2.

Joint probabilities ($P(E, C)$) for roof collapse are shown in Fig. 7.19 and Fig. 7.20. Curves of averaged energy becomes smooth as particle number increases for both scenario 1 and 2 (Fig. 7.19 and Fig. 7.20). The probabilities decrease with distance from vent for all classes for both scenario 1 and 2 (Fig. 7.19 and Fig. 7.20). The depression in curve around 900m from vent emerges only in scenario 1 (Fig. 7.19). Maximum value of probability is 0.16 for scenario 1 and around 0.35 for scenario 2 (Fig. 7.19 and Fig. 7.20).

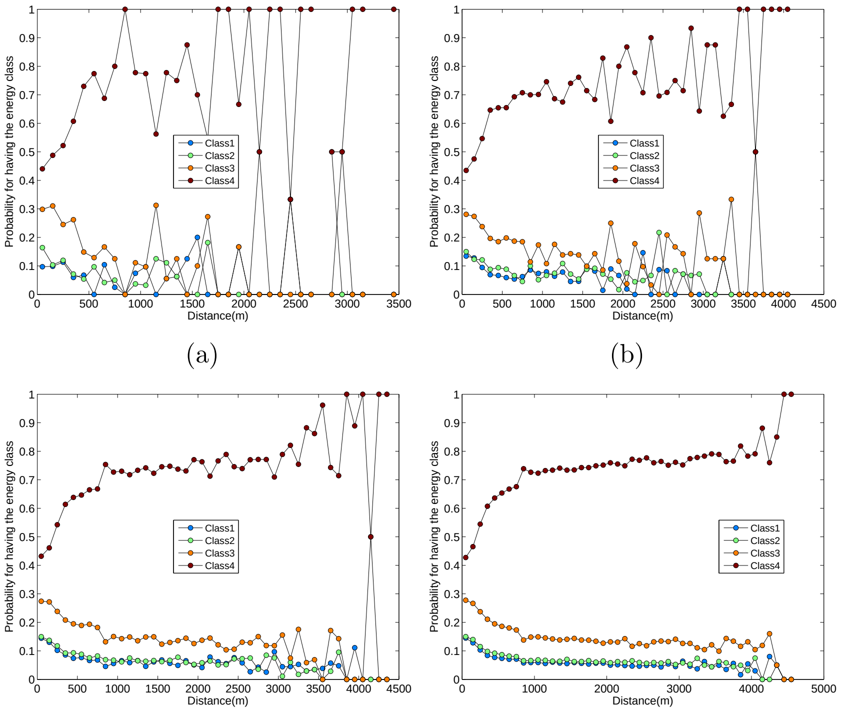

(a)

(b)

(c)

(d)

Fig. 7.13: Conditional probability $P(C \mid E)$ for scenario 1 (a) 10^3 particles, (b) 10^4 particles, (c) 10^5 particles and (d) 10^6 particles.

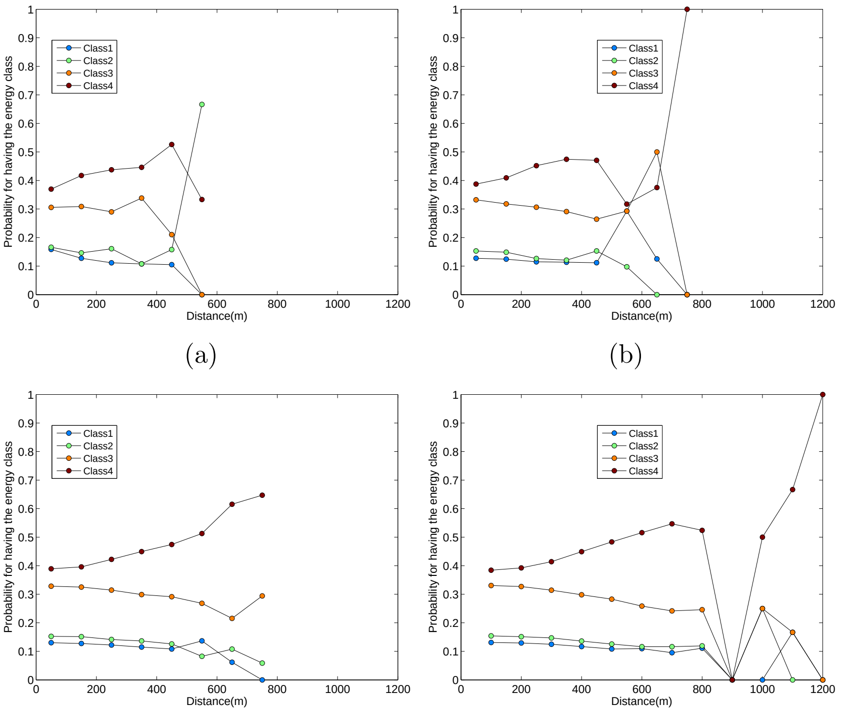

(a) (b)

(c) (d)

Fig. 7.14: Conditional probability $P(C \mid E)$ for scenario 2 (a) 10^3 particles, (b) 10^4 particles, (c) 10^5 particles and (d) 10^6 particles.

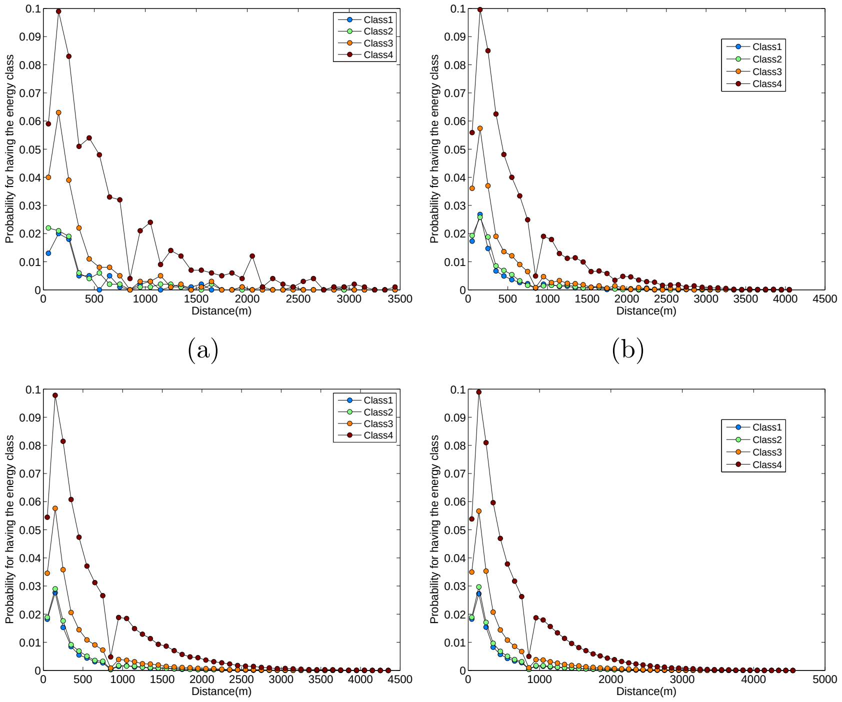

(a) (b)

(c) (d)

Fig. 7.15: Joint probability $P(E, C)$ for scenario 1 with (a) 10^3 particles, (b) 10^4 particles, (c) 10^5 particles and (d) 10^6 particles.

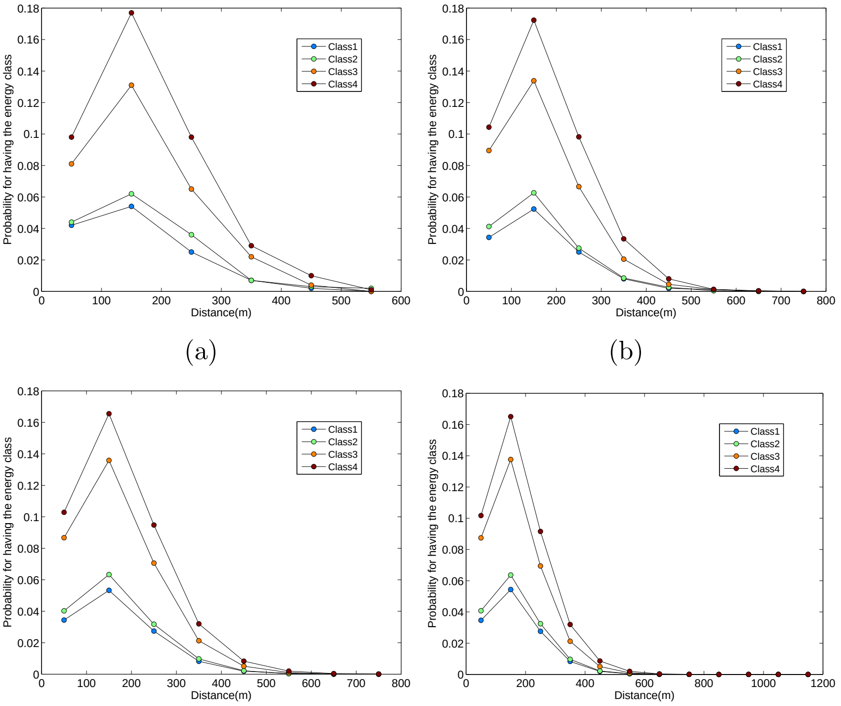

(a) (b)

(c) (d)

Fig. 7.16: Joint probability $P(E, C)$ for scenario 2 with (a) 10^3 particles, (b) 10^4 particles, (c) 10^5 particles and (d) 10^6 particles.

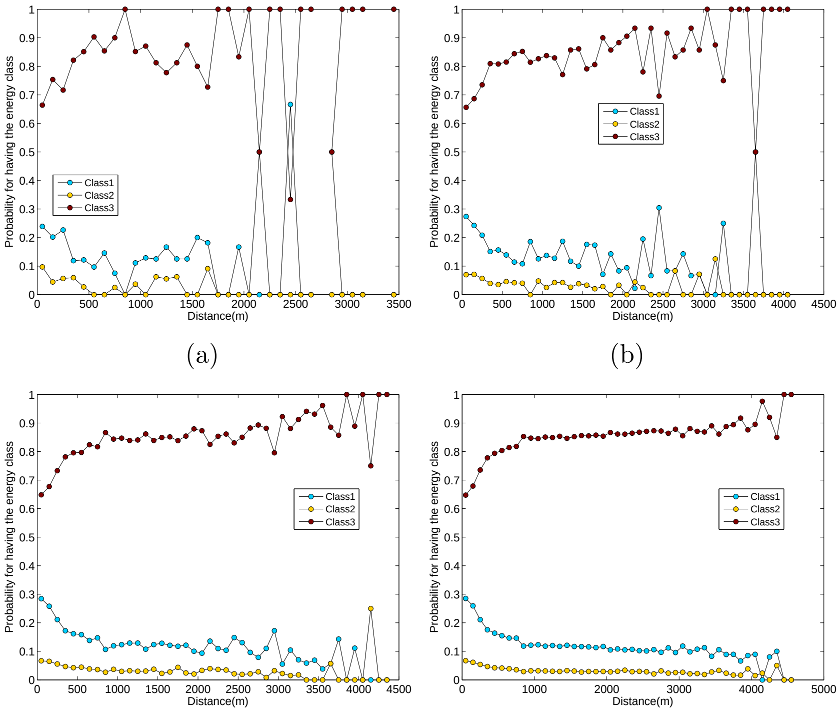

(a) (b)

(c) (d)

Fig. 7.17: Conditional probability $P(C \mid E)$ for scenario 1 (a) 10^3 particles, (b) 10^4 particles, (c) 10^5 particles and (d) 10^6 particles.

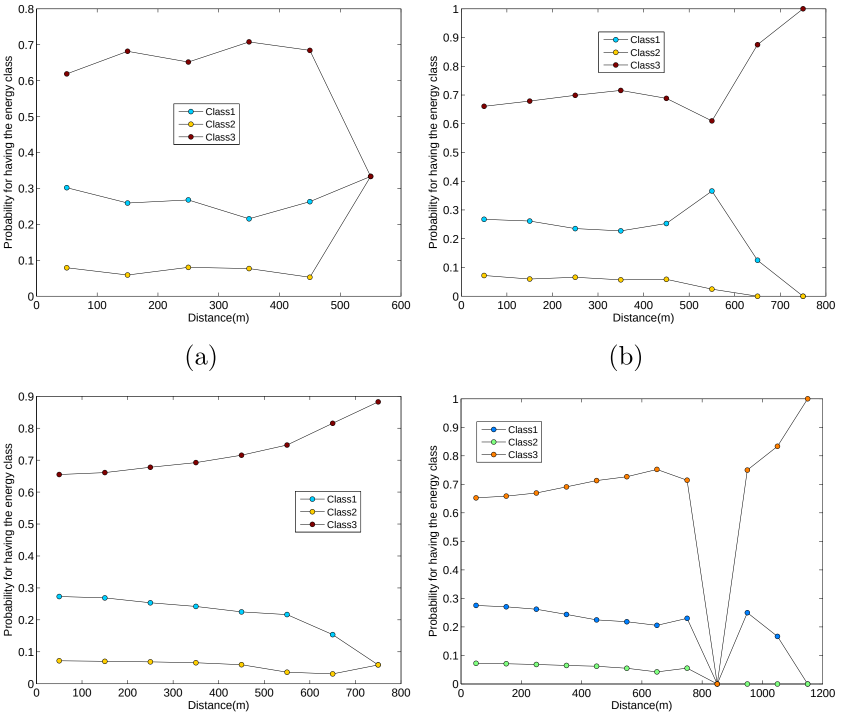

(a)

(b)

(c)

(d)

Fig. 7.18: Conditional probability $P(C \mid E)$ for scenario 1 (a) 10^3 particles, (b) 10^4 particles, (c) 10^5 particles and (d) 10^6 particles.

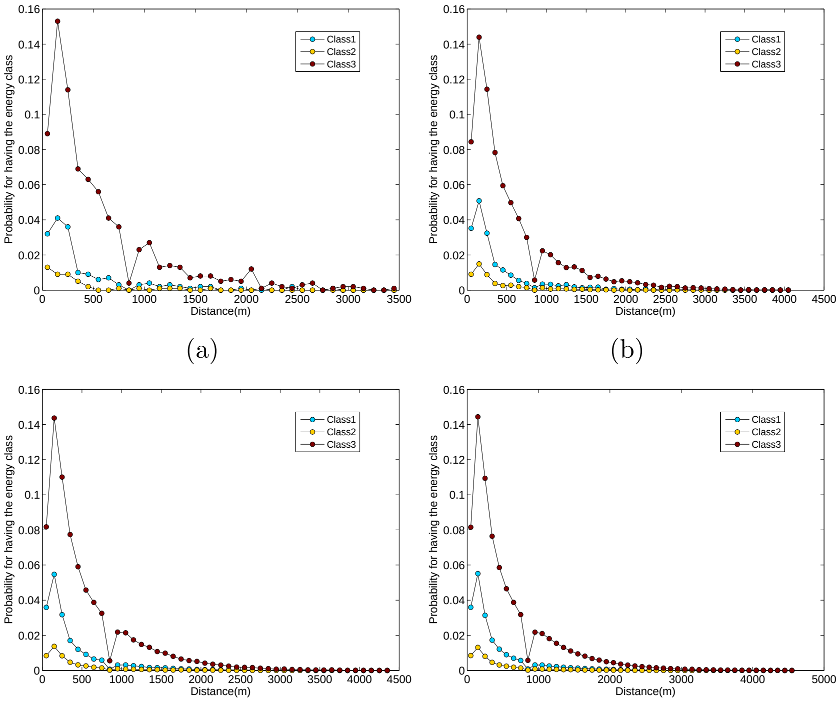

(a) (b)

(c) (d)

Fig. 7.19: Joint probability of roof collapse for scenario 1 (a) 10^3 particles, (b) 10^4 particles, (c) 10^5 particles and (d) 10^6 particles.

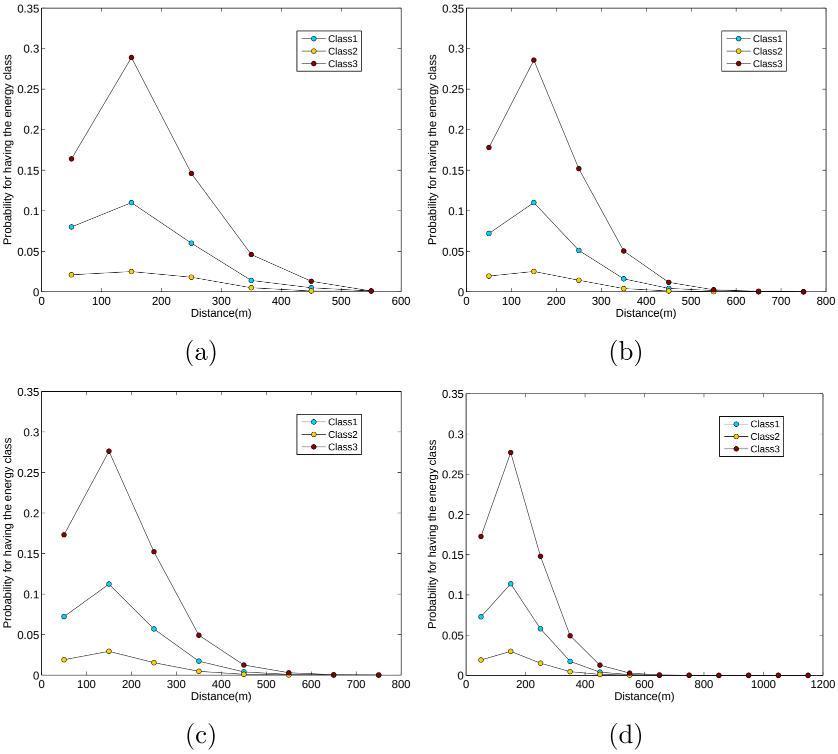

(a) (b)

(c) (d)

Fig. 7.20: Joint probability of roof collapse for scenario 2 (a) 10^3 particles, (b) 10^4 particles, (c) 10^5 particles and (d) 10^6 particles.

7.3.3 Probability maps

Number of particles in each envelop affects both probabilities $P(C \mid E)$ and $P(E, C)$ (Fig. 7.21 and Fig. 7.22). Particles of scenario 1 are widely distributed affecting all towns of Vulcano Islands (Fig. 7.21). On the other hand, particles of scenario 2 reach maximum distance of 1200 m from vent. 50% of Porto town is significantly affected by deposition of ballistics in Scenario 2.

Conditional probabilities for roof penetration are shown in Fig. 7.23- 7.30. For scenario 1, the whole island is characterized by low probabilities ($< 1\%$) for class 1-3 (Fig. 7.23-7.25). The probability of deposition for class 3 reaches 20-40% around the crater (< 400 m from vent) (Fig. 7.25). The probability of deposition of Class 4 is mostly > 60 % all over the island, and reaches more than 80% in the south. This zone crosses the road to the port of Gelso (Fig. 7.26). For scenario 2, the whole affected area shows low probabilities (< 1 %) for classes 1 and 2 (Fig. 7.27 and Fig. 7.28). For class 3, most affected area is covered by low probabilities (< 20 %)(Fig. 7.29). The area with the probability of 60-80 % includes the town of Porto for class 4 (Fig. 7.30).

Joint probabilities for roof penetration are shown in Fig. 7.31- 7.38. For scenario 1, most of the island is characterized by low probabilities (< 1 %) (Fig. 7.31 and Fig. 7.32). For class 3, the area with probabilities $\geq 1\%$ is larger but it does not affect populated areas (Fig. 7.33). For class 4, 50% fo the town of Porto is characterized by probabilities > 1 % (Fig. 7.34). The probabilities of scenario 2 are similar for all classes and most of them are < 1 %.

Conditional probabilities for roof collapse are shown in Fig. 7.39- 7.44. For scenario 1, most of island is characterized by low probabilities ($< 1\%$) for class 1 and 2 (Fig. 7.39 and Fig. 7.40). On the contrary, most of island is characterized by high probabilities ($< 80\%$) including all populated areas for class 3 (Fig. 7.41). For scenario 2, class 1 and 3 show similar distributions of probabilities (Fig. 7.42 and Fig. 7.44) and small part of the town of Porto is characterized by probabilities of 40-60%. For class 2, the whole affected area is characterized by low probabilities of $< 1\%$(Fig. 7.43).

Total sedimentation probabilites for roof collapse are shown in Fig. 7.45- 7.50. For scenario 1, most of the island is characterized by low probabilities (< 1 %). Also for class 2, most of the island is characterized by low probabilities (< 1 %). However, for class 3, the area of probabilities of > 1 % covers 80 % of the town of Porto and the area of probabilities of 2-4 % covers 20 % of town of Porto (Fig. 7.47). For class 1 and 2 of scenario 2, the populated area (town of Porto) is only characterized by low probabilities (< 1 %)(Fig. 7.48 and Fig. 7.49). For class 3 of scenario 2, 50 % of the town of Porto is characterized by the area of probabilities of $> 1\%$ and besides, 20 % of the town Porto is characyerized by the area of probabilities of 2-4 % (Fig. 7.50).

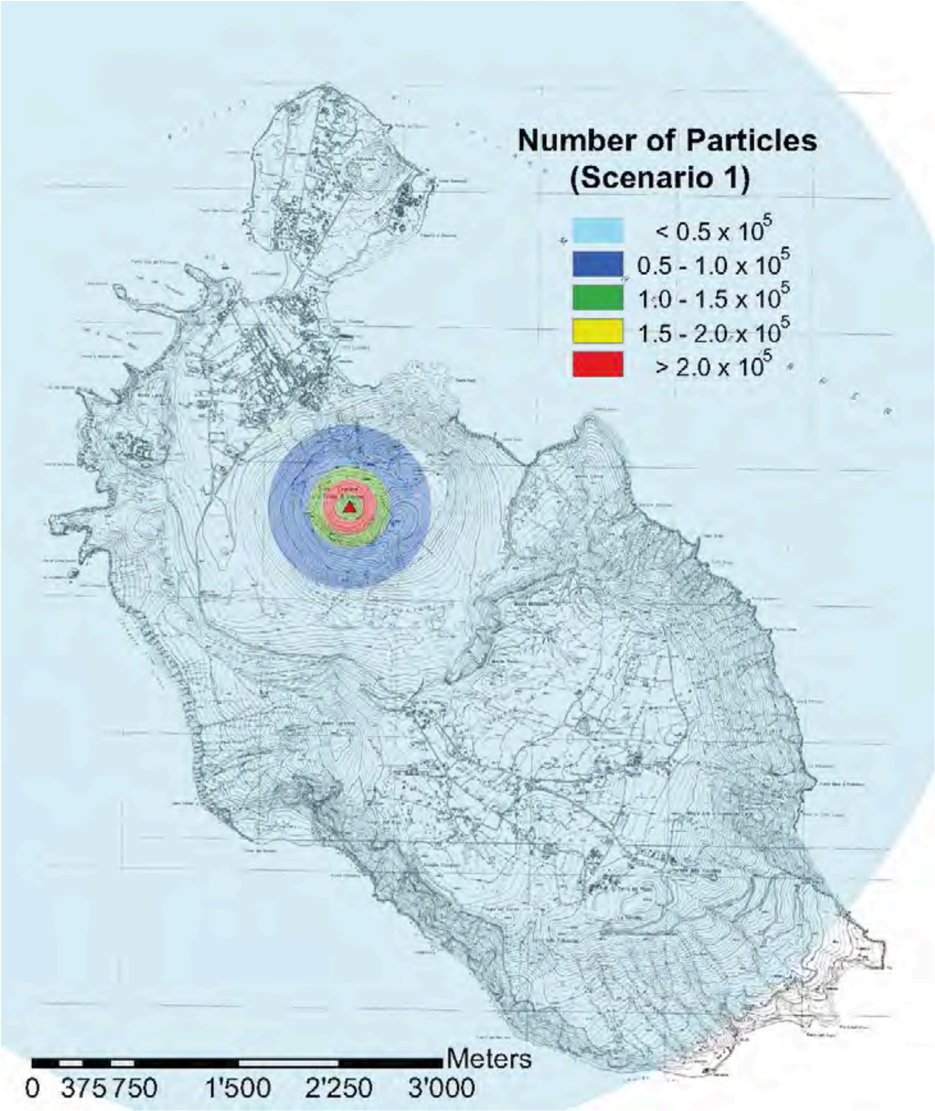

Fig. 7.21: Number of particles in each envelop for scenario 1. Total number of particles is 10^6.

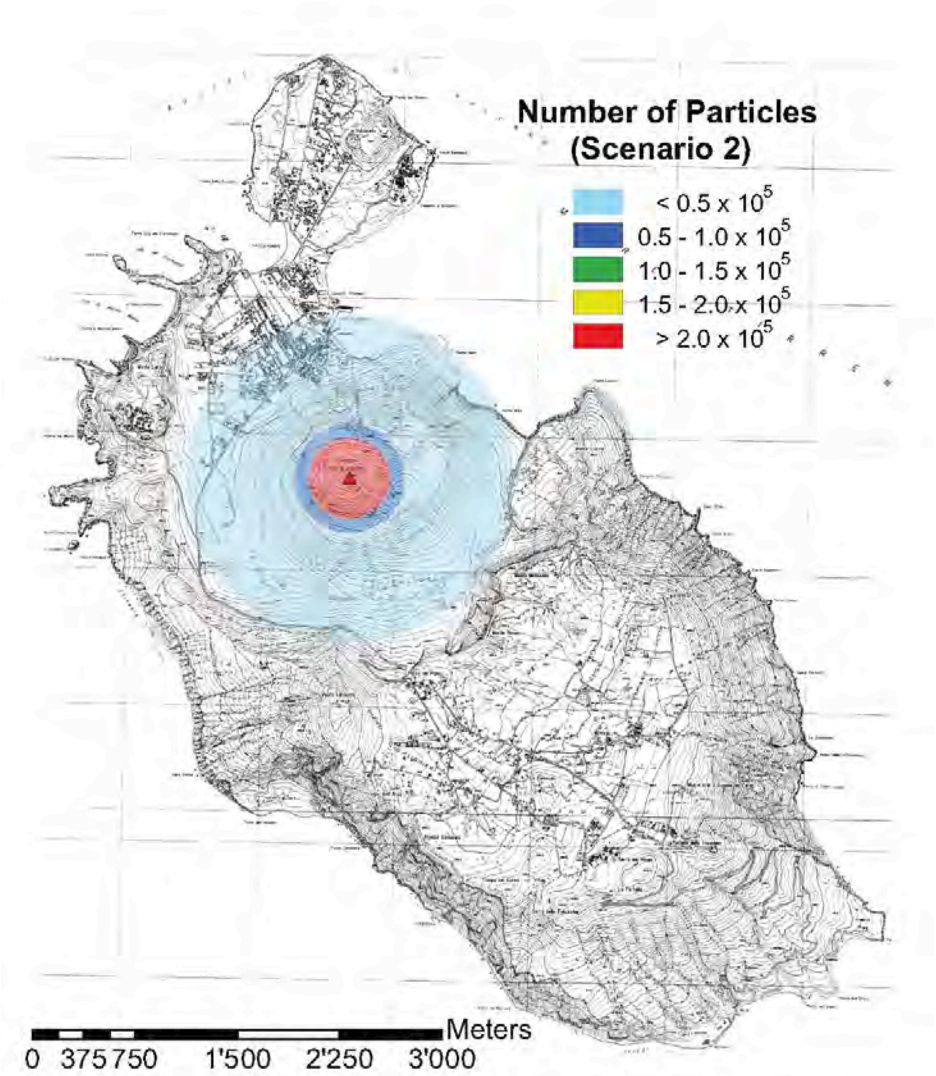

Fig. 7.22: Number of particles in each envelop for scenario 2. Total number of particles is 10^6.

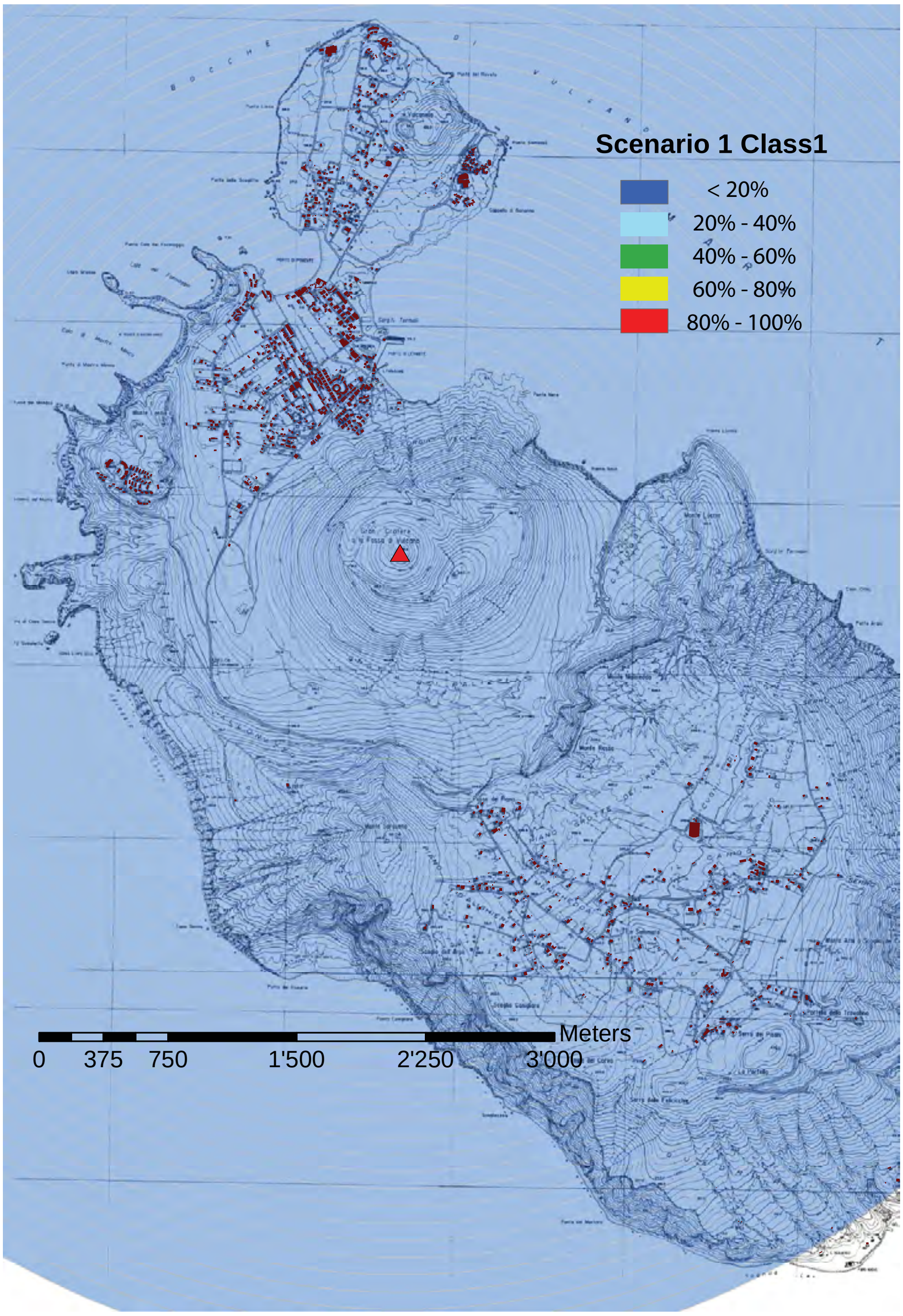

Fig. 7.23: Map of conditional probability $P(C \mid E)$ of penetration for scenario 1, Class 1.

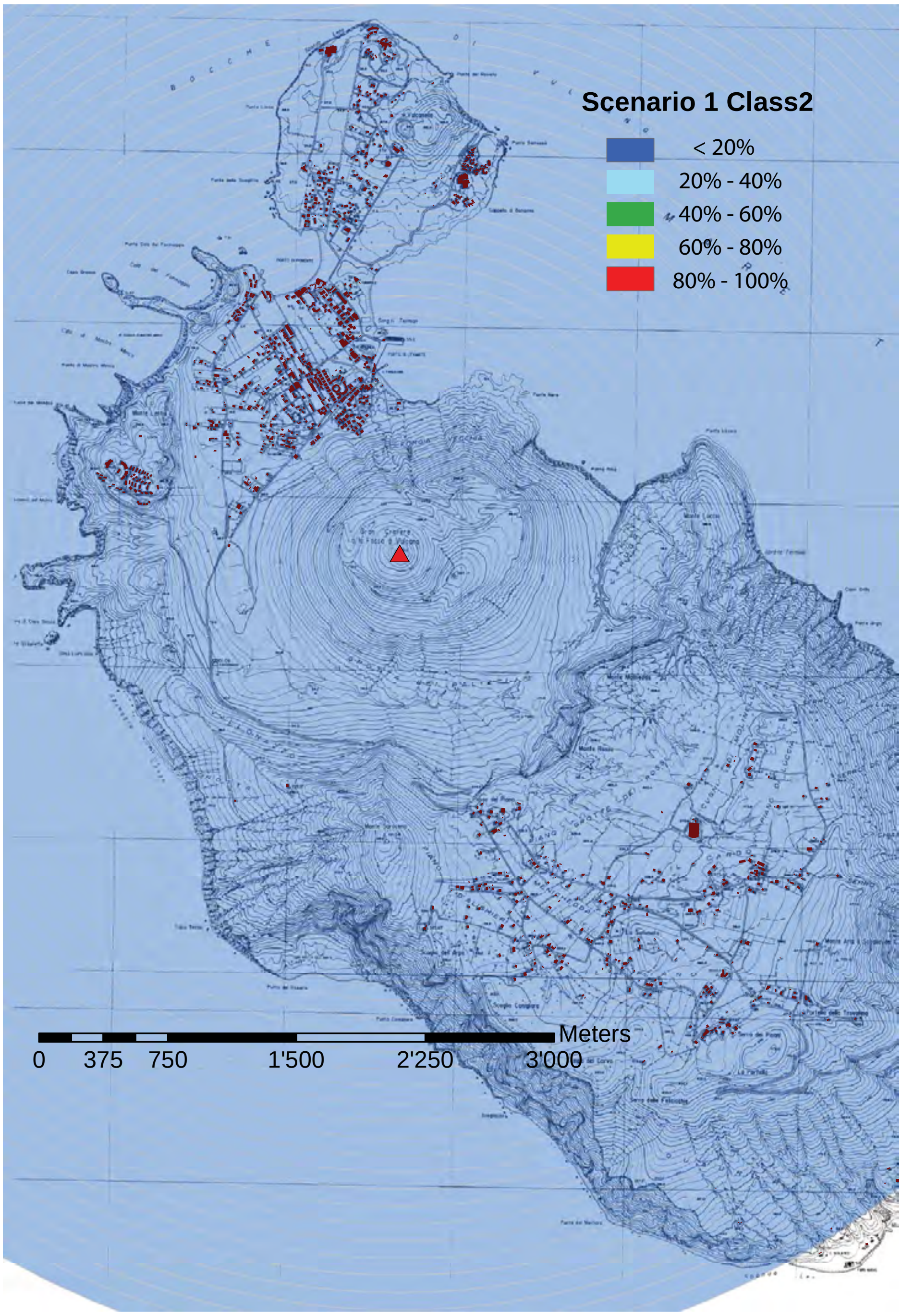

Fig. 7.24: Map of conditional probability $P(C \mid E)$ of penetration for scenario 1, Class 2.

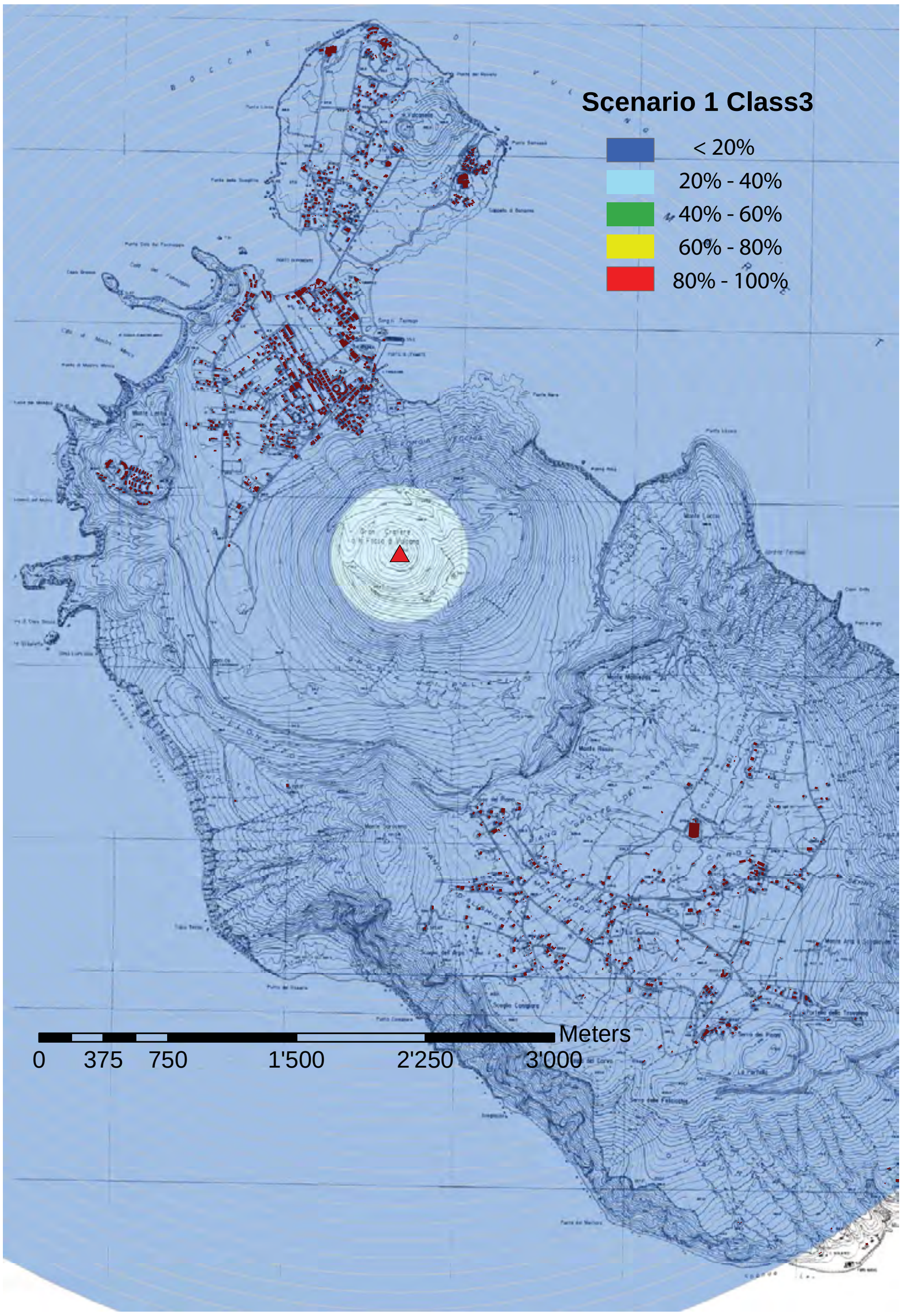

Fig. 7.25: Map of conditional probability $P(C \mid E)$ of penetration for scenario 1, Class 3.

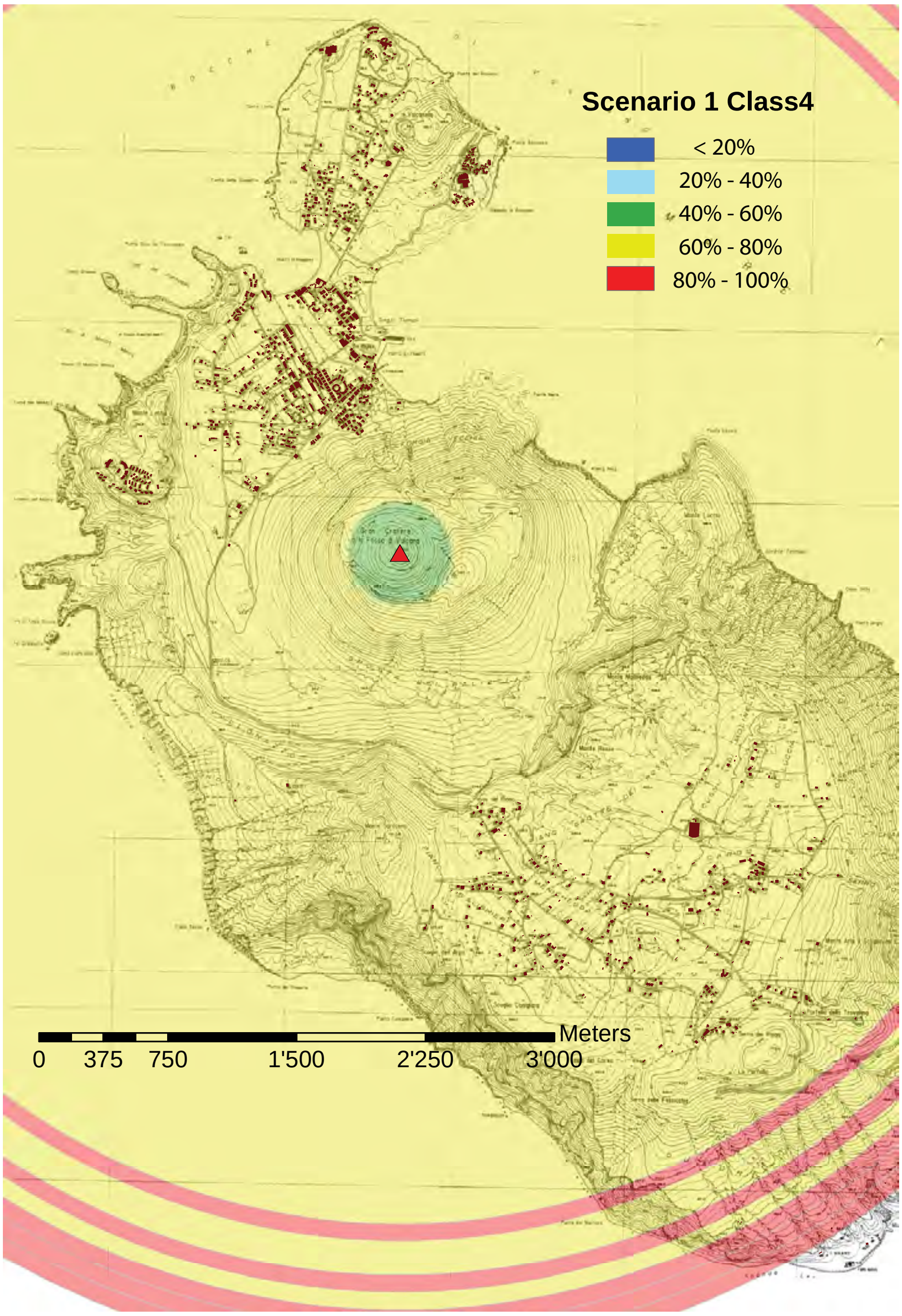

(a)

Fig. 7.26: Map of conditional probability $P(C \mid E)$ of penetration for scenario 1, Class 4.

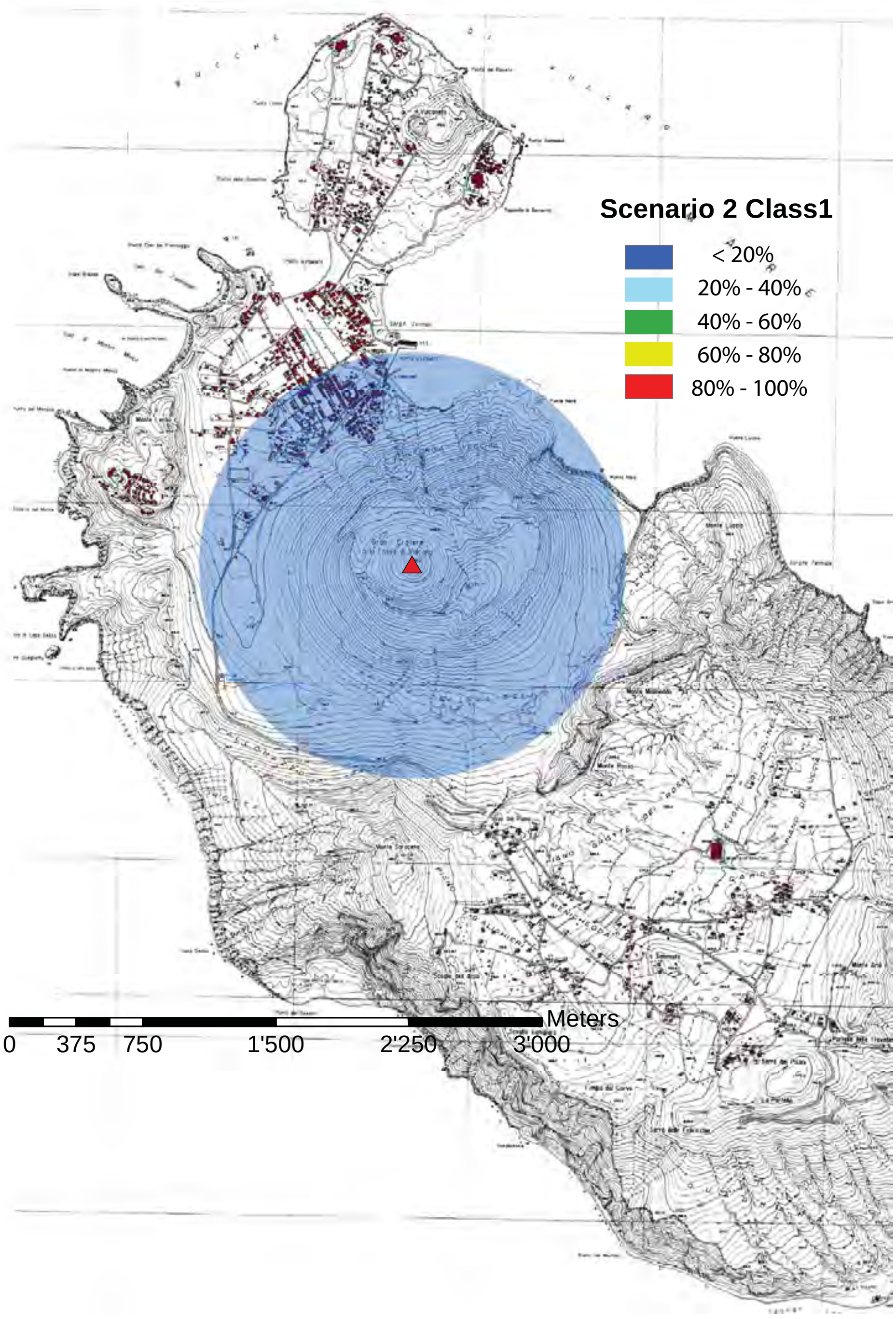

Fig. 7.27: Map of conditional probability $P(C \mid E)$ of penetration for scenario 2, Class 1.

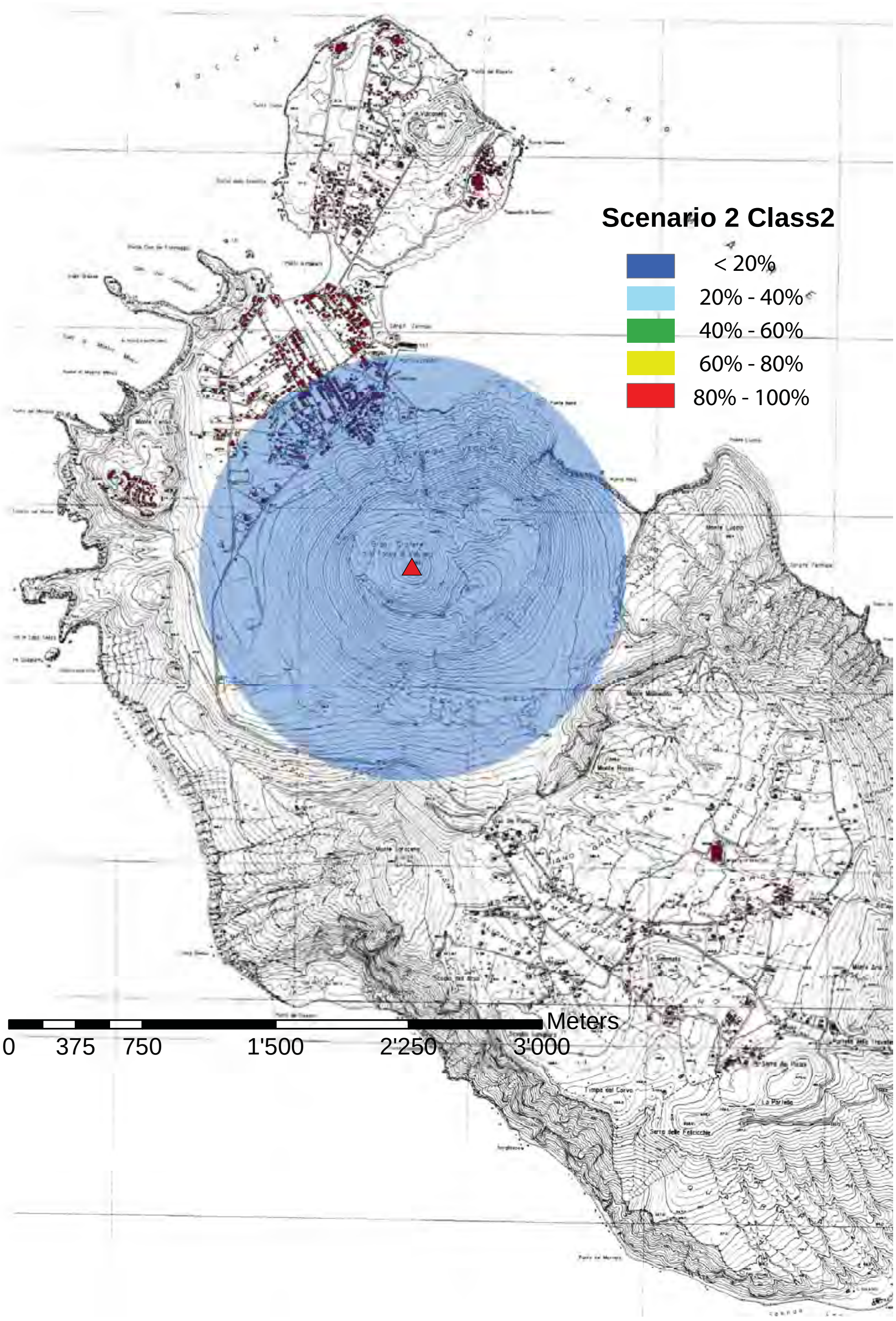

Fig. 7.28: Map of conditional probability $P(C \mid E)$ of penetration for scenario 2, Class 2.

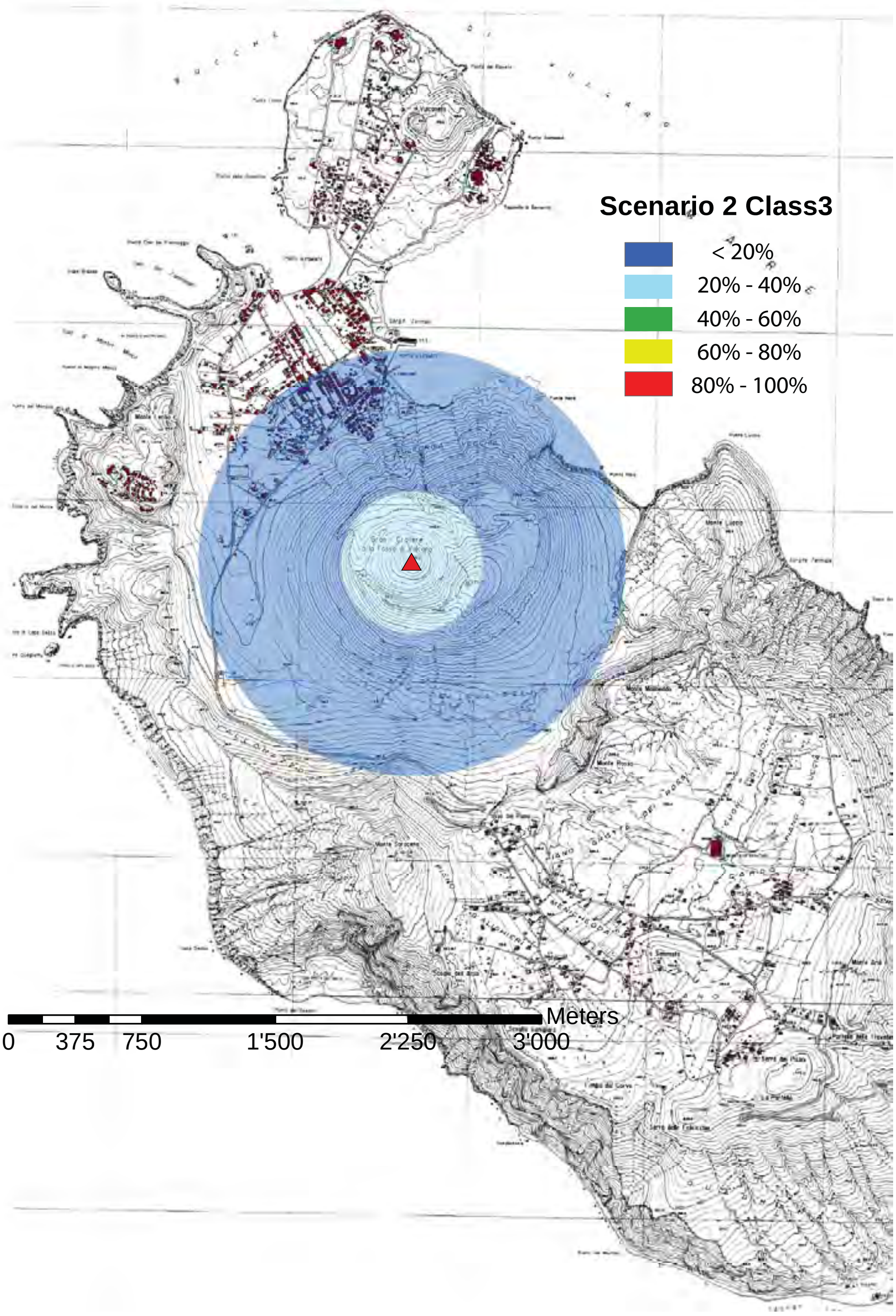

Fig. 7.29: Map of conditional probability $P(C \mid E)$ of penetration for scenario 2, Class 3.

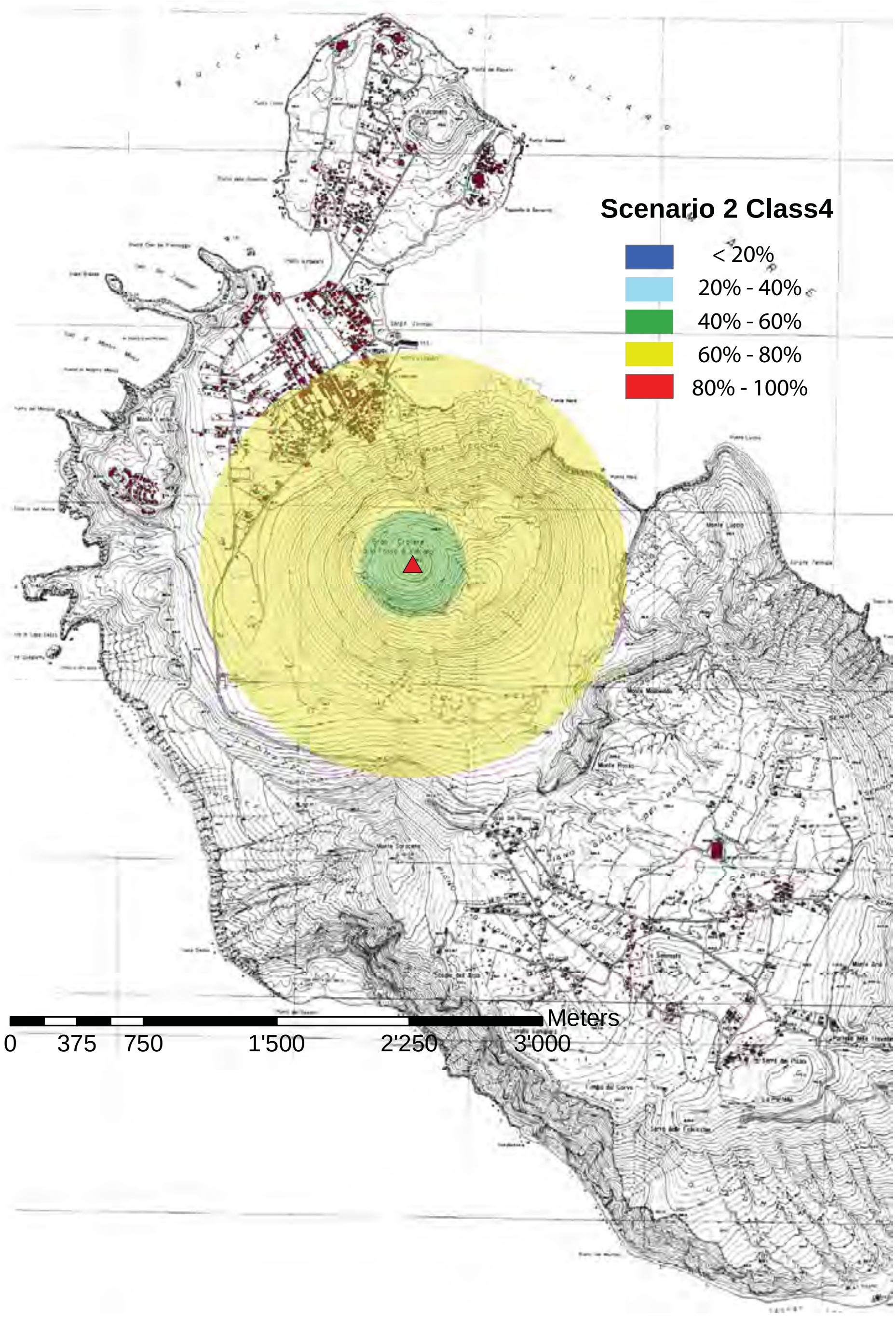

Fig. 7.30: Map of conditional probability $P(C \mid E)$ of penetration for scenario 2, Class 4.

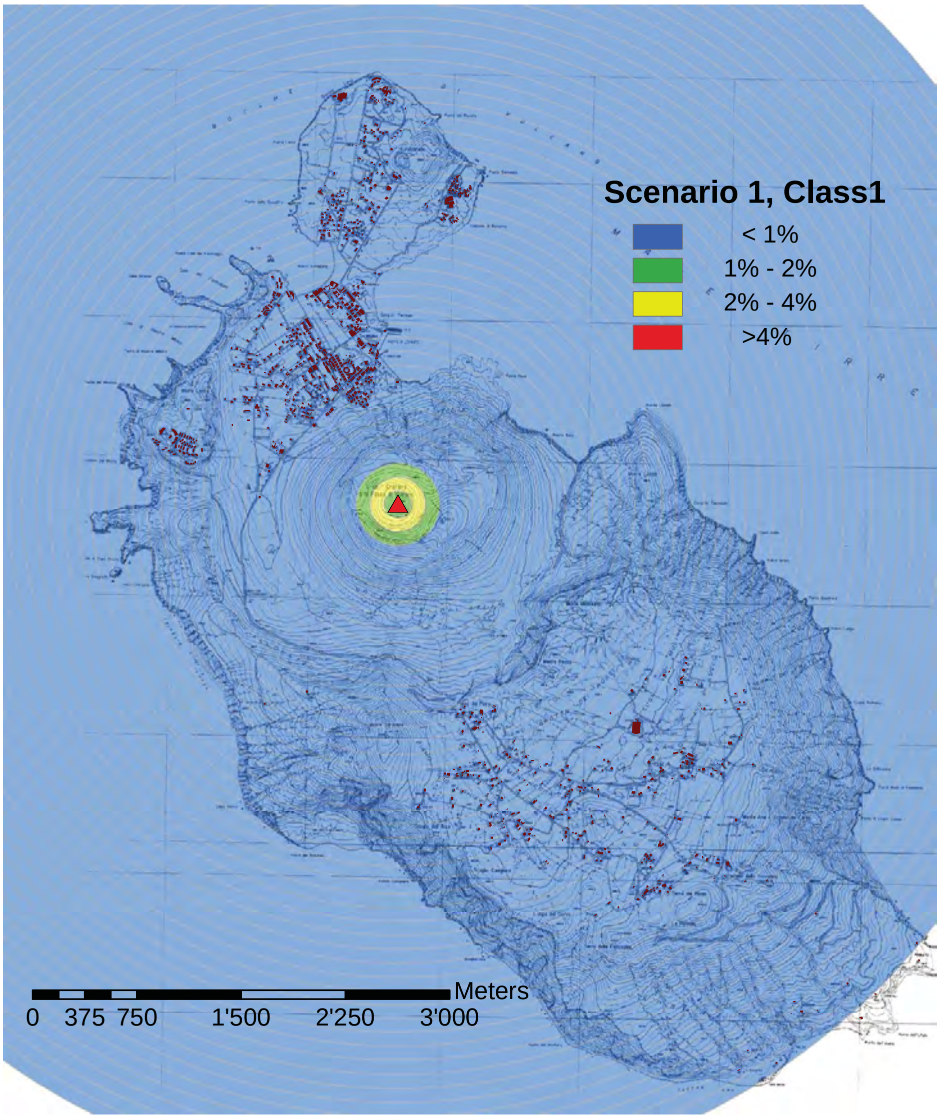

Fig. 7.31: Map of joint probability $P(E, C)$ of penetration for scenario 1, Class 1.

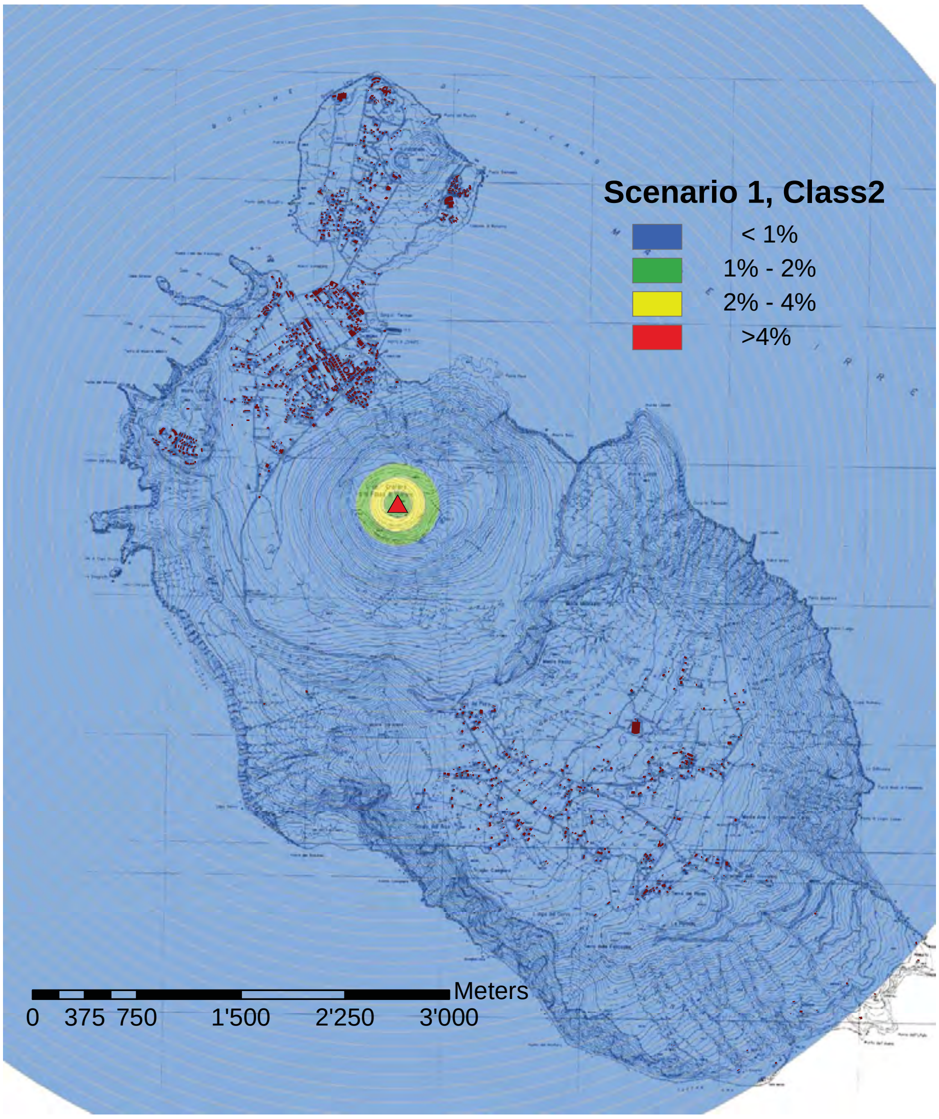

Fig. 7.32: Map of joint probability $P(E, C)$ of penetration for scenario 1, Class 2.

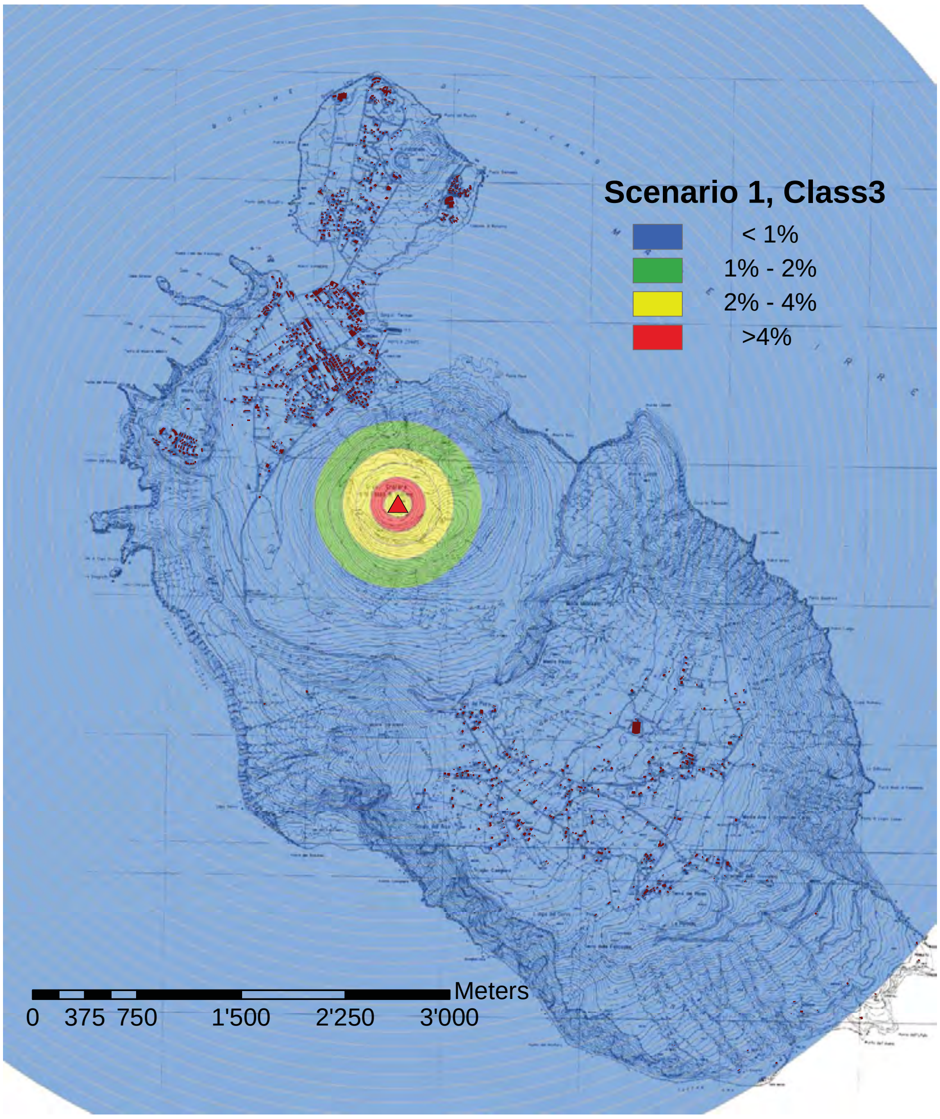

Fig. 7.33: Map of joint probability $P(E, C)$ of penetration for scenario 1, Class 3.

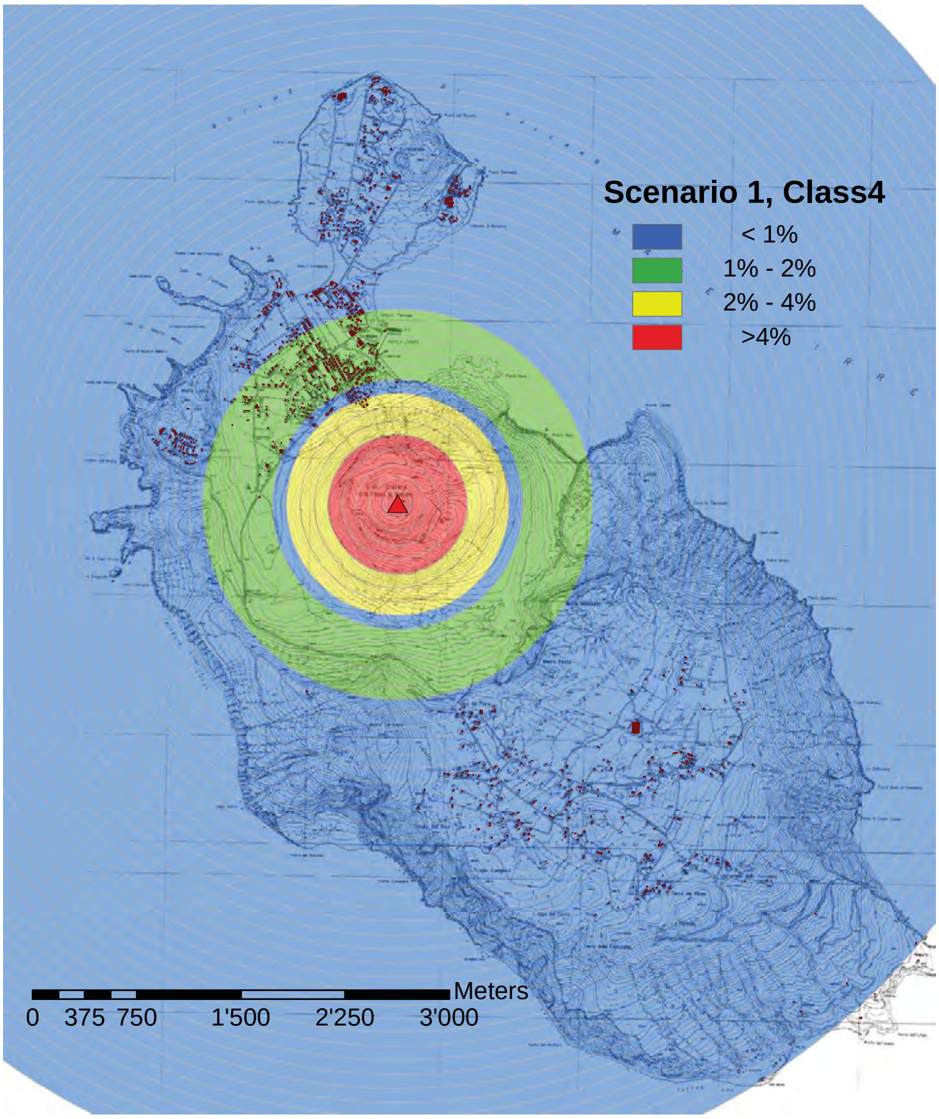

Fig. 7.34: Map of joint probability $P(E, C)$ of penetration for scenario 1, Class 4.

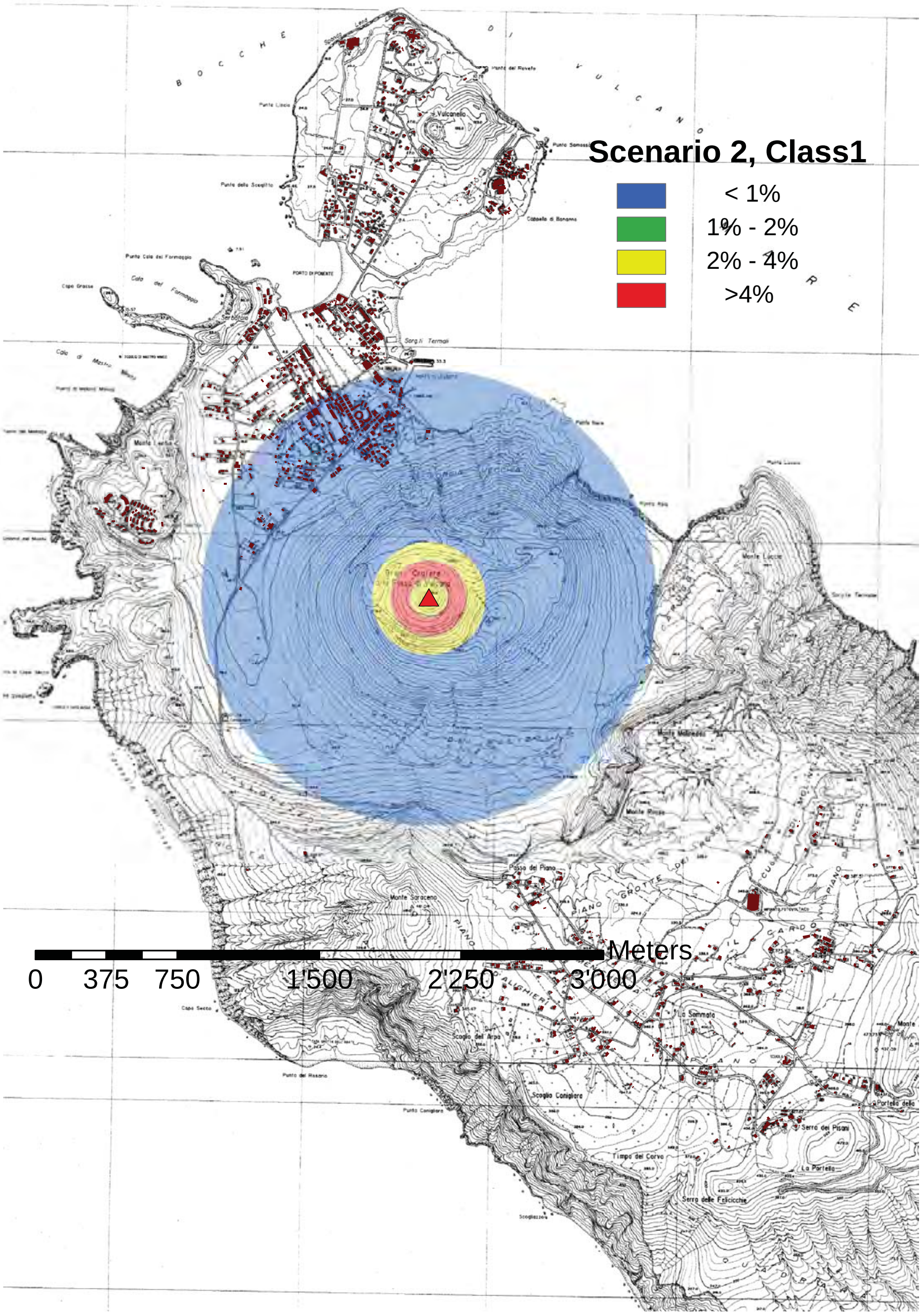

Fig. 7.35: Map of joint probability $P(E, C)$ of penetration for scenario 2, Class 1.

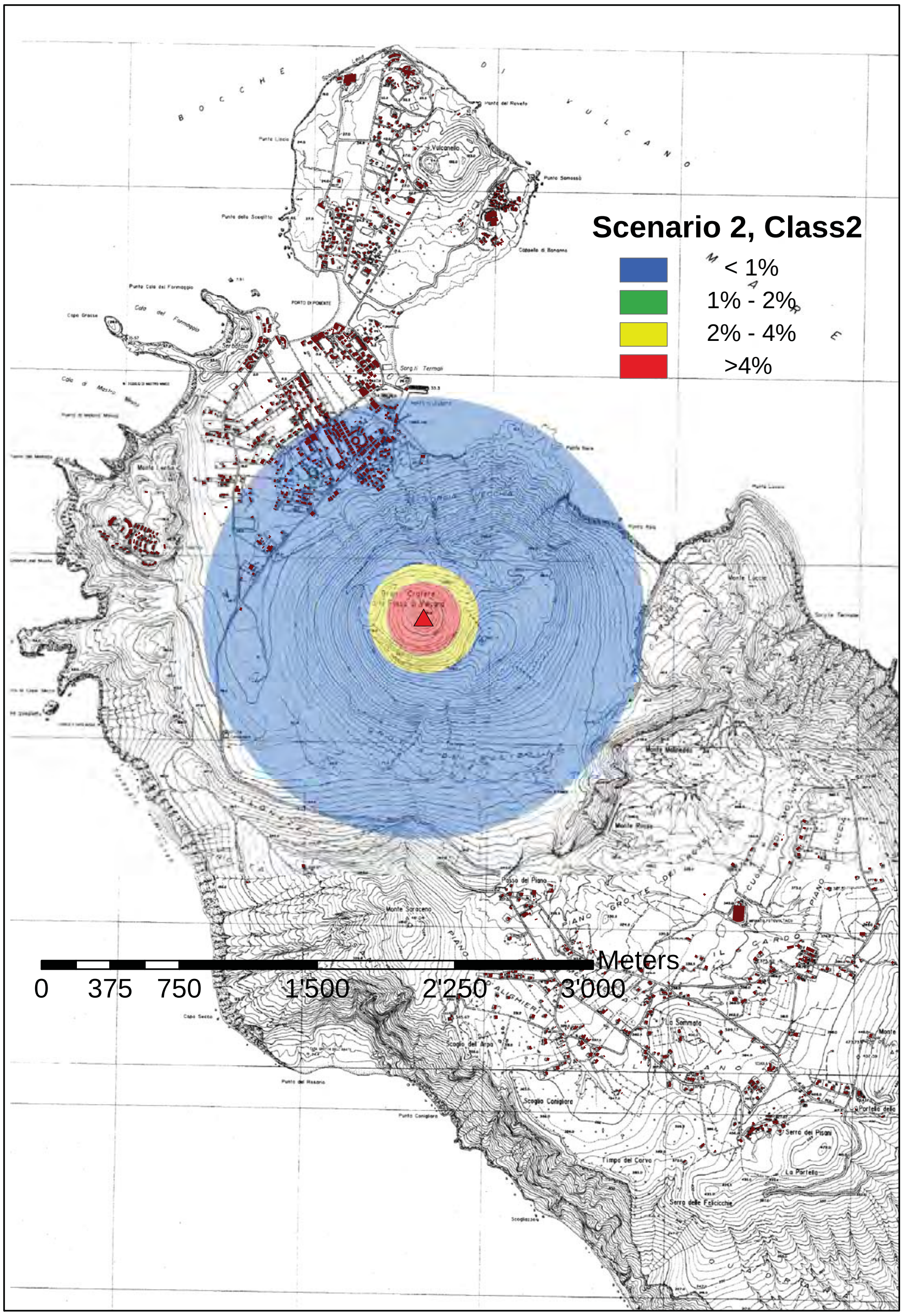

Fig. 7.36: Map of joint probability $P(E, C)$ of penetration for scenario 2, Class 2.

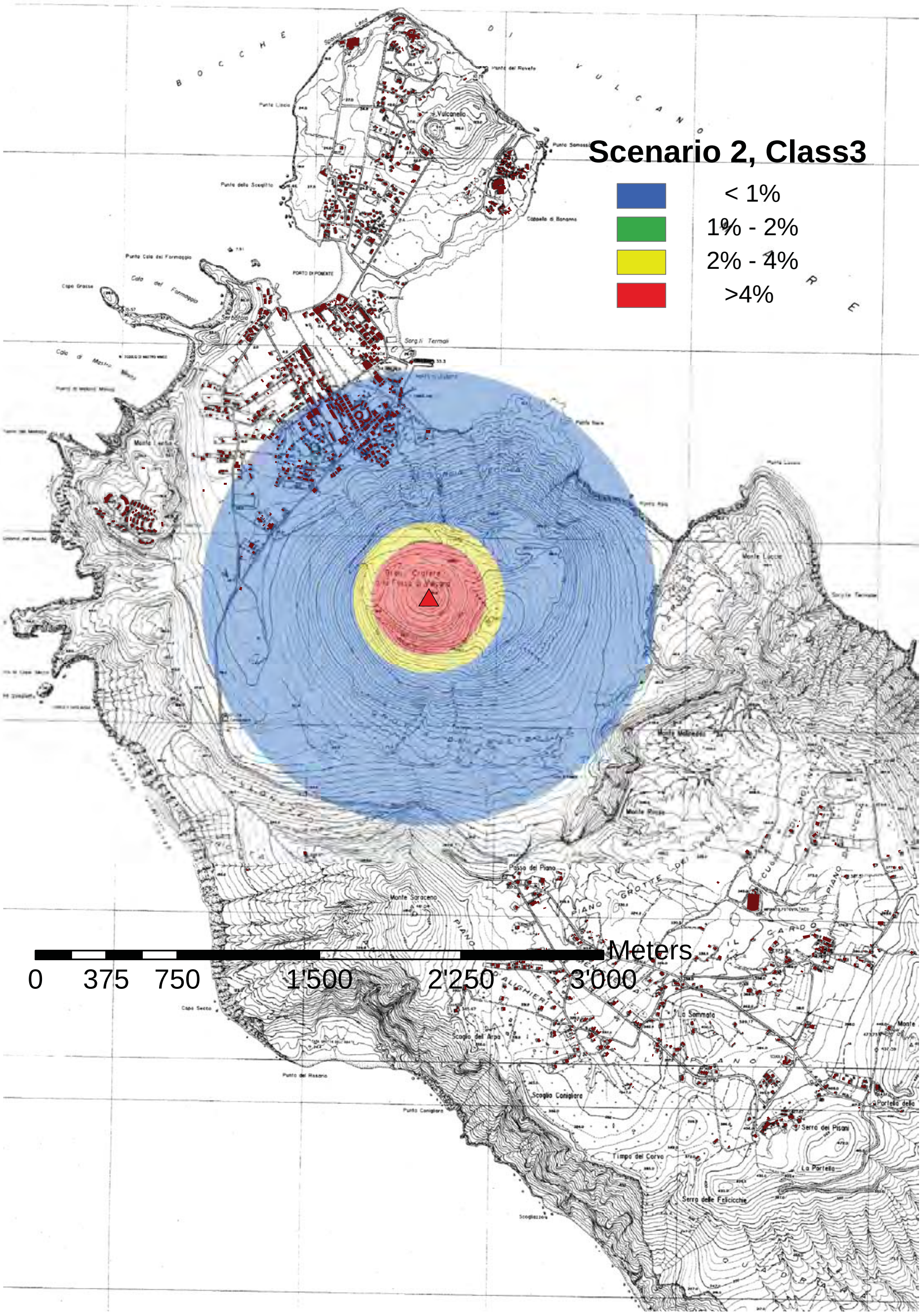

Fig. 7.37: Map of joint probability $P(E, C)$ of penetration for scenario 2, Class 3.

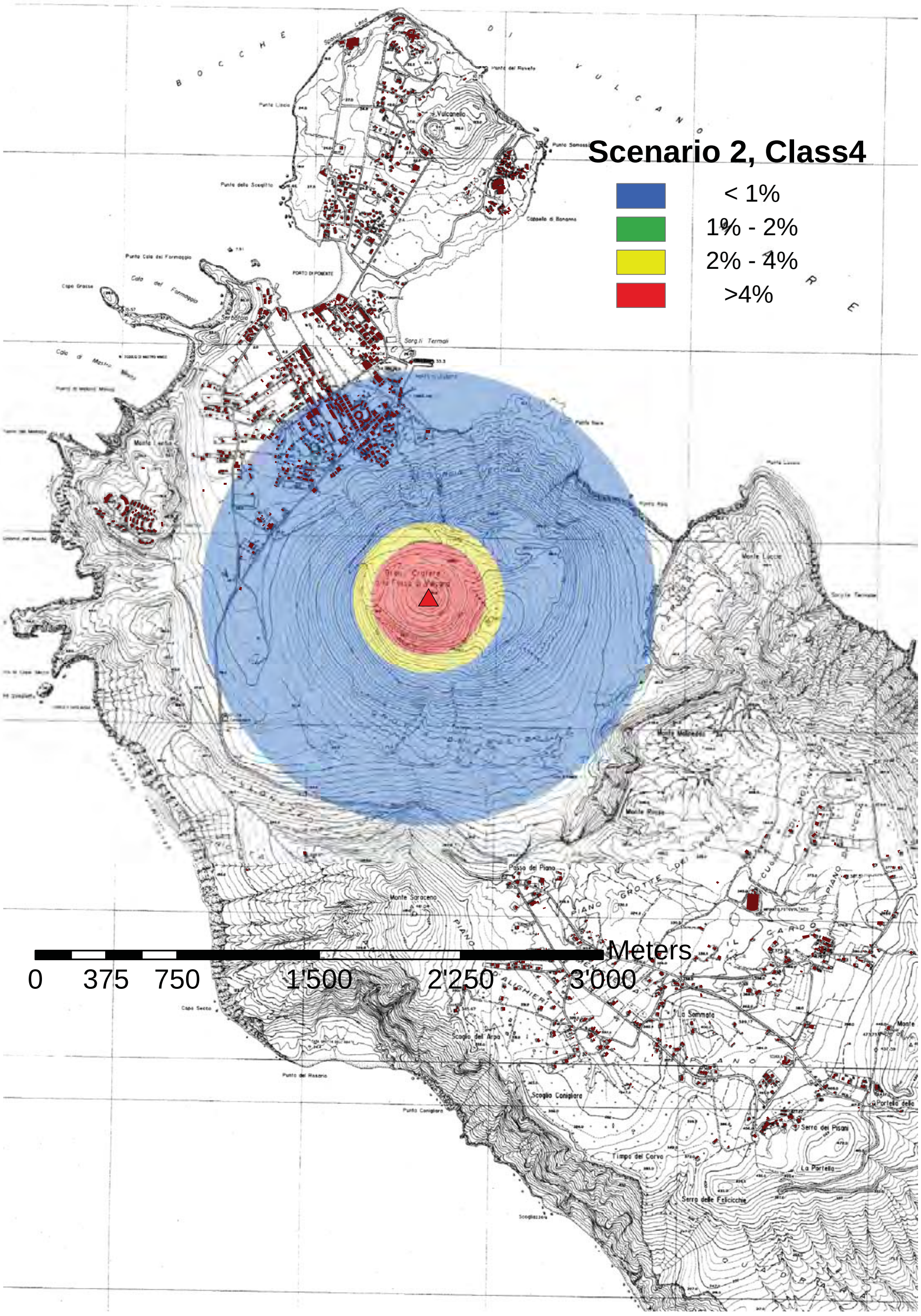

Fig. 7.38: Map of joint probability $P(E, C)$ of penetration for scenario 2, Class 4.

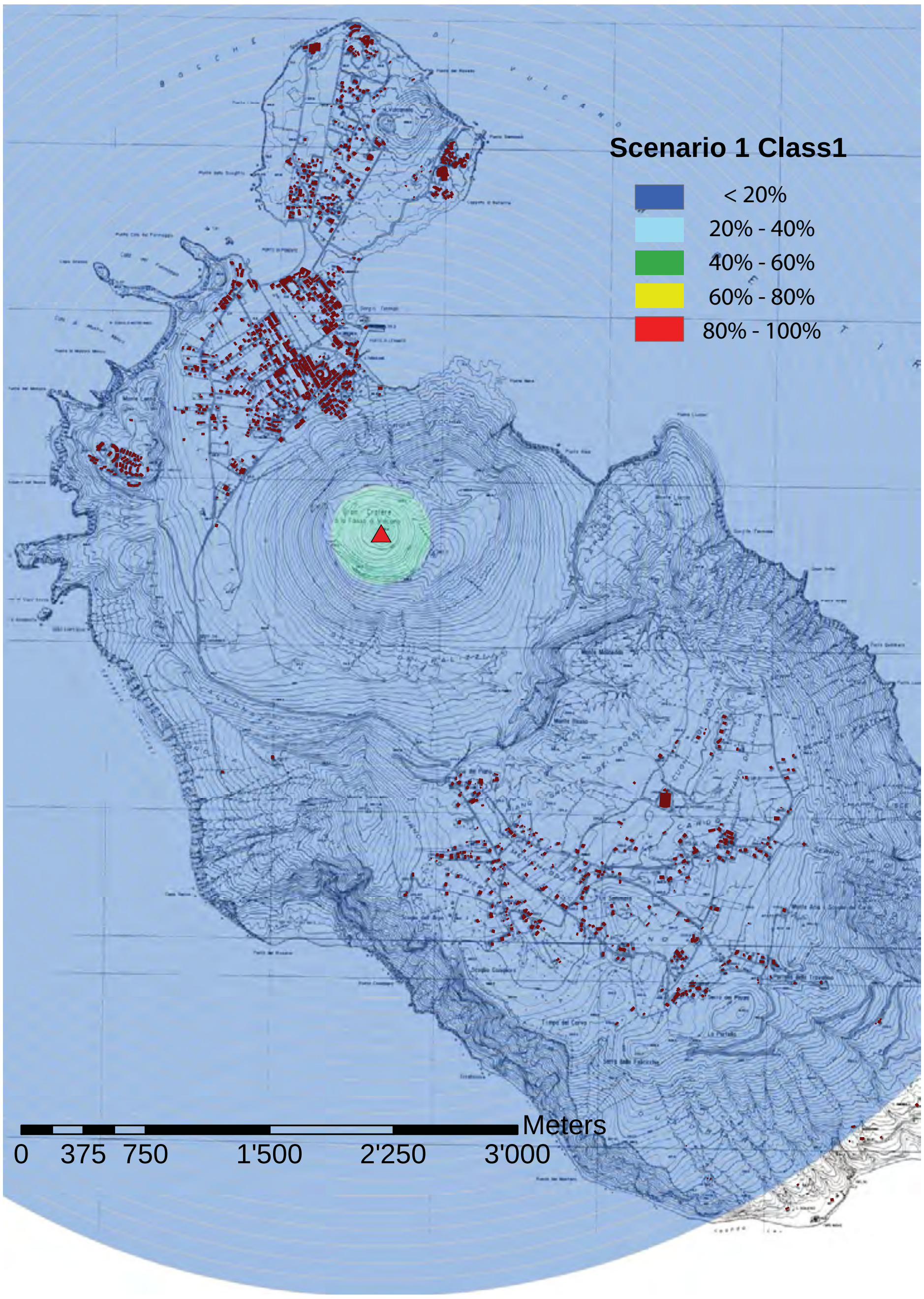

Fig. 7.39: Map of conditional probability $P(C \mid E)$ of roof collapse for scenario 1, Class 1.

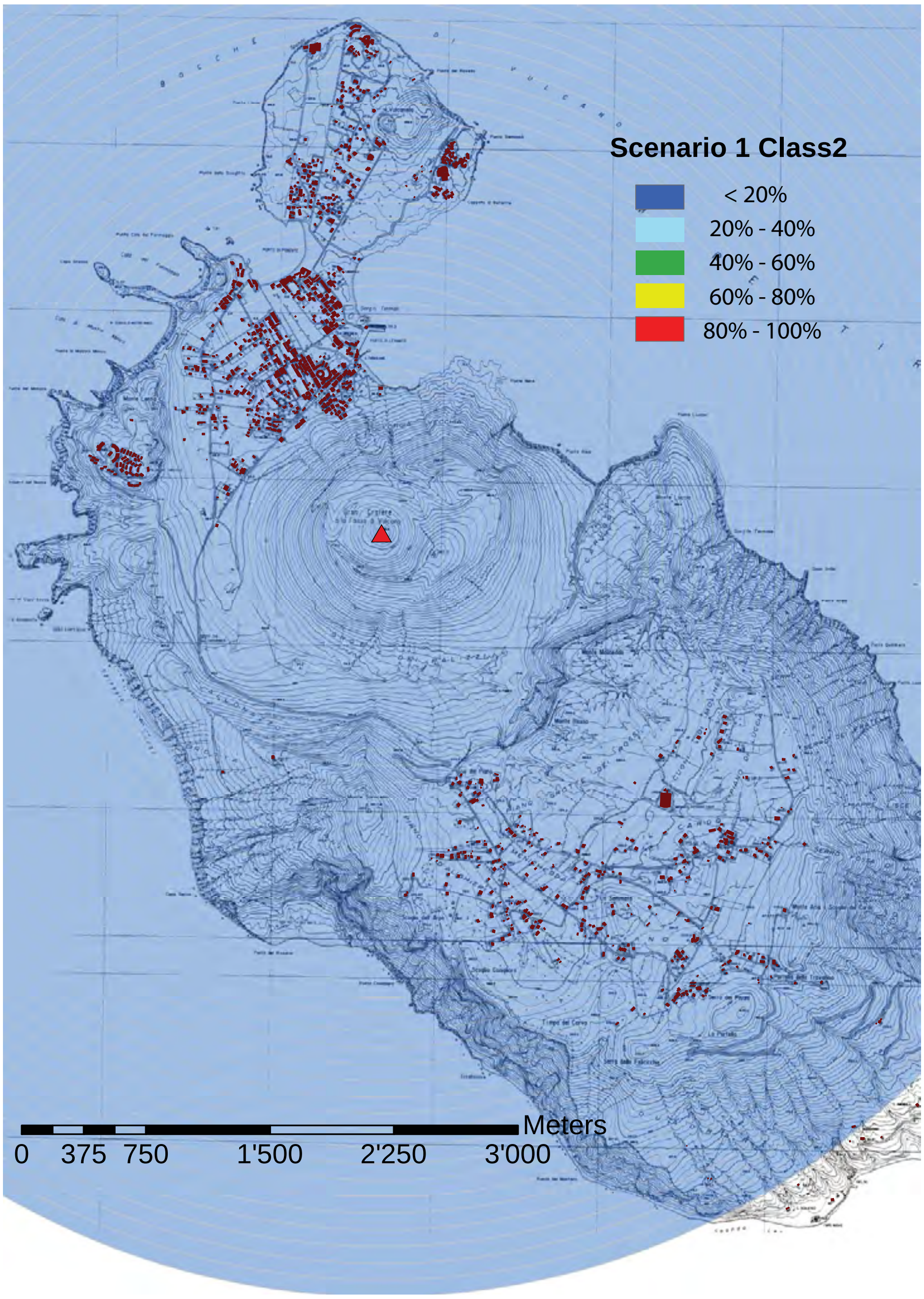

Fig. 7.40: Map of conditional probability $P(C \mid E)$ of roof collapse for scenario 1, Class 2.

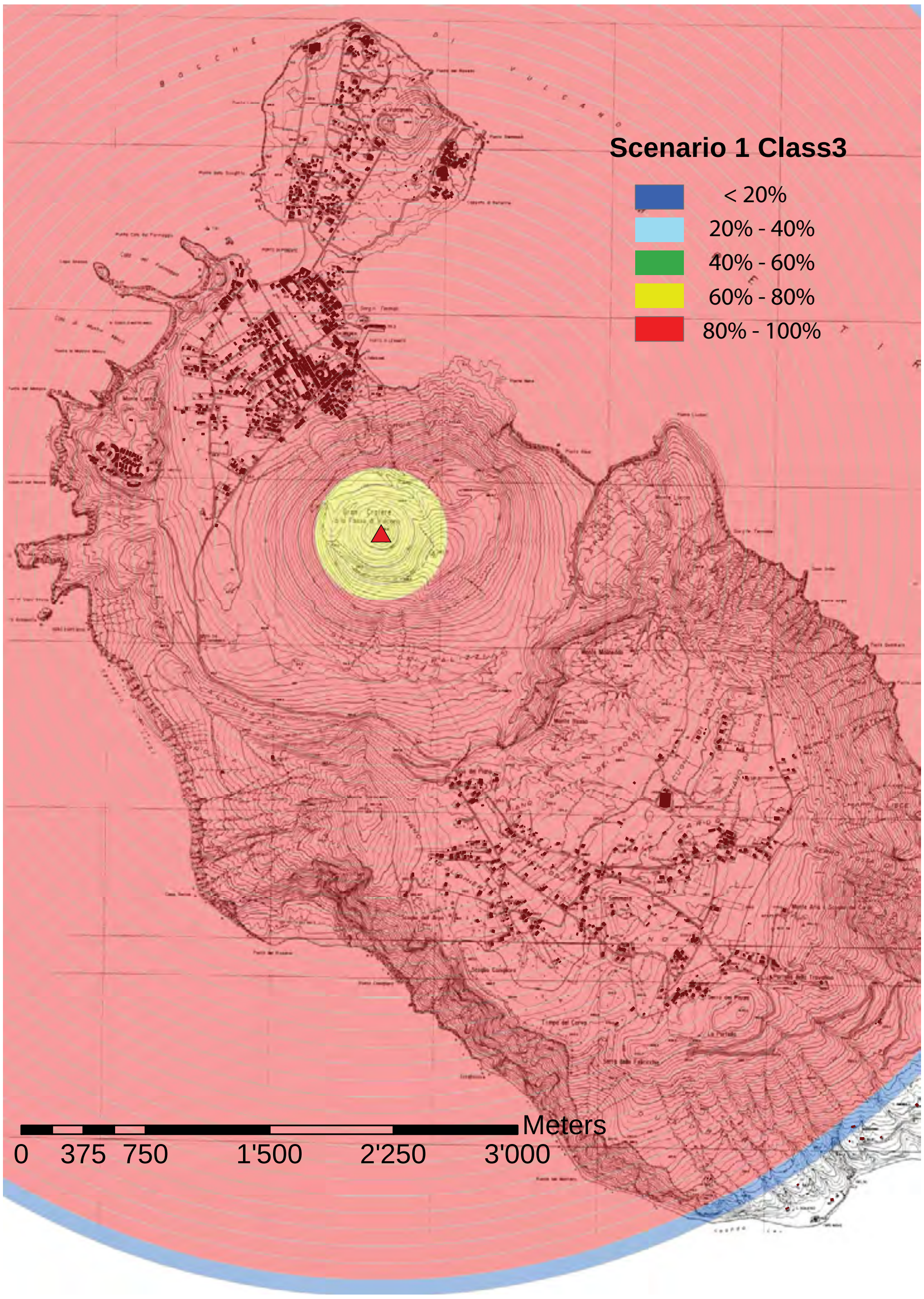

Fig. 7.41: Map of conditional probability $P(C \mid E)$ of roof collapse for scenario 1, Class 3.

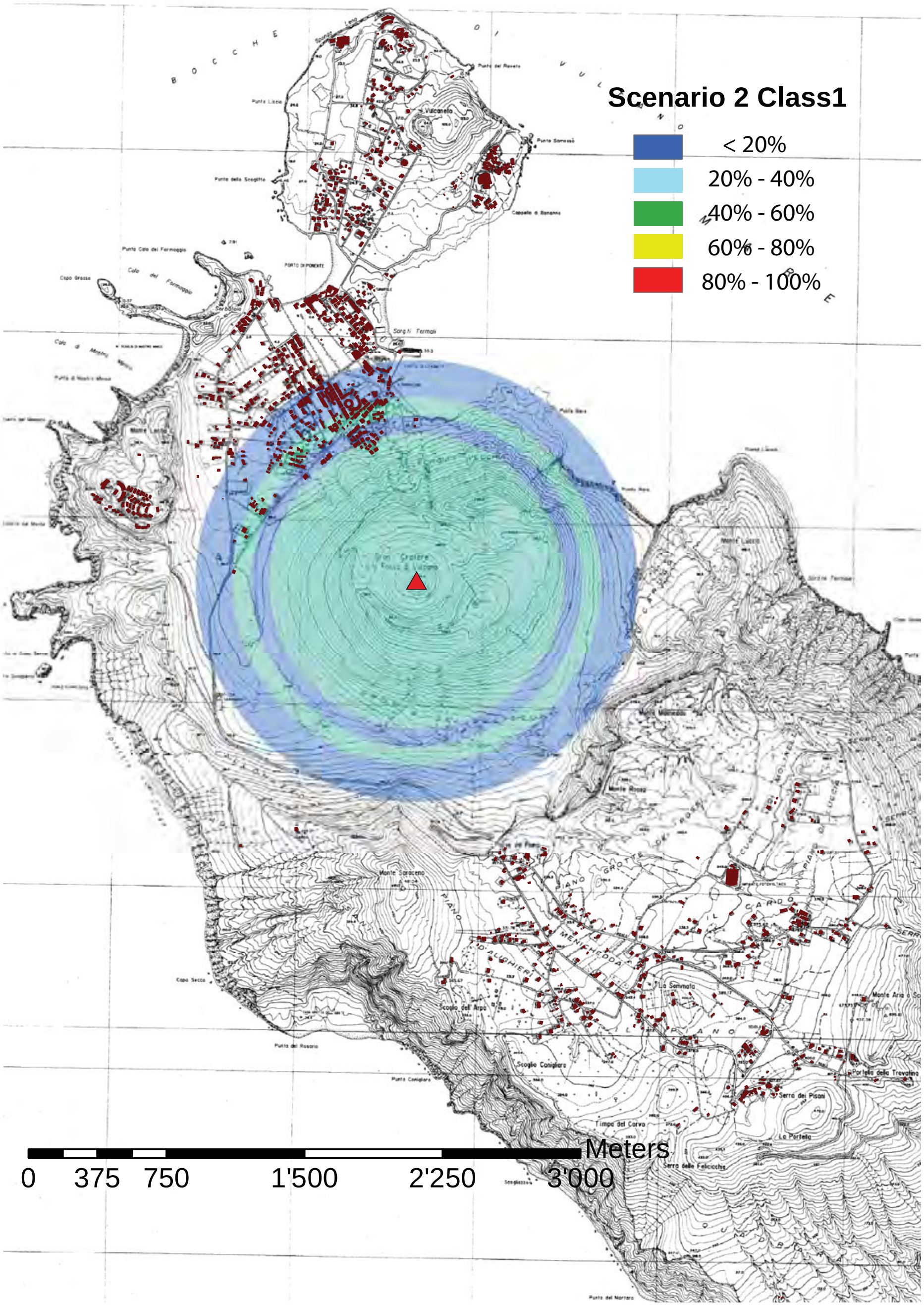

Fig. 7.42: Map of conditional probability $P(C \mid E)$ of roof collapse for scenario 2, Class 1.

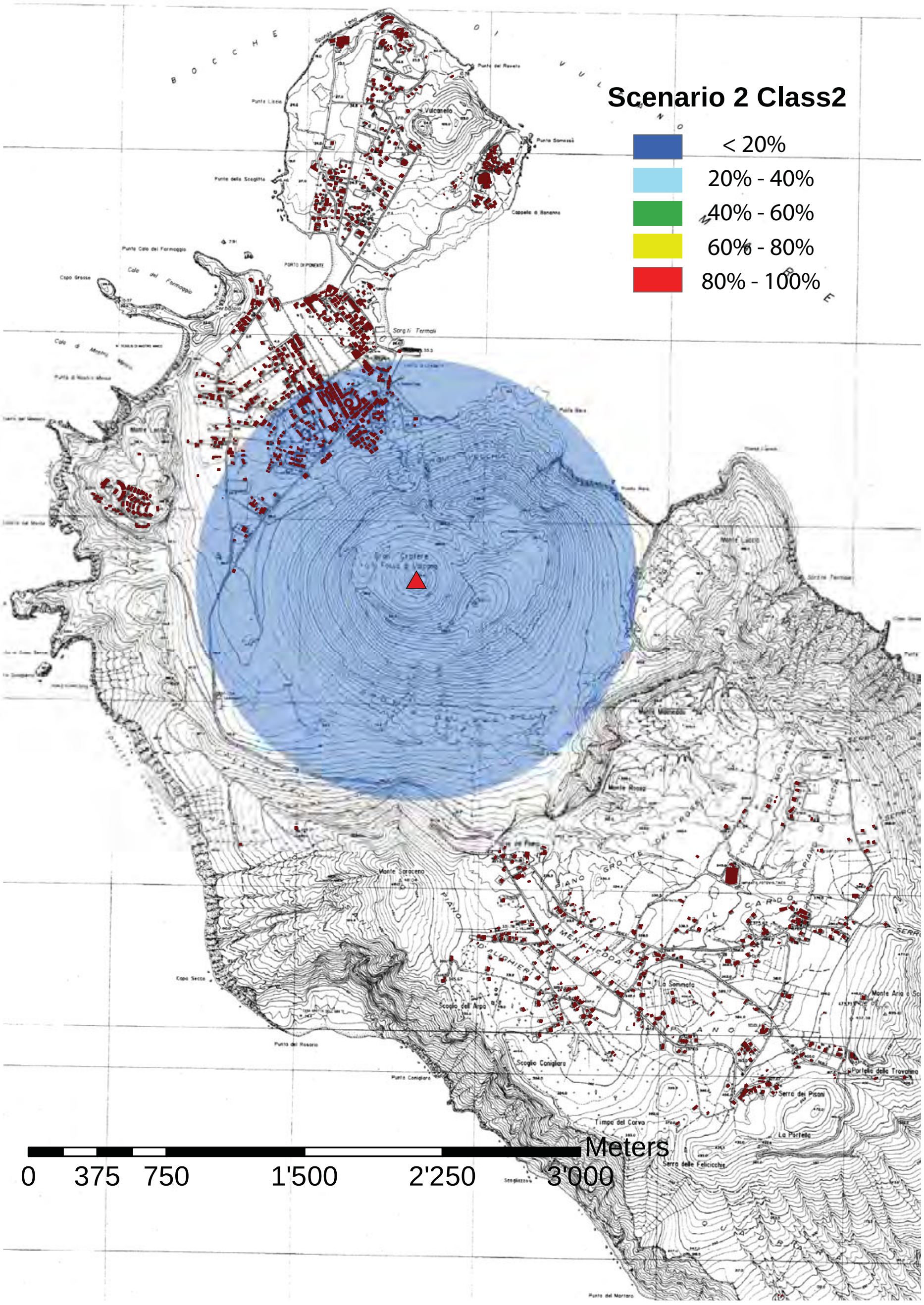

Fig. 7.43: Map of conditional probability $P(C \mid E)$ of roof collapse for scenario 2, Class 2.

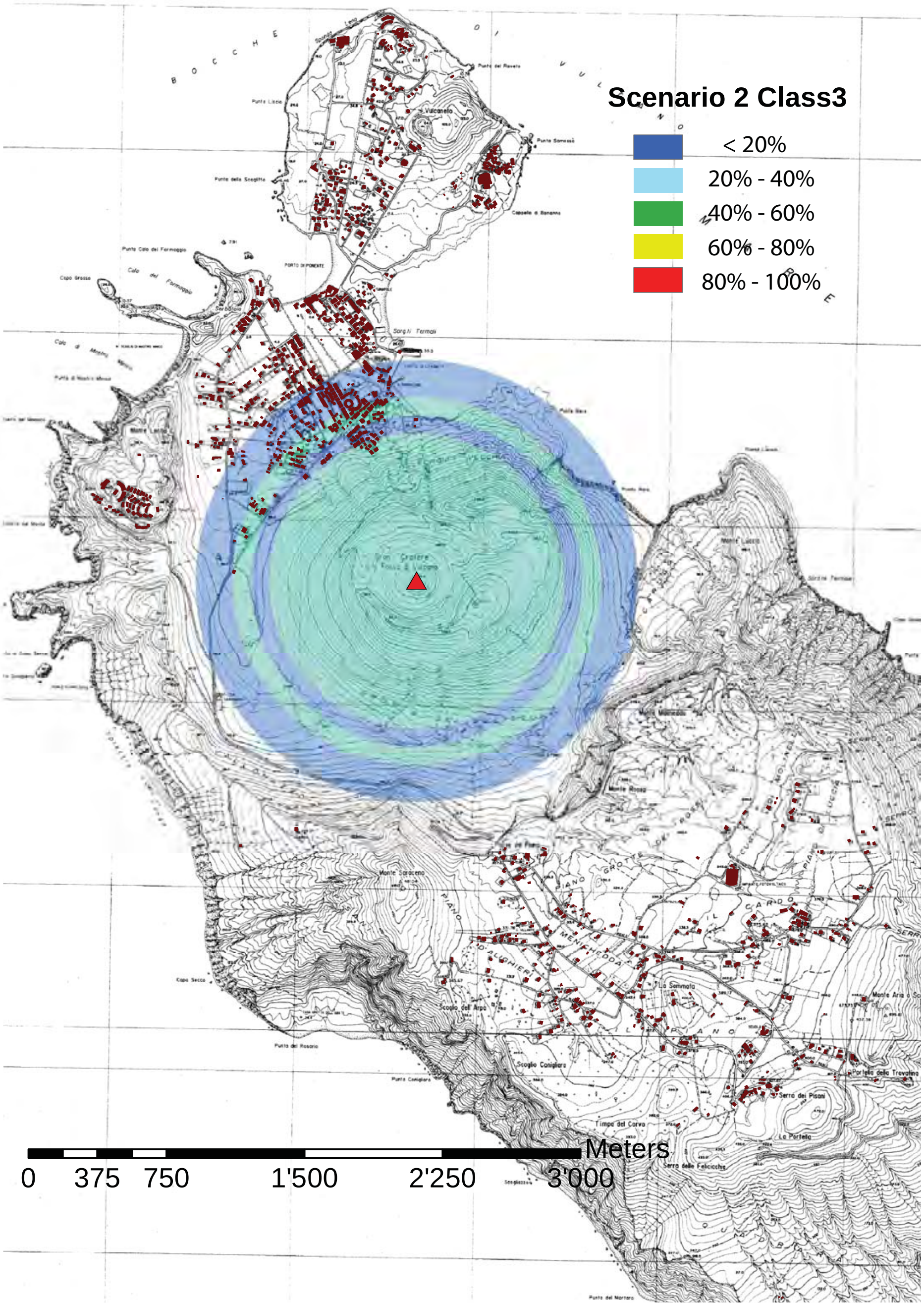

Fig. 7.44: Map of conditional probability $P(C \mid E)$ of roof collapse for scenario 2, Class 3.

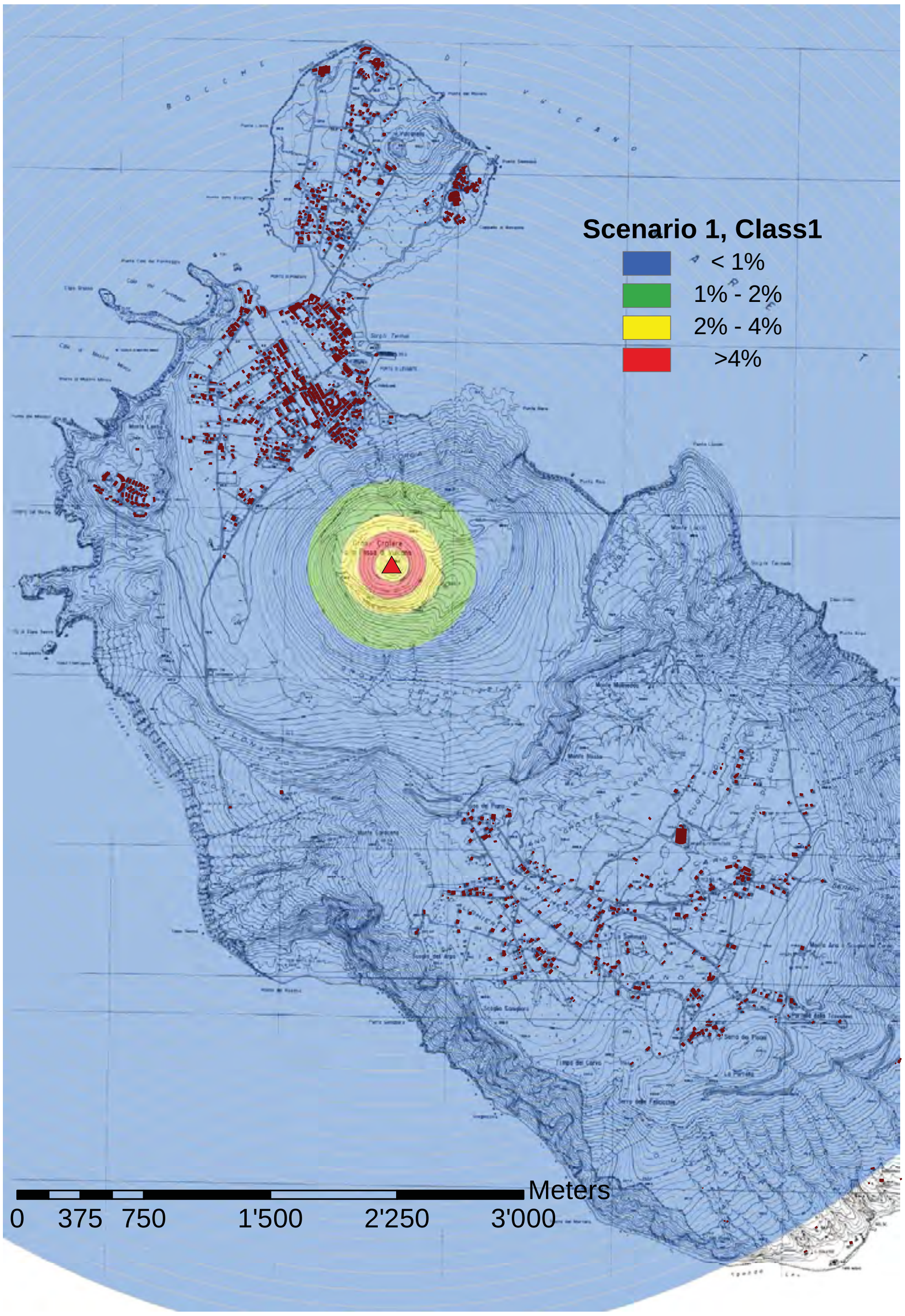

Fig. 7.45: Map of joint probability $P(E, C)$ of roof collapse for scenario 1, Class 1.

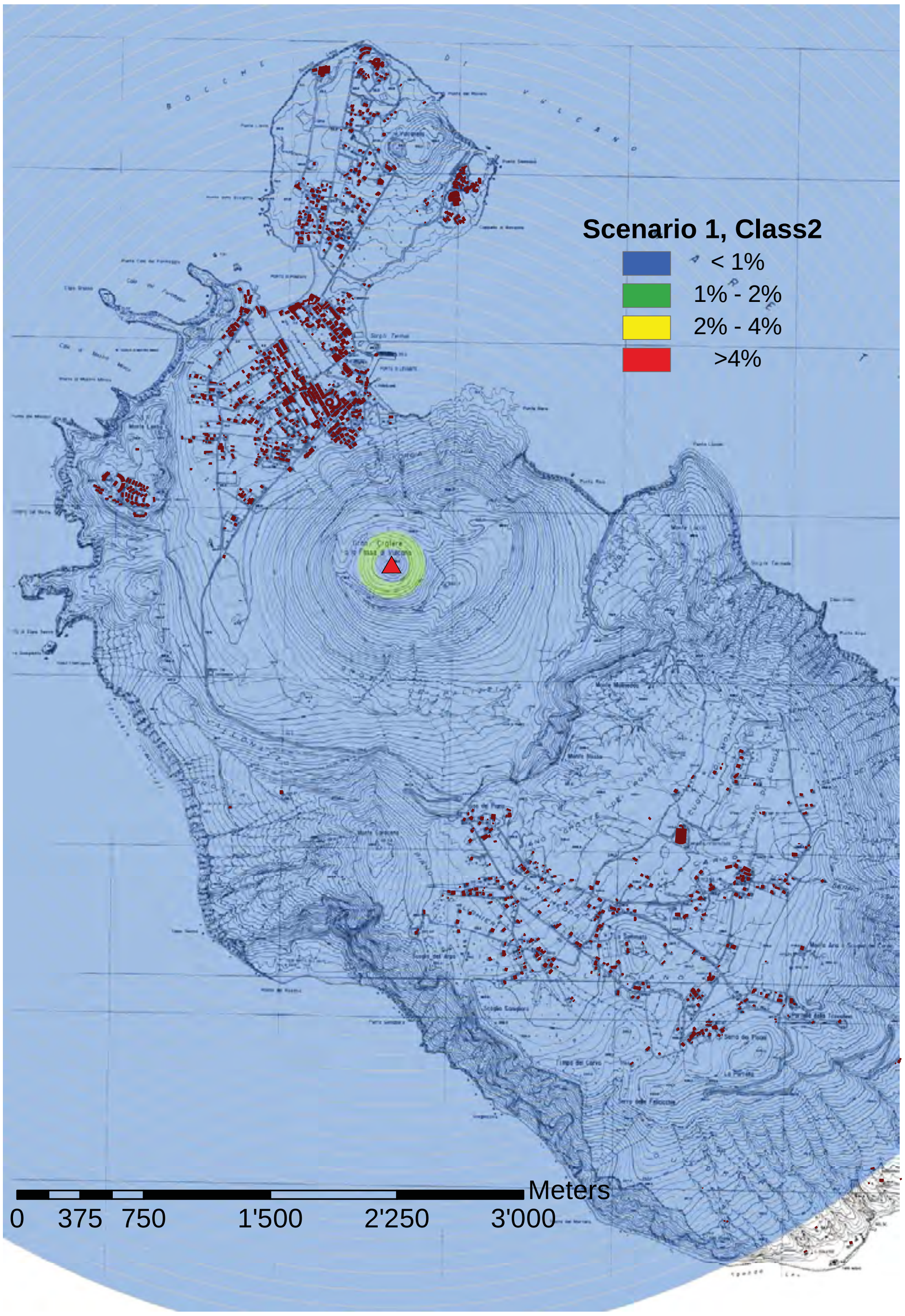

Fig. 7.46: Map of joint probability $P(E, C)$ of roof collapse for scenario 1, Class 2.

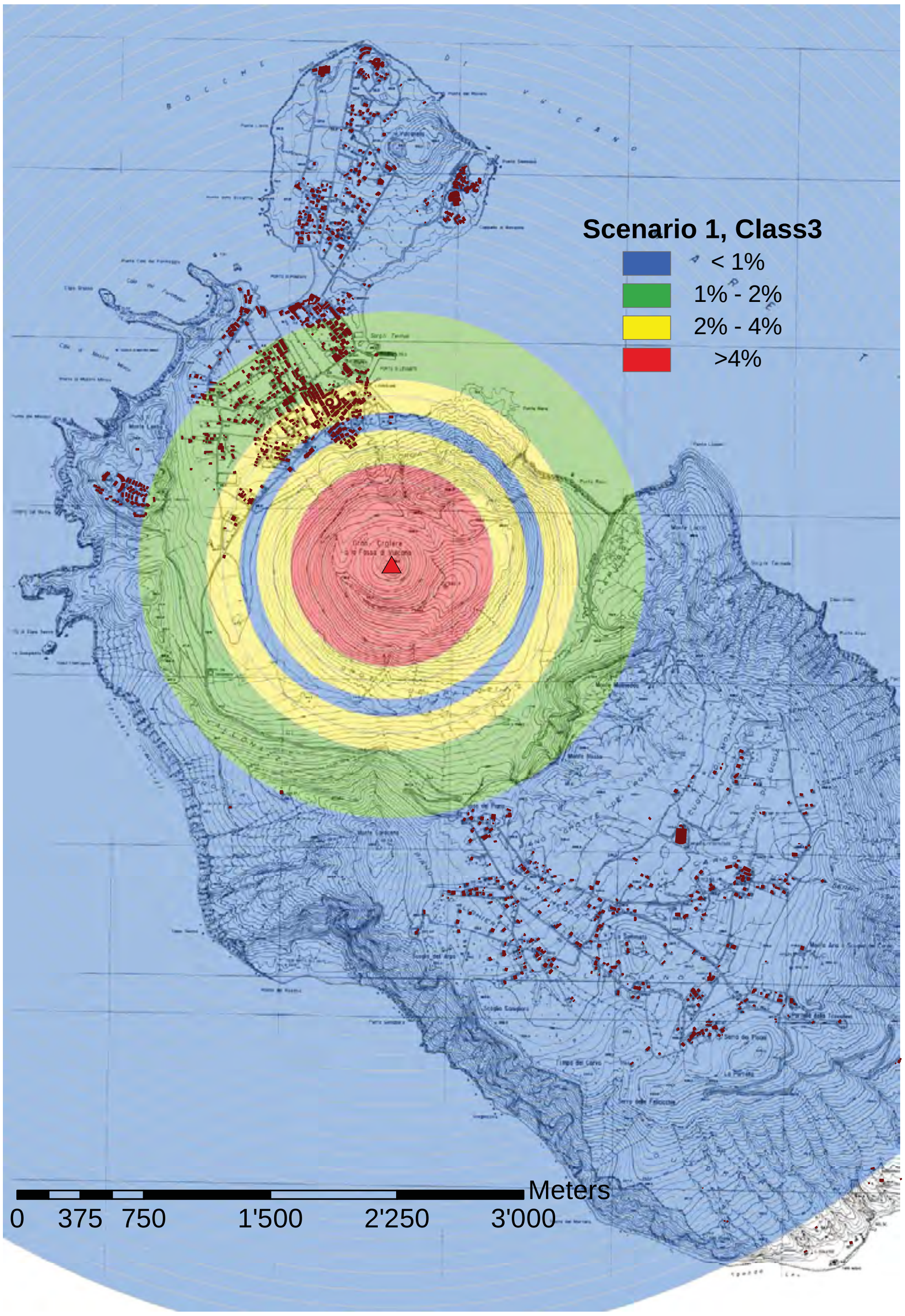

Fig. 7.47: Map of joint probability $P(E, C)$ of roof collapse for scenario 1, Class 3.

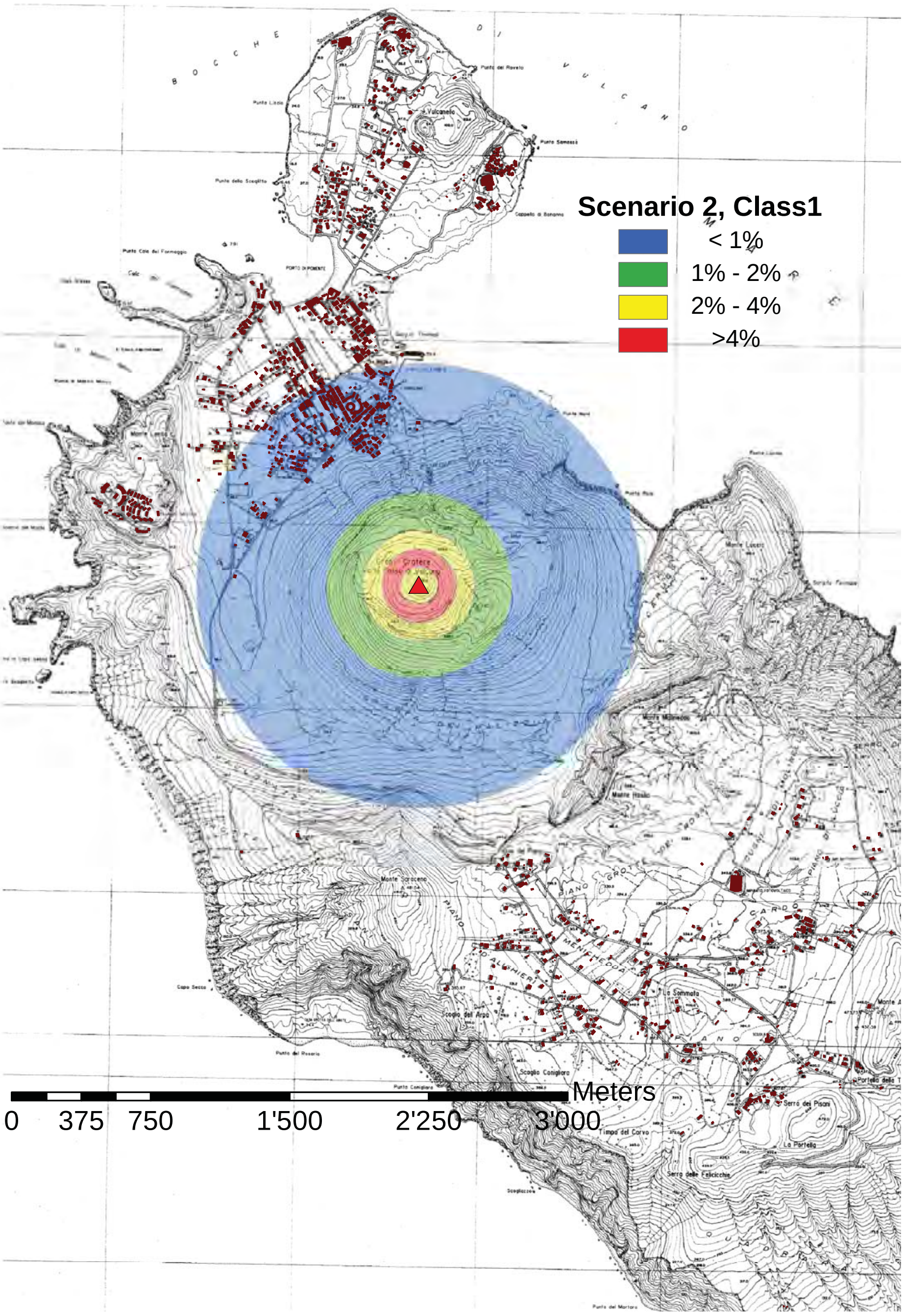

Fig. 7.48: Map of joint probability $P(E, C)$ of roof collapse for scenario 2, Class 1.

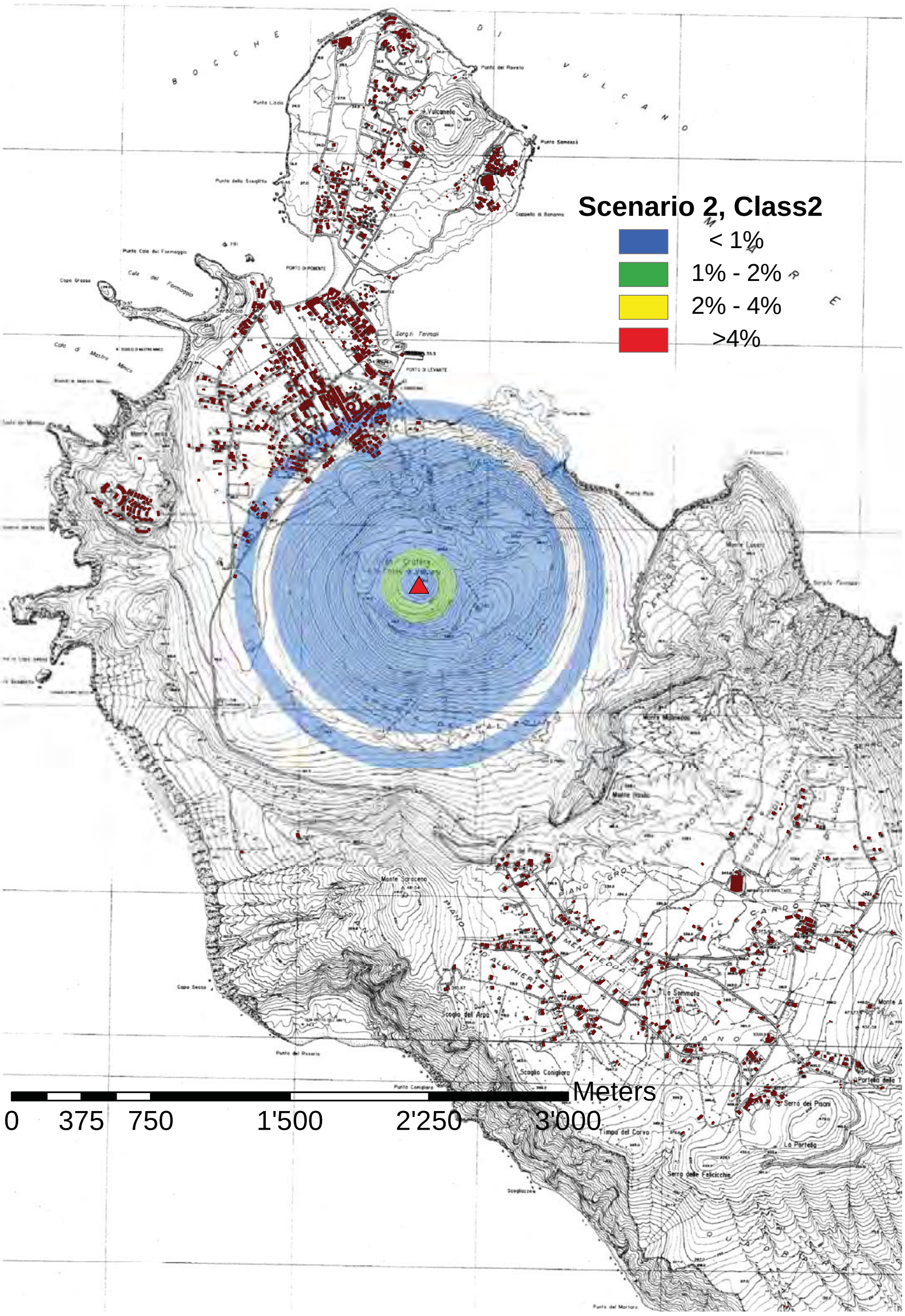

Fig. 7.49: Map of joint probability $P(E, C)$ of roof collapse for scenario 2, Class 2.

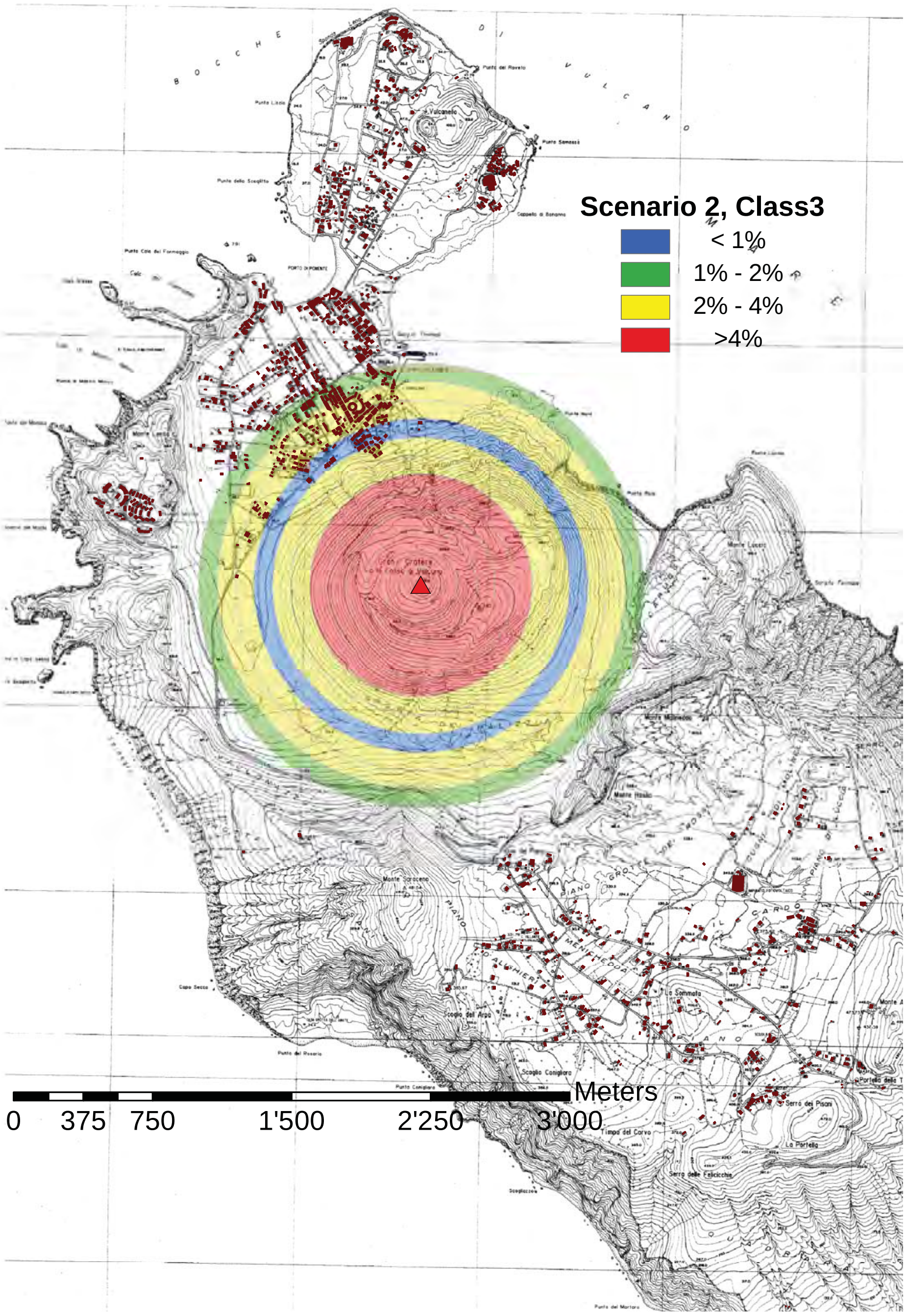

Fig. 7.50: Map of joint probability $P(E, C)$ of roof collapse for scenario 2, Class 3.

7.4 Discussion

Our 3D multiparticle ballistic model (Chapter 6) is useful for hazard assessment because it simulates 2D distribution of particles on the ground. However, as the results of simulations are analyzed axysimmetrically, 3D effect is neglected. Former models are sophisticated in implementation of drag force but most of them are single particle models (Wilson ,1972 [133]; Fagents and Wilson, 1993 [46]; Bower and Woods,1996 [18]; Mastin, 2002 [73]; Alatorre-Ibargüengoitia and Delgado-Granados, 2006 [1]), or multiparticle but not in 3D (Saunderson, 2008 [98]). Although our model does not include the drag force yet, could be implemented to include it (see section 6.4 of Chapter 6 for details).

It is important to use enough particles for the simulation to detect statistical characteristics. According to the results, 10^6 particles show the smoothest energy and probability curves (Fig. 7.9- Fig. 7.12, Fig. 7.13-Fig. 7.20). Therefore, 10^6 particles are enough to detect statistical characteristics regardless of actual number of particles in each eruption.

We have analyzed the distribbution of energy and probabilities as a function of distance from vent. In the Vulcano case, average ejection angle is expected to be vertical based on the shape of the crater although crater can change by erosion or collapse. Consequently, the distribution of the particles is circular and axisymmetric. Therefore it is possible to describe the probability trend as a function of distance from vent. In the case when the ejection angle is inclined, a different approach would be needed because the distribution of particles on the ground is not axisymmetric.

Two types of energy are calculated from the results of the simulations; averaged energy (Fig. 7.9 and Fig. 7.10) and cumulated energy (Fig. 7.11 and Fig. 7.12). Averaged energy is the average of the energy of all particles sedimented in a given envelop. It represents the most probable energy that can impact a given envelop. On the other hand, cumulative energy is sum of all energies associated with the particles sedimented in a given envelop. Averaged energy is dynamic because of instant impact, while cumulated energy is static because particle cumulates in a certain duration of eruption. In terms of hazard assessment, the averaged energy is the most representative of a potential damage associated with ballistic impact.

Our work shows how populated are is affected only by Scenario 1 because scenario 2 is associated with kinetic energy in Porto area $< 0.5 \times 10^5$ J. A comprehensive risk assessment needs to evaluate the relative occurrence of scenario 1 and 2 based on eruption history.

Conditional probability $P(C \mid E)$ does not account for the distance from vent. This shows the probability of the damage when a single particle arrives at a

certain point. In any scenario, the probability of highest energy class (class 4 of roof penetration and class 3 of roof collapse) increases with distance from vent (Fig. 7.13- 7.14 and Fig. 7.19 - 7.20). Therefore, the damage of the ballistic impact is larger in distal area than in proximal area. For example, Fig. 7.27 shows that the populated area is characterized by low probabilities for class 1, but Fig. 7.30 shows that the probability of receiving the damage of roof by class 4 of the south part of town of Porto is 60-80 %.
Joint probability $P(E, C)$ is a probability which accounts for the distance from vent. Thus, it includes the probability of receiving the particles iin a certain energy class at a certain distance. High probability zone ($\geq$ 1 %) of $P(E, C)$ of the roof penetration for class 4 and the $P(E, C)$ of the roof collapse for class 3 cover the south part of the town of Porto (Fig. 7.34 and Fig. 7.47), although $P(E, C)$ of other classes and scenario 2 only show low probabilities ($<$ 1 %) (Fig. 7.31-7.33, Fig. 7.35-7.38, Fig. 7.45-7.46 and Fig. 7.48-7.50). As a result, buildings located in the south part of Porto town would be the most affected by ballistic sedimentation.
Differently from the hazard associated with tephra load, the hazard associated with sedimentation of ballistic projectiles does not decrease monotonically with distance from the vent.

In fact, even though the highest probability of sedimentation is around the crater, the highest probability of sedimentation of high-energy projectiles is far from the vent. In our simplified simulation, $P(E, C)$ increases with the distance from vent but $P(C \mid E)$ decreases with the distance.
Fig. 7.26 and Fig. 7.41 show that the area of high probability ($\geq 60\%$) of high energy (scenario 1, class 4 of roof penetration is $> 10^4$ J and scenario 1, class 3 of roof collapse is $> 1.9 \times 10^3$ J) covers most of the island. As a result, mitigation measures, such as reinforcement of building roofs, should be implemented in the whole Porto area. Protection shelters should also be constructed in strategic areas in order to protect people in case of failure of most buildings during large Vulcanian eruptions. Finally, Porto Ponente and Porto Gelso are the least affected by ballistic sedimentation and should be preferred during evacuation procedures.

7.5 Conclusion

1. A 3D multiparticle ballistic model is useful for hazard assessment because it can provide 2D distributions of particles on the ground.

2. For a comprehensive statistical analysis of ballistic distribution in Vulcano, 10^6 particles are required regardless of the actual particle number

ejected during a given eruption.

3. Due to the axysimmetric ballistic sedimentation, 1D variations of average particle energy with distance from vent are representative of the distribution of ballistic hazard.

4. Conditional probability $P(C \mid E)$ shows the probability of ballistic sedimentation within each given envelop regardless of the distance from vent while joint probability $P(E, C)$ accounts for the sedimentation probability of a given energy class at a given distance from vent.

5. The town of Porto is characterized by a high probability of penetration and collapse of roofs. As a result, mitigation measures should be implemented (i.e., structural reinforcement with metallic bars). Protective shelters should also be constructed in strategic areas in order to protect people in case of a large Vulcanian explosion.

Chapter 8

Conclusions

8.1 Outcomes and summary

With this work I have explored new numerical strategies for the description of tephra dispersal and sedimentation and have applied them to dedicated case studies in order to find more efficient and optimized solutions that could bridge analytical and 3D sophisticated models. I have also investigated in detail the influence of the source term on the description of tephra dispersal with a special focus on the total grainsize distribution of the erupted material that significantly affects model outputs of particle concentration and mass loading on the ground. In particular, I have shown how tephra sampling should be based on the physical (i.e. plume height) and meteorological (i.e. wind direction and speed) conditions of a given volcanic eruption. In fact, a comprehensive total grainsize distribution could be obtained by sampling tephra deposits along the dispersal axis up to the maximum travel distance of the finest particles that mostly sediment individually (i.e., 3 ϕ, 125 μm). As an example, the representative sampling distance for strong plumes of about 25-30 km that developed in a 20-30 m/s wind speed should be sampled at least up to about 350 km from the vent, whereas strong plumes with similar intensity but that developed in no-wind conditions could be only sampled up to 120 km from the vent due to the lack of wind advection. Unfortunately most tephra deposits cannot be sampled up to the representative distance due to poor preservations, and the associated field-derived grainsize distributions should be regarded as fine depleted (e.g., Cotopaxi Layer 3 and 5, Askja D, Pululagua). Combinations of field observations and numerical simulations have also shown how tephra dispersal from plumes of same height are significantly affected by their latitude, due to the relation between maximum wind speed and tropopause height. In terms of identifying new numerical strategies for tephra dispersal, we have compared models of advection-diffusion-sedimentation based on both multiparticle Cellular Automata (CA) and Lattice Boltzmann (LB) methods showing how, due to the numerical stability constraints, the grid size of LB must be much smaller than CA. In fact, CA is unconditionally stable, and consequently the CA model is faster than the LB model. The accuracy of two methods is of the same level. In addition, I have also seen how CA methods simulate the advection process with anisotropic diffusion, which is not favorable. Nonetheless, the behavior of this anisotropy is well approximated by isotropic diffusion for high Peclet number. This work on CA-LB methods is published as Tsunematsu et al, (2011) [122].

The multiparticle CA model applied to two-dimensional (2D) tephra transport is presented in Chapter 4. Particles are released from the plume corner and the results of simulations show good agreement with field observations for large explosive eruptions (e.g. Askja 1875 eruption). On the contrary, the description of dispersal from bent-over plumes (e.g. Ruapehu 1996 eruption) and sedimentation controlled by aggregation processes (e.g. Mt. St. Helens 1980 eruption) need a better parameterization.This study is published as Tsunematsu et al, (2008) [121].

The 2D CA model has then been expanded to three dimensions (3D) (Chapter 5). As our 3D model describes the vertical velocity of volcanic plumes, it provides an accurate description of the source term which significantly improves the prediction of particle sedimentation with respect to 2D model with particle release from the plume corner. The turbulent fields in volcanic plumes and in the atmosphere are described by the stochastic rule of multiparticle CA with random velocity, and it is considered to be appropriate because turbulent flow is random. The relative value of diffusion coefficient is defined based on the turbulent theory and the absolute value is estimated by the parameter work. The value of diffusion coefficient estimated by the parameter work is similar to the value which is reported by other tephra transport models. The prominent feature of our multiparticle CA model is that it has the advantages of both Lagrangian and Eurlerian models such as particle tracking and facility to parallelize.

In order to complete the numerical descriptions of all particles ejected from the vent during explosive eruptions, we have also developed a dedicated model for the simulations of ballistic projectiles based on discrete event system (DES) (Chapter 6). Using our 3D model, we have simulated multiparticle processes with collisions between particles and have found that the collision probability is controlled by time intervals of bursts in strombolian eruptions. We also have found that collisions can either increase or decrease the travel distance of the particles and only few collisions are required for particles to travel farther. Besides, the mass difference of a colliding pair makes the particle travel significantly farther. When the particle mass of the collided pair is different, the lighter particle receives larger momentum by the heavier particle. Finally, we have found that our DES model is more efficient than a model based on continuous time system because of its fast computation by comparing the number of events of DES and the number of time steps of continuous time system.

Our ballistic model has been applied to the hazard and risk assessment of Vulcano island (Italy) combination of DES simulations and data processing within Geographical information system (GIS)(Chapter 7). We have analyzed the particle distribution on the ground and found that 10^6 particles are required to detect the statistical characteristics of ballistic sedimentation in Vulcano. Energy values are classified into four classes with respect to the roof penetration based on the standards of Spence et al, (2005) [109] and three classes with respect to the roof collapse based on dedicated engineering analysis for Vulcano (collaboration with theÉcole Polytechnique Fédérale de Lausanne (EPFL)). One-dimensional energy variation with the distance from the vent can represent the distribution of ballistic hazard due to the axysimmetric sedimentation. The envelop sedimentation probability and the total sedimentation probability are also calculated with the distance from the vent. Our results show how the town of Porto represents a high risk zone and mitigation measures, such as reinforcement of roofs, should be implemented. It is also recommended to construct protective shelters in order to protect people in case of a large Vulcanian explosion.

8.2 Outlook and perspectives

This work presents a detailed study of new numerical solutions for the description of both dispersal and sedimentation of all particles ejected during explosive volcanic eruptions that travel through the atmosphere (i.e. tephra) and that cause various hazards to populated areas and communities. Transports of small particles and ballistic projectiles are characterized by different interactions with the carrying fluid. In fact, ballistic projectiles decouple from the gas phase early in their transport and follow mostly parabolic trajectories sedimenting in proximal to medial areas. The discrimination between particles that are carried within the plume and particles that behave as ballistic projectiles is difficult and ballistic size varies with plume intensity. One possible answer is given by the simple comparison of vertical plume velocity and particle terminal velocity. However particle terminal velocity is calculated by assuming that the drag force of the surrounding gas and gravity is in balance. It might take some time for gravity and drag force to reach the equilibrium. Therefore, it is necessary to consider time dependency of the movement of particle and fluid. One possibility is to simulate a particle movement and surrounding fluid numerically. Lattice Boltzmann method has already given many solutions to such multiphase flow (solid particle and fluid.) This solution will give the necessary particle size, the height and the timing for efficient decoupling of particle from the volcanic plumes. Applying the decoupling threshold to the change of ballistic and tephra transport will describe the whole story of fall particles ejected by volcano.

Another aspect of this work is the combination of geological field work and numerical simulations providing a new perspective on the interpretation of grainsize distributions. In particular, this work has highlighted the importance of the representative sampling distance in order to obtain a representative total grainsize distribution. Given that most of old tephra deposits have been eroded away or are difficult to access, most total grainsize distributions available in literature should be regarded as fine-depleted. In order to obtain representative grainsize distributions we should focus on more recent eruptions and on the combination between field observations, remote-sensing retrievals and in-situ data obtained with airplane flights.

In terms of new numerical strategies for the description of tephra dispersal we have shown how Cellular Automata (CA) modeling can combine the advantages of both Lagrangian and Eulerian models. Typically, Lagrangian models describe the behavior of each particle, but they do not work with spatial grids. On the other hand, Eulerian models work with spatial grids but they do not describe the behavior of individual particles. Our multiparticle CA model can both describe individual particles and work with spatial grids, making the parallelization of easier implementation for a faster computation. CA and LB utilize the microscopic rule and can describe macroscopic dynamics. For example, our model applied random velocity to each particle. As a result, each particle behaves differently, but cumulated particle path showed the shape of strong plumes (Chapter 5). Therefore, these models are promising to detect the important dynamics of volcanic eruptions which does not emerge when small scale complexity is neglected. As an example, weak plumes are more difficult to describe than strong plumes. We have tested some existing models, but no model has given the accurate description of observed weak plumes. This is probably because of the complicated turbulent field which is strongly affected by wind velocity. If the bent-over feature is only due to the wind and vertical plume velocity, mean velocity of weak plumes are described easily. However, it seems that the turbulent fluctuations also affect the mean velocity and the center axis of weak plumes. Weak plumes could be better described by Lattice Boltzmann strategies that can capture the complexity of fluid dynamics.

So far, only few studies have been published on the hazard and risk assessment of ballistic projectiles because most ballistic models are not multiparticle (i.e. Blong, 1984 [10]; Allatorre-Ibarguëngoitia, 2006b [2]). We have shown the complexity and importance of identifying both roof penetration and roof collapse thresholds for a comprehensive hazard and risk assessment. This should be done in combination with dedicated engineering investigations and is made easier by the application in a GIS environment. As a result of my work on the numerical description of both dispersal and sedimentation of volcanic particles, I have realized the importance of an accurate description of the source term (e.g., exit velocity, plume height, vent geometry, plume temperature and density, grainsize distribution). I have shown how a stochastic treatment of initial conditions for the description of the source term can give good results when data are not available. Nonetheless, the development of new strategies for the determination of source-term parameters would provide a significant improvement to both the accuracy of teprha dispersal models and computation efficiency. As a conclusion, I can say that numerical models should be developed in close combination with new data-acquisition strategies for an optimal description of tephra dispersal and sedimentation which would also be crucial to the assessment of the associated hazards and risk.

Bibliography

[1] M. A. Alatorre-Ibargüengoitia and H. Delgado-Granados. Experimental determination of drag coefficient for volcanic materials: Calibration and application of a model to popocatpetl volcano (mexico) ballistic projectiles. *Geophys. Res. Let.*, 33(L11302):5PP, 2006.

[2] M. A. Alatorre-Ibargüengoitia, H. Delgado-Granados, and I. A. Farraz-Montes1. Hazard zoning for ballistic impact during volcanic explosions at volcn de fuego de colima (mxico). *Geological Society of America Special Papers*, 402:209–216, 2006.

[3] J. Banks and B.L. Nelson. *Discrete-event system simulation.* Prentice Hall, 2010. ISBN 9780136062127. URL `http://books.google.ch/books?id=cqSNnmrqqbQC`.

[4] F. Barberi, M. Coltelli, A. Frullani, M. Rosi, and E. Almeida. Chronology and dispersal characteristics of recently (last 5000 years) erupted tephra of cotopaxi (ecuador): implications for long-term eruptive forecasting. *J. Volcanol. Geotherm. Res.*, 69(3-4):217 – 239, 1995. ISSN 0377-0273. doi: 10.1016/0377-0273(95)00017-8. URL `http://www.sciencedirect.com/science/article/pii/0377027395000178`.

[5] J. Bernsdorf, S.E. Harrison, S.M. Smith, P.V. Lawford, and D.R. Hose. Numerical simulation of clotting processes: A lattice boltzmann application in medical physics. *Mathematics and Computers in Simulation*, 72(2-6):89 – 92, 2006. ISSN 0378-4754. doi: 10.1016/j.matcom.2006.05.008. URL `http://www.sciencedirect.com/science/article/pii/S0378475406001327`.

[6] P. L. Bhatnagar, E. P. Gross, and M. Krook. A model for collision processes in gases. i. small amplitude processes in charged and neutral one-component systems. *Phys. Rev.*, 94:511–525, May 1954. doi: 10.1103/PhysRev.94.511. URL `http://link.aps.org/doi/10.1103/PhysRev.94.511`.

[7] L. Bianchi. L'eruzione 1888-1890 di vulcano. Master's thesis, Universit'a di Pisa, Facolt'a di Scienze Matematiche, Fisiche e Naturali, 2007.

[8] S. Biass and C. Bonadonna. A quantitative uncertainty assessment of eruptive parameters derived from tephra deposits: the example of

two large eruptions of cotopaxi volcano, ecuador. *Bull Volcanol.*, 73: 73–90, 2011. ISSN 0258-8900. doi: 10.1007/s00445-010-0404-5. URL `http://dx.doi.org/10.1007/s00445-010-0404-5`.

[9] E. A. Blackburn and R. S. J. Sparks L. Wilson. Mechanisms and dynamics of strombolian activity. *J. Geol. Soc. London*, 132:429–440, 1976.

[10] R. J. Blong. *Volcanic Hazards: A Sourcebook on the Effects of Eruptions*. Academic Press, London, UK, 1984. ISBN 9780121071806.

[11] C. Bonadonna and A.Costa. Modeling of tephra sedimentation from volcanic plumes. In S. A. Fagents, T. K. P. Gregg, and R. M. C. Lopes, editors, *Modeling Volcanic Processes: The Physics and Mathematics of Volcanism*. Cambridge University Press, 2012.

[12] C. Bonadonna and B. F Houghton. Total grain-size distribution and volume of tephra-fall deposits. *Bull Volcanol.*, 67:441–456, 2005.

[13] C. Bonadonna and J.C. Phillips. Sedimentation from strong volcanic plumes. *J. Geophys. Res.*, 108(B7):2340–2368, 2003.

[14] C. Bonadonna, G.G. J. Ernst, and R. S. J. Sparks. Thickness variations and volume estimates of tephra fall deposits: the importance of particle reynolds number. . *J. Volcanol Geotherm Res*, 81:173–187, 1998.

[15] C. Bonadonna, C. B. Connor, B. F. Houghton, L. Connor, M. Byrne, A. Laing, and T. K. Hincks. Probabilistic modeling of tephra dispersal: Hazard assessment of a multiphase rhyolitic eruption at tarawera, new zealand. *J. Geophys. Res.*, 110(B03203), 2005.

[16] C. Bonadonna, J.C. Phillips, and B. F. Houghton. Modeling tephra sedimentation from a Ruapehu weak plume eruption. *J. Geophys. Res.*, 110(B8):1–22, 2005.

[17] C. Bonadonna, A. Folch, S. Loughlin, and H. Puempel. Future developments in modelling and monitoring of volcanic ash clouds: outcomes from the first iavcei-wmo workshop on ash dispersal forecast and civil aviation. *Bull Volcanol.*, 110:1–10, 2011. ISSN 0258-8900. doi: 10.1007/s00445-011-0508-6. URL `http://dx.doi.org/10.1007/s00445-011-0508-6`.

[18] S. M. Bower and A. W. Woods. On the dispersal of clasts from volcanic craters during small explosive eruptions. *J. Volcanol. Geotherm. Res.*,

73(1-2):19 – 32, 1996. ISSN 0377-0273. doi: 10.1016/0377-0273(96)00006-6. URL `http://www.sciencedirect.com/science/article/pii/0377027396000066`.

[19] M. I. Bursik. Effect of wind on the rise height of volcanic plumes. *Geophys. Res. Lett.*, 28(18):3621–3624, 2001.

[20] M. I. Bursik, S. N. Carey, and R. S. J. Sparks. A gravity current model for the may 18, 1980 mount st. helens plume. *Geophis Res Lett.*, 19 (16):1663–1666, 1992.

[21] M. I. Bursik, R. S. J. Sparks, J. S. Gilbert, and S. N. Carey. Sedimentation of tephra by volcanic plumes: I. theory and its comparison with a study of the fogo a plinian deposit, sao miguel (azores). *Bull Volcanol.*, 54:329–344, 1992.

[22] G. Carazzo, E. Kaminski, and S. Tait. On the dynamics of volcanic columns: A comparison of field data with a new model of negatively buoyant jets. *J. Volcanol. Geotherm. Res.*, 178(1):94 – 103, 2008. ISSN 0377-0273. doi: 10.1016/j.jvolgeores.2008.01.002. URL `http://www.sciencedirect.com/science/article/pii/S0377027308000176`.

[23] R. Carey, B. Houghton, and T. Thordarson. Tephra dispersal and eruption dynamics of wet and dry phases of the 1875 eruption of askja volcano, iceland. *Bulletin of Volcanology*, 72:259–278, 2010. ISSN 0258-8900. URL `http://dx.doi.org/10.1007/s00445-009-0317-3`. 10.1007/s00445-009-0317-3.

[24] S. Carey and R.S.J. Sparks. Quantitative models of the fallout and dispersal of tephra from volcanic eruption columns. *Bull. Volcanol.*, 48:109–125, 1986.

[25] S. N. Carey and H. Sigurdsson. Influence of particle aggregation on deposition of distal tephra from the may 18, 1980, eruption of mount st. helens volcano. *J. Geophys. Res.*, 87(B8):7061–7072, 1982.

[26] M Chahoud, D Fehly, H.-H Wehmann, and A Schlachetzki. Cellular-automata-based simulation of anisotropic crystal growth. *Journal of Crystal Growth*, 220(4):471 – 479, 2000. ISSN 0022-0248. doi: 10.1016/S0022-0248(00)00902-7. URL `http://www.sciencedirect.com/science/article/pii/S0022024800009027`.

[27] P. Chakraborty, G. Gioia, and S. W. Kieffer. Volcanic mesocyclones. *Nature*, 458(7237):497–500, 2009.

[28] B. Chopard and M. Droz. *Cellular Automata Modeling of Physical Systems.* Cambridge University Press, 1998.

[29] B. Chopard, P. O. Luthi, and P.-A. Queloz. Cellular automata model of car traffic in two-dimensional street networks. *J. Phys. A*, 29:2325–2336, 1996.

[30] B. Chopard, P. Luthi, A. Masselot, and A. Dupuis. Cellular automata and lattice boltzmann techniques: An approach to model and simulate complex systems. *Advances in Complex Systems*, 5(2):103–246, 2002. http://cui.unige.ch/∼chopard/FTP/CA/acs.pdf.

[31] B. Chopard, J-L. Falcone, and J. Latt. The lattice boltzmann advection-diffusion model revisited. *Eur. Phys. J. Special Topics.*, 171: 245–249, 2009.

[32] B. Chouet, N. Hamisevicz, and T. R. Mcgetchin. Photoballistics of volcanic jet activity at stromboll, italy. *J. Geophys. Res.*, 79(32):4961–4976, 1974.

[33] C. B Connor, B. E. Hill, B. Winfrey, N. M. Franklin, and P. C. La Femina. Estimation of volcanic hazards from tephra fallout. *Natural Hazards Revie*, 2(1):33–42, 2001.

[34] L. J. Connor and C. B. Connor. Inversion is the key to dispersion: Understanding eruption dynamics by inverting tephra fallout. In *Statistics in Volcanology.* Geological Society, London, 2006.

[35] A. Costa, G. Macedonio, and A. Folch. A three-dimensional eulerian model for transport and deposition of volcanic ashes. *Earth and Planetary Science Letters*, 241:634–647, 2006.

[36] L. Costantini. *Understanding basaltic explosive volcanism.* PhD thesis, Université de Genève, 2010.

[37] H. F. Dacre, A. L. M. Grant, R. J. Hogan, S. E. Belcher, D. J. Thomson, B. J. Devenish, F. Marenco, M. C. Hort, J. M. Haywood, A. Ansmann, I. Mattis, and L. Clarisse. Evaluating the structure and magnitude of the ash plume during the initial phase of the 2010 eyjafjallajökull eruption using lidar observations and name simulations. *J. Geophys. Res*, 116(D00U03):15 PP, 2011. doi: doi:10.1029/2011JD015608.

[38] R. D'Amours, A. Malo, R. Servranckx, D. Bensimon, S. Trudel, and J.-P. Gauthier-Bilodeau. Application of the atmospheric lagrangian

particle dispersion model mldp0 to the 2008 eruptions of okmok and kasatochi volcanoes. *J. Geophys. Res.*, 115(D00L11), 2010. doi: 10.1029/2009JD013602.

[39] R.R. Draxler and G.D. Hess. An overview of the hysplit 4 modeling system of trajectories, dispersion, and deposition. *Aust. Meteor. Mag.*, 47:295–308, 2011.

[40] A. Dupuis and B. Chopard. Lattice gas modeling of scour formation under submarine pipelines. *J. Comput. Phys.*, 178(1):161–174, 2002. ISSN 0021-9991. doi: http://dx.doi.org/10.1006/jcph.2002.7025.

[41] A. Dupuis and B. Chopard. Lattice gas modeling of scour formation under submarine pipelines. *J. Comp. Phys.*, 178:161–174, 2002.

[42] L. Edelstein-Keshet. *Mathematical models in biology.* Classics in applied mathematics. Society for Industrial and Applied Mathematics, 1988. ISBN 9780898715545. URL `http://books.google.ch/books?id=pp9pQgAACAAJ`.

[43] G. G. J. Ernst, J. P. Davis, and R.S.J. Sparks. Bifurcation of volcanic plumes in a crosswind. *Bull. Volcanol.*, 56:159–169, 1994. ISSN 0258-8900. URL `http://dx.doi.org/10.1007/BF00279601`. 10.1007/BF00279601.

[44] G. G. J. Ernst, R. S. J. Sparks, S. N. Carey, and M. I. Bursik. Sedimentation from turbulent jets and plumes. *J. Geophys. Res*, 101(B3): 5575–5589, 1996.

[45] E.W. and Llewellin. Lbflow: An extensible lattice boltzmann framework for the simulation of geophysical flows. part ii: usage and validation. *Computers and Geosciences*, 36(2):123 – 132, 2010. ISSN 0098-3004. doi: 10.1016/j.cageo.2009.08.003. URL `http://www.sciencedirect.com/science/article/pii/S0098300409002659`.

[46] S. A. Fagents and L. Wilson. Explosive volcanic eruptions: Vii. the ranges of pyroclasts ejected in transient volcanic explosions. *Geophys. J. Int.*, 113:359–370, 1993.

[47] A. Felpeto, J. Martí, and R. Ortiz. Automatic gis-based system for volcanic hazard assessment. *J. Volcanol. Geotherm. Res.*, 166(2): 106 – 116, 2007. ISSN 0377-0273. doi: 10.1016/j.jvolgeores.2007.07.008. URL `http://www.sciencedirect.com/science/article/pii/S0377027307002247`.

[48] J. Fierstein and M. Nathanson. nother look at the calculation of fallout tephra volumes. *Bull Volcanol*, 54:156–167, 1992.

[49] A. Folch, A. Costa, and G. Macedonio. Fall3d: A computational model for transport and deposition of volcanic ash. *Computers and Geosciences*, 35(6):1334–1342, 2009. ISSN 0098-3004. doi: 10.1016/j.cageo.2008.08.008. URL `http://www.sciencedirect.com/science/article/pii/S0098300408002781`.

[50] U. Frisch, B. Hasslacher, and Y. Pomeau. Lattice-gas automata for the navier-stokes equation. *Phys. Rev. Lett.*, 56:1505–1508, Apr 1986. doi: 10.1103/PhysRevLett.56.1505. URL `http://link.aps.org/doi/10.1103/PhysRevLett.56.1505`.

[51] I. Ginzburg. Equilibrium-type and link-type lattice boltzmann models for generic advection and anisotropic-dispersion equation. *Advances in Water Resources Pages*, 28(11):1171–1195, 2005.

[52] Z. L. Guo, B.C. Shi, and N.C. Wang. Fully lagrangian and lattice boltzmann methods for the advection-diffusion equation. *Journal of Scientific Computing*, 14(3):291–300, 1999.

[53] W. K. George H. J. Hussein, S. P. Capp. Velocity measurements in a high-reynolds-number, momentum-conserving, axisymmetric, turbulent jet. *J. Fluid Mech*, pages 31–75, 1994.

[54] K. Gersten H. Schlichting. *Boundary-Layer Theory.* McGraw Hill, New York, 1979, 8th edition, 1979. Corr. 2nd printing, 2000, XXIII, 801 p. 283 illus.

[55] M. Hirabayashi, M. Ohta, D. A. Rfenacht, and B. Chopard. A lattice boltzmann study of blood flow in stented aneurism. *Future Generation Computer Systems*, 20(6):925 – 934, 2004.

[56] K. P. Hoinka. Statistics of the global tropopause pressure. *Mon. Wea. Rev.*, 126:3303–3325, 1998.

[57] B. F. Houghton and H. M. Gonnermann. Basaltic explosive volcanism: Constraints from deposits and models. *Chemie der Erde*, 68:117–140, 2008.

[58] C. Huber, B. Chopard, and M. Manga. A lattice boltzmann model for coupled diffusion. *J. Comput. Phys.*, 229:7956–7976, October 2010. ISSN 0021-9991. doi: http://dx.doi.org/10.1016/j.jcp.2010.07.002. URL `http://dx.doi.org/10.1016/j.jcp.2010.07.002`.

[59] D. L. Inman. Measures for describing the size distribution of sediments. *J. Sediment. Petrol.*, 22:125 –145, 1952.

[60] T. Iwasaki, T. Maki, and K. Katayama. Tracer transport model at japan meteorological agency and its application to the etex data. *Atmos. Environ.*, 32:42854295, 1998.

[61] E. Kaminski and C. Jaupart. The size distribution of pyroclasts and the fragmentation sequence in explosive volcanic eruptions. *J. Geophys. Res.*, 103(B12):29759 –29779, 1998.

[62] L. L. B. Kier, P. G. Seybold, and C. K. Cheng. *Modeling Chemical Systems Using Cellular Automata.* Springer London, Limited, 2005. ISBN 9781402036903. URL `http://books.google.com/books?id=nkuXVkmcxBgC`.

[63] J. Kim, P. Moin, and R. Moser. Turbulence statistics in fully developed channel flow at low reynolds number. *J. Fluid Mech*, pages 133–166, 1987.

[64] D. Kunii and O. Levenspiel. *Fluidisation Engineering.* John Wiley, New York, 1969.

[65] J. Latt. *Hydrodynamic limit of lattice Boltzmann equations.* PhD thesis, University of Geneva, Geneva, Switzerland, 2007.

[66] J. Latt, B. Chopard, O. Malaspinas, M. Deville, and A. Michler. Straight velocity boundaries in the lattice Boltzmann method. *Phys. Rev. E*, 77:056703, 2008. doi: 10.1103/PhysRevE.77.056703.

[67] E. J. List. Turbuelnt jets and plumes. *Ann. Rev. Fluid Mech.*, 14: 189–212, 1982.

[68] Ye Liu. Risk assessment: Tephra fallout on the buildings of vulcano island, italy. Master's thesis, École Polytechnique Fédérale de Lausanne, the Netherlands, 2003.

[69] E.W. Llewellin. Lbflow: An extensible lattice boltzmann framework for the simulation of geophysical flows. part i: theory and implementation. *Computers and Geosciences*, 36(2):115 – 122, 2010. ISSN 0098-3004. doi: 10.1016/j.cageo.2009.08.004. URL `http://www.sciencedirect.com/science/article/pii/S0098300409002660`.

[70] G. Macedonio, A. Costa, and A. Longo. A computer model for volcanic ash fallout and assessment of subsequent hazard. *Computers and Geosciences*, 31(7):837 – 845, 2005. ISSN 0098-3004. doi: 10.1016/j.cageo.2005.01.013. URL `http://www.sciencedirect.com/science/article/pii/S0098300405000269`.

[71] A. Masselot and B. Chopard. A lattice boltzmann model for particle transport and deposition. *Europhys. Lett.*, 42:259–264, 1998.

[72] A. Masselot and B. Chopard. A lattice boltzmann model for particle transport and deposition. *Europhys. Lett.*, 42:259–264, 1998.

[73] L. G. Mastin. A simple calculator of ballistic trajectories for blocks ejected during volcanic eruptions. U.s. geological survey open-file report 01-45, version 1.1, U.S. Department of the Interior, U.S. Geological Survey, 2002.

[74] K. Moriyama and T. Inamuro. Lattice boltzmann simulations of water transport from the gas diffusion layer to the gas channel in pefc. *Commun. Comput. Phys.*, 9:1206–1218, 2011.

[75] N. L. Morrison and H. N. Webster. An assessment of turbulence profiles in rural and urban environments using local measurements and numerical weather prediction results. *Boundary-Layer Meteorology*, 115: 223–239, 2005. ISSN 0006-8314. URL `http://dx.doi.org/10.1007/s10546-004-4422-8`. 10.1007/s10546-004-4422-8.

[76] B. R. Morton, G.Taylor, and J. S. Turner. Turbulent gravitational convection from maintained and instantaneous sources. *Proceedings of the Royal Society of London. Series A. Mathematical and Physical Sciences*, 234(1196):1–23, 1956. doi: 10.1098/rspa.1956.0011. URL `http://rspa.royalsocietypublishing.org/content/234/1196/1.abstract`.

[77] P.J Murrow, WI Rose, and S. Self. etermination of the total grain size distribution in a vulcanian eruption column, and its implications to stratospheric aerosol perturbation. *Geophys. Res. Lett.*, 7:893896, 1980.

[78] K. Nagel and M. Schreckenberg. A cellular automaton model for freeway traffic. *J. Phys. I France*, 2(12):2221–2229, 1992. doi: 10.1051/jp1:1992277. URL `http://dx.doi.org/10.1051/jp1:1992277`.

[79] A. Neri and G. Macedonio. Numerical simulation of collapsing volcanic columns with particles of two sizes. *J. Geophys. Res.*, 101(B4):8153–8174, 1996.

[80] A. Neri, T. Esposti Ongaro, G. Macedonio, and D. Gidaspow. Multi-particle simulation of collapsing volcanic columns and pyroclastic flow. *J. Geophys. Res.*, 108(B4):2202, 1996. doi: 10.1029/2001JB000508.

[81] J. M. Oberhuber, M. Herzog, H-F Graf, and K. Schwanke. Volcanic plume simulation on large scales. *J. Volcanol. Geotherm. Res.*, 87: 29–53, 1998.

[82] A. Okabe, B. Boots, and K. Sugihara. *Spatial tessellations: concepts and applications of Voronoi diagrams.* Wiley, Chichester, 1992.

[83] E. Parfitt. A study of clast size distribution, ash deposition and fragmentation in a hawaiian-style volcanic eruption. *J. Volcanol. Geotherm. Res*, 84:197208, 1998.

[84] M. R. Patrick, A. J. L. Harris, M. Ripepe, J. Dehn, D. A. Rothery, and S. Calvari. Strombolian explosive styles and source conditions: insights from thermal (flir) video. *Bull. Volcanol.*, 69:769–784, 2007.

[85] T. Pfeiffer, A. Costa, and G. Macedonio. A model for the numerical simulation of tephra fall deposits. *J. Volcanol. Geotherm. Res.*, 140(4): 273 – 294, 2005. ISSN 0377-0273. doi: 10.1016/j.jvolgeores.2004.09.001. URL `http://www.sciencedirect.com/science/article/pii/S0377027304003117`.

[86] M. Pistolesi, M. Rosi, L. Pioli, A. Renzulli, A. Bertagnini, and D Andronico. The paroxysmal event and its deposits. In S. Calvari, S. Inguaggiato, G. Puglisi, M. Ripepe, and M. Rosi, editors, *The Stromboli Volcano, An Integrated Study of the 20022003 Eruption.* American Geophysical Union, 2008. ISBN 9780875904474.

[87] A. Pomonis, R. J. S. Spence, and P. J. Baxter. Residential buildings for an eruption of furnas volcano, sao miguel, the azores. *J. Volcanol. Geotherm. Res.*, 92:107131, 1999.

[88] S.B. Pope. *Turbulent flows.* Cambridge University Press, 2000. ISBN 9780521598866. URL `http://books.google.com/books?id=HZsTw9SMx-0C`.

[89] D. M. Pyle. The thickness, volume and grainsize of tephra fall deposits. *Bull. Volcanol.*, 51:115, 1989.

[90] Y. H. Qian, D. D'Humiéres, and P. Lallemand. Lattice bgk models for navier-stokes equation. *Europhysics Letters*, 17(6):479–484, 1992.

[91] B. Neuhierland E. Rank. Computational aeroacoustics by coupling the finite-element and the lattice-boltzmann-method. In C. A. Motasoares, J. A. C. Martins, H. C. Rodrigues, Jorge A. C. Ambrsio, C. A. B. Pina, C. M. Motasoares, E. B. R. Pereira, and J. Folgado, editors, *III European Conference on Computational Mechanics*, pages 153–153. Springer Netherlands, 2006. ISBN 978-1-4020-5370-2.

[92] J. Reitman. *Computer simulation applications: discrete-event simulation for synthesis and analysis of complex systems.* Wiley series on systems engineering and analysis. Wiley-Interscience, 1971. ISBN 9780471716259. URL `http://books.google.com/books?id=ZrjtAAAAIAAJ`.

[93] M. Ripepe and A.J. Harris. ynamics of the 5 april 2003 explosive paroxysm observed at stromboli by a near-vent thermal, seismic and infrasonic array. *Geophys. Res. Lett.*, 35(L07306):6, 2008. doi: 10.1029/2007GL032533.

[94] M. Ripepe, M. Rossi, and G. Saccorotti. Image processing of explosive activity at stromboli. *J. Volcanol. Geotherm. Res.*, 54:335–351, 1993.

[95] P. J. W. Roberts and D. R. Webster. Turbulent diffusion. In H.H. Shen, editor, *Environmental fluid mechanics: theories and applications.* American Society of Civil Engineers, 2002. ISBN 9780784406298. URL `http://books.google.ch/books?id=GtfEBCUDhHwC`.

[96] W. I. Rose, S. Self, P. J. Murrow, C. Bonadonna, A. J. Durant, and G. G. J. Ernst. Nature and significance of small volume fall deposits at composite volcanoes: Insights from the october 14, 1974 fuego eruption, guatemala. *Bull. Volcanol.*, 2008. doi: 10.1007/s00445-007-0187-5.

[97] M. Rosi, A. Bertagnini, A. J. L. Harris, L. Pioli, M. Pistolesi, and M. Ripepe. Case history of paroxysmal explosion at stromboli: Timing and dynamics of the april 5, 2003 event. *Earth Planet. Sci. Lett.*, 243: 594606, 2006.

[98] H. C. Saunderson. Equations of motion and ballistic paths of volcanic ejecta. *Comput. Geosci.*, 34:802–814, July 2008. ISSN 0098-3004. doi: 10.1016/j.cageo.2007.10.004. URL `http://dl.acm.org/citation.cfm?id=1365090.1365219`.

[99] M. M. Scase. Evolution of volcanic eruption columns. *J. Geophys. Res.*, 114(F04003):15PP, 2009. doi: 10.1029/2009JF001300.

[100] R. Schumacher. A reappraisal of mount st-helens ash clustersdepositional model from experimental-observation. *J. Volcanol. Geotherm. Res.*, 59(3):253–260, 1994.

[101] S. Scollo, A. Folch, M. Coltelli, and V. J. Realmuto. Three-dimensional volcanic aerosol dispersal: A comparison between multiangle imaging spectroradiometer (misr) data and numerical simulations. *J. Geophys. Res.*, 115(D24210), 2010. doi: 10.1029/2009JD013162.

[102] C. Searcy, K. Dean, and W. Stringer. Puff: A high-resolution volcanic ash tracking model. *J. Volcanol. Geotherm. Res.*, 80 (1-2):1–16, 1998. ISSN 0377-0273. doi: 10.1016/S0377-0273(97) 00037-1. URL `http://www.sciencedirect.com/science/article/pii/S0377027397000371`.

[103] P. D. Smith and J. G. Hetherington. *Blast and ballistic loading of structures*. Butterworth-Heinemann, 1994. ISBN 9780750620246. URL `http://books.google.ch/books?id=0vIeAQAAIAAJ`.

[104] R. S. J. Sparks. The initial giant umbrella cloud of the may 18th, 1980, explosive eruption of mount st helens. *. Volcanol Geotherm Res.*, 45: 347–350, 1986.

[105] R. S. J. Sparks and L. Wilson. Explosive volcanic eruptions v. observations of plume dynamics during the 1979 soufrire eruption, st vincent. *Geophysical Journal of the Royal Astronomical Society*, 69(2):551–570, 1982. ISSN 1365-246X. doi: 10.1111/j.1365-246X.1982.tb04965.x. URL `http://dx.doi.org/10.1111/j.1365-246X.1982.tb04965.x`.

[106] R. S. J. Sparks, L. Wilson, and H. Sigurdsson. The pyroclastic deposites of the 1875 eruption of askja, Iceland. *Philos. Trans. R. Soc. London*, 299:241–273, 1981.

[107] R. S. J. Sparks, M. I. Bursik, G. J. Ablay, R. M. E. Thomas, and S. N. Carey. Sedimentation of tephra by volcanic plumes. part 2: controls on thickness and grain-size variations of tephra fall deposits. *Bulletin*

of Volcanology, 54:685–695, 1992. ISSN 0258-8900. URL `http://dx.doi.org/10.1007/BF00430779`. 10.1007/BF00430779.

[108] R. S. J. Sparks, M. I. Bursik, S. N. Carey, J. S. Gilbert, L. S. Glaze, H. Sigurdsson, and A. W. Woods. *Volcanic Plumes*. John Wiley, New York, 1997.

[109] R. J. S. Spence, I. Kelman, P. J. Baxter, G. Zuccaro, and S. Petrazzuoli. Residential building and occupant vulnerability to tephra fall. *Natural Hazards and Earth System Science*, 5(4):477–494, 2005. doi: 10.5194/nhess-5-477-2005. URL `http://www.nat-hazards-earth-syst-sci.net/5/477/2005/`.

[110] A. Stohl, A. J. Prata, S. Eckhardt, L. Clarisse, A. Durant, S. Henne, N. I. Kristiansen, A. Minikin, U. Schumann, P. Seibert, K. Stebel, H. E. Thomas, T. Thorsteinsson, K. Tørseth, and B. Weinzierl. Determination of time- and height-resolved volcanic ash emissions for quantitative ash dispersion modeling: the 2010 eyjafjallajkull eruption. *Atmospheric Chemistry and Physics Discussions*, 11(2):5541–5588, 2011. doi: 10.5194/acpd-11-5541-2011. URL `http://www.atmos-chem-phys-discuss.net/11/5541/2011/`.

[111] Shinsuke Suga. Numerical schemes obtained from lattice boltzmann equations for advection diffusion equations. *Int. J. Mod. Phys. C*, 17 (11):1563–1577, 2006.

[112] M.C. Sukop and D.T. Thorne. *Lattice Boltzmann modeling: an introduction for geoscientists and engineers.* Springer, 2006. ISBN 9783540279815. URL `http://books.google.ch/books?id=nk0SLXCZetQC`.

[113] T. Suzuki. A theoretical model for dispersion of tephra. In D. Shimozuru and I. Yokoyama, editors, *Arc Volcanism, Physics and Tectonics*, pages 95–113. Terra Sci., Tokyo, 1983.

[114] Y. J. Suzuki and T. Koyaguchi. A three-dimensional numerical simulation of spreading umbrella clouds. *J. Geophys. Res.*, 114(B03209), 2009. doi: 10.1029/2007JB005369.

[115] Y. J. Suzuki, T. Koyaguchi, M. Ogawa, and I. Hachisu. Volcanic particle aggregation in explosive eruption columns. *J. Geophys. Res.*, 110 (B08201), 2005. doi: 10.1029/2004JB003460.

[116] C. Textor, H. F.Graf, M.Herzog, J. M.Oberhuber William, I. Rose, and G. G. J Ernst. Volcanic particle aggregation in explosive eruption columns. part i: Parameterization of the microphsics of hydrometeors and ash. *J. Volcanol. Geotherm. Res.*, 150:359–377, 2006.

[117] C. Textor, H. F.Graf, M.Herzog, J. M.Oberhuber William, I. Rose, and G. G. J Ernst. Volcanic particle aggregation in explosive eruption columns. part ii: Parameterization of the microphsics of hydrometeors and ash. *J. Volcanol. Geotherm. Res.*, 150:359–377, 2006.

[118] D. J. Thomson. Criteria for the selection of stochastic models of particle trajectories in turbulent flows. *J. Fluid Mech.*, 180:529–556, 1987.

[119] S. Thorarinsson. Tefrokronologiska studier på island. *Geog. Annals Stockholm*, 26:1–217, 1944.

[120] A. Tiesi, M.G. Villani, M. DIsidoro, A.J. Prata, A. Maurizi, and F. Tampieri. Estimation of dispersion coefficient in the troposphere from satellite images of volcanic plumes: Application to mt. etna, italy. *Atmospheric Environment*, 40(4):628 – 638, 2006. ISSN 1352-2310. doi: 10.1016/j.atmosenv.2005.09.079. URL `http://www.sciencedirect.com/science/article/pii/S1352231005009660`.

[121] K. Tsunematsu, J-L. Falcone, C. Bonadonna, and B. Chopard. Applying a cellular automata method for the study of transport and deposition of volcanic particles. *ACRI 2008 proceedings. LNCS 5191*, pages 393–400, 2008.

[122] K. Tsunematsu, B. Chopard, J-L. Falcone, and C. Bonadonna. Comparison of two advection-diffusion methods for tephra transport in volcanic eruptions. *Commun. Comput. Phys.*, 9:1324–1334, 2011. doi: doi:10.4208/cicp.311009.191110s.

[123] J. S. Turner. Turbulent entrainment: the development of the entrainment assumption, and its application to geophysical flows. *Journal of Fluid Mechanics*, 173:431–471, 1986. doi: 10.1017/S0022112086001222. URL `http://dx.doi.org/10.1017/S0022112086001222`.

[124] J.S. Turner. *Buoyancy Effects in Fluids*. Cambridge monographs on mechanics and applied mathematics. Cambridge University Press, 1980. ISBN 9780521297264. URL `http://books.google.com/books?id=x8NqYA97-wMC`.

[125] A.C.M. Volentik, C. Bonadonna, C. B. Connor, L. J. Connor, and M. Rosi. Modeling tephra dispersal in absence of wind: Insights from the climactic phase of the 2450bp plinian eruption of pululagua volcano (ecuador). *J. Volcanol. Geotherm. Res.*, 193(1-2):117 – 136, 2010. ISSN 0377-0273. doi: 10.1016/j.jvolgeores.2010.03.011. URL `http://www.sciencedirect.com/science/article/pii/S0377027310001046`.

[126] G. P. L. Walker. Explosive volcanic eruptions - a new classification scheme. *Geologische Rundschau*, 62:431–446, 1973. ISSN 0016-7835. URL `http://dx.doi.org/10.1007/BF01840108`. 10.1007/BF01840108.

[127] G. P. L. Walker. Grain-size characteristics of pyroclastic deposits. *The Journal of Geology*, 79(6):696–714, 1980.

[128] G. P. L. Walker. The taupo pumice: product of the most powerful known (ultraplinian) eruption? *J. Volcanol. Geotherm. Res.*, 8:69–942, 1980.

[129] J. M. Wallace and P. V. Hobbs. *Atmospheric science: an introductory survey*. International geophysics series. Elsevier Academic Press, 2006. ISBN 9780127329512. URL `http://books.google.fr/books?id=HZ2wNtDOU0oC`.

[130] P. W. Webley, K. Dean, R. Peterson, A. Steffke, M. Harrild, and J. Groves. Dispersion modelling of volcanic ash clouds: North pacific eruptions, the past 40 years: 1970 2010. *Natural Hazards*, 2011. doi: 10.1007/s11069-011-0053-9.

[131] H. N. Webster, D. J. Thomson, and N. L. Morrison. New turbulence profiles for name. *UK Met Office Turbulence and Diffusion Note*, (288), 2003.

[132] Wikipedia. Elastic collision, 2012. URL `http://en.wikipedia.org/wiki/Elastic_collision`.

[133] L. Wilson. Explosive volcanic eruptions-ii the atmospheric trajectories of pyroclasts. *Geophis J R astr Soc.*, 30:381392, 1972. doi: 10.1111/j.1365-246X.1972.tb05822.x.

[134] L. Wilson. Exploisive volcanic eruptions - 3. plinian eruption columns. *Geophis J R astr Soc.*, 45:543–556, 1976.

[135] L. Wilson and T.C. Huang. The influence of shape on the atmospheric settling velocity of volcanic ash particles. *J. Geophys. Res.*, 83(B4): 1829–1836, 1979.

[136] L. Wilson and G.P.L. Walker. Explosive volcanic eruptions vi- ejecta dispersal in plinian eruptions: the control of eruption conditions and atmospheric properties. *Geophis J R astr Soc.*, 89:651–679, 1987.

[137] L. Wilson, R.S.J. Sparks, T.C. Huang, and N.D. Watkins. The control of volcanic column heights by eruption energetics and dynamics. *J. Geophys. Res.*, 83(B4):1829–1836, 1978.

[138] Dieter A. Wolf-Gladrow. *Lattice-Gas Cellular Automata and Lattice Boltzmann Models: an Introduction.* Lecture Notes in Mathematics, 1725. Springer, Berlin, 2000.

[139] A. W. Woods. The fluid dynamics and thermodynamics of plinian eruption columns. *Bull Volcanol.*, 50:169–193, 1988.

[140] A. W. Woods and M. Bursik. Particle fallout, thermal disequilibrium and volcanic plumes. *Bull. Volcanol.*, 53:559–570, 1988.

[141] A. W. Woods and J. Kienle. The dynamics and thermodynamics of volcanic clouds: Theory and observations from the april 15 and april 21, 1990 eruptions of redoubt volcano, alaska. *J. Volcanol. Geotherm. Res.*, 62(1-4):273 – 299, 1994. ISSN 0377-0273. doi: 10.1016/0377-0273(94)90037-X. URL `http://www.sciencedirect.com/science/article/pii/037702739490037X`. ¡ce:title¿The 1989-1990 Eruptions of Redoubt Volcano, Alaska ¡/ce:title¿.

[142] H. M. N. Wright, K. V. Cashman, M. Rosi, and R. Cioni. Breadcrust bombs as indicators of vulcanian eruption dynamics at guagua pichincha volcano, ecuador. *Bull. Volcanol.*, 69:281300, 2007.

[143] B.P. Zeigler, H. Praehofer, and T.G. Kim. *Theory of modeling and simulation: integrating discrete event and continuous complex dynamic systems.* Academic Press, 2000. ISBN 9780127784557. URL `http://www.elsevierdirect.com/product.jsp?lid=0&iid=5&sid=0&isbn=0127784551`.